UNIVERSITY OF CALIFORNIA SAN DIEGO

Development of a versatile gene delivery system using silica nanobowls

A dissertation submitted in partial satisfaction of the
requirements for the degree Doctor of Philosophy

in

Nanoengineering

by

Madhura Som

Committee in charge:

Professor Ratneshwar Lal, Chair
Professor Liangfang Zhang, Co-Chair
Professor Shaochen Chen
Professor Jesse Jokerst
Professor Victor Ruiz-Velasco
Professor Veronica Shubayev

2020

The dissertation of Madhura Som is approved, and it is acceptable in quality and form for publication on microfilm and electronically:

_____

_____

_____

_____

_____

Co-Chair

_____

Chair

University of California San Diego

2020

DEDICATION

This dissertation is dedicated to Hazel, and all the strong women I know and yet to know…

EPIGRAPH

Out of the night that covers me,
Black as the pit from pole to pole,
I thank whatever gods may be
For my unconquerable soul.

In the fell clutch of circumstance
I have not winced nor cried aloud.
Under the bludgeonings of chance
My head is bloody, but unbowed.

Beyond this place of wrath and tears
Looms but the Horror of the shade,
And yet the menace of the years
Finds and shall find me unafraid.

It matters not how strait the gait,
How charged with punishments the scroll,
I am the master of my fate,
I am the captain of my soul.

Invictus, William Ernest Henley

TABLE OF CONTENTS

LIST OF ABBREVIATIONS

NB/NBs Nanobowl/Nanobowls

LNB/LNBs Lipid encapsulated nanobowl/nanobowls

TEOS Tetraethylorthosilicate

APTES 3-Aminopropyltriethoxysilane

DMF Dimethyl Formamide

DMSO Dimethyl Sulfoxide

TGA Thermogravimetric Analysis

SEM Scanning electron microscopy

TEM Transmission electron microscopy

DLS Dynamic Light Scattering

DRG Dorsal Root Ganglion

SCG Superior Cervical Ganglion

DNA Deoxyribonucleic acid

cDNA Complimentary DNA

DOTAP 1,2-dioleoyl-3-trimethylammonium-propane

DOPE 1,2-dioleoyl-sn-glycero-3-phosphoethanolamine

DPPC 1,2-dipalmitoyl-sn-glycero-3-phosphocholine

GPCR G-protein coupled receptor

GIRK G protein coupled inwardly rectifying potassium channel

RNA Ribonucleic Acid

siRNA Silencing RNA

SPION Superparamagnetic iron oxide nanoparticles

Dex Dexamethasone

SQUID Superconducting Quantum Interference Device

ICP-MS Inductively coupled plasma mass spectrometer

LIST OF FIGURES AND TABLES

ACKNOWLEDGEMENTS

I would like to acknowledge Professor Ratneshwar Lal for his support as the chair of my committee, for entrusting me with impactful research projects and connecting me with strong collaborations. I am grateful to all the Lal lab members for their support over the years, especially Dr. Deependra Ban.

I would like to acknowledge Professor Victor Ruiz-Velasco for his consistent support and encouragement that helped take the DNA delivery work to fruition. I would like to sincerely thank Dr. Sanjib Adhikary, Mr. Paul Herold and Dr. Laura Anselmi at Penn State College of Medicine, who have helped me immensely with numerous discussions, valuable technical assistance and welcomed me warmly as an extended family.

I would like to thank all my committee members for their continued support, advice, and encouragement in my projects. I would especially like to acknowledge Professors Shubayev and Ruiz-Velasco for introducing me to the field of anesthesiology and inspiring me with their work, kindness, and integrity.

I would like to acknowledge the Friends International Student Fellowship, the Joan and Irwin Jacobs fellowship, the Nanoengineering department, and the Mathematics Department for understanding the financial hurdles of graduate school and supporting me with fellowships and teaching assistantships along the way that helped pay the bills. I want to thank my students both in the lab (Jaime Castillo, Kenia Pardini, Denny Nguyen, and Diep Nguyen) and in the classrooms, who have kept the spirit of sharing of knowledge and joy in science alive in me all throughout this journey.

Although the pursuit of a PhD can sometimes become an incredibly isolating experience, I am grateful for all my friends who always filled me with strength to weather the ups and downs of this journey. They include but are not limited to Oishi, Sravani, Khyati, Harshita, Vidhya, Alex, Ouloide, Maria, Irem, Aditya, Bitan, Titas, Debayan, Saptarshi, Adithyavi, Lenord, Ayon, Santa, Kaapi and Sreemoyee.

Last but not the least, I would like to thank my mother (Suptasree Som), sister (Moyurie Som), father (Dr. Sudip K. Som), aunt (Dr. Suchitra Sen) and husband (Dr. Bharat Sridhar) for being my rock and pillars during the many hurdles and hardships of my PhD journey. Without their unconditional love and unwavering faith in my success, I would not have graduated.

Chapter 3, in part, has been published in ACS Bioconjugate Chemistry (2020) with coauthors Dr. Ratneshwar Lal and Dr. Victor Ruiz-Velasco. The dissertation author was the primary investigator and author of this material.

Chapter 4, in part, has been published in ACS Bioconjugate Chemistry (2020) with coauthors Dr. Ratneshwar Lal and Dr. Victor Ruiz-Velasco. The dissertation author was the primary investigator and author of this material.

Chapter 5, in part, has been published in ACS Bioconjugate Chemistry (2020) with coauthors Dr. Ratneshwar Lal and Dr. Victor Ruiz-Velasco. The dissertation author was the primary investigator and author of this material.

Chapter 6, in part, is being prepared for a patent application with Dr. Ratneshwar Lal as co-author. The dissertation author was the primary author of this chapter.

VITA

2011 Bachelor of Technology, Heritage Institute of Technology, Kolkata, India

2013 Master of Science, State University of New York at Stony Brook

2013-14 Research Intern, Brookhaven National Laboratory, New York

2014-2017 Research Assistant, University of California San Diego

2018-2020 Teaching Assistant, University of California San Diego

2020 Doctor of Philosophy, University of California San Diego

PUBLICATIONS

S. Hsu, A. Rodarte, **M. Som,** G. Arya and A.Tao, “Colloidal Plasmonic Nanocomposites: From Fabrication to Optical Function”, *Chem. Rev.* 2018, 118, 6, 3100-3120.

M. Som, R. Lal and V. Ruiz-Velasco, “Lipid-encapsulated silica nanobowls as an efficient and versatile DNA delivery system”, *Bioconjugate Chem*. 2020, 31, 12, 2697–2711.

FIELDS OF STUDY

Major Field: Nanoengineering

Studies in gene nano delivery

Professor Ratneshwar Lal and Professor Liangfang Zhang

ABSTRACT OF THE DISSERTATION

Development of a versatile gene delivery system using silica nanobowls

by

Madhura Som

Doctor of Philosophy in Nanoengineering

University of California San Diego, 2020

Professor Ratneshwar Lal, Chair

Professor Liangfang Zhang, Co-Chair

Non-mesoporous Janus silica nanobowls (NBs) are unique in that they possess two different non-porous surfaces per particle for loading biological molecules and can thus be designed with multifunctional properties. Although silica NBs have been successfully employed for both targeted therapeutic and diagnostic applications, their ability to deliver DNA has not yet been fully explored. The purpose of this study was to design and develop an *in vitro* transfection agent that would exploit the distinct characteristics of the silica NB. In this work, we have demonstrated that such silica NBs

can be used for *in vitro* (cell lines and primary neurons) and *ex vivo* transfections (dorsal root ganglia, DRG). We have shown that the NB system can be effectively used for supercoiled as well as linearized DNA loading and delivery in cells with dose-modulated protein expression efficiencies in a cell line dependent manner. NBs were shown to successfully internalize in vitro (cell lines and neurons), ex vivo (rat DRG) and in vivo (rat DRG and salivary gland) with high cell viability. This work also demonstrates the use of lipid encapsulation on the silica NBs to overcome vesicular entrapment following endocytosis, which is a well-known bottleneck to non-viral nano delivery systems.

After the characterization and optimization of the lipid encapsulated silica NB system (LNB), four different gene delivery applications show its versatility. First, controlled release of linearized DNA was demonstrated with NBs in the presence of reducing agents and their relative protein expression efficiencies were compared with other constructs i.e. linearized and supercoiled. Second, the LNB system was used to transfect neurons and glia in the DRG of rats *in vitro* or *ex vivo*. Thirdly, the LNB system was used to co-deliver three different constructs simultaneously to functionally reconstruct the coupling of two membrane proteins relevant in opioid-dose response in the nervous system. G-protein coupled opioid receptors and G-protein coupled inversely rectifying K^+ channels (GIRKs) were functionally co-expressed by LNB transfection in HEK cell line and demonstrated as an *in vitro* model for testing potent opioids like fentanyl and oxycodone with a high throughput membrane potential assay. Finally, the LNB system was further modified with SPIONS and explored as a dexamethasone/silencing RNA co-delivery platform relevant in therapeutic interventions in cancer and infectious diseases like Covid19.

Overall, these results lay the foundation for the use and further development of silica NBs as non-viral transfection agents.

Chapter 1

Introduction to gene delivery

1.1 Background

Nucleic acids like DNA (deoxyribonucleic acid) and RNA (ribonucleic acid), due to their phosphate backbones, are highly negatively charged, large molecules extremely prone to degradation from enzymes in the extracellular space. Additionally, the cell membrane, due to the charged ends of the phospholipids and embedded proteins, present a net negatively charged phospholipid bilayer barrier to the passage of nucleic acids. In nucleic acid delivery, the goal is to deliver different types of nucleic acid constructs from the extracellular space to the interior of the cell, overcoming physiological barriers like the plasma membrane. The overarching goal for nucleic acid delivery is to tune protein expression in a target cell either for investigative research into protein function/localization/interactions or for therapeutic reasons (gene therapy). In either case, delivering the gene will lead to expression of a protein when it is not normally expressed by the cell or silence/down regulate the expression of a protein that is naturally expressed by the target cell. Following the principles of the 'central dogma' of molecular biology [1], we know that the code for a protein is encrypted in the genome of the cell in the form of chromosomal DNA located within the nucleus. In order to produce the protein, the first step is the 'transcription' of the gene coding for the protein into messenger RNA or mRNA, a process that occurs in the nucleus. After transcription, the mRNA travels to the ribosomes in the cytoplasm and here, it is used as a template for the synthesis of the protein i.e., translation. The final destination of the nucleic acid delivery within the cell

could be the nucleus or the cytoplasm. It depends on the type of nucleic acids delivered and where they are processed inside the cell.

From a clinical perspective, with advances in human genome sequencing and newer gene engineering tools[2] like TALEN, ZFN and CRISPR/Cas 9, more and more diseases are being recognized as application targets for gene therapy efforts[3]. There are many current clinical approaches that are being investigated to apply gene therapy- 1) Replacing a mutated/defective/malfunctioning gene with a correct one 2) Blocking the function of a defective gene to prevent it from producing an aberrant protein/down regulate the expression of the protein 3) Introducing new genes (not naturally present in the genome) into the cells transiently or permanently into the genome to a) express a protein not naturally produced by the target cells for therapy b) for future protection from diseases (vaccines). In recent times, gene therapy is being used for a multitude of diseases, including ones caused by single gene defects like cystic fibrosis[4][3], and acquired ones like cancer, cardiovascular disease, neurodegenerative disorders[3], [5], and infectious diseases[3]. The ongoing Covid19 pandemic has also seen the clinical application of gene therapy by companies like Moderna, Pfizer etc. towards vaccine development[6].

Table 1.1 Types of nucleic acids commonly delivered and their characteristics [2], [3]

Nucleic acid	Sub-types	Size (bp)	Strands	Effect	Destination in Cell
DNA	Plasmids (e.g. single/multiple protein expression, CRISPR/Cas9, ZFN, TALENs, transposons)	~2-10k	Double	Protein expression or base edits in genomic DNA	Nucleus
	Vector less/ linear	~0.5-10k	"	Protein expression/integration into chromosomal DNA	‘’
RNA	mRNA	~0.5-5k	Single	Expression	Cytoplasm/ Ribosomes
	Base modified RNA	‘’	‘’	Expression	‘’
	Self-amplifying RNA (can also be delivered as a plasmid DNA)	‘’	‘’	Expression	‘’
Oligonucleotides	Silencing RNA or siRNA	<30	Double	Silence/downregulate	Cytoplasm
	Anti-sense RNA		Single	Silence/downregulate	‘’
	microRNA or miRNA		Single	Silence/downregulate	‘’

Finally, because of the barriers to nucleic acid delivery i.e. plasma membrane and nuclear membrane, the usefulness of all the constructs listed in Table 1.1 is solely dependent on the ability to deliver them successfully to their intracellular target and do so efficiently. In fact, the efficiency of each of these nucleic acids towards their final goal is only as good as the efficiency of the delivery system[7], [8]. Although plasma membrane is the ultimate barrier to nucleic acid delivery, from a clinical perspective, apart from *in vitro*, *ex vivo* and *in vivo* gene delivery are also important goals for therapeutic development. The holy grail of gene delivery technology development for clinical use is achieving high loading of genetic efficiency and low toxicity/immunogenicity from the delivery vehicle. Therefore, engineering of an efficient nucleic acid delivery system is of utmost importance to the outcome. Efforts towards pushing the boundaries of the delivery system has far reaching implications on removing the bottlenecks that exist today in gene delivery[7] and will therefore have far reaching implications on the future of medicine and healthcare, especially in a post Covid19 world.

Today, there is a broad array of technologies at play for nucleic acid delivery. They can be broadly classified into (a) Biological techniques (b) Physical techniques and (c) Chemical techniques. This chapter has focused on the biological (viral) and physical (non-viral) techniques. Chemical techniques mostly consist of synthetic nanomaterials used for gene delivery which is discussed in the following Chapter 2.

1.2 Biological gene delivery systems

Biological gene delivery systems consist of viruses that have been genetically modified to carry and deliver the gene of interest [9]–[12] . This process is called transduction. Viruses are highly evolved biological entities that can efficiently enter host cells and use the cell's own machinery to replicate (infection pathway). Ideal viruses for transduction are those that can exploit this infection pathway to deliver genes of interest without the expression of the viral gene itself and its subsequent replication and toxicity in the target. Viral transduction technique in theory can be applied to somatic cells or germline cells but in practice gene delivery is limited to the former due to ethical concerns [10]. Viruses used for transduction fall in the following 5 categories[9].

a. Adenoviruses : Adenoviruses (Ad) represent one of the oldest and, clinically and biologically most studied gene delivery system [9]. They are non-enveloped double stranded DNA virus with the packaging capacity of 8 kbp, which does not integrate into the host genome. Since an unfortunate death of an 18-year-old patient due to the toxicity related to a high dose of adenoviral (Ad) vectors for via the hepatic artery, Ad vectors have undergone extensive engineering to remove immunogenic effects for clinical use. Through many generations of development, the helper dependent Ad vectors which have all their viral genes deleted shows the most promise for less immunogenicity and prolonged transgene expression with increased theoretical packaging capacity to 30 kbp [9], [13], [14].

b. Adeno associated viruses (AAV) : AAV is a single stranded DNA carrying parvovirus[9], [10], [13]. 96% of its genome can be modified to package a foreign

expression cassette. After receptor binding mediated endocytosis and release from vesicles, they enter the nucleus where they un coat and release their ssDNA, which is then converted into a double stranded DNA template for the transcription and translation of the gene. AAVs have several unique advantages for clinical applications i.e., broad tropism, low immunogenicity and ease of production and it rarely integrates into the host genome. Many clinical applications of gene therapy have used AAVs and most prominently, in 2019, the FDA approved AAV-based gene therapy drug Zolgensma for the treatment of spinal muscular dystrophy [13].

c. Herpes simplex virus : HSV1 is a promising viral delivery system for therapeutic applications. It is a complex virus that is one of the largest being considered for gene therapy applications[9], [12], [15]. The main reason for this is that this is a virus that has a very large packaging capacity (40 kbp) of foreign DNA that can potentially deliver single large or multiple cassettes of therapeutic protein expression sequences in one vector. Using an amplicon approach, this capacity can be further expanded to 150 kbp that allows for delivery of very large genomic sequences of therapeutically relevant genes that are not possible by other viral transduction methods e.g., the complete genomic human hypoxanthine phosphoribosyltransferase locus (115 kb). HSV-1 has a natural tropism towards sensory neurons and therefore finds applicability in many disorders of the nervous system.

d. Retrovirus : Retroviruses are enveloped viruses that carry two copies of a single stranded positive sense RNA genome. Upon entry to the host cell, the virus uses reverse transcriptase to transcribe its RNA genome to a double stranded DNA which

subsequently integrates into the host genome by the viral integrase. This ability to permanently alter the host genome is the biggest advantage of this viral vector family. RVs have been extensively used for clinical gene therapy applications like monogenic disorders, cancer, and infectious diseases[9], [15]. Currently, RV mediated gene therapy applications have been reinvigorated with lentiviral delivery systems described below.

e. Lentivirus : Lentiviruses are RNA viruses of the retrovirus family and uses reverse transcription to convert into a cDNA in the host cytoplasm[9], [16]. The lentiviral cDNA, complexed with other viral factors (pre-initiation complex) and a structural feature called the 'DNA flap', able to translocate through nuclear membrane and lead to successful transduction of differentiated, non-diving cells as well as cells of monocyte/macrophage lineage [16]. Lentiviral vectors have broad tropism and can get integrated into the host genome. This integration can induce oncogenesis in some applications. There are 2 main types of lentiviral vectors (a) human derived (HIV1 and HIV2) (b) non-human primate derived (simian, feline, equine, etc.). Non-primate origin LVs need a lot more engineering of their genome to prevent unwanted immunogenicity in the clinical setting. LVs are characterized by their long latent incubation periods with low level of viral pathogenicity [16]. Kymriah and Yescarta are two FDA approved chimeric antigen receptor (CAR-T) cell therapy targeting B cell lymphomas in the US. In this therapy, the T-cells of a patient or host are genetically modified ex-vivo with lentiviral vectors and then transfused into the patient's circulation[16].

1.2.1 Preparation of viral vectors for gene delivery

For the preparation of therapeutic viral transduction systems, some of the coding regions from the viral genome are deleted, especially those which lead to toxicity, leaving intact only those genes *in cis* that are responsible for packaging the viral genome within the capsid and the integration of the viral DNA into the host's genome. Then the expression cassette i.e., the genetic sequence of interest is added in place of the deleted genes in the edited viral DNA. At this point, the deleted viral genes that are responsible for packaging functions like replication or capsid protein expression are engineered into a different construct to provide helper functions to the main edited viral DNA *in trans*. Both the constructs are then transfected into a packaging host cell line where viral recombination and scale up occurs. The viral particles are then purified usually by chromatographic separation methods in high titers for clinical use[9]**.**

1.2.2 Advantages and drawbacks of viral transduction systems

Viruses are still the most efficient gene delivery system for cell lines but more importantly with primary cells, tissue targets *in vivo* and, most importantly, difficult to transfect non-dividing cells like neurons [9].

The main drawback of viral transduction systems is their various toxic side effects on the host system. Firstly, viruses can trigger an immune response as in many cases the body's immune system is unable to differentiate between therapeutic viral loads and wild types. AVs are the most immunogenic viral systems as they are known to have cytotoxic T-lymphocyte responses from transduced cells and also potent cytokine

inflammatory response to the viral capsid. Lentiviral and AAV vectors on the other hand show less immunogenicity. Viral transduction induced immunogenicity is complex, dependent on viral titers used and the route of administration. Another cause of adverse side effects of viral vector-based gene delivery is the risk of insertional mutagenesis for integrating retroviruses and integrating rAAV. Besides the immunogenicity and toxicity of viral systems, most viruses have broad tropism and therefore are not selective in their target. Although viruses are extremely efficient in their ability to deliver genetic material, one viral particle can only carry one expression cassette gene copy. This means that to reach therapeutic doses, often high titers are administered. All these factors combine into the fact that at therapeutic doses, it is often exposing the whole body to the various inflammatory, immunogenic, toxic, and mutagenic side effects of the viral titer. Although viral systems are constantly undergoing engineering to improve capsid targeting, synthesis of hybrid/recombinant varieties and reduce immunogenicity by viral genome modifications, these design efforts require incredible infrastructure and expertise that will make this operation quite expensive, slow, and complicated. From a clinical perspective, handling most viruses also requires higher expenditure maintaining Biosafety Level 2 (BSL2) workspaces to prevent exposure to the staff. Although a number of labs and biotech companies are invested in this technology, in the face of the Covid19 pandemic, most of the companies developing a vaccine (Moderna/NIH, Pfizer/BioNTech) have chosen a non-viral technology possibly because of such drawbacks and the considerably less complicated route to regulatory approval in a global pandemic where speed of development/regulatory approval could potentially save millions of lives across the globe.

Table 1.2 Characteristics of viral transduction systems in gene therapy [9], [15]**.**

Virus family	**Nucleic acid payload**	**Packaging capacity (kb)**	**Tropism**	**Host genome integration**	**NIH Risk Group**	**Advantage**
Adenovirus (AV)	dsDNA	8 30 (helper dependent)	Broad	Episomal	2 (BSL2)	Highly efficient transduction of most tissues
Adeno Associated Virus (AAV)	ssDNA	< 5	Broad	Episomal (>90%) Integrated (>10%)	1 (BSL1)	Nonimmunogenic, non-pathogenic
Retrovirus (RV)	RNA	8	Dividing cells only	Integrated	2 (BSL2)	Persistent gene transfer in most tissues
Lentivirus (LV)	RNA	8	Broad	Integrated	3 (HIV) (BSL2)	Persistent gene transfer in most tissues
Herpes simplex virus (HSV1)	dsDNA	40 150 (amplicon)	High, Sensory neurons	Episomal	2 (BSL2)	Large packaging capacity, specificity for sensory neurons

1.3 Physical gene delivery systems

Physical gene delivery systems create transient holes in the cell membrane of the target and directly deliver the nucleic acids in the target cell cytoplasm without any external vehicles. These techniques are categorized into the following:

1.3.1. Electroporation

Electroporation is the technique of using a short series of high voltage pulses applied to cells/tissues in suspension in a buffer containing the nucleic acids to be delivered[17]–[20]. The application of the voltage allows physical pores to form transiently on the cell membrane of the suspended cells allowing buffer with nucleic acids to diffuse physically through them. Voltages like 100 V/cm for larger cells and 1-2 kV/cm for small cells like bacteria are common[17]. The voltage, pulse lengths, numbers of pulses and amount of nuclear material in suspension require optimization to reach a protocol that is not too toxic for cells. Electroporation works well with various nucleic acid constructs like DNA, RNA, silencing RNA, etc. DNA of various sizes up to 100kbp can be used, however, larger DNA sizes are expressed with less efficiency[17], [18], [20]. This is because, electroporation is a multi-step process, starting with interaction of the DNA with the cell membrane pores, trafficking into the cytoplasm, intracellular transport, and entry into the nucleus[17].

In the case of DNA, once it reaches the cell cytoplasm, it still needs to make its way into the nucleus to access the transcription machinery while battling rapid degradation in the cytoplasm due to nucleases. For this reason, the efficacy of

electroporation is the highest in mitotic cells, whereby the DNA can enter the nucleus due to the absence of the nuclear envelope between metaphase and anaphase and remain trapped inside when the nuclear membrane is reformed at telophase[20]. There have been reports of enhancements to electroporation (called 'iontoporation'[20]) by combining it with nuclear membrane disrupting amphipathic molecules like TCHD to improve delivery of plasmid DNA into the nucleus of post-mitotic primary cells like mature neurons[20].

Because of the inherent risks of voltage application, transfection with electroporation is most applicable for *in vitro* on suspended cells and tissues. From a clinical perspective, CAR-T cell therapy is the most promising application area for electroporation-based gene delivery[18]. Since a lot of viral delivery systems suffer from drawbacks of immunogenic responses from introduction of transduced cells *in vivo* as well as limitation to the size of nucleic acid payload delivered by viruses, electroporation is clearly far more advantageous. To deliver several expression cassettes concurrently to express chimeric antigen receptors, electroporation is a good strategy. It allows delivery of large plasmids (up to 100 kbp) and no immunogenicity downstream[18]. *In vivo* electroporation has been reported for a number of tissues like skin, liver, lung, kidney bladder, brain, adipose tissue[17], [20]. *In vivo* electroporation can be quite invasive with various types of needles and array electrodes.

1.3.2. Sonoporation/ultrasound assisted gene transfer (UAGT)

The physical disruption of cell membranes by acoustic pressure waves in the ultrasound range of the spectrum (20K-GHz) resulting in holes from nanometers to several microns is called sonoporation[21]–[25], [25], [26]. It has been used to deliver

DNA of various sizes, and less popularly antisense oligonucleotides, siRNA, and mRNA. In many cases, ultrasound i.e. sonoporation technique is used in conjunction with other gene delivery vehicles like viruses[17], [26], [27], gold nanoparticles, polymers, etc. to achieve much higher efficiencies that can be individually achieved by either method. The two main mechanisms ascribed to ultrasound mediated cell permeabilization[28] are (a) stable cavitation mediated microstreaming where cavitation bubbles are oscillating close the cell membrane (b) jetting forces due to inertial cavitation induced by a cavitation bubble collapse[22]. Although the final goal of sonoporation is *in vivo* delivery, *in vitro* work by many researchers have helped understand the inherent mechanisms involved and further optimize the system for *in vivo* use. One disadvantage of UAGT is the cavitation induced local hyperthermia and reactive oxygen species formation, all of which lead to significant loss of transfected cell population by apoptosis, necrosis, or cell disruption. These effects can be more pronounced *in vitro* and therefore require extensive tuning and optimization of ultrasound parameters. Therefore, many researchers have concluded that *in vivo* applications are more promising with this technique[28]. By fine tuning ultrasound parameters, very little overall toxicity is observed in a wide range of tissues. In addition, exceptional targeting ability of UAGT can be achieved by using diagnostic ultrasound to locate the organ of interest. Some promising *in vivo* targets [17], [29]–[31] have been salivary gland of mouse, skin, tumors in mouse models, rat skeletal muscles, mouse myocardium and rat/mouse kidneys.

1.3.3. Biolistic particle delivery/gene gun

High velocity bombardment of exogenous nucleic acids bound to microparticles is called biolistics or microparticle bombardment or micro bombardment [32]–[35]. The microprojectile is aimed at biological tissues or cells for nucleic acid delivery whereby high gas flow rates provide enough momentum to the microprojectiles to physically enter the cells and nuclei. This type of transfection is non-specific and can be damaging to cells/tissues due to high velocity impact from microprojectiles. Biolistics find wide application in plant cells which are very large and have significant barriers to nucleic acid delivery like cell walls composed of cellulose. Biolistics are used in various gene expression studies in plants and in improving plant characteristics for agriculture (e.g. soybean, corn, wheat [36], etc.) like increased resistance to abiotic environmental stress and plant pathogens, weed control, increased antioxidants in fruits, increased yield, increased oil production, improving fruit/seed quality, etc. [37]. Several types of animal tissues have also been transfected with biolistics i.e. postnatal mouse cerebellum [33], murine acute cortical brain slices [32], HEK cells, dissociated neurons [33], [38] and mouse ear[38], porcine skin [39], human breast carcinoma cells[39] and *in vivo* in mouse skin and liver[40]. There have also been reports of biolistics applied in microorganisms like fungi, algae, and bacteria.

The branch of biolistics has recently also expanded into “nanobiolistics” where instead of micron (~ 1-1.5 µm diameter) sized beads (Gold or Tungsten) , nucleic acids are condensed onto nanoparticles (<500 nm diameter) and applied into cells and tissues as a projectiles in a similar gene gun set up[38]–[42]. The most commonly used

nanomaterials for nanobiolistics are mesoporous silica, carbon nanotubes (CNTs) and gold nanoparticles[43]. This is because: (a) these nanostructures can be made in different sizes, shapes, porosities, and tunable surface chemistries. (b) plant cells are larger than animal cells (up to 60µm) often have organelles like chloroplasts that are in the same size range as micron sized biolistic projectiles which can't efficiently penetrate them (c) for applications in animal tissues, several groups have demonstrated the advantage of nanobiolistics in significantly less tissue damage with comparable transfection efficiencies [38]–[41]. In the clinical sphere, biolistics seem most applicable to gene delivery in the skin[44]–[47] i.e. genetic vaccinations that need to reach the epidermal layer, genetic immunizations[44], [48], wound healing[47], and suicide gene therapy to treat cancer. Some promising results have also been reported for liver[49] and brain [50], [51] as clinical targets for biolistics.

1.3.4. Microinjection

Microinjection is the process of physically and directly injecting nuclear material in precise locations in the target cell i.e., cytoplasm or nucleus. When the injection is done in the target cell's nucleus, usually for DNA delivery, it is called nucleofection[52]. Usually, a cell membrane impermeable dye mixed into the sample is used to determine the success of injection and cells that survive the injection process have 100% transduction efficiency. Compared to other physical or chemical gene delivery systems, microinjection is the least stressful to cells if done correctly and multiple constructs of any size can be easily co-injected. Microinjections are most popular in primary cells like embryos and neurons.

Microinjections are extremely labor intensive, requires a dedicated equipment set up and extensive training to acquire the expertise of injecting cells and ensure viability post-injection. Although microinjections lead to theoretically 100% efficiency, only a few cells can be transfected at a time and the results are not scalable for analysis with protein expression assays like Western blotting, immunoprecipitation, etc. For diving cell lines, the effect of gene delivery can easily be diluted as the cells divide. Clinically, microinjections are relevant in producing transgenic animals, in understanding neuronal communication and *in vitro* fertilization (IVF) applications within ethical and regulatory guidelines.

1.4 Bibliography

[1] G. P. Rédei, “Central Dogma,” *Encycl. Genet. Genomics, Proteomics Informatics*, vol. 227, pp. 309–309, 2008, doi: 10.1007/978-1-4020-6754-9_2672.

[2] S. Tong, B. Moyo, C. M. Lee, K. Leong, and G. Bao, “Engineered materials for in vivo delivery of genome-editing machinery,” *Nat. Rev. Mater.*, vol. 4, no. 11, pp. 726–737, 2019, doi: 10.1038/s41578-019-0145-9.

[3] L. W. Seymour and A. J. Thrasher, “Gene therapy matures in the clinic,” *Nat. Biotechnol.*, vol. 30, no. 7, pp. 588–593, 2012, doi: 10.1038/nbt.2290.

[4] A. Da Silva Sanchez, K. Paunovska, A. Cristian, and J. E. Dahlman, “Treating Cystic Fibrosis with mRNA and CRISPR,” *Hum. Gene Ther.*, vol. 31, no. 17–18, pp. 940–955, 2020, doi: 10.1089/hum.2020.137.

[5] M. Simonato, J. Bennett, N. M. Boulis, M. G. Castro, D. J. Fink, W. F. Goins, S. J. Gray, P. R. Lowenstein, L. H. Vandenberghe, T. J. Wilson, J. H. Wolfe, and J. C. Glorioso, “Progress in gene therapy for neurological disorders,” *Nat. Rev. Neurol.*, vol. 9, no. 5, pp. 277–291, 2013, doi: 10.1038/nrneurol.2013.56.

[6] M. D. Shin, S. Shukla, Y. H. Chung, V. Beiss, S. K. Chan, O. A. Ortega-Rivera, D. M. Wirth, A. Chen, M. Sack, J. K. Pokorski, and N. F. Steinmetz, “COVID-19 vaccine development and a potential nanomaterial path forward,” *Nat. Nanotechnol.*, vol. 15, no. 8, pp. 646–655, 2020, doi: 10.1038/s41565-020-0737-y.

[7] T. M. Reineke, R. T. Raines, and V. M. Rotello, “Delivery of Proteins and Nucleic Acids: Achievements and Challenges,” *Bioconjug. Chem.*, vol. 30, no. 2, pp. 261–262, 2019, doi: 10.1021/acs.bioconjchem.9b00096.

[8] J. van Haasteren, J. Li, O. J. Scheideler, N. Murthy, and D. V. Schaffer, “The delivery challenge: fulfilling the promise of therapeutic genome editing,” *Nat. Biotechnol.*, vol. 38, no. 7, pp. 845–855, 2020, doi: 10.1038/s41587-020-0565-5.

[9] C. E. Thomas, A. Ehrhardt, and M. A. Kay, “Progress and problems with the use of viral vectors for gene therapy,” *Nat. Rev. Genet.*, vol. 4, no. 5, pp. 346–358, 2003, doi: 10.1038/nrg1066.

[10] Y. K. Sung and S. W. Kim, “Recent advances in the development of gene delivery systems,” *Biomater. Res.*, vol. 23, no. 1, pp. 1–7, 2019, doi: 10.1186/s40824-019-0156-z.

[11] M. K. Riley and W. Vermerris, “Recent advances in nanomaterials for gene delivery—A review,” *Nanomaterials*, vol. 7, no. 5, pp. 1–19, 2017, doi: 10.3390/nano7050094.

[12] D. L. Puhl, A. R. D’Amato, and R. J. Gilbert, “Challenges of gene delivery to the central nervous system and the growing use of biomaterial vectors,” *Brain Research Bulletin*, vol. 150. Elsevier Inc., pp. 216–230, Aug. 01, 2019, doi: 10.1016/j.brainresbull.2019.05.024.

[13] C. Li and R. J. Samulski, “Engineering adeno-associated virus vectors for gene therapy,” *Nat. Rev. Genet.*, vol. 21, no. 4, pp. 255–272, 2020, doi: 10.1038/s41576-019-0205-4.

[14] P. Boucher, X. Cui, and D. T. Curiel, “Adenoviral vectors for in vivo delivery of CRISPR-Cas gene editors,” *Journal of Controlled Release*, vol. 327. Elsevier B.V., pp. 788–800, Nov. 10, 2020, doi: 10.1016/j.jconrel.2020.09.003.

[15] S. Ghosh, A. M. Brown, C. Jenkins, and K. Campbell, “Viral Vector Systems for Gene Therapy : A Comprehensive Literature Review of Progress and Biosafety Challenges,” vol. 25, no. 1, pp. 7–18, 2020, doi: 10.1177/1535676019899502.

[16] A. M. Munis, “Gene therapy applications of non-human lentiviral vectors,” *Viruses*, vol. 12, no. 10, 2020, doi: 10.3390/v12101106.

[17] D. J. Wells, “Electroporation and ultrasound enhanced non-viral gene delivery in vitro and in vivo,” *Cell Biol. Toxicol.*, vol. 26, no. 1, pp. 21–28, 2010, doi: 10.1007/s10565-009-9144-8.

[18] E. Harris and J. J. Elmer, “Optimization of electroporation and other non-viral gene delivery strategies for T cells,” *Biotechnol. Prog.*, no. June, 2020, doi:

10.1002/btpr.3066.

[19] Z. Zhang, T. Zheng, and R. Zhu, “Single-cell individualized electroporation with real-time impedance monitoring using a microelectrode array chip,” *Microsystems Nanoeng.*, vol. 6, no. 1, 2020, doi: 10.1038/s41378-020-00196-0.

[20] A. De La Rossa and D. Jabaudon, “In vivo rapid gene delivery into postmitotic neocortical neurons using iontoporation,” *Nat. Protoc.*, vol. 10, no. 1, pp. 25–32, 2015, doi: 10.1038/nprot.2015.001.

[21] D. L. Miller, S. V. Pislaru, and J. F. Greenleaf, “Sonoporation: Mechanical DNA delivery by ultrasonic cavitation,” *Somatic Cell and Molecular Genetics*, vol. 27, no. 1–6. Somat Cell Mol Genet, pp. 115–134, Nov. 2002, doi: 10.1023/A:1022983907223.

[22] Z. Fan, R. E. Kumon, and C. X. Deng, “Mechanisms of microbubble-facilitated sonoporation for drug and gene delivery,” *Therapeutic Delivery*, vol. 5, no. 4. Future Science Ltd, pp. 467–486, 2014, doi: 10.4155/tde.14.10.

[23] M. Tomizawa, F. Shinozaki, Y. Motoyoshi, T. Sugiyama, S. Yamamoto, and M. Sueishi, “Sonoporation: Gene transfer using ultrasound,” *World J Methodol*, vol. 3, no. 4, pp. 39–44, 2013, doi: 10.5662/wjm.v3.i4.39.

[24] B. Helfield, X. Chen, S. C. Watkins, and F. S. Villanueva, “Biophysical insight into mechanisms of sonoporation,” *Proc. Natl. Acad. Sci. U. S. A.*, vol. 113, no. 36, pp. 9983–9988, Sep. 2016, doi: 10.1073/pnas.1606915113.

[25] S. Mehier-Humbert and R. H. Guy, “Physical methods for gene transfer: Improving the kinetics of gene delivery into cells,” *Advanced Drug Delivery Reviews*, vol. 57, no. 5. Elsevier, pp. 733–753, Apr. 05, 2005, doi: 10.1016/j.addr.2004.12.007.

[26] Y. Jang, D. Kim, H. Lee, H. Jang, S. Park, G. E. Kim, H. J. Lee, H. J. Kim, and H. Kim, “Development of an ultrasound triggered nanomedicine-microbubble complex for chemo-photodynamic-gene therapy,” *Nanomedicine Nanotechnology, Biol. Med.*, vol. 27, p. 102194, Jul. 2020, doi: 10.1016/j.nano.2020.102194.

[27] C. H. Peng, L. C. Woung, K. H. Lu, C. Y. Tsai, S. D. Lee, C. S. Huang, T. C. Lin, K. H. Chien, and D. K. Hwang, “Acoustic waves improves retroviral transduction in human retinal stem cells,” *J. Chinese Med. Assoc.*, vol. 81, no. 9, pp. 830–836, 2018, doi: 10.1016/j.jcma.2018.05.002.

[28] M. P. Stewart, R. Langer, and K. F. Jensen, “Intracellular delivery by membrane disruption: Mechanisms, strategies, and concepts,” *Chem. Rev.*, vol. 118, no. 16, pp. 7409–7531, 2018, doi: 10.1021/acs.chemrev.7b00678.

[29] C. R. Hill and G. R. Ter Haar, “High intensity focused ultrasound - Potential for

cancer treatment," *British Journal of Radiology*, vol. 68, no. 816. British Institute of Radiology, pp. 1296–1303, 1995, doi: 10.1259/0007-1285-68-816-1296.

[30] M. J. Passineau, L. Zourelias, L. MacHen, P. C. Edwards, and R. L. Benza, "Ultrasound-assisted non-viral gene transfer to the salivary glands," *Gene Ther.*, vol. 17, no. 11, pp. 1318–1324, 2010, doi: 10.1038/gt.2010.86.

[31] M. A. Oberli, C. M. Schoellhammer, R. Langer, and D. Blankschtein, "Ultrasound-enhanced transdermal delivery: Recent advances and future challenges," *Therapeutic Delivery*, vol. 5, no. 7. Future Science Ltd, pp. 843–857, Jul. 01, 2014, doi: 10.4155/tde.14.32.

[32] M. I. K. Hamad, S. Daoud, P. Petrova, O. Rabaya, A. Jbara, N. Melliti, S. Stichmann, G. Reiss, J. Herz, and E. Förster, "Biolistic transfection and expression analysis of acute cortical slices," *J. Neurosci. Methods*, vol. 337, p. 108666, May 2020, doi: 10.1016/j.jneumeth.2020.108666.

[33] R. C. Murphy and A. Messer, "Gene transfer methods for CNS organotypic cultures: A comparison of three nonviral methods," *Mol. Ther.*, vol. 3, no. 1, pp. 113–121, Jan. 2001, doi: 10.1006/mthe.2000.0235.

[34] G. Transfer, "Get Right on Target With Precise Gene Delivery Systems Biolistic Delivery Systems." Accessed: Nov. 21, 2020. [Online]. Available: www.bio-rad.com/genetransfer/.

[35] J. A. O'brien and S. C. R. Lummis, "Biolistic transfection of neuronal cultures using a hand-held gene gun," 2006, doi: 10.1038/nprot.2006.145.

[36] Y.-C. Wang, T. M. Klein, M. Fromm, J. Cao, J. C. Sanford, and R. Wu, "Transient expression of foreign genes in rice, wheat and soybean cells following particle bombardment."

[37] N. J. Baltes, J. Gil-Humanes, and D. F. Voytas, *Genome Engineering and Agriculture: Opportunities and Challenges*, 1st ed., vol. 149. Elsevier Inc., 2017.

[38] J. A. O'brien and S. C. Lummis, "Nano-biolistics: a method of biolistic transfection of cells and tissues using a gene gun with novel nanometer-sized projectiles," 2011. doi: 10.1186/1472-6750-11-66.

[39] N. Zilony, A. Tzur-Balter, E. Segal, and O. Shefi, "Bombarding cancer: Biolistic delivery of therapeutics using porous si carriers," *Sci. Rep.*, vol. 3, pp. 1–6, 2013, doi: 10.1038/srep02499.

[40] J. Xia, A. Martinez, H. Daniell, and S. N. Ebert, "Evaluation of biolistic gene transfer methods in vivo using non-invasive bioluminescent imaging techniques," 2011. doi: 10.1186/1472-6750-11-62.

[41] A. Roychoudhury, “Journal of Molecular and Cellular Biology Forecast Nanobiolistics : New Generation Transfection System for Animals and Plants,” vol. 3, no. iii, pp. 1–4, 2020.

[42] R. G. Moulick, S. Das, N. Debnath, and K. Bandyopadhyay, “Potential use of nanotechnology in sustainable and ‘smart’ agriculture: advancements made in the last decade,” *Plant Biotechnol. Rep.*, vol. 14, no. 5, pp. 505–513, 2020, doi: 10.1007/s11816-020-00636-3.

[43] F. J. Cunningham, G. S. Demirer, N. S. Goh, H. Zhang, and M. P. Landry, “Chapter 7 Nanobiolistics: An Emerging Genetic Transformation Approach,” doi: 10.1007/978-1-0716-0356-7_7.

[44] B. Lu, G. Scott, and L. A. Goldsmith, “A model for keratinocyte gene therapy: preclinical and therapeutic considerations.,” *Proc. Assoc. Am. Physicians*, vol. 108, no. 2, pp. 165–172, Mar. 1996, Accessed: Nov. 22, 2020. [Online]. Available: https://europepmc.org/article/med/8705736.

[45] S. Wang, S. Joshi, and S. Lu, “Delivery of DNA to skin by particle bombardment.,” *Methods Mol. Biol.*, vol. 245, pp. 185–196, 2004, doi: 10.1385/1-59259-649-5:185.

[46] A. T. Larregina, S. C. Watkins, G. Erdos, L. A. Spencer, W. J. Storkus, D. Beer Stolz, and L. D. Falo, “Direct transfection and activation of human cutaneous dendritic cells,” *Gene Ther.*, vol. 8, no. 8, pp. 608–617, 2001, doi: 10.1038/sj.gt.3301404.

[47] J. M. Davidson, T. Krieg, and S. A. Eming, “Particle-mediated gene therapy of wounds,” *Wound Repair Regen.*, vol. 8, no. 6, pp. 452–459, Jan. 2000, doi: 10.1046/j.1524-475X.2000.00452.x.

[48] B. I. Loehr, P. Willson, L. A. Babiuk, and S. van Drunen Littel-van den Hurk, “Gene Gun-Mediated DNA Immunization Primes Development of Mucosal Immunity against Bovine Herpesvirus 1 in Cattle,” *J. Virol.*, vol. 74, no. 13, pp. 6077–6086, Jul. 2000, doi: 10.1128/jvi.74.13.6077-6086.2000.

[49] S. Kuriyama, A. Mitoro, H. Tsujinoue, T. Nakatani, H. Yoshiji, T. Tsujimoto, M. Yamazaki, and H. Fukui, “Particle-mediated gene transfer into murine livers using a newly developed gene gun,” *Gene Ther.*, vol. 7, no. 13, pp. 1132–1136, 2000, doi: 10.1038/sj.gt.3301192.

[50] G. Zhang and M. E. Selzer, “In vivo transfection of lamprey brain neurons by Gene Gun delivery of DNA,” *Exp. Neurol.*, vol. 167, no. 2, pp. 304–311, Feb. 2001, doi: 10.1006/exnr.2000.7584.

[51] H. Sato, S. Hattori, S. Kawamoto, I. Kudoh, A. Hayashi, I. Yamamoto, M. Yoshinari, M. Minami, and H. Kanno, “In vivo gene gun-mediated DNA delivery into rodent

brain tissue," *Biochem. Biophys. Res. Commun.*, vol. 270, no. 1, pp. 163–170, Apr. 2000, doi: 10.1006/bbrc.2000.2369.

[52] P. Lorenz, U. Harnack, and R. Morgenstern, "Efficient gene transfer into murine embryonic stem cells by nucleofection," *Biotechnol. Lett.*, vol. 26, no. 20, pp. 1589–1592, 2004, doi: 10.1023/B:BILE.0000045658.33723.d6.

Chapter 2

Synthetic nano gene delivery systems

Non-viral vectors, such as nanomaterials, have been employed for gene delivery applications for the past two decades[1], [2]. Nanomaterials have large surface area to volume ratios, and their porosity allows for high DNA condensation efficiencies. In addition to low cost and scalable synthesis, nano vectors possess other favorable attributes[2]. For instance, their size, shape, surface chemistry, optical and magnetic properties are tunable. Furthermore, their tunable biocompatibility and stealth properties allow for a reduced immune recognition and efficient cellular internalization. Inorganic nanoparticles[2], [3] are attractive candidates for DNA delivery as they have robust structures that can retain their shape and chemical properties upon extended exposure to the biological milieu. Moreover, inorganic nanoparticles possess optical and magnetic properties that can be exploited for simultaneous tracking and diagnostic applications. Finally, the emerging trend in nano materials engineering for gene delivery is to use combinations or hybrids of two or more different types mentioned above. For example, Zhuang et. al. showed the application of *in vivo* silencing RNA delivery with metal organic frameworks (zeolitic imidazolate framework-8) coated with platelet membranes [12].

2.1 Lipid based delivery systems

Lipids are amphiphilic molecules with a polar head group (hydrophilic) and a non-polar (hydrophobic) tail. Lipids can self-assemble into various nanostructures i.e. liposomes or bilayer lipid vesicles, micelles, and solid lipid nanoparticles based on various environmental conditions and concentration. Lipid based gene delivery systems are one

of the oldest and most heavily investigated among all non-viral methods. In 1987, lipid mediated gene delivery was coined ‘lipofection’[1]. In this method, a cationic head group containing lipids (DOTAP, DOTMA, DMRIE, DODAP, DODMA, etc.) can complex with nucleic acids (negatively charged) due to complex intermolecular interactions to form ‘lipoplex’ formulations. Cells endocytose the lipoplex which then ends up in an endocytic vesicle where the lipid interacts with the endosomal membrane to destabilize it, releasing the nucleic acid payload into the cytoplasm. Cationic lipids have 3 parts to their molecular structure i.e. cationic headgroup, hydrophobic tail and a linker group between them[4]. Each of these moieties have been widely investigated and chemically engineered to improve transfection efficiency. For example, tail group length, single vs. multivalent and linear vs branched cationic head groups to increase charge density, linker group modifications to cleave on light or pH trigger have been investigated to improve lipoplex transfection efficiency[1]. There is a class of neutral lipids called ‘helper’ lipids which are usually used in conjunction with cationic lipids for transfections, i.e., phospholipids like DOPE, DSPC, DOPC. Helper lipids have been demonstrated to aid in membrane fusion and endocytic vesicle destabilization for more efficient release of nucleic acid payload into the cytoplasm. Additionally, to confer stability against degradation in serum for *in vivo* applications, often other additives like cholesterol, PEG, etc. are added into the lipoplex formulation[1]. Lipofectamine is a commercially available lipid formulation that is widely used for *in vitro* transfections in research[5].

Solid lipid nanoparticles (SLNs) are another emerging lipid-based gene delivery technology which combines advantages of polymeric nanoparticles and liposomes into one system[6]–[8]. SLNs consist of a solid phospholipid-based core matrix that

encapsulates the nucleic acid payload (DNA, RNA, oligonucleotides)[4], [7]. The matrix is stabilized by surfactants and hence stable and solid at room temperature. SLNs can adopt a micellar configuration or can have a bilayer configuration which is non-continuous along the periphery of the core unlike liposomes[4], [7], [8]. SLNs have better stability, longer shelf life, better protection of the payload from degradation, and ability to co-deliver hydrophobic/hydrophilic drugs and functionalize the nano-bio interface in various ways to tune targeting, surface charge, protein corona formation, etc. [4], [6]–[11].

From a clinical perspective, lipid-based gene delivery systems have many advantages i.e., ability to deliver any nucleic acid construct, co-delivery of hydrophobic/hydrophilic drugs, high cellular uptake, and transfection efficiency. Cationic liposomes were successfully used for *in vivo* DNA delivery to many organs like lung, brain, tumors and skin[3]. Some disadvantages of lipid-based gene delivery system is their acute toxicity to primary cells like neurons, inflammation, hematologic and serologic changes reported in studies of systemic administration. There are also concerns regarding their pharmacological properties and bioaccumulation in liver and RES system due to their large size and positive surface charge[4]. Therefore, there are widespread efforts within both academia and industry to synthesize a library of lipids and adopt a combinatorial approach to lipid formulation development to maximize transfection efficiency with improved biocompatibility and pharmacology. Additionally, to avoid immunogenicity of synthetic lipids, there is an emerging area of therapeutics using the phospholipid bilayer sourced from biological source i.e. cell membrane of RBCs and platelets [12]. The first FDA approved non-viral gene therapy drug was ‘Onnpatro’, which was an IV formulation of silencing RNA targeting the gene for transthyretin encapsulated

in an optimized ionizable cationic lipid DLin-MC3- DMA for treatment of amyloidosis in the liver[4]. Today, in the Covid19 pandemic, there are various mRNA vaccine candidates in phase 3 clinical trials that are encapsulated in solid lipid nanoparticle-based formulations for delivery[13], [14]. There are many ongoing clinical trials for lipid nanoparticle mediated gene delivery for cystic fibrosis and cancer therapy[4].

2.2 Polymeric systems

Polymeric systems are also extensively studied for *in vitro* and *in vivo* gene delivery[1],[15]–[17]. Among the various polymers, Polyethyleneimine (PEI), a cationic polymer, is still considered a gold standard of transfection efficiency much like Lipofectamine[1]. This success of transfection is usually attributed to its ability to release DNA from vesicles post-endocytosis due to the proton sponge effect. PEI can be synthesized in linear or branched conformation, with a range of molecular weights, of which 5-25 kDa is known to be most efficient[1]. Various chemical modifications have been done on PEI to improve its transfection efficiency (e.g. addition of cholesterol groups to amines), stability (e.g. PEGylation) and reduce cytotoxicity (e.g. conjugation with cyclodextrin), increase biodegradability (i.e. add reducible/hydrolysable disulfide/ester linkages)[1],[15]–[17]. Many other polymeric systems have been investigated [15]–[17] for gene delivery like synthetic (PLL, PDMAEMA, PAA, PAMAM) , biodegradable (PHP, PAGA), carbohydrate-based (dextran, chitosan, cyclodextrin), dendrimer forms (PLL,PPI, PAMAM) and polypeptides (Tat peptide, MPG peptide). Switchable, controlled release systems have also been engineered with polymeric systems where DNA delivery was triggered by chemical reactions, pH changes and light [18]–[21]. Although polymeric systems are highly versatile, efficient and have the ability to multi-functionalize with

modifications, they have shown poor performance in clinical trials for various reasons like immunogenicity and complex interactions with the biological milieu to create unpredictable protein coronas[15], [16]. Nonetheless, polymeric systems are also continually used in conjunction with other gene delivery systems like SLNs and inorganic nanoparticles to provide additional stability, desirable *in vivo* circulation properties and for protection of payloads from degradation and diffusion[3],[22].

2.3 Metallic nanomaterials

The synthesis and chemistry of nanomaterials made of metals like gold, silver, palladium, platinum, etc. are well characterized in literature[23]. Usually, they are synthesized in solution, from their corresponding metal salts by controlled reduction, often in the presence of surfactants or other stabilizers to prevent aggregation during nucleation and growth[23]. Metallic nanoparticles have easily tunable sizes and shapes like nanospheres, nano shells, nanowires, nanorods, etc. Au nanoparticles and clusters are the most widely reported nanostructures for gene delivery for their lower toxicity than other metallic systems like silver[3], [24]–[28]. AuNP surface chemistry is easily tunable by grafting various ligands, polymers, proteins, peptides, fluorophores, nucleic acids as well as RBC membranes by forming a self-assembled monolayer on the surface using the Au-S bond or by electrostatics mediated assembly on the surface. The same strategies have been used extensively to graft oligonucleotides on the Au surface. Many of these applications deliver silencing RNA for biomedical applications[3], [24]–[28]. Some applications of oligonucleotide delivery with Au nanoparticles have explored controlled release of nucleic acid payloads by (a) chemical bond cleavage[29] (b) DNA denaturation due to local heating caused by plasmonic excitation with a light source[29]–[31] (c) DNA

release due to breaking of the Au-S bond due to Au NP surface melting caused by plasmonic excitation by a pulsed femtosecond laser[30]. One of the drawbacks of silencing RNA loaded nano gold systems is that they become highly negatively charged which makes it difficult to shuttle them across the negatively charged plasma membrane of the cell. In a recent study, this issue was circumvented by using ultrasound guided propelling on siRNA loaded Au nanowires [32]. Au nanomaterials are also valuable for diagnostics due to their plasmonic properties[33]–[35] as well as photodynamic therapy due to their ability to generate local hyperthermia in response to NIR excitation[26]. These properties make them attractive candidates for use in gene therapy applications.

2.4 Carbon based nanostructures

The family of carbon nanomaterials includes carbon nanotube (CNT), graphene, zero-dimensional graphene, and carbon quantum dots. These carbon-based nanomaterials are highly attractive candidates for biomedical applications due to their unique surface properties and interactions with DNA[36]. They have been demonstrated for DNA delivery[3], [36]–[42] as well silencing RNA delivery[3], [38], [43], [44]. They have also been used to supplement other transfection systems like PEI[38].Although carbon-based nanomaterials are generally biocompatible and have an inert surface, they are not naturally dispersed or soluble in aqueous media and need robust functionalization for biomedical applications in such media. Their greatest advantage is the high surface area to volume ratio and in the case of single or multiwalled carbon nanotubes, the presence of two different surfaces for loading payloads like DNA/silencing RNA/oligonucleotides and simultaneous outer functionalization[3], [38]. Generally, carbon-based nanomaterials are not degradable, and therefore, their eventual biological fate, bioaccumulation and

adverse effects on the biological system need further clarity and therefore they are not as attractive for therapeutic gene delivery applications[3].

2.5 Iron oxides

Iron oxide nanoparticles, especially magnetite (Fe_3O_4) are attractive for gene delivery applications because of their magnetic properties and their sorting, guiding and magnetic hyperthermia properties[3]. Usually, iron oxide nanoparticles are often used with suitable coatings to make them more stable, biocompatible and improve their ability to be chemically modified and functionalized appropriately for various applications[3]. The most commonly used coating is a silica shell around a magnetite core[3], [45]. Iron oxide nanoparticles have been demonstrated for both silencing RNA as well as DNA delivery[46]–[50]. Many of these applications load nucleic acids on magnetic iron oxide nanoparticles by covalent bonds rather than using electrostatics based interactions[46], [47], [51].

2.6 Quantum dots

Quantum dots are small nanoparticles (usually < nm) comprising of II–VI or III–V semiconductors e. g. CdS, CdSe, ZnS, ZnSe, ZnO, GaAs, InAs, etc[3], [52]. They are relevant in biomedical applications due to their superior optical properties caused by quantum confinement giving them the ability to fluoresce at high quantum efficiency and resistance to photobleaching[3], [52]. Quantum dots are usually capped with ligands/surfactants to retain their size and prevent aggregation[52]. But in addition, they can be coated with silica, polymers, peptides, antibodies for improving solubility, stability, biocompatibility, or specific targeting[3]. Because of their small size, they are very

efficiently taken up by cells. Quantum dots have been demonstrated for both silencing RNA[3], [53], [54] and DNA delivery[3], [55], [56]. One of the biggest hurdles to applications of quantum dots in gene therapy is their toxicity. It has been shown that QDs can start the formation of photoinitiated radicals in the presence of Cd^{2+}, as well as surface dissolution and diffusion of ions by cellular metallothioneins. Even if their outer surface is passivated by coatings like silica, their long-term biodegradation, accumulation, and toxicity to the biological system is complex and depends on a number of contributing factors like composition, capping, etc.[52]. Their main application is still in imaging[52] and tracking of nucleic acids in cells[56].

2.7 Upconversion nanomaterials

Upconversion nanomaterials are an emerging type of nanoscale material that have unique optical properties useful for gene delivery and other biomedical applications. They are made of trivalent ions (Er^{3+}, Tm^{3+}, Ho^{3+}) from the Lanthanide group of elements in the periodic table doped into a compatible inorganic matrix ($NaYF_4$,Y_2O_3,La_2O_3 and Lu_2O_3). These materials demonstrate upconversion luminescence, which is an emission phenomenon where several low energy photons are absorbed (NIR) and a higher energy photon (red, green, blue or UV) is emitted by appropriate choice of dopant[57]. They are also able to emit at multiple colors with single excitation, making them favorable for image guided *in vivo* diagnostics and imaging applications[58], [59], [59]–[61]. The efficiency of emission is several orders of magnitude higher than other non-linear multiphoton absorption phenomena, allowing the use of low cost continuous wave lasers rather than pulsed laser systems for multiphoton imaging[58]. They have been shown to be generally biocompatible (75% or higher viability) in various cell lines at 2-2500 µg/ml concentrations

from 4-48 hrs incubation times[57]. They are easily scalable in size and their surface chemistry can be tuned in various ways (surface silanization, ligand exchange, ligand removal, ligand attraction, layer-by-layer assembly) with silica, polymers like PEG and PEI, and proteins [57]. Both DNA [57], [59], [62], [63] and siRNA [57], [58], [60], [64] delivery has been widely explored with these nanomaterials. The real advantage of this delivery system is the ability to monitor/track gene delivery during transfection[58], [64].

2.8 Calcium phosphate

Calcium phosphate are inorganic nanostructures made of the inorganic component of biological hard tissues like bones. This is a very simple technique whereby DNA/oligonucleotides are simply mixed in with calcium chloride and phosphate buffered saline solutions and allowed to complex and grow into nano and microstructures. Subsequently the complexes are added to cells for transfection. The advantage of this material is its high affinity to DNA for complexation and inherent biocompatibility[3]. The complexation is usually uncontrolled, leading to precipitates of various sizes. The transfection efficiency with this method depends on pH, temperature, calcium chloride concentration, temperature and time between DNA addition and transfection. Results of transfection vary widely between cell lines and were not easily reproducible. However, several groups have investigated controlled nanocomplex formations of defined sizes by rapid precipitation and surface passivation with nucleic acids/proteins like BSA and precise control of Ca:P ratios[3]. Nucleic acids loaded onto calcium phosphate nanoparticles are often prone to diffusion and degradation, which can be prevented by DNA incorporation in multi-shell calcium phosphate delivery systems. Finally, although

calcium phosphate systems are highly biocompatible and biodegradable, they still can lead to toxicity due to accumulation and increase of Ca^{2+} concentration inside the cells[3].

2.9 Silica based nanomaterials

Among inorganic nanomaterials, silica nanomaterials[65]–[67] are particularly useful for DNA delivery. Silica nanostructures are categorized into mesoporous and non-mesoporous. Both microporous[1] and mesoporous silica nanostructures[2], [3], [65]–[69] have been previously employed *in vitro* gene delivery. The difference between the two types of nanostructures is the nature of their porosities. By IUPAC nomenclature, materials with pore sizes <2 nm, 2-50 nm and >50 nm are categorized as microporous, mesoporous, and microporous, respectively [70]. Therefore, mesoporous silica nanomaterials (MSNs) have a porous matrix with porosities ranging from 2-50 nm that is engineered into the matrix during a sol-gel synthesis method with appropriately chosen surfactants that create the pores of different sizes[1], [65]–[68]. These pores are resolvable in transmission electron microscopy and can be used for loading and release of appropriately sized payloads like small molecule drugs, etc. However, for gene/oligonucleotide delivery with MSNs due to the large sizes of nucleic acid molecules like RNA and DNA, these pores are still not sufficiently large for loading/release from inside the matrix[68]. However, there are examples of delivery of GFP, IL-10 genes and silencing RNA with MSNs. Most applications of gene delivery with MSNs use the external particle surface for nucleic acid loading, which still leaves the payload vulnerable for loss in transmission by diffusion or nuclease degradation. Some applications use lipid/polymer encapsulations to protect the DNA and add additional functionalities to the delivery

system like targeting, stability, etc. Nevertheless, the MSNs have the advantage of having two surfaces, potentially to load other smaller therapeutic molecules e.g. cancer drugs.

In contrast, microporous silica have pores that are much smaller <2 nm, usually synthesized by one of two approaches (a) Stöber synthesis (b) microemulsion method. In Stöber synthesis method, a silica precursor like tetraethylorthosilicate (TEOS) undergoes simultaneous polymerization and condensation in water and alcohol, catalyzed by ammonium hydroxide[71], [72]. The size of the particles formed can be tuned by the stoichiometry of solvents and precursors, and reaction time. The porosity of these nanoparticles are not resolvable in TEM, the pore structures are very complex and tortuous inside the matrix, and therefore not readily available for molecules larger than gases or solvents to easily access[73]. Due to this reason, only the outer surface is available for gene loading and no additional surfaces for drug/diagnostic molecule loading. Such microporous silica nanoparticles have been demonstrated for their application in gene delivery as well as in aiding other DNA transfection systems by acting as the mediators of DNA delivery. Irrespective of the type of silica nanomaterial both are highly attractive candidates for gene delivery applications because of the following favorable properties.

1. Low cost and scalable synthesis- The synthesis of silica nanoparticles of any kind are easily scalable and use low-cost reagents for synthesis and purification.

2. Controllable porosities, sizes, and shapes-The particle size in any of synthesis are easily tunable from sub-100 nm sizes to larger going up to 1 μm. Porosities of MSNs are controllable by the size of the surfactant chosen. Different shapes can also be

synthesized easily by using surfactants to bind to certain facets of the seed during nucleation and direct polymerization/condensation in a specific direction giving shapes like rods.

3. Tunable surface chemistry-The silica matrix consists of a complex network of Si-O-Si siloxane bonds whereas both types of silica nanoparticles have silanol groups (terminated with -OH) that are easily chemically modifiable using different types of chemistries. One popular approach is changing the silica nanoparticle surface chemistry to amine or thiol groups by using appropriately functionalized silanes like aminopropyltriethoxysilane (APTES), mercaptopropyltriethoxysilane (MPTMS), etc. After these chemical modifications, further modifications are still possible with the salinized surface. Thus, the surface chemistry of silica nanoparticles are easily tunable for the different demands of gene delivery applications.

4. Two different surfaces- In case of MSNs, because of their porous matrix, we have access to two different surfaces for loading of multiple different types of payloads i.e. large, charged nucleic acid molecules and small hydrophilic/hydrophobic drug/diagnostic molecules[68].

5. Easy wet or dry storage- Silica nanoparticles can be stored in aqueous or in lyophilized forms.

6. Biocompatibility-Most *in vitro* work report less than 20% toxicity from various viability assays like MTT, CellTracker, etc. Cell morphologies and dividing capabilities are maintained well after treatment[74]–[76].

Silica Nanobowls [69], [77]–[80] are a new class of Janus nanoparticles with an engineered cavity to hold different types of payloads. The outside and inside surfaces of the cavity can be differentially functionalized to add stabilizing polymers like polyethylene glycol (PEG), specific targeting moieties and special properties like ferromagnetism, plasmonic scattering[77], [78]. However, the use of non-mesoporous silica nanobowls[78], [80] as gene delivery vehicles have not yet been explored. These silica nanobowls are non-mesoporous, however, because of the cavity engineered into its structure by a polymeric template, it also has the benefit of two different surfaces that can be independently functionalized and loaded with drugs, nucleic acids, etc. In addition, past reports have demonstrated that these nanobowls can be functionalized with superparamagnetic iron oxide nanoparticles and gold coating, which give them additional functionalities like magnetism and plasmonic scattering that are relevant in diagnostics and photothermal therapies. However, the use of non-mesoporous silica nanobowls [78], [80] as gene delivery vehicles have not yet been explored.

2.10 Bibliography

[1] M. A. Mintzer and E. E. Simanek, “Nonviral vectors for gene delivery,” *Chemical Reviews*, vol. 109, no. 2. American Chemical Society, pp. 259–302, Feb. 11, 2009, doi: 10.1021/cr800409e.

[2] M. Riley and W. Vermerris, “Recent Advances in Nanomaterials for Gene Delivery—A Review,” *Nanomaterials*, vol. 7, no. 5, p. 94, Apr. 2017, doi: 10.3390/nano7050094.

[3] V. Sokolova and M. Epple, “Inorganic Nanoparticles as Carriers of Nucleic Acids into Cells,” *Angew. Chemie Int. Ed.*, vol. 47, no. 8, pp. 1382–1395, Feb. 2008, doi: 10.1002/anie.200703039.

[4] J. Buck, P. Grossen, P. R. Cullis, J. Huwyler, and D. Witzigmann, “Lipid-based DNA therapeutics: Hallmarks of non-viral gene delivery,” *ACS Nano*, vol. 13, no. 4, pp. 3754–3782, 2019, doi: 10.1021/acsnano.8b07858.

[5] F. Cardarelli, L. Digiacomo, C. Marchini, A. Amici, F. Salomone, G. Fiume, A. Rossetta, E. Gratton, D. Pozzi, and G. Caracciolo, “The intracellular trafficking mechanism of Lipofectamine-based transfection reagents and its implication for gene delivery,” *Sci. Rep.*, vol. 6, no. March, pp. 1–8, 2016, doi: 10.1038/srep25879.

[6] J. E. N. Dolatabadi, H. Valizadeh, and H. Hamishehkar, “Solid lipid nanoparticles as efficient drug and gene delivery systems: Recent breakthroughs,” *Adv. Pharm. Bull.*, vol. 5, no. 2, pp. 151–159, 2015, doi: 10.15171/apb.2015.022.

[7] Y. Duan, A. Dhar, C. Patel, M. Khimani, S. Neogi, P. Sharma, N. Siva Kumar, and R. L. Vekariya, “A brief review on solid lipid nanoparticles: Part and parcel of contemporary drug delivery systems,” *RSC Adv.*, vol. 10, no. 45, pp. 26777–26791, 2020, doi: 10.1039/d0ra03491f.

[8] R. Paliwal, S. R. Paliwal, R. Kenwat, B. Das Kurmi, and M. K. Sahu, “Solid lipid nanoparticles: a review on recent perspectives and patents,” *Expert Opin. Ther. Pat.*, vol. 30, no. 3, pp. 179–194, 2020, doi: 10.1080/13543776.2020.1720649.

[9] N. Bono, F. Ponti, D. Mantovani, and G. Candiani, “Non-viral in vitro gene delivery: It is now time to set the bar!,” *Pharmaceutics*, vol. 12, no. 2, 2020, doi: 10.3390/pharmaceutics12020183.

[10] Exelead, “Liposomes and Lipid Nanoparticles as Delivery Vehicles for Personalized Medicine,” *Exelead*, no. December, pp. 96–97, 2019, [Online]. Available: https://www.exeleadbiopharma.com/news/liposomes-and-lipid-nanoparticles-as-delivery-vehicles-for-personalized-medicine.

[11] W. Li and F. C. Szoka, “Lipid-based nanoparticles for nucleic acid delivery,” *Pharm. Res.*, vol. 24, no. 3, pp. 438–449, 2007, doi: 10.1007/s11095-006-9180-5.

[12] J. Zhuang, H. Gong, J. Zhou, Q. Zhang, W. Gao, R. H. Fang, and L. Zhang, “Targeted gene silencing in vivo by platelet membrane-coated metal-organic framework nanoparticles,” *Sci. Adv.*, vol. 6, no. 13, 2020, doi: 10.1126/sciadv.aaz6108.

[13] “Nanomedicine and the COVID-19 vaccines,” p. 19, doi: 10.1038/s41565-020-00820-0.

[14] M. D. Shin, S. Shukla, Y. H. Chung, V. Beiss, S. K. Chan, O. A. Ortega-Rivera, D. M. Wirth, A. Chen, M. Sack, J. K. Pokorski, and N. F. Steinmetz, “COVID-19 vaccine development and a potential nanomaterial path forward,” *Nat. Nanotechnol.*, vol. 15, no. 8, pp. 646–655, 2020, doi: 10.1038/s41565-020-0737-y.

[15] B. Shi, M. Zheng, W. Tao, R. Chung, D. Jin, D. Ghaffari, and O. C. Farokhzad, “Challenges in DNA Delivery and Recent Advances in Multifunctional Polymeric DNA Delivery Systems,” *Biomacromolecules*, vol. 18, no. 8, pp. 2231–2246, 2017, doi: 10.1021/acs.biomac.7b00803.

[16] P. Zhang and E. Wagner, “History of Polymeric Gene Delivery Systems,” *Top. Curr. Chem.*, vol. 375, no. 2, pp. 1–39, 2017, doi: 10.1007/s41061-017-0112-0.

[17] T. G. Park, J. H. Jeong, and S. W. Kim, “Current status of polymeric gene delivery systems,” *Adv. Drug Deliv. Rev.*, vol. 58, no. 4, pp. 467–486, 2006, doi: 10.1016/j.addr.2006.03.007.

[18] Y. J. Ooi, Y. Wen, J. Zhu, X. Song, and J. Li, “Surface Charge Switchable Polymer/DNA Nanoparticles Responsive to Tumor Extracellular pH for Tumor-Triggered Enhanced Gene Delivery,” *Biomacromolecules*, vol. 21, no. 3, pp. 1136–1148, 2020, doi: 10.1021/acs.biomac.9b01521.

[19] Z. Li, W. Ho, X. Bai, F. Li, Y. jui Chen, X. Q. Zhang, and X. Xu, “Nanoparticle depots for controlled and sustained gene delivery,” *J. Control. Release*, vol. 322, no. February, pp. 622–631, 2020, doi: 10.1016/j.jconrel.2020.03.021.

[20] Q. Zhang, G. Kuang, S. He, H. Lu, Y. Cheng, D. Zhou, and Y. Huang, “Photoactivatable Prodrug-Backboned Polymeric Nanoparticles for Efficient Light-Controlled Gene Delivery and Synergistic Treatment of Platinum-Resistant Ovarian Cancer,” *Nano Lett.*, vol. 20, no. 5, pp. 3039–3049, 2020, doi: 10.1021/acs.nanolett.9b04981.

[21] C. K. Chen, P. K. Huang, W. C. Law, C. H. Chu, N. T. Chen, and L. W. Lo, “Biodegradable polymers for gene-delivery applications,” *Int. J. Nanomedicine*, vol. 15, pp. 2131–2150, 2020, doi: 10.2147/IJN.S222419.

[22] E. Haglund, M. M. Seale-Goldsmith, and J. F. Leary, “Design of multifunctional nanomedical systems,” *Ann. Biomed. Eng.*, vol. 37, no. 10, pp. 2048–2063, 2009, doi: 10.1007/s10439-009-9640-2.

[23] Y. Xia and N. J. Halas, “Shape-Controlled Surface Plasmonic Nanostructures,” *MRS Bull.*, vol. 30, no. May, pp. 338–348, 2005.

[24] A. K. R. Lytton-Jean, R. Langer, and D. G. Anderson, “Five years of siRNA delivery: Spotlight on gold nanoparticles,” *Small*, vol. 7, no. 14, pp. 1932–1937, 2011, doi: 10.1002/smll.201100761.

[25] W. Gao, C. M. J. Hu, R. H. Fang, B. T. Luk, J. Su, and L. Zhang, “Surface functionalization of gold nanoparticles with red blood cell membranes,” *Adv. Mater.*, vol. 25, no. 26, pp. 3549–3553, 2013, doi: 10.1002/adma.201300638.

[26] B. Shrestha, L. Wang, H. Zhang, C. Yu Hung, and L. Tang, “Gold nanoparticles mediated drug-gene combinational therapy for breast cancer treatment,” *Int. J. Nanomedicine*, vol. 15, pp. 8109–8119, 2020, doi: 10.2147/IJN.S258625.

[27] C. Delivery, “Gold Nanoparticles in Conjunction with Nucleic Cellular Delivery,” 2020.

[28] S. Siddique and J. C. L. Chow, “Gold nanoparticles for drug delivery and cancer therapy,” *Appl. Sci.*, vol. 10, no. 11, 2020, doi: 10.3390/app10113824.

[29] C. H. Lu and I. Willner, “Stimuli-Responsive DNA-Functionalized Nano-/Microcontainers for Switchable and Controlled Release,” *Angew. Chemie - Int. Ed.*, vol. 54, no. 42, pp. 12212–12235, 2015, doi: 10.1002/anie.201503054.

[30] A. M. Goodman, N. J. Hogan, S. Gottheim, C. Li, S. E. Clare, and N. J. Halas, “Understanding Resonant Light-Triggered DNA Release from Plasmonic Nanoparticles,” *ACS Nano*, vol. 11, no. 1, pp. 171–179, 2017, doi: 10.1021/acsnano.6b06510.

[31] J. Zheng, Y. Nie, S. Yang, Y. Xiao, J. Li, Y. Li, and R. Yang, “Remote-controlled release of DNA in living cells via simultaneous light and host-guest mediations,” *Anal. Chem.*, vol. 86, no. 20, pp. 10208–10214, 2014, doi: 10.1021/ac502280z.

[32] B. Esteban-Fernández De Ávila, C. Angell, F. Soto, M. A. Lopez-Ramirez, D. F. Báez, S. Xie, J. Wang, and Y. Chen, “Acoustically Propelled Nanomotors for Intracellular siRNA Delivery,” *ACS Nano*, vol. 10, no. 5, pp. 4997–5005, 2016, doi: 10.1021/acsnano.6b01415.

[33] Y. Wang, A. Khan, M. Som, S. Y. Leigh, D. Wang, Y. Chen, P. McVeigh, B. C. Wilson, and J. T. C. Liu, “Rapid multiplexed molecular phenotyping of *ex vivo* and *in vivo* tissues with targeted SERS NPs,” in *Translational Biophotonics*, May 2014, vol. 9155, p. 91550Z, doi: 10.1117/12.2057716.

[34] Y. “Winston” Wang, A. Khan, M. Som, D. Wang, Y. Chen, S. Y. Leigh, D. Meza, P. Z. McVeigh, B. C. Wilson, and J. T. C. Liu, “Rapid ratiometric biomarker detection with topically applied SERS nanoparticles,” *TECHNOLOGY*, vol. 02, no. 02, pp. 118–132, Jun. 2014, doi: 10.1142/s2339547814500125.

[35] S. Y. Leigh, M. Som, and J. T. C. Liu, “Method for Assessing the Reliability of Molecular Diagnostics Based on Multiplexed SERS-Coded Nanoparticles,” *PLoS One*, vol. 8, no. 4, p. e62084, Apr. 2013, doi: 10.1371/journal.pone.0062084.

[36] H. Sun, J. Ren, and X. Qu, “Carbon Nanomaterials and DNA: From Molecular Recognition to Applications,” *Acc. Chem. Res.*, vol. 49, no. 3, pp. 461–470, 2016, doi: 10.1021/acs.accounts.5b00515.

[37] X. Liu, Y. Zhang, D. Ma, H. Tang, L. Tan, Q. Xie, and S. Yao, “Biocompatible multi-walled carbon nanotube-chitosan-folic acid nanoparticle hybrids as GFP gene delivery materials,” *Colloids Surfaces B Biointerfaces*, vol. 111, pp. 224–231, 2013, doi: 10.1016/j.colsurfb.2013.06.010.

[38] M. K. Riley and W. Vermerris, “Recent advances in nanomaterials for gene delivery—A review,” *Nanomaterials*, vol. 7, no. 5, pp. 1–19, 2017, doi: 10.3390/nano7050094.

[39] C. Geyik, S. Evran, S. Timur, and A. Telefoncu, “The covalent bioconjugate of multiwalled carbon nanotube and amino-modified linearized plasmid DNA for gene delivery,” *Biotechnol. Prog.*, vol. 30, no. 1, pp. 224–232, 2014, doi: 10.1002/btpr.1836.

[40] S. Jain, K. Thanki, N. K. Pandi, and V. Kushwah, “Estradiol functionalized multi-walled carbon nanotubes as renovated strategy for efficient gene delivery,” *RSC Adv.*, vol. 6, no. 13, pp. 10792–10801, 2016, doi: 10.1039/c5ra26115e.

[41] M. Yu, S. Z. Zu, Y. Chen, Y. P. Liiu, B. G. Han, and Y. Liu, “Spatially controllable DNA condensation by a water-soluble supramolecular hybrid of single-walled carbon nanotubes and ß-cyclodextrin-tethered ruthenium complexes,” *Chem. - A Eur. J.*, vol. 16, no. 4, pp. 1168–1174, 2010, doi: 10.1002/chem.200902627.

[42] M. Mohajeri, B. Behnam, and A. Sahebkar, “Biomedical applications of carbon nanomaterials: Drug and gene delivery potentials,” *J. Cell. Physiol.*, vol. 234, no. 1, pp. 298–319, 2018, doi: 10.1002/jcp.26899.

[43] K. S. Siu, D. Chen, X. Zheng, X. Zhang, N. Johnston, Y. Liu, K. Yuan, J. Koropatnick, E. R. Gillies, and W. P. Min, “Non-covalently functionalized single-walled carbon nanotube for topical siRNA delivery into melanoma,” *Biomaterials*, vol. 35, no. 10, pp. 3435–3442, 2014, doi: 10.1016/j.biomaterials.2013.12.079.

[44] J. Kurreck, “RNA interference: From basic research to therapeutic applications,” *Angew. Chemie - Int. Ed.*, vol. 48, no. 8, pp. 1378–1398, 2009, doi: 10.1002/anie.200802092.

[45] T. Sen, A. Sebastianelli, and I. J. Bruce, “Mesoporous silica-magnetite nanocomposite: Fabrication and applications in magnetic bioseparations,” *J. Am. Chem. Soc.*, vol. 128, no. 22, pp. 7130–7131, 2006, doi: 10.1021/ja061393q.

[46] M. Magro, T. Martinello, E. Bonaiuto, C. Gomiero, D. Baratella, G. Zoppellaro, G. Cozza, M. Patruno, R. Zboril, and F. Vianello, “Covalently bound DNA on naked iron oxide nanoparticles: Intelligent colloidal nano-vector for cell transfection,” *Biochim. Biophys. Acta - Gen. Subj.*, vol. 1861, no. 11, pp. 2802–2810, 2017, doi: 10.1016/j.bbagen.2017.07.025.

[47] S. Biswas, L. E. Gordon, G. J. Clark, and M. H. Nantz, “Click assembly of magnetic nanovectors for gene delivery,” *Biomaterials*, vol. 32, no. 10, pp. 2683–2688, 2011, doi: 10.1016/j.biomaterials.2010.12.047.

[48] S. Jiang, A. A. Eltoukhy, K. T. Love, R. Langer, and D. G. Anderson, “Lipidoid-coated iron oxide nanoparticles for efficient DNA and siRNA delivery,” *Nano Lett.*, vol. 13, no. 3, pp. 1059–1064, 2013, doi: 10.1021/nl304287a.

[49] S. C. McBain, H. H. P. Yiu, A. El Haj, and J. Dobson, “Polyethyleneimine functionalized iron oxide nanoparticles as agents for DNA delivery and transfection,” *J. Mater. Chem.*, vol. 17, no. 24, pp. 2561–2565, 2007, doi:

10.1039/b617402g.

[50] F. M. Kievit and M. Zhang, “Surface engineering of iron oxide nanoparticles for targeted cancer therapy,” *Acc. Chem. Res.*, vol. 44, no. 10, pp. 853–862, 2011, doi: 10.1021/ar2000277.

[51] M. Magro, D. Baratella, P. Jakubec, G. Zoppellaro, J. Tucek, C. Aparicio, R. Venerando, G. Sartori, F. Francescato, F. Mion, N. Gabellini, R. Zboril, and F. Vianello, “Triggering mechanism for DNA electrical conductivity: Reversible electron transfer between DNA and iron oxide nanoparticles,” *Adv. Funct. Mater.*, vol. 25, no. 12, pp. 1822–1831, 2015, doi: 10.1002/adfm.201404372.

[52] metode penelitian Nursalam, 2016 and A. . Fallis, *済無No Title No Title*, vol. 53, no. 9. 2013.

[53] W. B. Tan, S. Jiang, and Y. Zhang, “Quantum-dot based nanoparticles for targeted silencing of HER2/neu gene via RNA interference,” *Biomaterials*, vol. 28, no. 8, pp. 1565–1571, 2007, doi: 10.1016/j.biomaterials.2006.11.018.

[54] S. Li, Z. Liu, F. Ji, Z. Xiao, M. Wang, Y. Peng, Y. Zhang, L. Liu, Z. Liang, and F. Li, “Delivery of quantum dot-siRNA nanoplexes in SK-N-SH cells for BACE1 gene silencing and intracellular imaging,” *Mol. Ther. - Nucleic Acids*, vol. 1, no. 4, p. e20, 2012, doi: 10.1038/mtna.2012.11.

[55] H. N. Yang, J. S. Park, S. Y. Jeon, W. Park, K. Na, and K. H. Park, “The effect of quantum dot size and poly(ethylenimine) coating on the efficiency of gene delivery into human mesenchymal stem cells,” *Biomaterials*, vol. 35, no. 29, pp. 8439–8449, 2014, doi: 10.1016/j.biomaterials.2014.06.024.

[56] C. Srinivasan, J. Lee, F. Papadimitrakopoulos, L. K. Silbart, M. Zhao, and D. J. Burgess, “Labeling and Intracellular Tracking of Functionally Active Plasmid DNA with Semiconductor Quantum Dots,” *Mol. Ther.*, vol. 14, no. 2, pp. 192–201, 2006, doi: 10.1016/j.ymthe.2006.03.010.

[57] W. F. Lai, A. L. Rogach, and W. T. Wong, “Molecular design of upconversion nanoparticles for gene delivery,” *Chem. Sci.*, vol. 8, no. 11, pp. 7339–7358, 2017, doi: 10.1039/c7sc02956j.

[58] G. Chen, H. Qiu, P. N. Prasad, and X. Chen, “Upconversion nanoparticles: Design, nanochemistry, and applications in Theranostics,” *Chem. Rev.*, vol. 114, no. 10, pp. 5161–5214, 2014, doi: 10.1021/cr400425h.

[59] J. H. Wang, H. Y. Chen, C. C. Chuang, and J. C. Chen, “Study of near-infrared light-induced excitation of upconversion nanoparticles as a vector for non-viral DNA delivery,” *RSC Adv.*, vol. 10, no. 67, pp. 41013–41021, 2020, doi: 10.1039/d0ra05385f.

[60] S. Jiang, Y. Zhang, K. M. Lim, E. K. W. Sim, and L. Ye, “NIR-to-visible upconversion

nanoparticles for fluorescent labeling and targeted delivery of siRNA," *Nanotechnology*, vol. 20, no. 15, 2009, doi: 10.1088/0957-4484/20/15/155101.

[61] L. Rao, Q. F. Meng, L. L. Bu, B. Cai, Q. Huang, Z. J. Sun, W. F. Zhang, A. Li, S. S. Guo, W. Liu, T. H. Wang, and X. Z. Zhao, "Erythrocyte membrane-coated upconversion nanoparticles with minimal protein adsorption for enhanced tumor imaging," *ACS Appl. Mater. Interfaces*, vol. 9, no. 3, pp. 2159–2168, 2017, doi: 10.1021/acsami.6b14450.

[62] X. Liu, M. Liu, J. Chen, Z. Li, and Q. Yuan, "Rational design and biomedical applications of DNA-functionalized upconversion nanoparticles," *Chinese Chem. Lett.*, vol. 29, no. 9, pp. 1321–1332, 2018, doi: 10.1016/j.cclet.2018.03.004.

[63] H. Guo, R. Hao, H. Qian, S. Sun, D. Sun, H. Yin, Z. Liu, and X. Liu, "Upconversion nanoparticles modified with aminosilanes as carriers of DNA vaccine for foot-and-mouth disease," *Appl. Microbiol. Biotechnol.*, vol. 95, no. 5, pp. 1253–1263, 2012, doi: 10.1007/s00253-012-4042-z.

[64] J. Yao, C. Huang, C. Liu, and M. Yang, "Upconversion luminescence nanomaterials: A versatile platform for imaging, sensing, and therapy," *Talanta*, vol. 208. Elsevier B.V., p. 120157, Feb. 01, 2020, doi: 10.1016/j.talanta.2019.120157.

[65] C. Hom, J. Lu, and F. Tamanoi, "Silica nanoparticles as a delivery system for nucleic acid-based reagents," *J. Mater. Chem.*, vol. 19, no. 35, pp. 6308–6316, Aug. 2009, doi: 10.1039/b904197d.

[66] Y. Zhou, G. Quan, Q. Wu, X. Zhang, B. Niu, B. Wu, Y. Huang, X. Pan, and C. Wu, "Mesoporous silica nanoparticles for drug and gene delivery," *Acta Pharmaceutica Sinica B*, vol. 8, no. 2. Chinese Academy of Medical Sciences, pp. 165–177, Mar. 01, 2018, doi: 10.1016/j.apsb.2018.01.007.

[67] I. I. Slowing, J. L. Vivero-Escoto, C. W. Wu, and V. S. Y. Lin, "Mesoporous silica nanoparticles as controlled release drug delivery and gene transfection carriers," *Advanced Drug Delivery Reviews*, vol. 60, no. 11. Elsevier, pp. 1278–1288, Aug. 17, 2008, doi: 10.1016/j.addr.2008.03.012.

[68] C. Argyo, V. Weiss, C. Bräuchle, and T. Bein, "Multifunctional mesoporous silica nanoparticles as a universal platform for drug delivery," *Chemistry of Materials*, vol. 26, no. 1. American Chemical Society, pp. 435–451, Jan. 14, 2014, doi: 10.1021/cm402592t.

[69] L. Xiong and S. Z. Qiao, "A mesoporous organosilica nano-bowl with high DNA loading capacity-a potential gene delivery carrier," *Nanoscale*, vol. 8, no. 40, pp. 17446–17450, Oct. 2016, doi: 10.1039/c6nr06777h.

[70] B. Naik and N. Ghosh, "A Review on Chemical Methodologies for Preparation of Mesoporous Silica and Alumina Based Materials," *Recent Pat. Nanotechnol.*, vol. 3, no. 3, pp. 213–224, 2009, doi: 10.2174/187221009789177768.

[71] F. Badalà, K. Nouri-mahdavi, and D. A. Raoof, “Synthesis and surface functionalization of silica nanoparticles for nanomedicine,” *Surf. Sci. rep*, vol. 144, no. 5, pp. 724–732, 2008, doi: 10.1016/j.surfrep.2014.07.001.Synthesis.

[72] P. A. Bazuła, P. M. Arnal, C. Galeano, B. Zibrowius, W. Schmidt, and F. Schüth, “Highly microporous monodisperse silica spheres synthesized by the Stöber process This paper is dedicated to Prof. Thomas Bein on the occasion of his 60th Birthday.,” *Microporous Mesoporous Mater.*, vol. 200, pp. 317–325, 2014, doi: 10.1016/j.micromeso.2014.07.051.

[73] S. Li, Q. Wan, Z. Qin, Y. Fu, and Y. Gu, “Understanding Stöber silicas pore characteristics measured by gas adsorption,” *Langmuir*, vol. 31, no. 2, pp. 824–832, 2015, doi: 10.1021/la5042103.

[74] Q. Gan, D. Dai, Y. Yuan, J. Qian, S. Sha, J. Shi, and C. Liu, “Effect of size on the cellular endocytosis and controlled release of mesoporous silica nanoparticles for intracellular delivery,” *Biomed. Microdevices*, vol. 14, no. 2, pp. 259–270, 2012, doi: 10.1007/s10544-011-9604-9.

[75] M. Ekkapongpisit, A. Giovia, C. Follo, G. Caputo, and C. Isidoro, “Biocompatibility, endocytosis, and intracellular trafficking of mesoporous silica and polystyrene nanoparticles in ovarian cancer cells: Effects of size and surface charge groups,” *Int. J. Nanomedicine*, vol. 7, pp. 4147–4158, 2012, doi: 10.2147/IJN.S33803.

[76] I. I. Slowing, J. L. Vivero-Escoto, C. W. Wu, and V. S. Y. Lin, “Mesoporous silica nanoparticles as controlled release drug delivery and gene transfection carriers,” *Adv. Drug Deliv. Rev.*, vol. 60, no. 11, pp. 1278–1288, 2008, doi: 10.1016/j.addr.2008.03.012.

[77] A. H. Mo, P. B. Landon, C. D. Emerson, C. Zhang, P. Anzenberg, S. Akkiraju, and R. Lal, “Synthesis of nano-bowls with a Janus template,” *Nanoscale*, vol. 7, no. 2, pp. 771–775, Jan. 2015, doi: 10.1039/c4nr05153j.

[78] A. H. Mo, P. B. Landon, K. S. Gomez, H. Kang, J. Lee, C. Zhang, W. Janetanakit, V. Sant, T. Lu, D. A. Colburn, S. Akkiraju, S. Dossou, Y. Cao, K. F. Lee, S. Varghese, G. Glinsky, and R. Lal, “Magnetically-responsive silica-gold nanobowls for targeted delivery and SERS-based sensing,” *Nanoscale*, vol. 8, no. 23, pp. 11840–11850, Jun. 2016, doi: 10.1039/c6nr02445a.

[79] F. Guignard and M. Lattuada, “Template-assisted synthesis of Janus silica nanobowls,” *Langmuir*, vol. 31, no. 16, pp. 4635–4643, Apr. 2015, doi: 10.1021/acs.langmuir.5b00727.

[80] Z. J. Chen, S. C. Yang, X. L. Liu, Y. Gao, X. Dong, X. Lai, M. H. Zhu, H. Y. Feng, X. Di Zhu, Q. Lu, M. Zhao, H. Z. Chen, J. F. Lovell, and C. Fang, “Nanobowl-Supported Liposomes Improve Drug Loading and Delivery,” *Nano Lett.*, vol. 20, no. 6, pp. 4177–4187, Jun. 2020, doi: 10.1021/acs.nanolett.0c00495.

Chapter 3

Characterization of the silica NB system

3.1 Physico-chemical characterization of NBs

3.1.1. Methods

NB synthesis and functionalization.

NBs were synthesized with 100 nm carboxyl terminated polystyrene (PS) spheres (Polysciences, Inc.) as templates as previously described as either large (60 ml) or small scale (6 ml) as previously described[1], [2]. Briefly, 7 ml (or 0.7 ml) deionized water, 40 ml (or 4 ml) isopropyl alcohol (Sigma Aldrich), and 13 ml (1.3 ml) ammonium hydroxide (Sigma Aldrich) were magnetically stirred together. Thereafter, 550 µl (55 µl) tetraethylorthosilicate (TEOS, Sigma Aldrich ≥99% purity) and 1 ml (100 µl) PS spheres (2.5% solids w/v) were added simultaneously to the above mixture and allowed to react by stirring at high speed for 2 hrs at room temperature. The solution was then centrifuged at 500g for 10 mins to separate large aggregates formed during NB synthesis. The supernatant containing single dispersed NBs were washed 3 times in ethanol (EtOH, Sigma Aldrich) by centrifugation at 3221g for 15 mins in order to precipitate single NBs. The purified NBs were re-dispersed in EtOH and allowed to air dry overnight. After synthesis, the dried NBs were re-dispersed (1 mg/ml) in anhydrous dimethyl formamide i.e. DMF (Sigma Aldrich) and heated for 3 hrs in a silicone oil bath at 60^{o}C with magnetic stirring in order to dissolve the polystyrene template and expose the cavity. The NBs were next washed 4 times in EtOH and air dried. To amine functionalize for cDNA loading, the dried DMF-washed NBs were re-dispersed in a 1:1 ethanol:toluene (Sigma Aldrich) at 0.5

mg/ml and allowed to react with 10 mM 3-aminopropyltriethoxysilane (APTES; Sigma Aldrich) at 60^{o}C for 3 hrs under rapid magnetic stirring. The NBs were then washed 4 times in EtOH and air-dried. In another set of experiments, Stöber silica nanoparticles were synthesized as previously described[3] without the use of a polystyrene template and APTES-modified as described above for NB to allow for cDNA loading.

Thermogravimetric analysis (TGA).

Purified amine-coated and DMF-washed NBs were air-dried until a white powder was formed. Approximately 4-5 mg of material were placed into a high-temperature platinum sample pan and incubated in a furnace. A 5 min purge of inert gas at room temperature preceded the measurements to remove air from the furnace. Balance flow and furnace flow were both set to 25 ml/min which resulted in a 100 ml/min of total gas flow through the sample. The temperature was equilibrated at 100^{o}C and the sample was heated to 1000^{o}C at 10^{o}C/min. All measurements were performed in a Discovery TGA-MS (TA Instruments). The weight loss (%) was calculated with respect to starting weight at room temperature before furnace temperature was ramped up. All measurements were performed in Materials Characterization Lab, Materials Research Institute, Penn State University, PA.). The results were analyzed similarly to those previously described[4].

Transmission electron microscopy (TEM).

Between 5 and 10 µl of purified NBs (suspended in ethanol) were drop cast on a 400 Cu mesh with Formvar/Carbon Film, Cat: FCF400-Cu (Electron Microscopy Sciences). The samples were dried by wicking excess solvent with the edge of a soft filter paper and then air-dried at room temperature. All images were taken at 60 kV. All

measurements were performed in the Microscopy Imaging Core, Penn State College of Medicine, PA.

Scanning electron microscopy (SEM).

After removing the polystyrene core, the NBs were purified by centrifugal washing three times and re-dispersed in ethanol. A small volume was applied onto a microscope stub and air dried. The image were acquired with a Zeiss Sigma 500 scanning electron microscope at 2 kV. The images were processed at Nano3 Materials Characterization core facility at University of California San Diego.

Adsorption/Desorption measurements.

Post-synthesis, silica nanoparticles and silica NBs were purified by washing multiple times in ethanol and subsequently vacuum dried into an amorphous powder. Nitrogen adsorption measurements were taken in Micromeritics ASAP 2020 gas adsorption/surface area measurement apparatus at the UC San Diego MRSEC Materials Characterization Facility (MCF). Measurements and analysis done as previously described[5].

Dynamic light scattering (DLS).

The NBs were purified and re-constituted in water at approximately 50 µg/ml concentrations at various steps. For sizing measurements, the sample dispersions were pipetted onto a disposable polystyrene sizing cuvette (Malvern ZEN0040) and measurements were taken at 90^{o} scattering angle. Zeta potential measurements were obtained with a folded capillary cell (Malvern DTS1070). Both measurements were taken

at room temperature in a Zetasizer Nano (Malvern Instruments) at the UC San Diego MRSEC Materials Characterization Facility (MCF).

3.1.2. Results and discussion

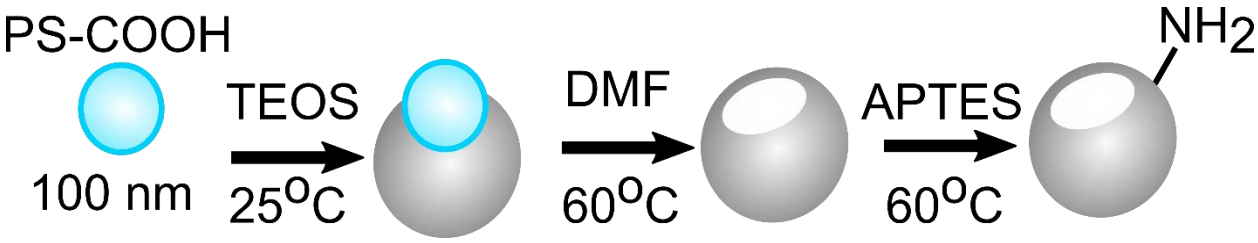

Figure 3.1.1. Schematic of NB synthesis & functionalization. Schematic of NB synthesis and surface functionalization. 100 nm polystyrene (PS) template was used to generate an eccentric cavity in the NB synthesis from tetraethyl orthosilicate (TEOS) condensation. Dimethyl formamide (DMF) was used to dissolve away the PS template, followed by amine functionalization with 3-aminopropyltriethoxysilane (APTES).

Figure 3.1.1 is a schematic illustrating the synthesis of the NBs designed to transfect cells with cDNA. Silica NBs were synthesized by polymerization of TEOS around a 100 nm polystyrene (PS) template as per previously published protocols[1], [2]. After removal of the PS template, the NB surface was functionalized with amine groups by silanization with APTES.

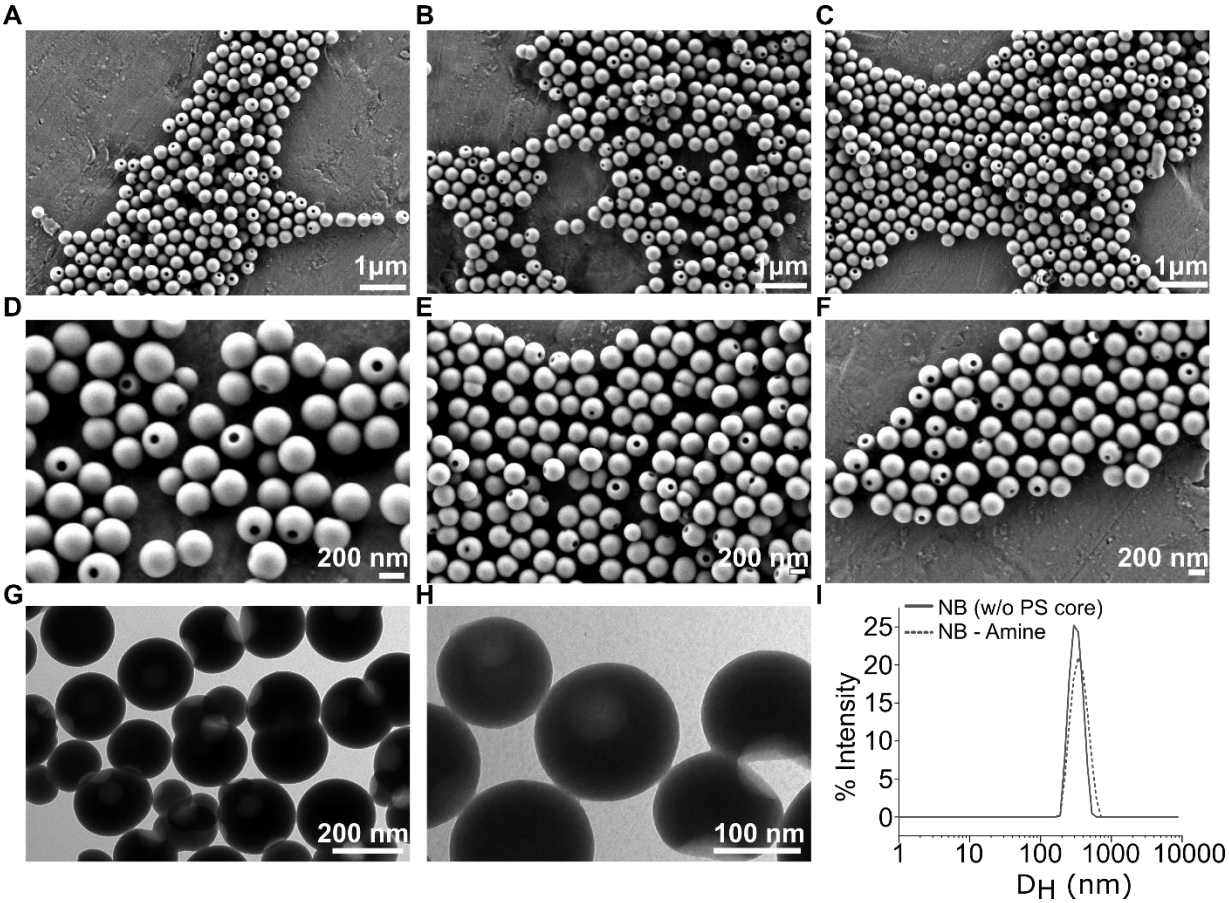

Figure 3.1.2. Characterization of NB size distribution. A-F. Scanning electron microscopy (SEM) **G-H.** Transmission electron microscopy (TEM) images of DMF washed, polystyrene core removed and purified silica NBs. **I.** Dynamic light scattering (DLS) raw intensity data showing a representative NB hydrodynamic size distribution in water before and after APTES (amine) functionalization.

The representative TEM micrograph in Figure 3.1.2 shows DMF washed NBs with a hydrodynamic size distribution (Table 3.1.1) of approximately 314.1 ± 6.6 nm (PDI=0.032 ± 0.025) and a mean engineered cavity of about 65 ± 8 nm. Our laboratory previously reported these features (Mo et al.[1]) in which we found that 70-95% of the synthesized product are Janus NBs, with approximately30% single cavity, approximately 40% double cavity and about 30% NBs with >2 cavities (i.e. >2 polystyrene cores incorporated). Silica NBs are also made by a typical Stöber polycondensation method and therefore both silica Stöber nanospheres as well as NBs are non-mesoporous except for the presence of the

engineered cavity. In order to test this, we compared the pore sizes measured by BET between dried powders of each one (DMF washed silica NBs and Stöber nanospheres of comparable hydrodynamic diameters). Our results showed that NBs and NPs have comparable BET surface area but the average pore size of silica NP ~ 6 nm (microporous) whereas NBs show ~43 nm pore size. This pore size is most likely the result of averaging all pores of the NB material, including its engineered ~65 nm cavity. Our BET results also show that NBs have more than double pore area and 4 times more pore volume than Stöber NPs of similar size (Table 3.1.1).

Table 3.1.1. Characterization of NB porosity in BET.

Type of nanomaterial (Stöber synthesis)	Pore Size	BET specific surface area	Pore Area	Cumulative Pore Volume
	nm	m^2/g	m^2/g	cm^3/g
JNB-PS dissolved	43.03	0.23	0.99	0.04
Silica NP	6.11	0.27	0.41	0.01

Table 3.1.2. Characterization of size and surface charge of NBs. NBs were purified in each case as described in methods and re-dispersed at ~50 µg/ml concentration in deionized water and measurements were acquired at least in triplicate.

Sample Description	Hydrodynamic diameter (nm)	Polydispersity Index (PDI)	Zeta Potential (mV)
NBs (no PS core)	314.1 ± 6.6	0.032 ± 0.025	-34.5 ± 0.6
NBs (Amine functionalized)	343.4 ± 5.3	0.114 ± 0.037	+36.8± 0.8

APTES is an amine functionalized silane that can be used to convert the hydroxyl terminated silica surface into a positively charged one. Positively charged nanoparticle

surfaces have been shown to be useful in condensing nucleic acids on nano delivery systems, for molecule/protein conjugations and driving endocytosis into the negatively charged cell membrane due to electrostatic interactions in buffered media. APTES loading on silica can have various conformations and densities. The grafting density and close packing of the salinized amine functionalized silica surface will affect the functions of the nanocomposite. Therefore, we have characterized the APTES coated NBs for their surface charge (DLS) and APTES loading density (TGA). Following APTES functionalization, the zeta potential, measured in water, of the NBs changed from -34.5 ± 0.6 mV to 36.8± 0.8 mV (Table 3.1.2). This confirmed that APTES loading had successfully changed the NB surface chemistry from a negatively charged to a positively charged surface in water.

Additionally, APTES loading was confirmed by measuring the mass loss due to incremental heating in a Nitrogen environment from 100–1,000^{o}C in thermogravimetric analysis (TGA). The TGA results (Fig. 3.1.3 and Table 3.1.3) indicate that the bare NBs exhibited a lower overall % mass loss than the APTES silanized NBs over the same temperature range. We measured a loading of approximately 210 µmol/g APTES (Table 3.1.3). In our silanization protocol, we add 10 mM i.e. 4.42 mg APTES per mg NB which is equivalent to 20 µmole/mg NB or 20,000 µmole/g NB. We observe from our APTES loading data (Table 3.1.3), we find that (1/100)th of the added APTES is actually loaded on the NB surface.

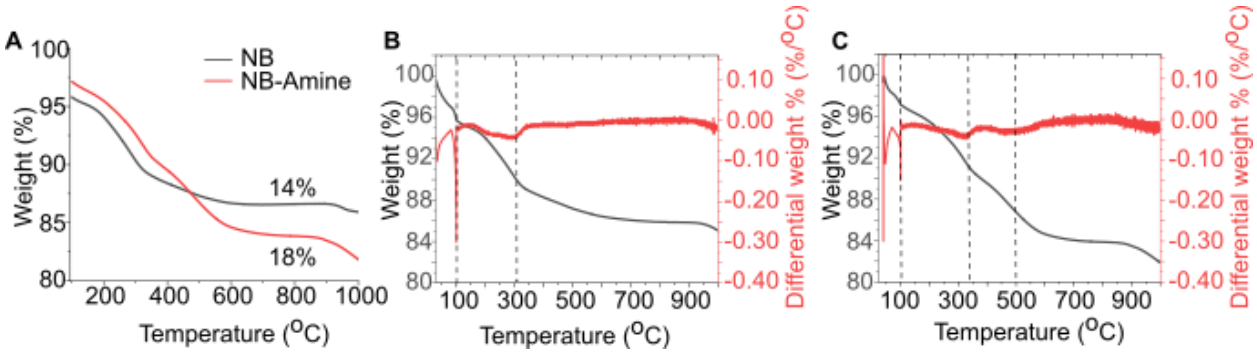

Figure 3.1.3. Thermogravimetric analysis (TGA) of NB and amine-functionalized NB. A. Total weight loss profile from 100-1000°C of NB (black) and amine-functionalized NBs (red). Individual weight loss (black) and differential of weight loss (red) are plotted with respect to temperature for B. NBs post-DMF wash and C. NBs coated with APTES post-DMF wash. Peaks (local minima) in the differential graphs indicate major regions of weight loss. Below 100°C, weight loss in both samples are caused by loss of adsorbed water. Between 100-300°C, weight loss is caused by loss of bound water and solvents like ethanol, DMF that are used in the synthesis and purification of NBs. These two mass losses are similar between both samples B and C. Above 300°C, the mass loss is higher in the amine functionalized NBs due to presence of bound amines due to APTES salinization that burns off and causes weight loss between 300°C to 1000°C. Weight loss values in different temperature regimes are presented in Table 3.1.3.

Table 3.1.3. TGA weight losses categorized in NBs and amine-functionalized NBs. The weight loss beyond 300°C in amine-functionalized NBs was first background subtracted from NB only sample. 4.64% ± 0.67% net weight loss was determined to attribute to APTES based surface functionalization of NBs. Average and standard deviations from duplicate measurements (n=2). This mass loss was calculated to be equivalent to 209.6 µmol g^{-1} APTES (M_w =221.4 g/mol) loading. Alternatively, by considering mass loss of NB-Amine in 300-500°C and 500-1000°C regimes separately, and background subtracting from DMF washed NBs only, 5.21 ± 0.91% total mass loss is calculated which results in 236.7 µmoles g^{-1}. Assuming 1 mole of amine groups come from decomposition of 1 mole of APTES, we report here 209.6-236.7 µmoles g^{-1} amine loading on the NBs.

Temperature ranges	**Materials contributing to weight loss**	**NB (% Weight loss)**		**NB-Amine (% Weight Loss)**	
		Average	**Std Dev**	**Average**	**Std Dev**
Weight loss % <= 100°C	Water	4.25	0.03	2.88	0.02
Weight loss % >100°C and < 300°C	Solvents	5.66	0.25	5.60	0.66
Weight loss % > 300°C	Other bound organics	5.00	0.21	9.64	0.64

3.2. *In vitro* and *in vivo* uptake of NBs

3.2.1. Methods

TEM of NBs in cell lines.

Tissue samples were fixed with 2.5% glutaraldehyde and 2% paraformaldehyde (Electron Microscopy Sciences) in 0.1 M phosphate buffer (pH 7.4) and further fixed in 1% osmium tetroxide (Electron Microscopy Sciences) in 0.1 M phosphate buffer (pH 7.4) for 60 mins. Samples were dehydrated in a graduated ethanol series, acetone and embedded in LX-112 (Ladd Research). The sections (60 nm) were stained with uranyl acetate and lead citrate (Electron Microscopy Sciences) and viewed in a JEOL JEM 1400 Transmission Electron Microscope (JEOL USA Inc.). All images were taken at 60 kV. All measurements were performed in the Microscopy Imaging Core, Penn State College of Medicine, PA.

Preparation of Cy3 tagged NBs for tissue uptake.

NBs were synthesized and amine functionalized as described previously. Following amine functionalization, NBs were dried and dispersed in anhydrous DMSO at 1mg/ml concentration followed by conjugation with Cy3-NHS (Lumiprobe) added at 5 µg/ml. The mixture was stirred overnight at high stir rate at room temperature protected from light, followed by centrifugal washing in ethanol 5 times followed by 2 times in water to remove unbound Cy3. Following purification, Cy3-NBs were dried and re-dispersed at 3.3 mg/ml concentration in DPBS for animal injections.

Salivary gland and DRG tissue injections in rats.

The animal studies were approved by the Penn State College of Medicine Institutional Animal Care and Use Committee (IACUC) approved the animal studies. Sprague-Dawley rats were initially anaesthetized with CO_2, injected with Cy3 loaded NBs at 3.3 mg/ml concentration with a 30G needle. For DRG injections an appropriate spot between the L_4 and L_5 of the rat spinal cord was injected. Injection volume <=300 µl. Ultrasound was used for guiding the needle and leg kick reflex upon needle entry was used as indication of successful injection at DRG. For salivary gland injections, the right and left side were injected similarly with a volume of ~150 µl using the 30G needle and ultrasound scanning guidance. Post-injection, the rat was removed from anesthesia and placed back in the cage for 1 hr. Following this incubation time, the rats were placed back under anesthesia and rapidly decapitated with a laboratory guillotine. The tissues were then isolated by dissection, incubated in a fixative (OCT, Electron Microscope Services), frozen and sectioned (15-17µm thin sections). The DRG neurons (L_4 and L_5) were isolated as described previously[6], [7]. DRG tissues were then cleared of connective tissue in ice-cold Hanks' balanced salt solution. Thereafter, the tissue was enzymatically dissociated in Earle's balanced salt solution containing 0.6 mg/ml collagenase D (Roche Applied Science), 0.4 mg/ml trypsin (Worthington Biochemical), and 0.1 mg/ml DNase (Sigma-Aldrich) in a shaking water bath at 35°C for 60 mins. Thereafter, the neurons were dispersed by vigorous shaking, centrifuged twice for 6 mins at 44xg, and resuspended in Minimum Essential Media (MEM, Thermo-Fisher Scientific) supplemented with 10% fetal bovine serum, 1% penicillin-streptomycin, and 1% glutamine (Thermo-Fisher Scientific).

Finally, the neurons were plated onto 35 mm poly-L-lysine-coated dishes and stored in a humidified incubator supplied with 5% CO_2/95% air at 37°C.

Fluorescence microscopy.

Phase contrast and fluorescence images were obtained with a Nikon TE2000 microscope, an Orca-ER CCD camera (Hamamatsu Photonics), iVision software for acquisition (Biovision Tech.) and Photo Fluor II (89 North) for illumination. The images were processed, and pseudo-colored with iVision software.

3.2.2. Results and discussion

To demonstrate the applicability of NBs in gene and drug delivery, we first show that NBs can be taken up successfully in cells *in vitro* and *in vivo*. To achieve this, we first functionalized the NBs with an amine coating as described in 3.1. The amine coated NBs were re-dispersed in 1:1 DPBS:Opti-MEM at 30 µg/ml and applied to immortalized cell lines (HEK 298, ND7/23, HeLa and L-cells) and dissociated neurons (sensory, DRG and sympathetic, SCG) grown on a petri dish. We incubated for 4 hrs and then rinsed several times to remove unbound NBs from the dish. Following this, we fixed the tissue, sectioned into 60 nm sections, and imaged with negative staining in a transmission electron microscope. Our images show that within 4 hrs and at as low as 30 µg/ml concentrations, the NBs were internalized within the cell lines (Fig. 3.2.1 F-I) as well as neurons (Fig. 3.2.1 D-E). The NB uptake is observed to happen irrespective of the identity of the cells, in primary cells as well as immortalized cell lines tested. This suggests that NB uptake is non-specific.

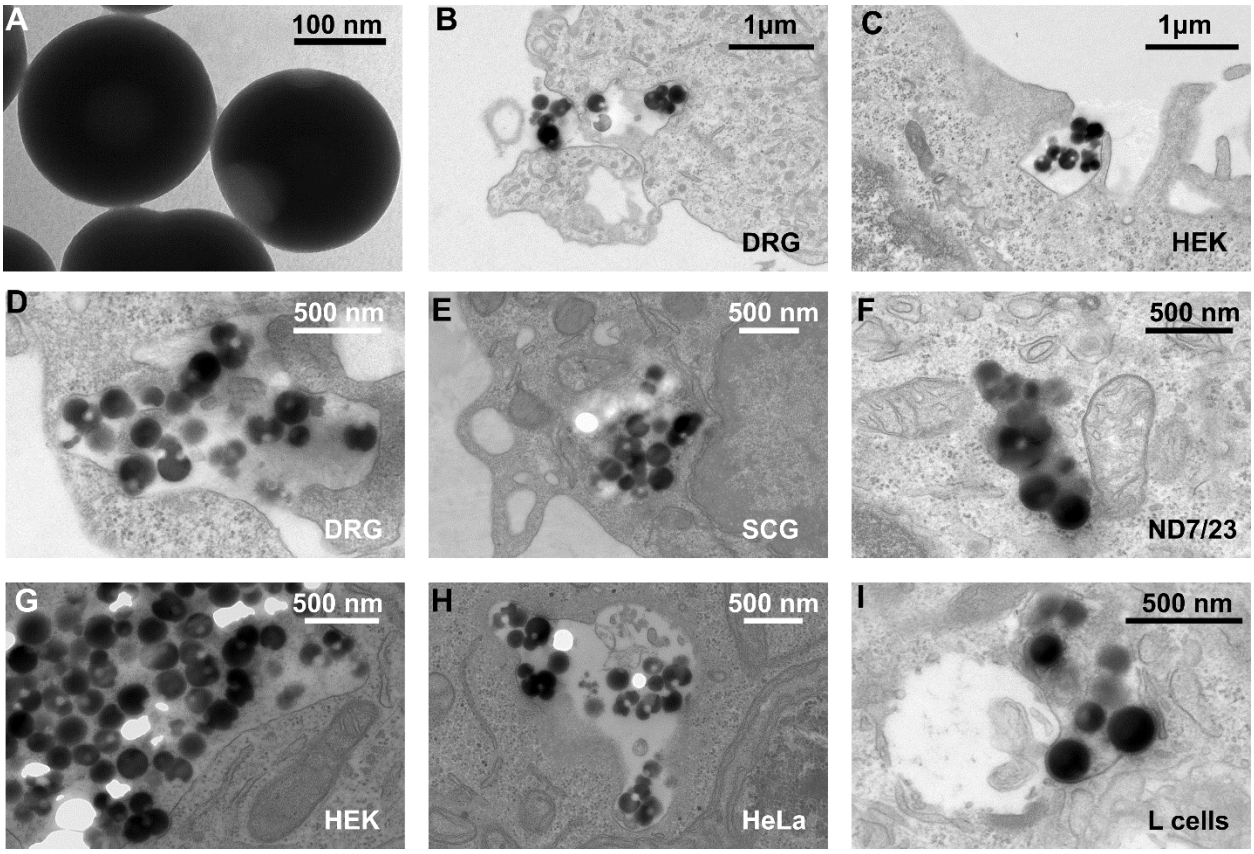

Figure 3.2.1. *In vitro* internalization of NBs in cell lines and neurons. A. Unstained TEM image of purified NBs. TEM images of acutely dissociated DRG neurons (B,D), SCG neurons (E), HEK cells (C,G), ND7/23 (F), HeLa (H) and L-cells (I) following a 4 hrs incubation with NBs (30 µg/ml). The TEM images (B-I) were taken from 60 nm thin sections with negative staining. Note that images in B and C show NBs at the point of internalization. DRG= dorsal root ganglion (sensory neuron) and SCG= superior cervical ganglion (sympathetic neurons).

We also observed in these images that the internalized NBs are always surrounded by a region of markedly different contrast than the rest of the surrounding cytoplasm (lighter contrast in Fig. 3.2.1 D, E, G-I and darker contrast in Fig. 3.2.1 F). These observations suggest that the internalized NBs were encapsulated in vesicles inside the cell cytoplasm. Additionally, we also observed, certain sections imaged the NBs at the points of internalization (Fig. 3.2.1 B-C). In these TEM images we see that the cell membrane extends into arms or cytoskeletal protrusions that start to surround a cluster of NBs. This observation suggests that the uptake of NBs in these cell lines and neurons

might be through the macro pinocytic route of entry into the cell cytoplasm. Further studies (beyond the scope of this work) is needed to confirm the pathway of endocytosis of NBs. Macropinocytosis is a clathrin- and caveolae-independent endocytosis mechanism where the cell cytoplasm restructures into extensions which then fuse back onto the plasma membrane creating a large vesicle (0.2–5 μm) that traps a large volume (bulk non-specific uptake) of extracellular medium containing dissolved molecules and particles. This process of endocytosis has been reported to be the pathway used by larger nanoparticles which cannot enter via other clathrin/caveolae dependent routes[8], [9]. Our TEM studies also shows that in the same cell line (DRG neurons, Fig. 3.2.1 B,D and HEK cells, Fig. 3.2.1 C,G) at the same NB concentration (30 μg/ml) and incubation time (4 hrs), there are NBs at various stages of uptake i.e. at the point of internalization where the cell protrusions are in the process of encapsulation of the NB cluster (Fig. 3.2.1. B,C) as well as completely internalized and entrapped in vesicles (Fig. 3.2.1 D, G). This suggests that the internalization process is highly dynamic and likely continues beyond 4 hrs. Further TEM and fluorescence microscopy results in HEK cells showed that NBs remain internalized 24 hrs after the initial 4 hrs incubation and subsequent washing.

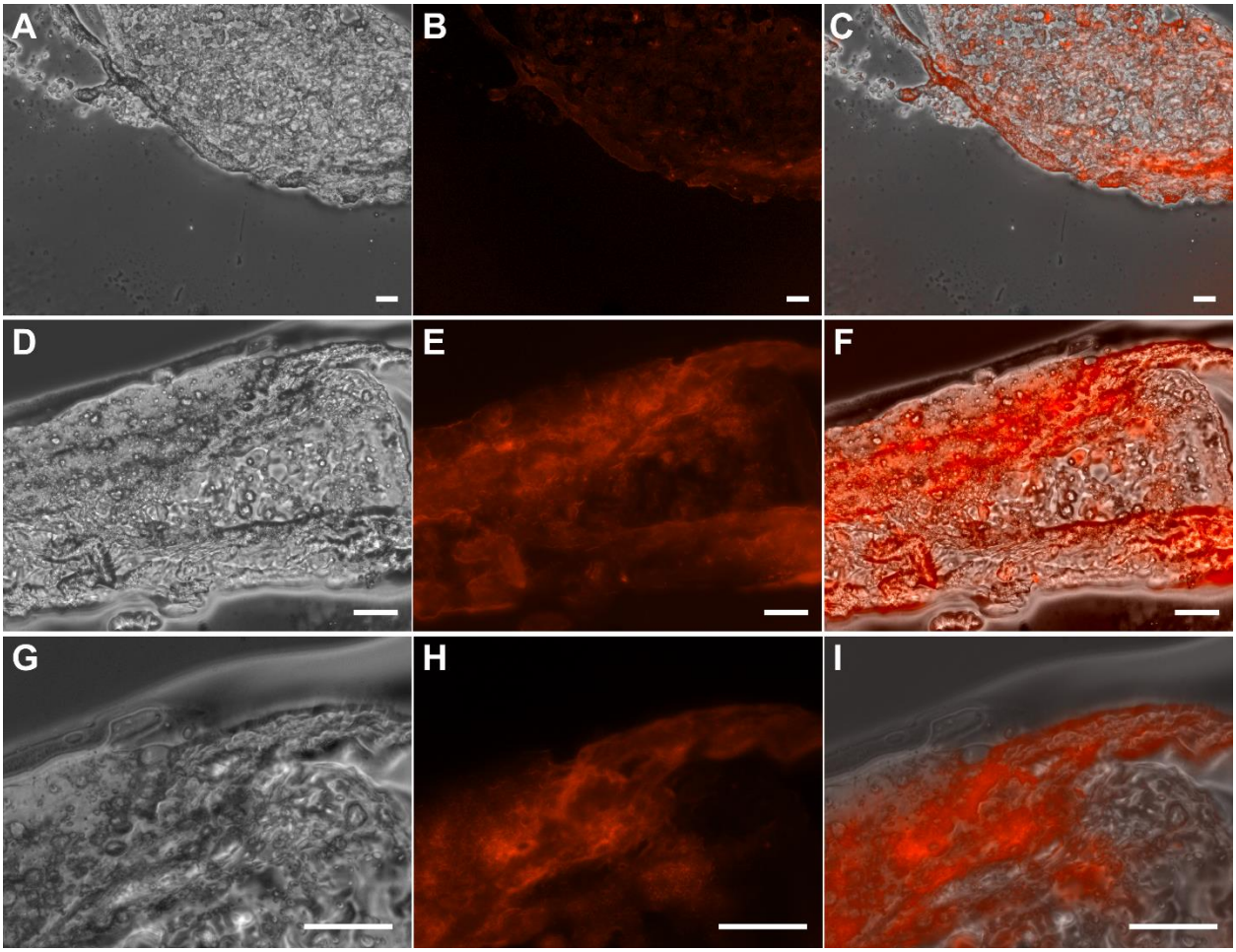

Figure 3.2.2. Internalization of NBs in rat DRG tissue. NBs were injected (~ 1 mg) in the DRG of a rat between L4 and L5 with a 30G needle. Post injection, the rat was kept alive for 1 hr before sacrifice followed by collection of the DRG, fixation, freezing and sectioning. Red color was put in post-processing (pseudo color) to represent the fluorescence emission from the Cy3 dye chemically conjugated to the injected NBs. B,E,H fluorescence and C,F,I overlay images of 3 different sections from 2 injected DRG tissues (right and left) on one rat. A-C. Images were taken with a 10x objective. D-F. Images were taken with a 20x objective. G-I. Images were taken with a 40x objective. All scale bars depict 50 µm.

To test the ability of these NBs to be taken up *in vivo*, we chose some target organs of a rat model i.e., dorsal root ganglion (DRG) and salivary gland (SG). The choice of these target organs was driven mainly by (a) the ability to easily locate them with ultrasound (b) locally inject a NB bolus by avoiding the systemic circulation and side effects. Additionally, DRG is mainly composed of sensory neurons which form the essential network of pain transmission from the peripheral nervous system to the brain.

These neurons comprise of sodium channels, which are ion channel proteins used by the DRG neurons to transmit action potentials. Specifically, Na_V 1.8 and 1.9 are tetrodotoxin (TTX) resistant and are used extensively to study pain transmission. For example, silencing the expression of these channel proteins will prevent pain signal transmission to the brain and therefore silence pain (nociception). In the face of the opioid crisis, silencing Nav1.8 and 1.9 is a viable strategy to opioid-free pain management. For the same reasons, there is also a need for development of localized delivery systems to release local anesthetics through these DRG targeted injections without the need for systemic distribution[9]. Therefore, the DRG is an excellent clinical target for the development of a novel gene delivery system to modulate and study protein function *in vivo*.

Rat salivary gland (SG) is also a good target for testing uptake of NBs. This is because the SG is a tissue without circulation or tissue barriers and the injected NB bolus can directly access the tissue without barriers or forces of fluid diffusion clearing it quickly. Clinically, SG is a relevant target for gene therapy for example, in cases of xerostomia[10], patients who undergo radiotherapy for head and neck cancers and have radiation damaged salivary glands which are unable to secrete saliva. There being no standard treatment available for radiation induced xerostomia, one approach is heterologous expression of the aquaporin channels in the salivary gland tissue. Viral transduction techniques, although efficient, have concerns of toxicity and undesirable immune response. Thus, NBs can be tested for their ability to internalize in these two *in vivo* targets in a rat model to set the stage to develop a NB based non-viral gene delivery system.

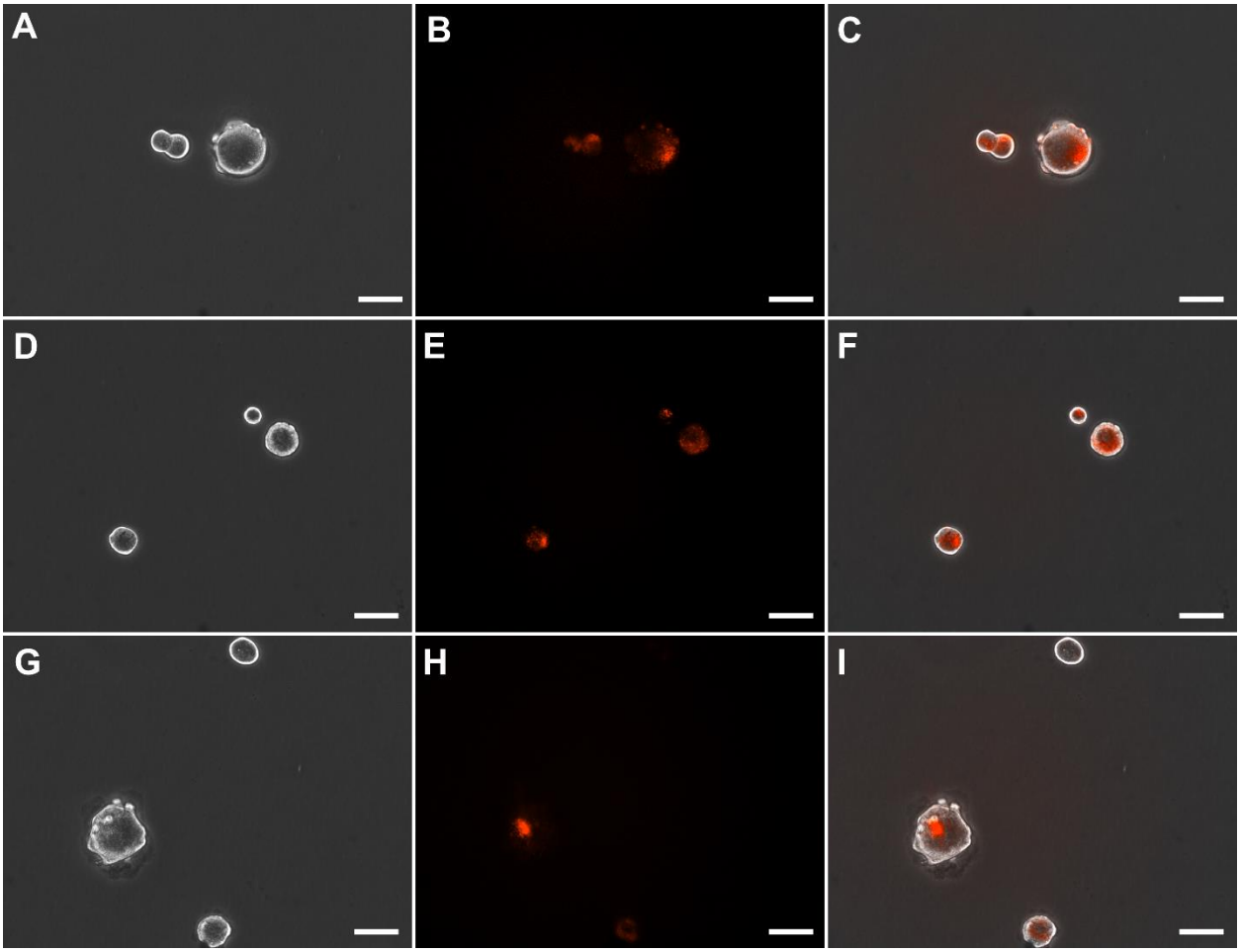

Figure 3.2.3. Internalization of NBs in neurons post-DRG injection. NBs were injected (~ 1 mg) in the DRG of a rat between L4 and L5 with a 30G needle. Post injection, the rat was kept alive for 1 hr before sacrifice followed by collection of the DRG and enzymatic dissociation. The neurons were allowed at least 4-5 hrs to attach to the dish (PLL coated, 35 mm petri dish) before imaging. Red color was put in post-processing (pseudo color) to represent the fluorescence emission from the Cy3 dye chemically conjugated to the injected NBs. A, D, G. Phase, B,E,H fluorescence and C,F,I overlay images from a single injection. All images were acquired with a 20x objective and scale bars depict 50 µm.

Figure 3.2.2&3 show the results of ultrasound guided Cy3-tagged NB injection in rat DRG tissues located between L4 and L5 segments of the spinal column. Post-injection, rats were woken up from anesthesia, kept alive for 1 hr and then sacrificed. The DRG was then isolated, fixed, and sectioned into 15-17 µm thick. The sections were mounted onto a glass slide with cover slip and imaged. Our results (Fig. 3.2.2) show that Cy3-NBs were successfully taken up in the DRG tissue. However, DRG is composed of

neurons, glia, and connective tissue. Figure 3.2.2 does not clarify if neurons of DRG have successfully taken up the Cy3-NBs. In order to elucidate this, a better analysis method is

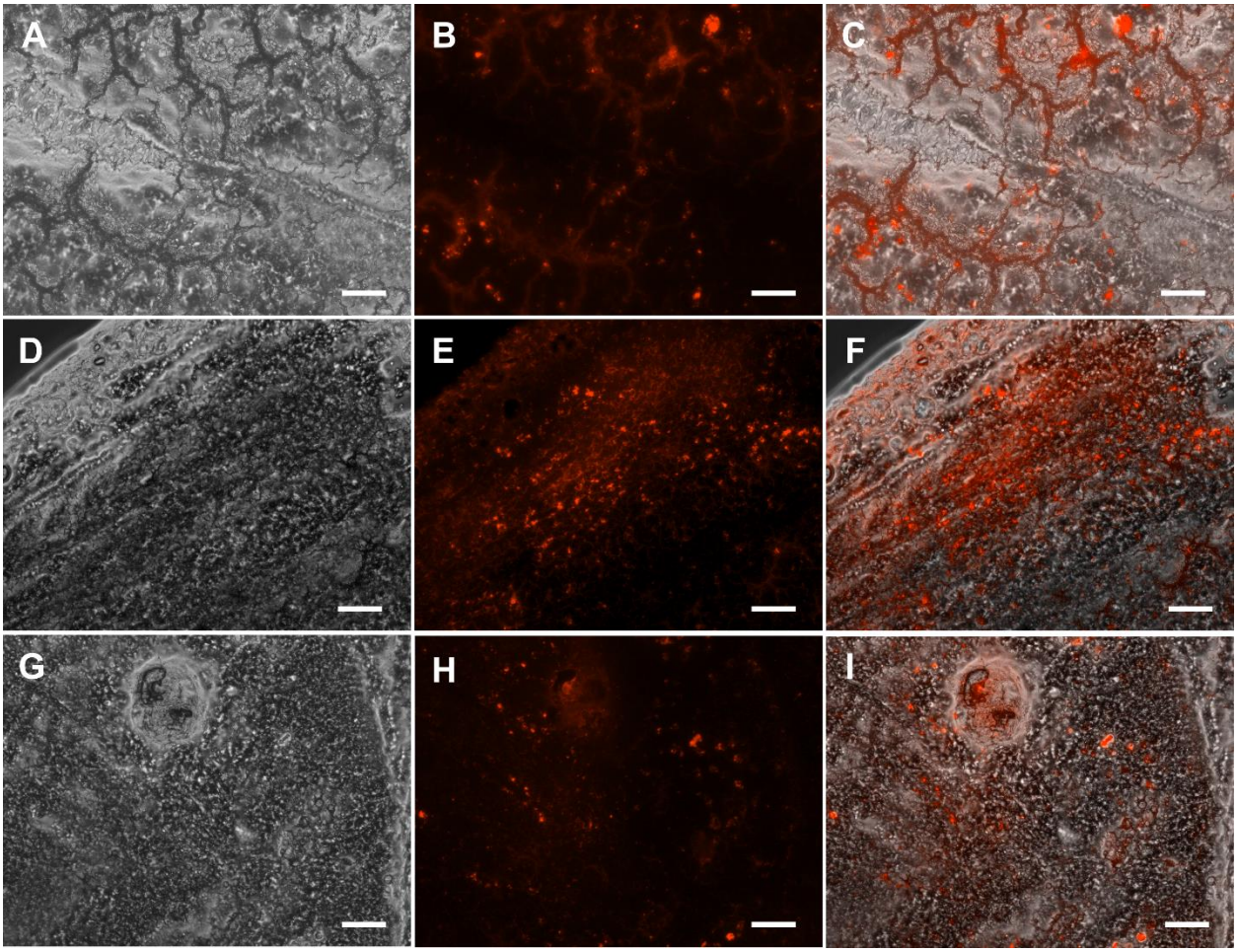

Figure 3.2.4. Internalization of NBs in rat salivary gland. A, D, G. Phase, B,E,H fluorescence and C,F,I overlay images of 3 different sections from injected salivary glands (right and left) of one rat. NBs were injected (~ 0.5 mg) in the salivary gland of a rat with a 30G needle. Post injection, the rat was kept alive for 1 hr before sacrifice followed by collection of the salivary gland, fixation, freezing and sectioning. Red color was put in post-processing (pseudo color) to represent the fluorescence emission from the Cy3 dye chemically conjugated to the injected NBs. Images depict representative results from n=2 experiments. Images were acquired with a 20x objective. All scale bars depict 50 µm.

to enzymatically dissociate the DRG after injection and isolation, collect the DRG neurons by centrifugation and check with microscopy if there is any Cy3 emission co-localizing with the acutely dissociated neurons. Our results from acutely dissociated neurons from *in vivo* DRG injections (Fig. 3.2.3) reveal that there is co-localization and successful

internalization of Cy3-NBs. The fluorescence emission from these neurons also show a punctate form which indicates that the emission is coming from NB clusters and not leached out Cy3 diffusion.

Similar injections with ultrasound guidance was performed in a rat model in the SG. Each bolus contained 0.5 mg of Cy3-NBs in DBPS in an injection volume of ~150 µl. After 1 hr of injection, the rat was sacrificed, the whole SG was isolated, fixed, frozen and sectioned. Our fluorescent images (Fig. 3.2.4) of rat SG depict robust internalization of the Cy3-NBs. Figure 3.2.4. A-C depict uptake of the Cy3-NBs around the salivary ducts.

Although our experiments have resulted in successful internalization of NBs, the uptake results of the DRG uptake studies were highly variable depending on the success of the injection itself. Ultrasound was used for guiding the NB injection needle and leg kick reflex upon needle entry was used as indication of successful injection at the DRG. Yet, the injection location is still variable with respect to the DRG and affects where the bolus is released and how much of it is lost in the intercellular space or surrounding connective tissues. Even with a perfect injection, the NBs face multiple barriers on their way to the DRG neurons in the form of connective tissue, glia, and blood/CSF in the intercellular space near the injection spot. Due to this reason, the surface chemistry of the NBs needs to be optimized by PEGylation, conjugation of neuron targeting or glia targeting proteins to allow specific uptake and guiding/localization mechanisms like magnetic/ultrasound guiding to overcome these barriers and ensure reliable uptake by DRG neurons.

Nevertheless, our results show promise of *in vivo* applications of gene/drug delivery with NBs. To that end, the remaining chapters show work developing the NB

system as a viable DNA, silencing RNA, and drug delivery system, optimizing, and showing successful application *in vitro* in 4 cell lines , freshly dissociated DRG neurons and *ex vivo* in DRGs.

Chapter 3, in part, has been published in ACS Bioconjugate Chemistry (2020) with coauthors Dr. Ratneshwar Lal and Dr. Victor Ruiz-Velasco. The dissertation author was the primary investigator and author of this material.

3.3 Bibliography

[1] A. H. Mo, P. B. Landon, C.D. Emerson, C. Zhang, P. Anzenberg, S. Akkiraju and R. Lal, "Synthesis of nano-bowls with a Janus template," *Nanoscale*, vol. 7, no. 2, pp. 771–775, Jan. 2015.

[2] A. H. Mo, P. B. Landon, K. S. Gomez, H. Kang, J. Lee, C. Zhang, W. Janetanakit, V. Sant, T. Lu, D. A. Colburn, S. Akkiraju, S. Dossou, Y. Cao, K. F. Lee, S. Varghese, G. Glinsky and R. Lal, "Magnetically-responsive silica-gold nanobowls for targeted delivery and SERS-based sensing," *Nanoscale*, vol. 8, no. 23, pp. 11840–11850, Jun. 2016.

[3] S. Li, Q. Wan, Z. Qin, Y. Fu, and Y. Gu, "Understanding Stöber silicas pore characteristics measured by gas adsorption," *Langmuir*, vol. 31, no. 2, pp. 824–832, Jan. 2015.

[4] F. Kunc, V. Balhara, Y. Sun, M. Daroszewska, Z. J. Jakubek, M. Hill, A. Brinkmann and L. J. Johnston, "Quantification of surface functional groups on silica nanoparticles: Comparison of thermogravimetric analysis and quantitative NMR," *Analyst*, vol. 144, no. 18, pp. 5589–5599, Sep. 2019.

[5] S. Li, Q. Wan, Z. Qin, Y. Fu, and Y. Gu, "Understanding Stöber silicas pore characteristics measured by gas adsorption," *Langmuir*, vol. 31, no. 2, pp. 824–832, 2015.

[6] M. Farrag, J. K. Drobish, H. L. Puhl, J. S. Kim, P.B. Herold, M. P. Kaufman and V. Ruiz-Velasco, "Endomorphins potentiate acid-sensing ion channel currents and enhance the lactic acid-mediated increase in arterial blood pressure: effects amplified in hindlimb ischaemia," *J. Physiol.*, vol. 595, no. 23, pp. 7167–7183, Dec. 2017.

[7] W. Margas, K. Sedeek, and V. Ruiz-Velasco, "Coupling Specificity of NOP Opioid Receptors to Pertussis-Toxin-Sensitive Gα Proteins in Adult Rat Stellate Ganglion Neurons Using Small Interference RNA," *J. Neurophysiol.*, vol. 100, no. 3, pp. 1420–1432, Sep. 2008.

[8] J. Sun, Y. Liu, M. Ge, G. Zhou, W. Sun, D. Liu, X. J. Liang and J. Zhang, “A Distinct Endocytic Mechanism of Functionalized-Silica Nanoparticles in Breast Cancer Stem Cells,” *Sci. Rep.*, vol. 7, no. 1, pp. 1–13, 2017.

[9] Q. Gan, D. Dai, Y. Yuan, J. Qian, S. Sha, J. Shi and C. Liu, “Effect of size on the cellular endocytosis and controlled release of mesoporous silica nanoparticles for intracellular delivery,” *Biomed. Microdevices*, vol. 14, no. 2, pp. 259–270, 2012.

[10] M. J. Passineau, L. Zourelias, L. MacHen, P. C. Edwards, and R. L. Benza, “Ultrasound-assisted non-viral gene transfer to the salivary glands,” *Gene Ther.*, vol. 17, no. 11, pp. 1318–1324, 2010.

Chapter 4

Development of the NB system for DNA delivery

In this report, we describe the development of DNA-loaded silica nanobowls (NBs) that can be internalized within 4 hrs in immortalized mammalian cell lines. We also show that the successful transfection (i.e., release of DNA) relied on coating the NBs with 'helper' lipids. These nanovectors can be engineered to physisorb DNA at high loading efficiencies. We further demonstrate that the NBs are capable of transfecting cells when loaded with either linearized or supercoiled cDNA constructs.

4.1. Methods

DNA linearization and functionalization.

For cDNA loading and transfections, we chose clover (vector: pcDNA 3.1) and tdTomato, (vector: pEGFP-N1) which code for two high quantum efficiency fluorescent proteins of the GFP family[1]. Polymerase chain reaction (PCR) was performed to introduce either amine or azide functional groups into linear DNA. Forward primers with appropriate functional groups were designed to hybridize at the start of the CMV promoter region of the pcDNA3.1 plasmid containing the clover DNA insert. The modifications at the 5' end of the forward primer was either a carboxyl or an azide group followed by a disulfide bond. The reverse primer was not modified and was designed to hybridize at the end of the polyadenylation sequence of the plasmid. All primers (Integrated DNA Technologies, IDT) were custom designed. The sequences of the primers were the following:

Clover primers:

Forward primer (FWD): 5'- GTTGACATTGATTATTGACTAGTTATTAATAGTAAT-3'

Reverse primer (REV): 5'-CCATAGAGCCCACCGCAT-3'

tdTomato primers:

Forward primer (FWD): TAGTTATTAATAGTAATCAATTACGGGGTC

Reverse primer (REV): GCAGTGAAAAAAATGCTTTATTTGTG

PCR was performed using the OneTaq HotStart 2X master mix (New England Biolabs). The PCR products were purified using commercially available standard DNA clean and concentrator kits (Zymo Research, 25 µg columns or Qiagen, 10 µg columns) and reconstituted in DNAse, RNase free molecular biology grade water. The purified products were quantified using the Qubit dsDNA BR assay kit (Thermo-Fisher Scientific) as per manufacturer's protocol. All linearized PCR products were visualized on agarose gel electrophoresis/tapestation to confirm size (clover ~ 1.7 kbp & tdT ~ 2.4 kbp, see text for data).

NB-DNA loading assay.

The dried, amine-coated NBs were resuspended in Dulbecco's Phosphate Buffered Saline DPBS (with Ca^{2+} and Mg^{2+}; Thermo-Fisher Scientific) with light sonication for 5 mins at a final 1 mg/ml concentration. In addition, 2—50 µg of supercoiled or linearized cDNA was added to 1 ml (1 mg/ml) of NB-DPBS solution and allowed to bind overnight at $4^{o}C$ with gentle shaking. Once the DNA was loaded, the NBs were

centrifuged at 3221g for 30 mins and the supernatants were collected for DNA quantification with Qubit assay kit (Thermo-Fisher Scientific). All loading efficiencies (%) were calculated as µg cDNA bound*100/µg cDNA added per mg NB.

mRNA synthesis and loading.

mRNA was synthesized from linearized clover template using an *in vitro* transcription kit i.e., HiScribe™ T7 High Yield RNA Synthesis Kit (New England Biolabs) as per manufacturer's protocols. The synthesis products were treated with RNase free DNase post-synthesis to remove any template DNA remaining in the product. Afterwards, the mRNA was purified by Monarch RNA purification column of 100 µg capacity per column, as per manufacturer's protocols. 25 µg of purified mRNA was added to 1 mg NB (amine functionalized) in 1 ml DPBS and allowed to mix gently with a rotator at 4^{o}C for an hr. Afterwards, the bound mRNA was separated by centrifugation as described above and quantified with Nanodrop with appropriate background subtraction.

NB-DNA lipid encapsulation.

The lipids 1,2-dioleoyl-sn-glycero-3-phosphoethanolamine i.e., 18:1 (Δ9-Cis) PE (DOPE) and 1,2-dioleoyl-3-trimethylammonium-propane (chloride salt) i.e., 18:1 TAP (DOTAP; both from Avanti Polar Lipids) were mixed at a 1:1 molar ratio in chloroform and transferred to a pre-etched round bottom glass flask. The chloroform was dried with a gentle nitrogen stream. Thereafter, approximately 1.5 gr of 2 mm glass beads (Sigma Aldrich) were added to the bottom of the flask and a lipid reconstitution buffer (KCl 100 mM Tris 10 mM HEPES 10 mM pH 8.4) was added to obtain a 1 mg/ml lipid solution. The liposomes were prepared by swirling the flask with the glass beads continuously for 5

mins. The liposome solution was then serially filtered through 0.45 µm (Pall diagnostics) and 0.22 µm (Pall diagnostics) sterile filters. Afterwards, the liposome solution was extruded through a 0.10 µm filter (Avanti Polar Lipids) using a mini extruder setup with gas tight syringes (Avanti Polar Lipids), with 4 passes through the filter per 1 ml extruded. Finally, 1 ml of 100 nm extruded liposome solution was mixed via gentle shaking with 1 ml NB-DNA conjugate (1 mg/ml) in DPBS for 60 mins with gentle shaking at room temperature. The NBs were then centrifuged and washed once in 1 ml DPBS at 3221g for 30 mins. The lipid encapsulated NBs (LNBs) were finally resuspended in 1:1 DPBS:Opti-MEM (Thermo-Fisher Scientific) at the desired final LNB concentration for transfection. To show effect of addition of polymers to the LNB encapsulation layer, similar protocols were followed but with the addition of 1:1:0.1 DOPE:DOTAP:DOPE-PEG-NHS (Nanocs). Data for this is presented in Chapter 7.

NB toxicity assays.

<u>MTT Assays:</u>

Human embryonic kidney (HEK), ND7/23, L-cells and HeLa cells were purchased from ATCC. The cells were plated at a density of 25,000 cells/well in glass bottom 96-well plates 24 hrs before the experiment. On the day of the experiment, the cells were incubated in 0.05, 0.125, 0.25, 0.5 and 1.0 mg/ml LNBs in 1:1 DPBS:Opti-MEM (200 µl final volume/well) at 37^{o}C for 4 hrs. The null LNB (Control) group was incubated in vehicle (DPBS:Opti-MEM). Following the incubation period, the wells were gently rinsed in warm DMEM twice and 100 µl of warm DMEM (without phenol red) mixed with 10 µl of 12 mM MTT solution (Vybrant MTT assay kit, Thermo-Fisher Scientific) were added to the wells for 4 hrs at 37^{o}C. Thereafter, 85 µl of supernatant per well was discarded and gently

replaced with 100 µl DMSO. The plate was incubated for 30 mins at 37^{o}C and kept on a rotary shaker for 30 mins at room temperature to allow the uniform dissolution of formazan. The plates were scanned for absorbance at 540 nm in FlexStation3 microplate reader (Molecular Devices). The absorbances were normalized to the live cell control and converted to % viability. Cells treated with 70% ethanol for 1 hr were used as dead cell control and showed viability of 10% or less (not shown on bar graphs in Fig. 4.2.18).

Flow cytometry:

HEK cells were plated on 6-well plates at 120,000 cells/well 24 hrs prior to the start of the experiment. Cells were incubated with LNB (0.05—1.0 mg/ml) loaded with 10 µg/mg linearized clover for 4 hrs in a humidified atmosphere at 37^{o}C in 5% CO_2/95% air. Each condition was performed in duplicate. Following the incubation period, the wells were rinsed with warm DMEM (without phenol red) and returned to the incubator for an additional 44 hrs. The negative control group was incubated in 1 mg/ml LNB in DPBS:Opti-MEM. The positive control group (i.e., clover-expressing cells) was transfected with supercoiled clover cDNA (4 µg) employing Lipofectamine 2000 (Thermo-Fisher Scientific) per well, followed by washing with warm, clear DMEM and 24 hrs incubation before analysis. Prior to performing flow cytometry, phase contrast and fluorescence images were obtained with a Nikon TE2000 microscope, an Orca-ER CCD camera (Hamamatsu Photonics), iVision software for acquisition (Biovision Tech.) and Photo Fluor II (89 North) for illumination. The images were processed, and pseudo-colored with iVision software. For flow cytometry analysis, the wells for each condition were combined and reconstituted in DPBS at 10^6 cells/ml and stained with 7-Aminoactinomycin (7-AAD) flow cytometry viability dye (Thermo-Fisher Scientific). The

cells were run in a 10 color BD FACS Canto with 488 nm excitation filter and 530 nm (clover) and 695 nm (7AAD) detection filters. Each sample was run until approximately 100,000 events were detected. Analysis was done by gating out debris and multi-cell clusters from original side scatter vs forward scatter plot, and then viable and clover expressing populations were analyzed from the single cell events by applying appropriate compensation of these detector channels and setting thresholds (10^3 units) for background emissions. Dead cells (killed by 5 mins of rapid freeze thawing) were used as positive controls for 7-AAD. 4µg/Lipofectamine 2000 treated HEK cells (4 hr treatment, followed by rinsing and incubation for 24 hrs) were used as the positive GFP control. All measurements were performed in the Flow Cytometry Core, Penn State College of Medicine, PA.

Western blotting assays.

In this set of experiments, HEK and ND7/23 cells were plated at 120,000/well in 6-well plates 24 hrs prior to transfection. Linearized or supercoiled clover was loaded onto NBs, lipid encapsulated, and re-dispersed in DPBS:Opti-MEM at 0.5 mg/ml as described above. Each well was then incubated in 1 ml of this solution for 4 hrs at 37ºC and then rinsed 3 times in warm DPBS. After 48 hrs post-transfection, the cells were trypsinized, dissolved in a lysis buffer containing β-marcaptoethanol. Protein extraction, purification, and collection were performed with the Nucleospin RNA/Protein kit (Macherey-Nagel, Inc.). The protein samples were quantified with the Qubit protein kit (Thermo-Fisher Scientific). The Western blot experiments were then performed with the Wes system (Protein Simple). The microplate was loaded with protein concentrations ranging from 0.025—0.25 µg/µl, primary antibodies and secondary antibodies. The rabbit monoclonal

anti-clover (Abcam, Inc.) and anti-vinculin (housekeeping gene, Abcam, Inc.) antibodies were employed at 1:1000 and 1:500, respectively. Protein detection and quantification were performed with the Compass software (Protein Simple).

Transmission electron microscopy (TEM).

Between 5 and 10 µl of purified NBs (suspended in ethanol or water if lipid coated) were drop cast on a 400 Cu mesh with Formvar/Carbon Film, Cat: FCF400-Cu (Electron Microscopy Sciences). LNB samples were stained in partially dried state by adding a small drop of 2% urenyl acetate (Electron Microscopy Sciences). The samples were dried by wicking excess solvent with the edge of a soft filter paper and then air-dried at room temperature. Tissue samples were fixed with 2.5% glutaraldehyde and 2% paraformaldehyde (Electron Microscopy Sciences) in 0.1 M phosphate buffer (pH 7.4) and further fixed in 1% osmium tetroxide (Electron Microscopy Sciences) in 0.1 M phosphate buffer (pH 7.4) for 60 mins. Samples were dehydrated in a graduated ethanol series, acetone and embedded in LX-112 (Ladd Research). The sections (60 nm) were stained with uranyl acetate and lead citrate (Electron Microscopy Sciences) and viewed in a JEOL JEM 1400 Transmission Electron Microscope (JEOL USA Inc.). All images were taken at 60 kV. All measurements were performed in the Microscopy Imaging Core, Penn State College of Medicine, PA.

4.2. Results

I. Development of the LNB transfection system

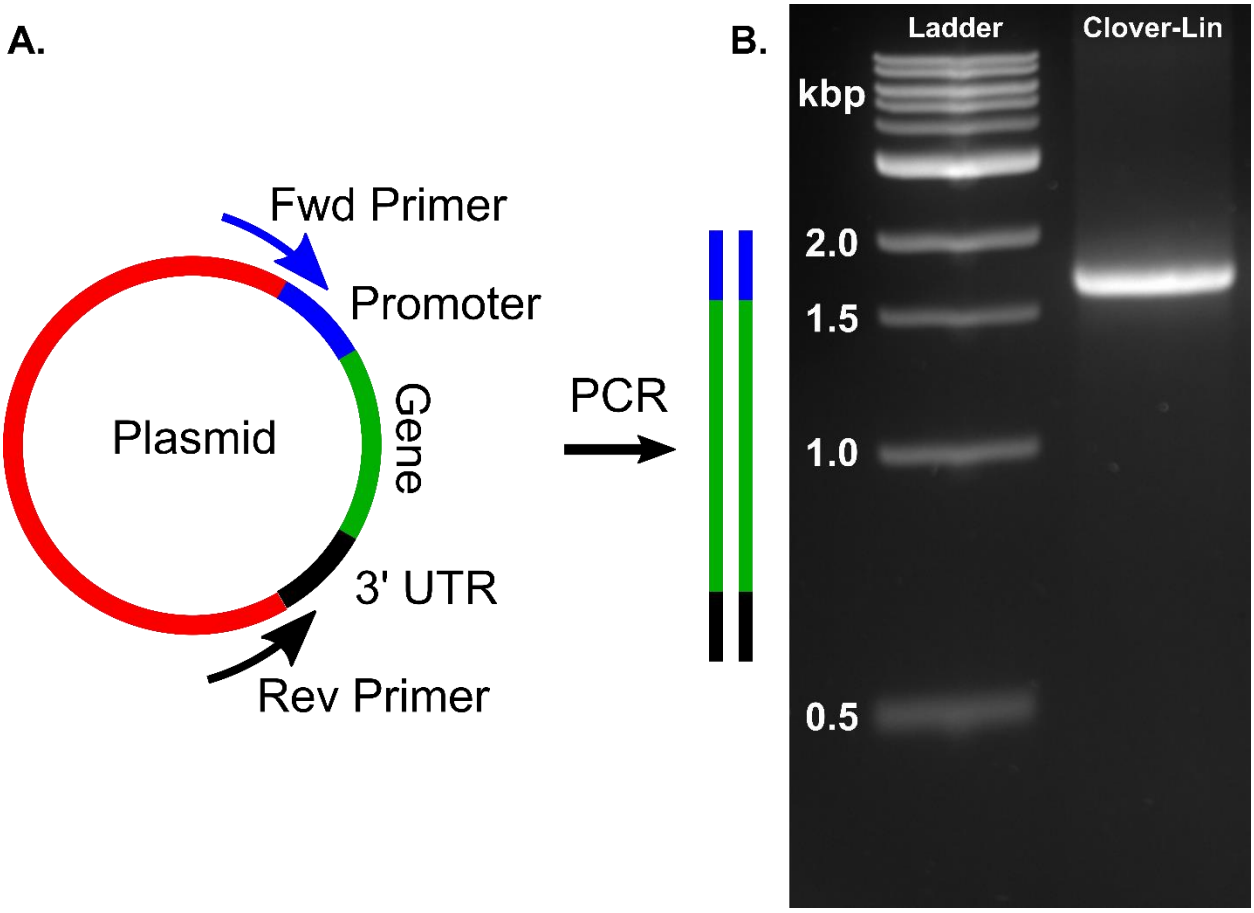

Figure 4.2.1. Synthesis of linearized constructs for transfection. A. The schematic shows the synthesis of linearized DNA from a plasmid (vectored, supercoiled) template by polymerase chain reaction (PCR). Amplification of the gene is achieved by appropriate design of forward and reverse PCR primers spanning the promoter region on the 5' end and the poly A tail region on the 3' end. B. Gel electrophoresis image on a 1% agarose gel and stained with SYBR Safe dye depicts the size of the linearized PCR product (Clover-Lin) after column purification. This product was produced from the PCR linearization of clover cDNA plasmid with a vector pcDNA3.1 and a CMV promoter region.

Table 4.2.1. Optimization of PCR linearization reaction. Clover plasmid template amounts were varied (10-100 ng) per 50 µl PCR reaction volume leading to varying yields of linearized clover. As template amount was increased, amplification decreased.

Clover plasmid starting amount (ng) / 50 µl reaction vol.	**Yield of purified linear product (µg) / 50 µl reaction vol.**	**Amplification Linear (ng) /plasmid (ng)**
10	2.9	290
20	3.3	165
50	**3.6**	**72**
100	3.5	35

.

The cDNA constructs employed for transfecting in this study were either linearized (i.e., vectorless) or supercoiled. This proof-of-concept work has been performed with cDNA constructs in the enhanced fluorescent protein family, specifically clover (green emission) and tdTomato (red emission)[1]. To synthesize linearized cDNA, the coding region of a supercoiled, vectored cDNA template was amplified with primers that were specific for the CMV promoter region (forward primer) and the polyA tail region (reverse primer) of the template plasmid by polymerase chain reaction (PCR). The linearization scheme is shown in Figure 4.2.1. In order to demonstrate this linearization scheme, we used clover plasmid (with pcDNA 3.1 vector) as the template. PCR was optimized with the chosen primer sequences and varying starting clover plasmid template amounts (10-100 ng) per 50 µl reaction volume. 50 ng plasmid per 50 µl PCR reaction volume at 50^{o}C annealing temperature gave the most optimized yield of 3.6 µg purified linearized clover. The linearization of the product was confirmed with a 1% agarose gel electrophoresis with

the appearance of a clear single band within 1.5-2.0 kbp size (Fig. 4.2.1 B). Calculations from the sequence information of pcDNA 3.1 vector suggest the size of linearized clover ~1.7 kbp. The PCR linearization reaction was optimized with various starting quantities of clover plasmid template (Table 4.2.1) 10-100 ng/50 µl reaction volume. Our optimizations showed that increasing ng amounts of the template increased the yield of purified product until 50 ng, beyond which the yield saturated. Simultaneously, amplification of product decreased consistently from 10-100 ng from 290 to 35 times (calculated by the ratio of product (ng)/template(ng) per reaction). In order to maximize yield per reaction with a reasonable amplification, we chose 50 ng as the optimal template amount per reaction for future work.

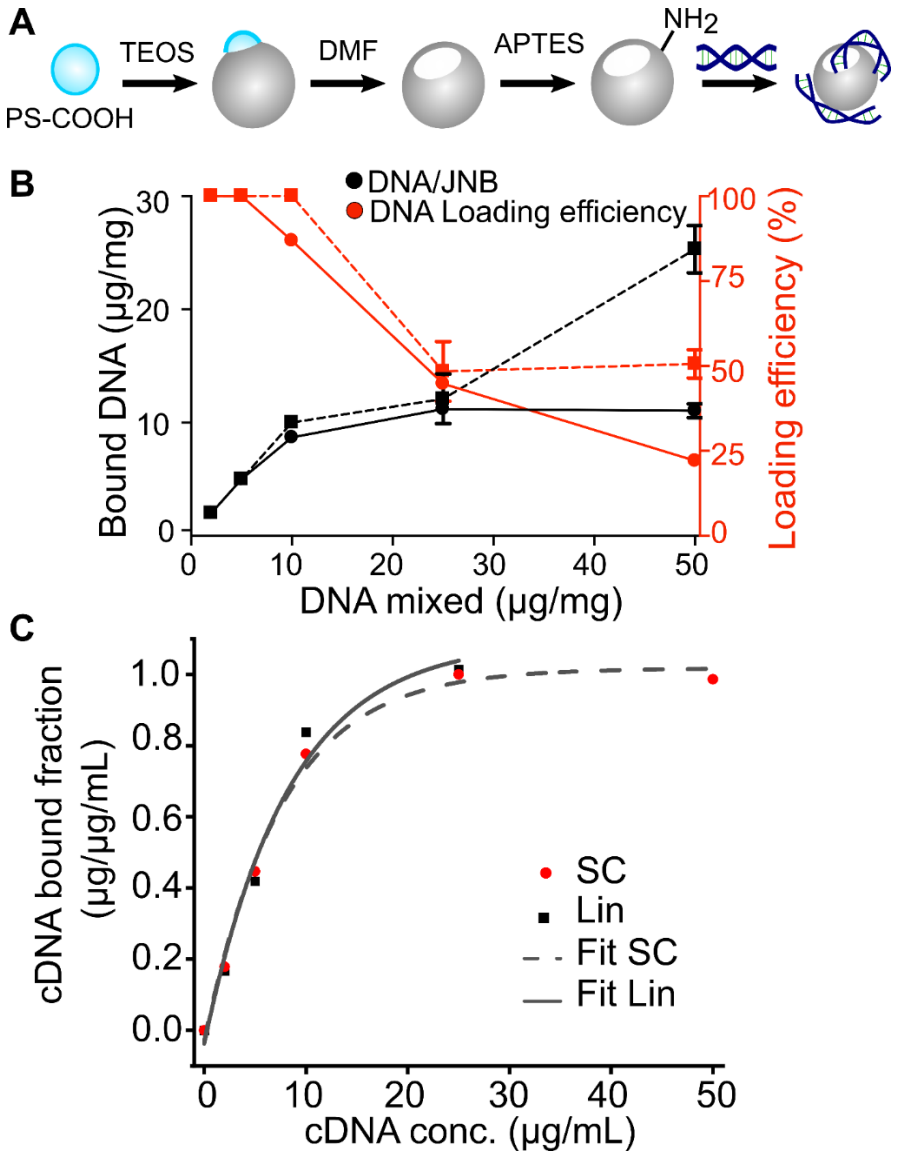

Figure 4.2.2. Development of NBs for cDNA transfection. A. Schematic of NB synthesis and surface functionalization. 100 nm polystyrene (PS) template was used to generate an eccentric cavity in the NB synthesis from tetraethyl orthosilicate (TEOS) condensation. Dimethyl formamide (DMF) was used to dissolve away the PS template, followed by amine functionalization with 3-aminopropyltriethoxysilane (APTES). B. cDNA loading curves showing µg of cDNA bound per mg of amine functionalized NB (left y-axis, black) and % cDNA loading efficiency calculated as % of mixed cDNA that bound (right y-axis, red). Circles and squares depict data from supercoiled cDNA and linearized cDNA, respectively. The points depict ±SEM from mean values, performed in triplicate. C. Binding data for linear (Lin) and supercoiled (SC) clover were plotted and fitted. SC can be easily fit with an exponential increase model reaching a saturation plateau in the entire range from 0-50 µg/mg DNA dosage(red circles and black dotted line). However, linearized DNA binding on NB does not follow the same pattern of saturating binding as supercoiled. We were able to fit linear loading data in the range <= 25 µg/mg (black squares and solid black line). In this range, the binding pattern follows an increasing exponential form, which is consistent between both types of DNA constructs. Y-axis was normalized to saturation binding value of supercoiled at 50 µg/ml and binding value of linearized at 25 µg/ml within a scale of 0 to 1.

Figure 4.2.2 A shows the scheme of NB synthesis, amine functionalization and DNA loading. APTES functionalized positively charged NBs (+36.8± 0.8 mV, ref. Chapter 3) post purification were dried and redispersed in DPBS at 1 mg/ml for DNA loading overnight. Post incubation with various added amounts of DNA (0-50 µg/mg NB), the NBs were spun down, and the supernatant was collected for unbound DNA quantification. Figure 4.2.2 B is a plot that shows amine coated NBs can load both linearized and supercoiled cDNA constructs. Unlike linearized cDNA, the adsorption profile of the supercoiled construct showed an exponential trajectory with a saturation plateau (Fig. 4.2.2 C). The maximum bound cDNA achieved was 11 µg/mg NB for supercoiled (black circles) and 25 µg/mg linearized (black squares) clover cDNA. Figure 4.2.2 B also indicates that the loading efficiency decreased with increasing cDNA concentrations. At the highest DNA tested (50 µg/mg), the loading efficiencies for linearized (red circles) and supercoiled (red squares) cDNA were 22% and 50%, respectively. The profile observed for supercoiled cDNA suggests that NBs possess a monolayer saturation adsorption capacity. The K_D value from the exponential fit was 5.5 µg/ml for supercoiled cDNA. On the other hand, linearized cDNA constructs exhibited a similar binding profile up to 25 µg/ml after which there is a linear increase in binding without reaching a saturation point with the highest amount of cDNA tested (Fig. 4.2.2 C). Therefore, it was not possible to fit the entire range of the linearized cDNA binding data with a single exponential equation. However, fitting the data to an exponential equation up to 25 µg/ml, the K_D obtained was 5.9 µg/ml (R^2=0.98) (Fig. 4.2.2 C).

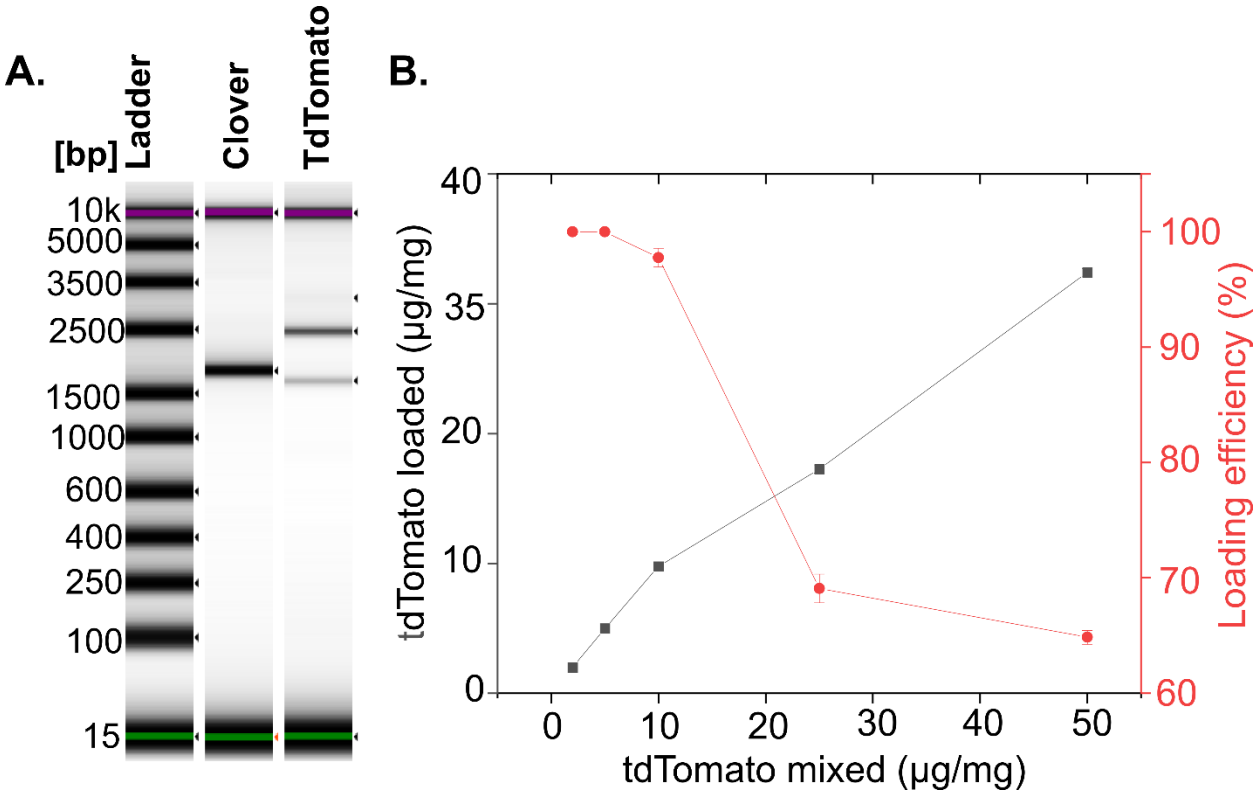

Figure 4.2.3. Loading of linearized TdTomato DNA on NBs. A. Gel like image of linearized and purified Tdtomato in comparison to linearized clover run on a Tapestation. 65% of the intensity from the linearized TdTomato lane was recorded from the band at 2.46 kbp. Both clover and tdTomato were loaded at 5 ng/lane. B. Amount of Tdtomato (linearized) cDNA loaded (black) and loading efficiency (red) at various amounts mixed with NBs (0-50 µg/mg). Red and black traces show representative loading profiles, with mean and ±SEM values, performed in duplicate.

We next examined whether increasing the size of the linearized DNA would alter the loading curve. In this set of experiments, we employed the cDNA construct coding for the fluorescent protein, tdTomato (tdT) in a plasmid vector peGFPN1. Tapestation results (Fig. 4.2.3. A) confirm the size of the main band (~65%) from purified linearized tdTomato is 2.46 kbp (calculated size from vector map~ 2.4 kbp). There was a lighter band at a lower size that appeared as an impurity (either due to some non-specific amplification during PCR or impurities in the tdTomato plasmid maxiprep stock solution). Our results (Fig. 4.2.3 B) indicate that the tdT binding profile was steeper than that observed for clover (Fig. 4.2.2 B). The maximum loading capacity observed at 50 µg/mg loading was 32

µg/mg, slightly greater than the linearized clover (25 µg/mg). However, based on the higher molecular weight of linearized tdT (2.4 kDa) than clover (1.7 kDa), we determined that a comparable cDNA copy number was adsorbed on the NB surface per mg (New England Biolabs NEBiocalculator^{TM} : tdT copy number = $1.3*10^{13}$ and clover copy number = $1.4*10^{13}$).

Table 4.2.2. Representative loading amounts of different types of nucleic acid constructs measured per mg of amine functionalized NB. For all constructs, amount added for mixing with NB was 25 µg/mg NB, except for siRNA which was added at 10 µg/mg NB. All DNA construct loading amounts were measured with Qubit dsDNA assay, and all RNA constructs were measured with Nanodrop. See methods for more details.

Type of nucleic acid construct	Strands (1 or 2)	Size (bp)	Configuration (Linear /supercoiled)	Loading (µg/mg NB)	Copy Number/mg NB ($x10^{12}$)
Clover plasmid	2	6127	Supercoiled	11.2	1.78
Linear clover	2	1700	Linear	12.1	6.94
Linear tdTomato	2	2400	Linear	17.3	7.02
Clover mRNA (uncapped)	1	1500	Linear	10.9	13.61
Silencing RNA	2	22	Linear	3.9	142.42

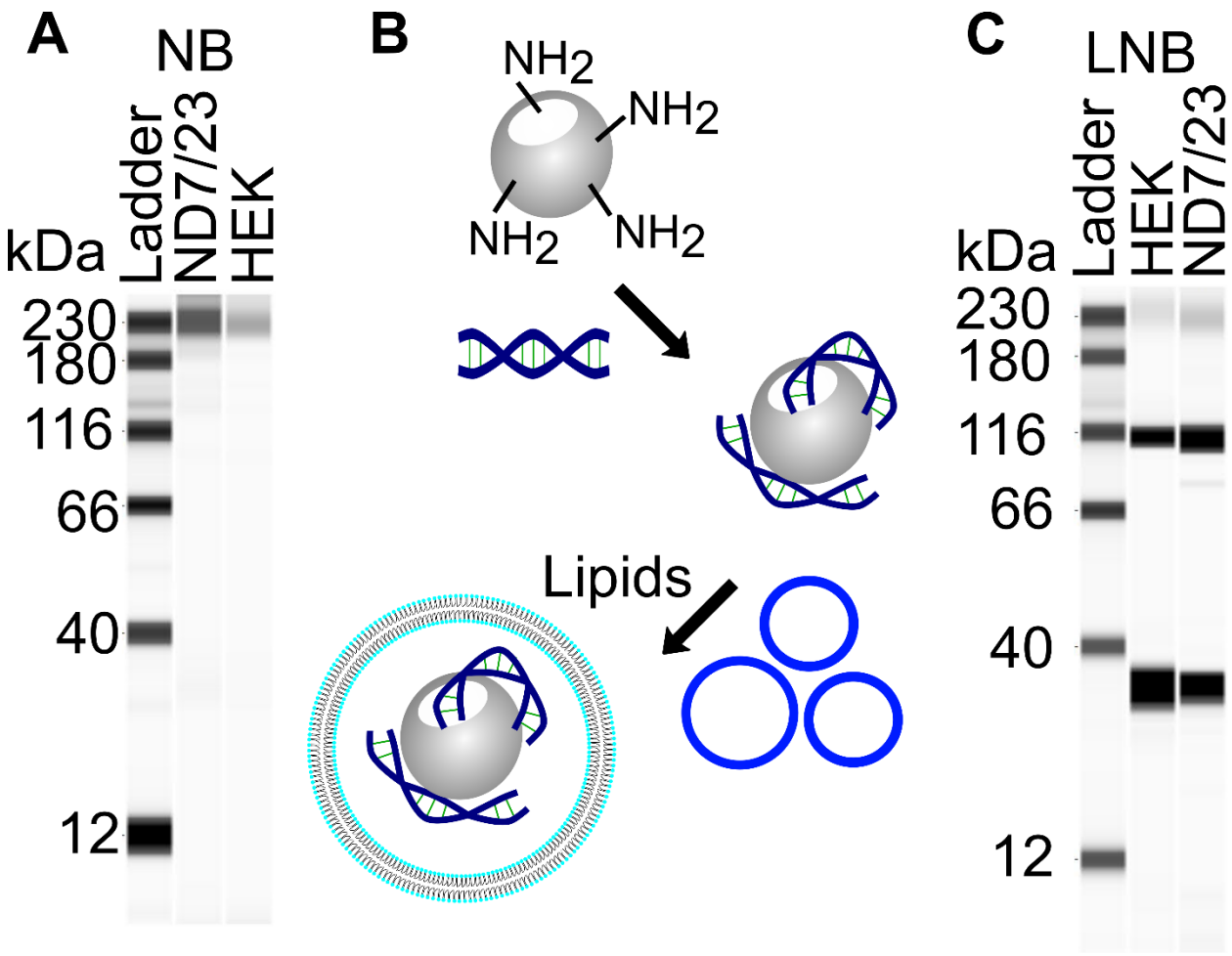

Figure 4.2.4. Encapsulation of NBs with 'helper' lipids results in clover expression. A, C. Western blots of clover expression in HEK and ND7/23 cells transfected with NB loaded with supercoiled clover cDNA without (A) and with 1:1 DOPE:DOTAP coating (C). In A, each lane was loaded with 0.2 µg/µl for a total protein assay; while for C, 0.075 and 0.25 µg/µl per lane were loaded for HEK and ND7/23 cells, respectively. The 36 kDa band represents clover. Vinculin (116 kDa) was used as the loading control. B. Schematic drawing showing 100 nm extruded lipids were mixed with DNA-loaded NBs to prepare lipid-encapsulated NBs (LNBs).

Furthermore, we see from Table 4.2.2 that different types of constructs load different total number of copies or molecules per mg NB. For example, for clover, mRNA which is essentially a single stranded version of the linearized clover, loads 1.96 i.e., ~2 times as much as the double stranded version of the same gene. On the other hand, if we drastically reduce the number of base pairs and consequently, the length of the construct, i.e., a silencing RNA of ~22 base pairs, we see that compared to linearized clover, we are able to load 20.5 times higher number of nucleic acid molecules per mg

NB. Finally, we also observe that, for the same amount of clover DNA added per mg NB, we get 3.9 times higher number of molecules loaded per mg NB for linearized construct compared to supercoiled construct. These observations suggest that the number of strands, number of base pairs and DNA configurations have an effect on their loading on the NB surface.

Next, we applied the clover DNA loaded NBs to cell lines for transfection. Although the clover cDNA-loaded NBs were internalized by all cell types, clover fluorescence was not observed up to 72 hrs post-transfection with NB concentrations up to 0.5 mg/ml. To confirm the lack of clover expression, HEK and ND7/23 cells were transfected with 0.1 mg NBs carrying 2 µg/mg clover cDNA for 4 hrs and cell protein was isolated 72 hrs post transfection. Western blotting assays were employed to detect clover expression and the blot shown in Figure 4.2.4 A indicates neither cell type was successfully transfected.

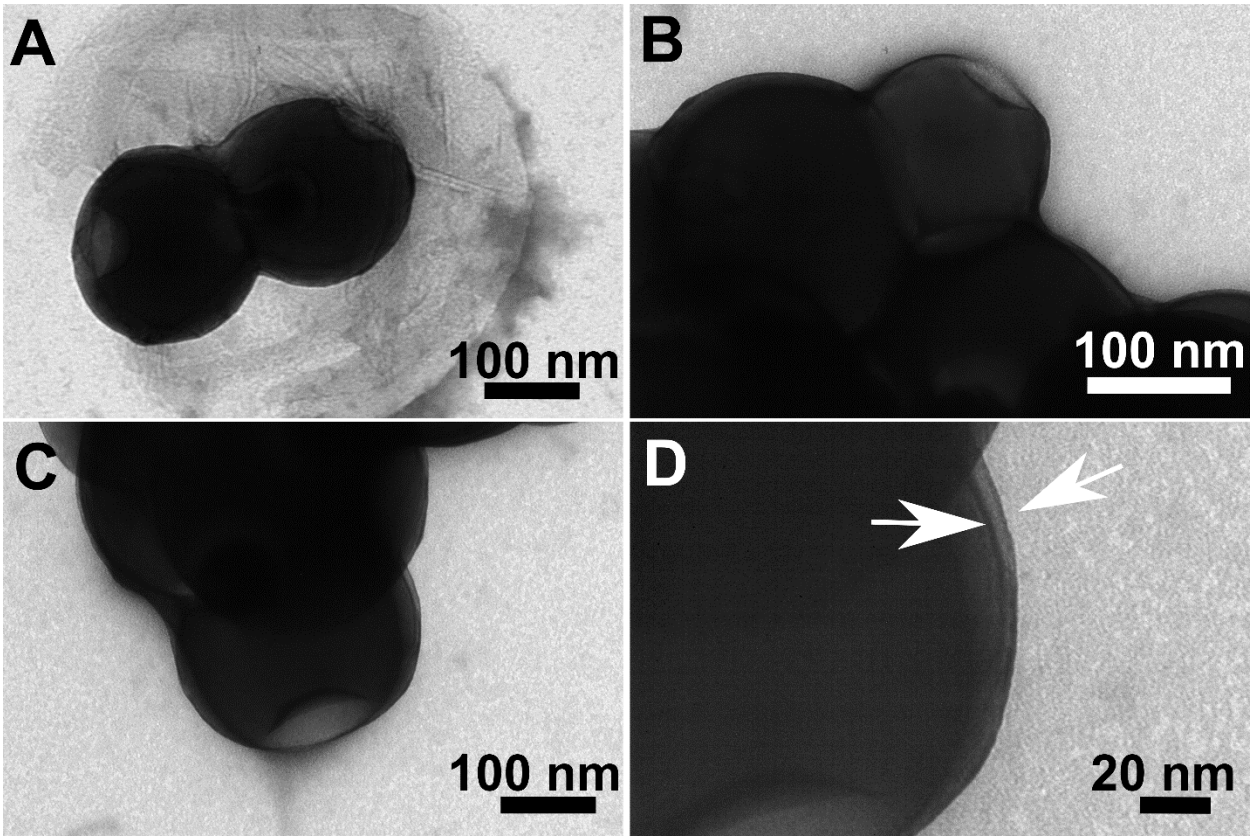

Figure 4.2.5. Characterization of lipid coated nanobowls (LNBs). A-C. Transmission electron microscopy (TEM) images of LNBs with negative staining. D. TEM image showing a lipid layer (approx. 5 nm diameter) surrounding LNBs. White arrows indicate the thickness of the lipid layer on the NB.

The lack of clover expression suggested that the internalized NBs were trapped within endocytic vesicles and unable to release the cDNA. Consequently, the NBs were next coated with the lipids DOPE and DOTAP at 1:1 molar ratio (Fig. 4.2.4 B), which have been reported to act as 'helper agents' in other transfection systems. The TEM micrographs shown in Figure 4.2.5 indicate that the lipid-coated NBs (LNBs) have a lipid coating of approximately 5 nm. HEK and ND7/23 cells were transfected for 4 hrs with LNBs (0.5 mg/ml) carrying linear or supercoiled clover cDNA constructs (10 µg/mg). Clover protein expression levels were then determined with Western blotting assays. Figure 4.2.4 C shows that, unlike NBs, LNBs loaded with supercoiled clover cDNA

resulted in protein expression in both cell lines. Furthermore, the TEM micrographs shown in Figure 4.2.6 indicate that LNBs were internalized in HEK cells (Fig. 4.2.6 top) within 24 hrs of incubation. In contrast to NBs without lipid coating (Fig. 4.2.6 bottom), some LNB clusters were found in the cytoplasm that seem to have escaped endosomal entrapment (white arrows, Fig. 4.2.6 top). We also observe that 24 hrs after treatment with LNBs, not 100% of the LNB clusters have been released into the cytoplasm. This indicates that either the endosomal release process takes longer than 24 hrs or that the endosomolytic properties of the DOPE/DOTAP combination needs further optimization to improve the efficiency of endosomal release of LNBs.

After we confirmed that this DOPE/DOTAP coated LNBs could lead to successful transfection and got successfully internalized in HEK cells at 24 hrs, we set out to determine the concentration dependent uptake of all 4 cell lines at that time point. For this, we first conjugated Cy3-NHS to NBs as shown in Chapter 3. Then, we coated the Cy3-conjugated NBs with lipids (1:1 DOPE:DOTAP) and re-dispersed them at various concentrations (0, 50, 125, 250, 500 and 1000 μg/ml in a 1:1 DPBS:Opti-MEM cocktail. Our results (Fig. 4.2.7-10) show that after 24 hrs, there is a clear concentration dependence of NB uptake in the cell lines. The punctate or clustered fluorescence from the images suggests that the fluorescence comes from Cy3 conjugated on NB clusters rather than leached, unbound Cy3 dye. At lower concentrations, there are less clusters indicating less LNBs internalized. The uptake amount increases with increasing concentration of LNBs. All cell lines show maximum uptake in the maximum LNB concentration i.e., 1 mg/ml. All cell lines look healthy at all LNB concentrations tested. HEK cells and L-cells show maximum uptake at 1 mg/ml concentrations.

Since these (Fig. 4.2.7-10) are optical microscopy images, we can only conclude that there is co-localization of LNB clusters and cell growth patches. To conclude successful internalization, we will have to do TEM as a confirmatory test. We were not able to perform TEM confirmatory test for all 4 cell lines. But our TEM imaging work on HEK cells (Fig. 4.2.6 top) as well as ND7 (data not shown) at 24 hrs with 0.5 mg/ml LNBs confirm our fluorescence microscopy to depict successful internalization.

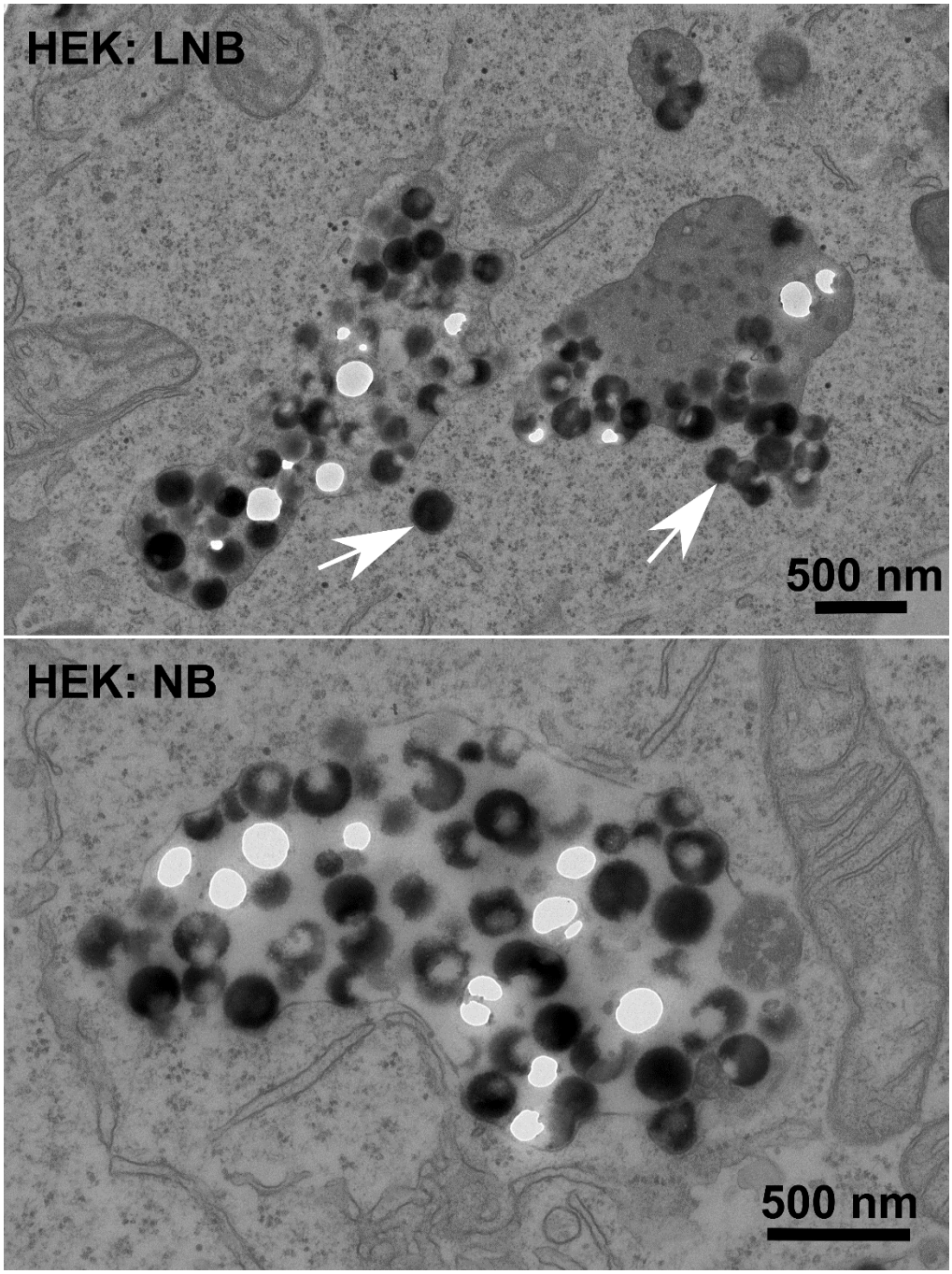

Figure 4.2.6. Lipid encapsulation helps LNBs get released into the cytoplasm. Transmission electron microscopy (TEM) images of HEK cells 24 hrs after treatment with 0.5 mg/ml. Top. LNB. Bottom. NB (no lipid). White arrows indicate LNBs or LNB clusters found in the cytoplasm. TEM images were taken from 60 nm thin sections with negative staining.

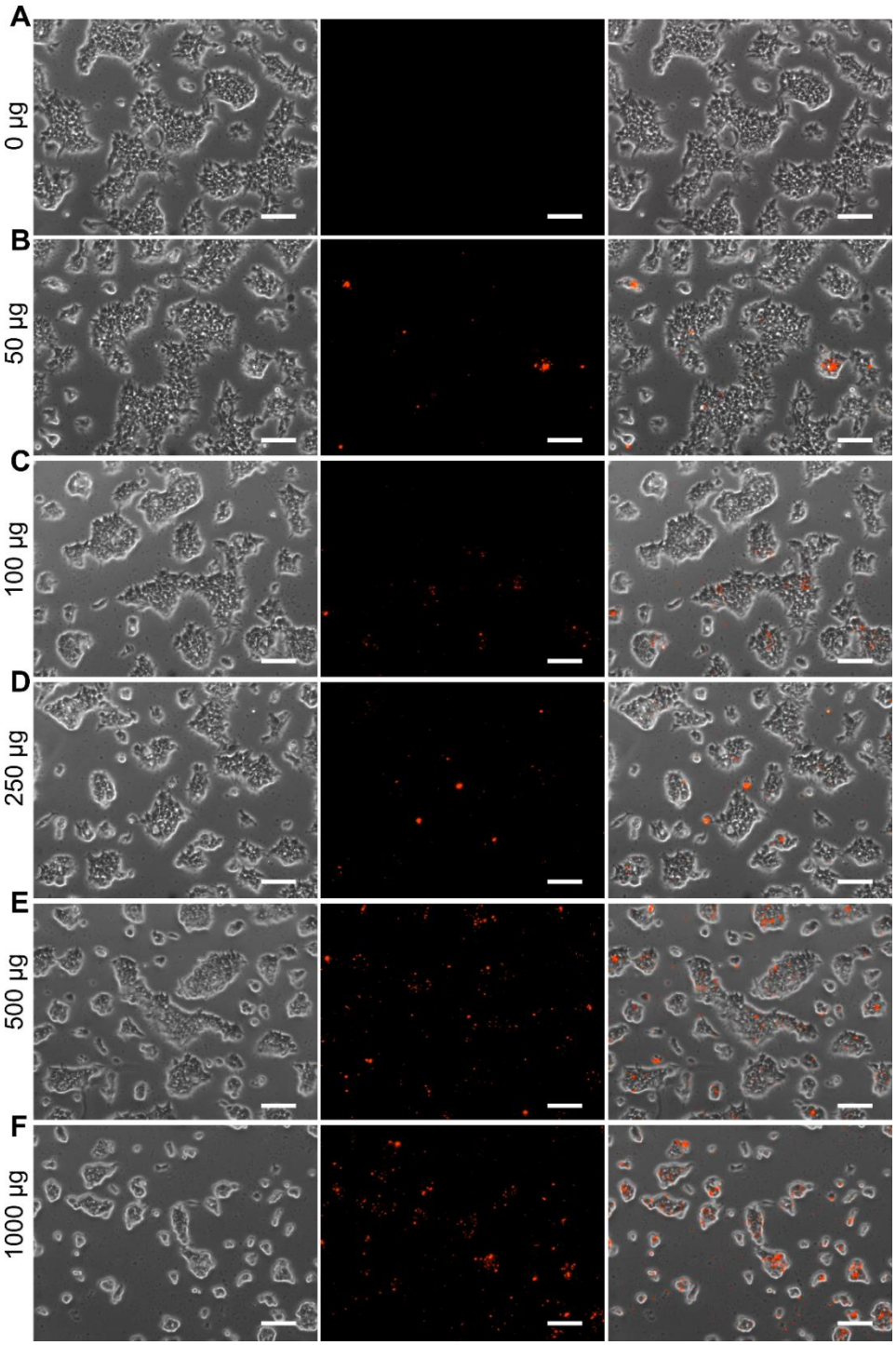

Figure 4.2.7. Concentration dependent NB uptake in HEK cells. Phase (left), fluorescence (center) and overlay (right) images of HEK cells 24 hrs after introduction of Cy3-tagged LNBs at various concentrations (0-1000 µg/ml). LNBs were incubated for 4 hrs in the cell culture, then rinsed with warm media to remove unbound LNBs. The cells were then allowed to incubate for 24 hrs, then fixed in 4% PFA and imaged in DPBS. All images taken with a 10x objective. Scale bars depict 100 µm.

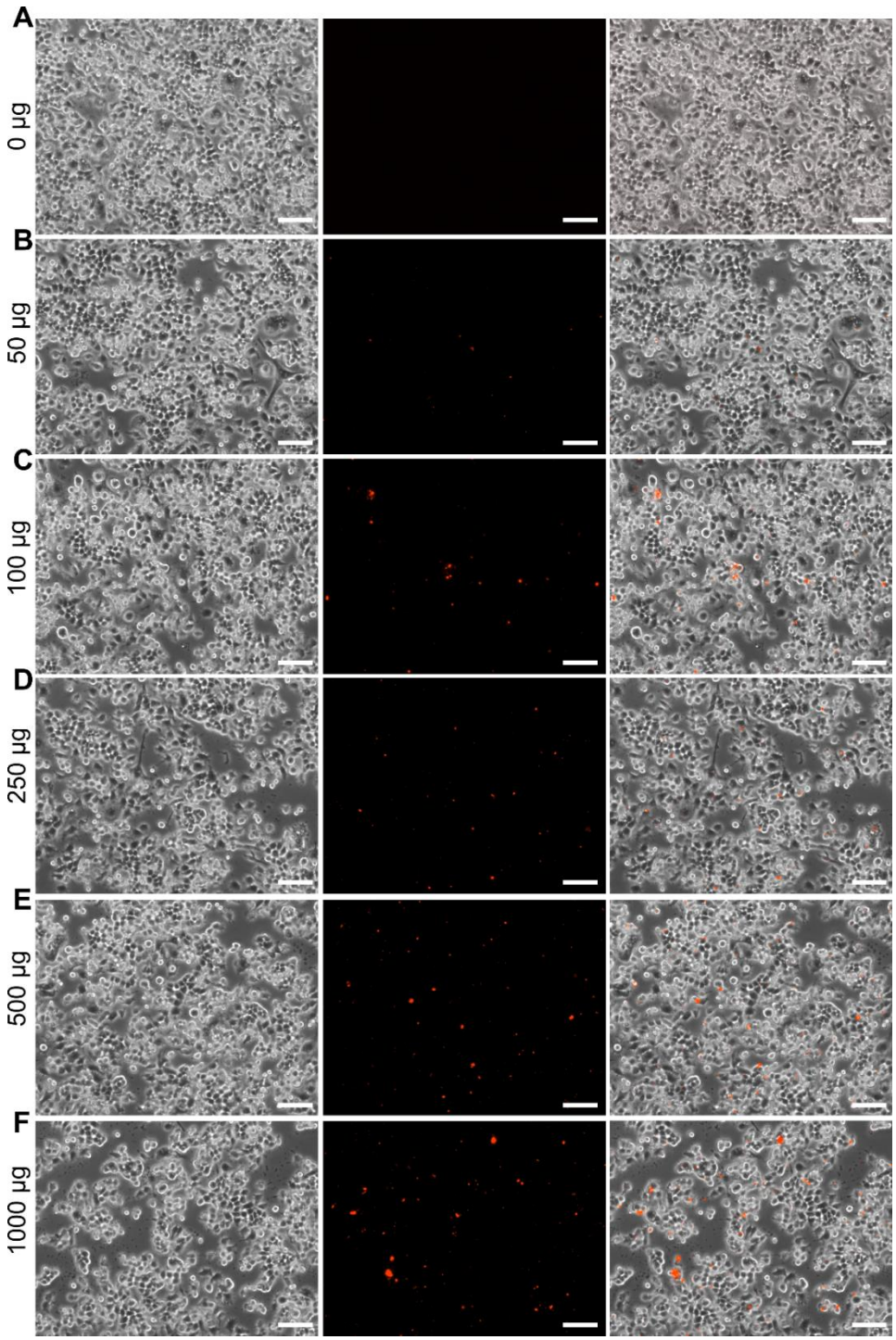

Figure 4.2.8. Concentration dependent NB uptake in ND7/23 cells. Phase (left), fluorescence (center) and overlay (right) images of ND7/23 cells 24 hrs after introduction of Cy3-tagged LNBs at various concentrations (0-1000 µg/ml). LNBs were incubated for 4 hrs in the cell culture, then rinsed with warm media to remove unbound LNBs. The cells were then allowed to incubate for 24 hrs, then fixed in 4% PFA and imaged in DPBS. All images taken with a 10x objective. Scale bars depict 100 µm.

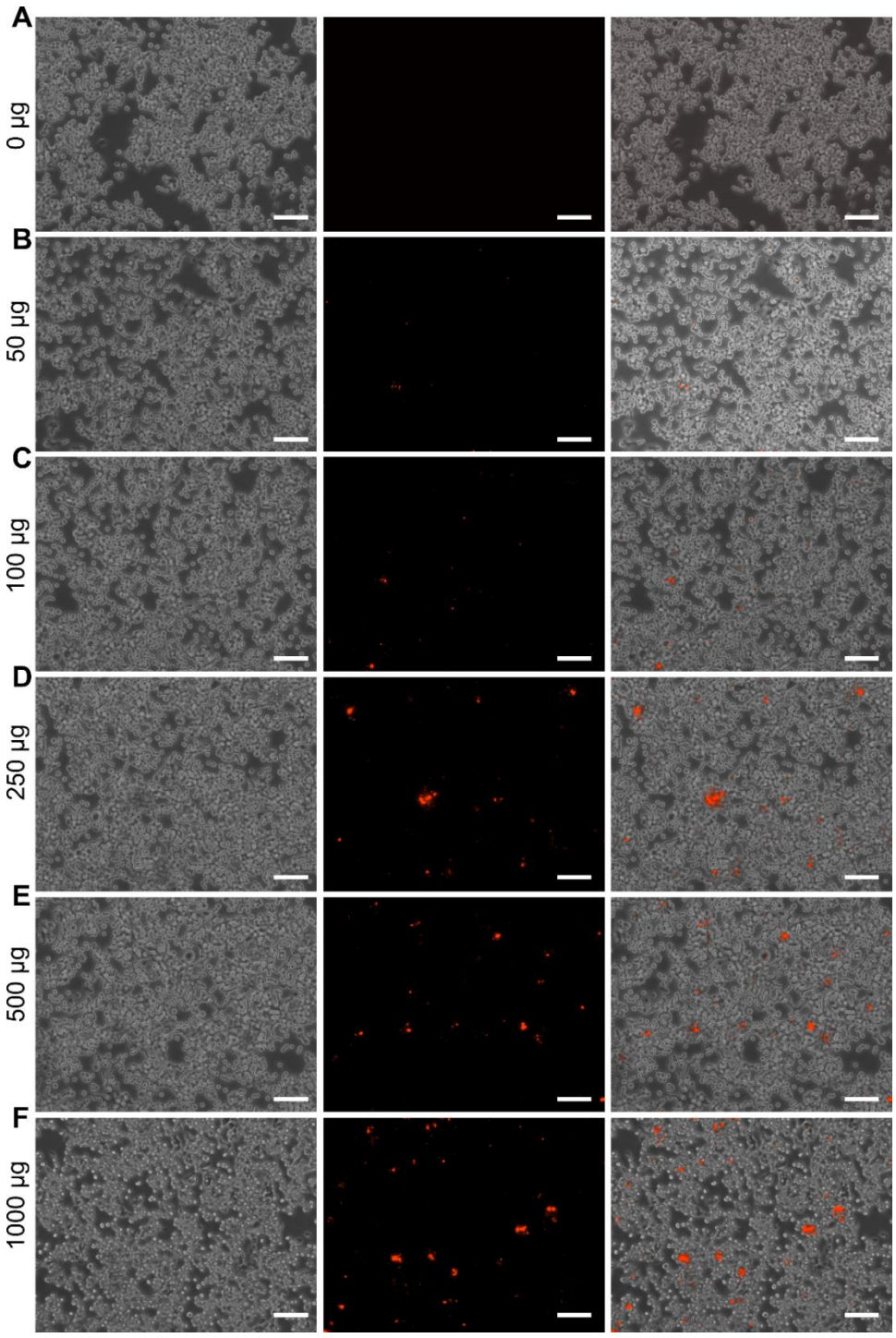

Figure 4.2.9. Concentration dependent NB uptake in HeLa cells. Phase (left), fluorescence (center) and overlay (right) images of HeLa cells 24 hrs after introduction of Cy3-tagged LNBs at various concentrations (0-1000 µg/ml). LNBs were incubated for 4 hrs in the cell culture, then rinsed with warm media to remove unbound LNBs. The cells were then allowed to incubate for 24 hrs, then fixed in 4% PFA and imaged in DPBS. All images taken with a 10x objective. Scale bars depict 100 µm.

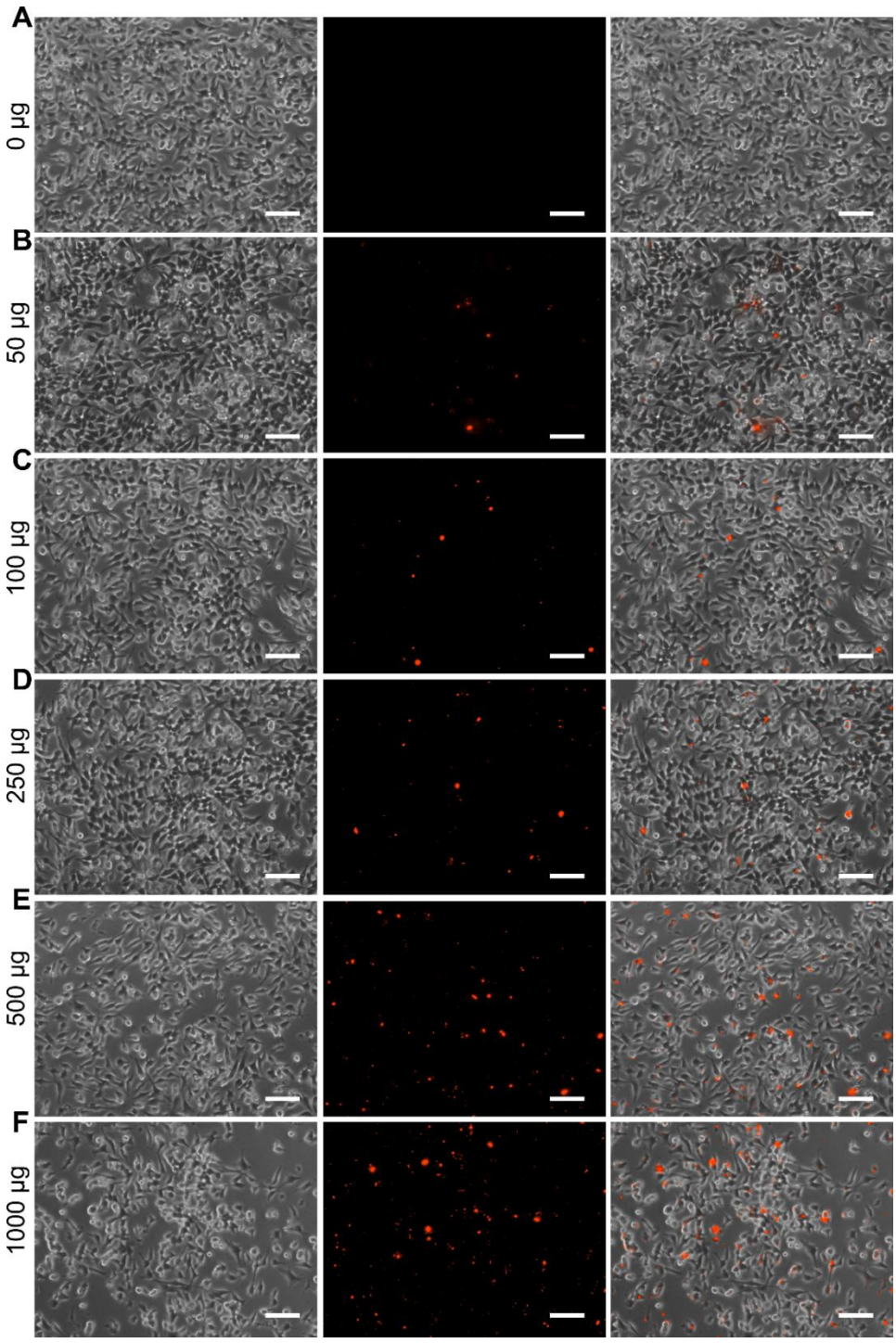

Figure 4.2.10. Concentration dependent NB uptake in L-cells. Phase (left), fluorescence (center) and overlay (right) images of L-cells cells 24 hrs after introduction of Cy3-tagged LNBs at various concentrations (0-1000 µg/ml). LNBs were incubated for 4 hrs in the cell culture, then rinsed with warm media to remove unbound LNBs. The cells were then allowed to incubate for 24 hrs, then fixed in 4% PFA and imaged in DPBS. All images taken with a 10x objective. Scale bars depict 100 µm.

II. Characterization of the transfection efficiency of the LNB system

After it was confirmed that DOPE/DOTAP coating was led to successful transfections, we set out to fully characterize the LNB system for its ability to transfect all 4 cell lines (HEK, ND7/23, HeLa and L-cells) and transfection efficiencies. First, we added 10 µg/mg loaded LNBs and applied to all 4 cell lines at 0.5 mg/ml concentrations. Our results (Fig. 4.2.11-12) show that both supercoiled and linearized clover loaded LNBs can successfully lead to clover expression in all 4 cell lines. Our results also show that linearized constructs (Fig. 4.2.11) lead to generally higher transfection efficiencies than the supercoiled constructs (Fig. 4.2.12) in all 4 cell lines. We also observe that the intensity of clover fluorescence is highly variable within a given field of view especially for the linearized clover (Fig. 4.2.11). In both types of constructs, HEK cell line has the highest efficiency of clover expression (i.e. highest number of cells transfected/total number of cells in the field of view). We also tested 0-50 µg dose responses of supercoiled clover DNA in HEK and ND7/23 cells by transfecting them at a fixed 0.5 mg/ml NB dosage. After 48 hrs, we observe that both cell lines show different transfection efficiencies at different µg loading amounts. For example, in HEK cells (Fig. 4.2.13), we observe that increasing the µg/mg supercoiled clover DNA loading on LNBs clearly increases the transfection efficiency and the maximum efficiency is reached at 50 µg/mg DNA loading. On the other hand, in ND7/23 cells, the same trend is observed, but the maximum efficiency is reached at 25 µg/mg DNA loading. However, fluorescence microscopy gives a qualitative characterization of transfection efficiency. Therefore, a more rigorous quantitative technique is required to make concrete conclusions about transfection properties of the LNB system.

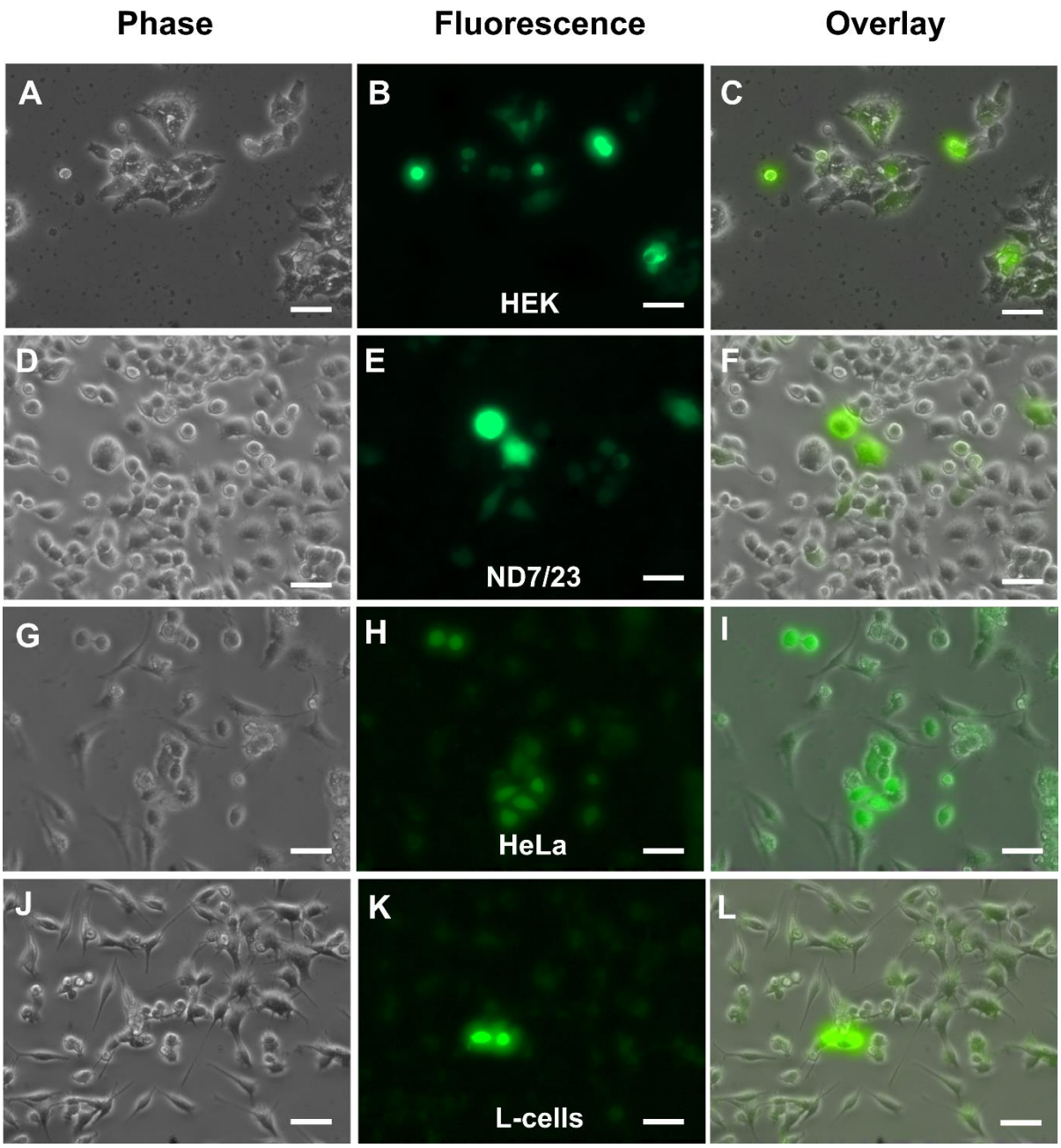

Figure 4.2.11. Linearized clover transfections of 4 cells lines with LNBs. Phase (A, D, G, J), fluorescence (B, E, H, K) and overlay (C, F, I, L) images acquired with 20X objective showing clover expression in transfected cells with linearized clover at 10 µg/mg LNB (0.5 mg/ml) after 48 hrs in 4 cell lines HEK, ND7/23, HeLa and L-cells. All scale bars measure 50 µm.

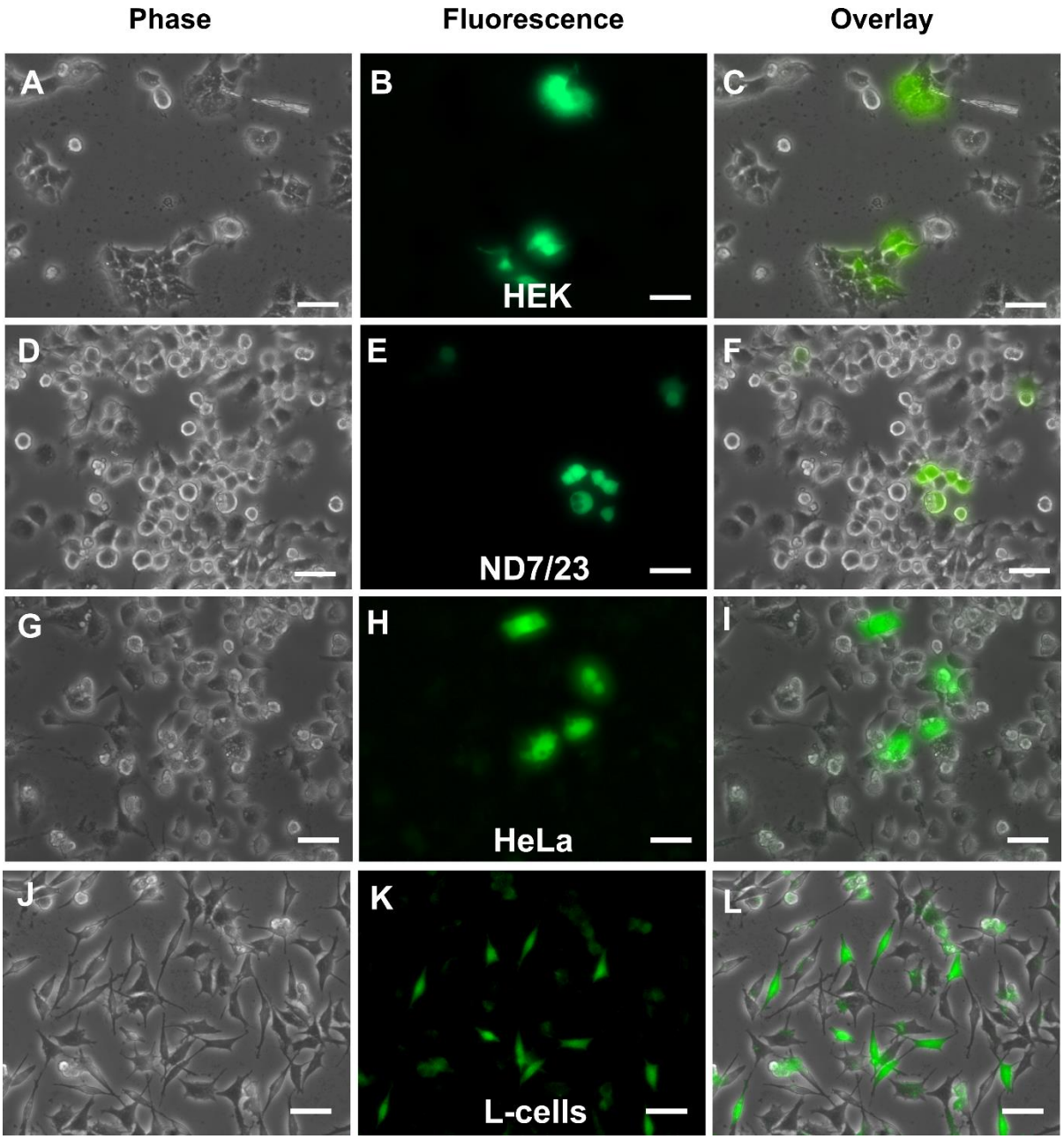

Figure 4.2.12. Supercoiled clover transfections of 4 cells lines with LNBs. Phase (A, D, G, J), fluorescence (B, E, H, K) and overlay (C, F, I, L) images acquired with 20X objective showing clover expression in transfected cells with supercoiled clover at 10 µg/mg LNB (0.5 mg/ml) after 48 hrs in 4 cell lines HEK, ND7/23, HeLa and L-cells. All scale bars measure 50 µm.

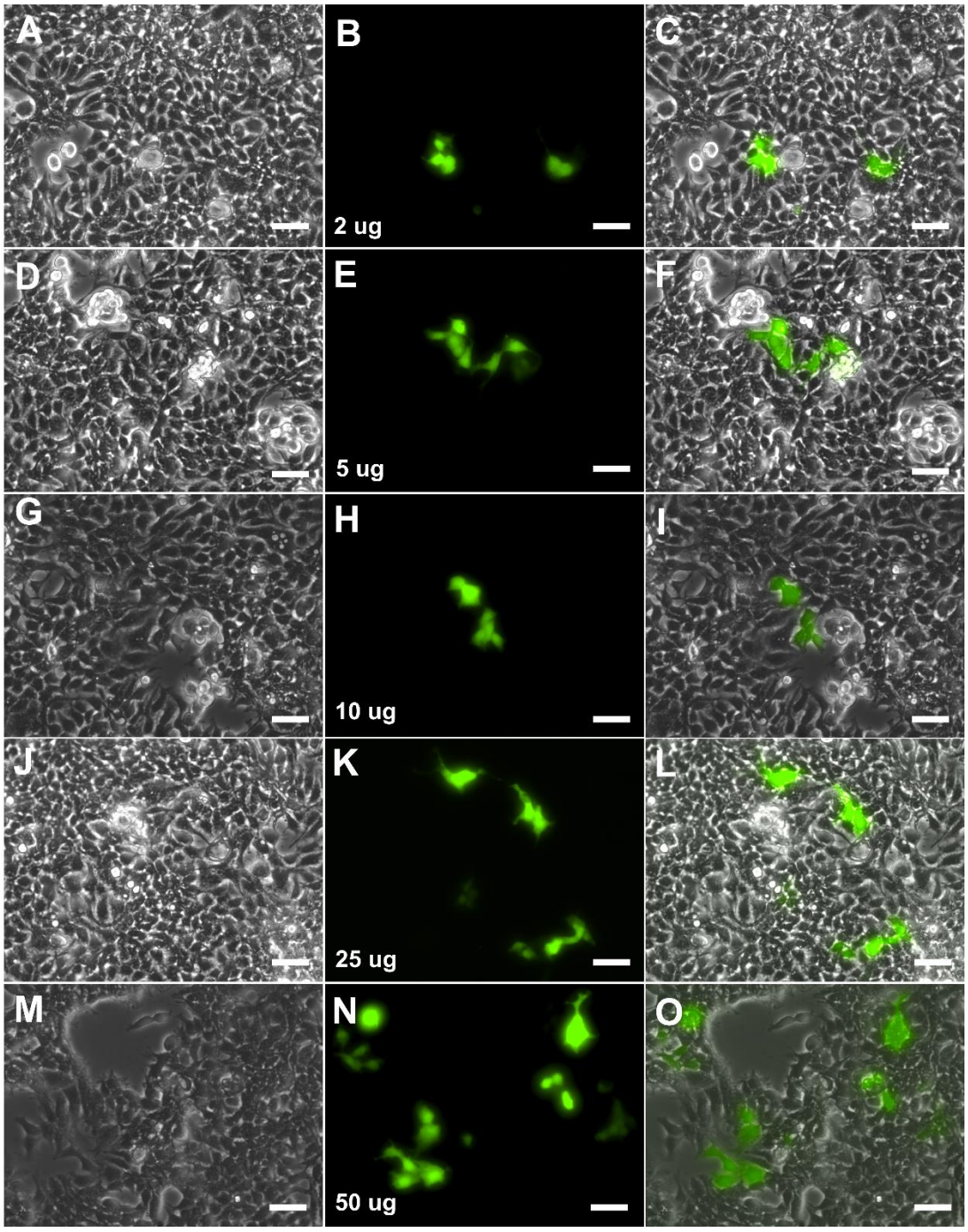

Figure 4.2.13. Clover dose (µg) response in LNB transfected HEK cells. Phase (A, D, G, J, M), fluorescence (B, E, H, K, N) and overlay (C, F, I, L, O) images acquired with 20X objective showing clover expression in transfected HEK cells at various loading amounts of supercoiled clover 0-50 µg/mg LNB (0.5 mg/ml) after 48 hrs. All scale bars measure 50 µm.

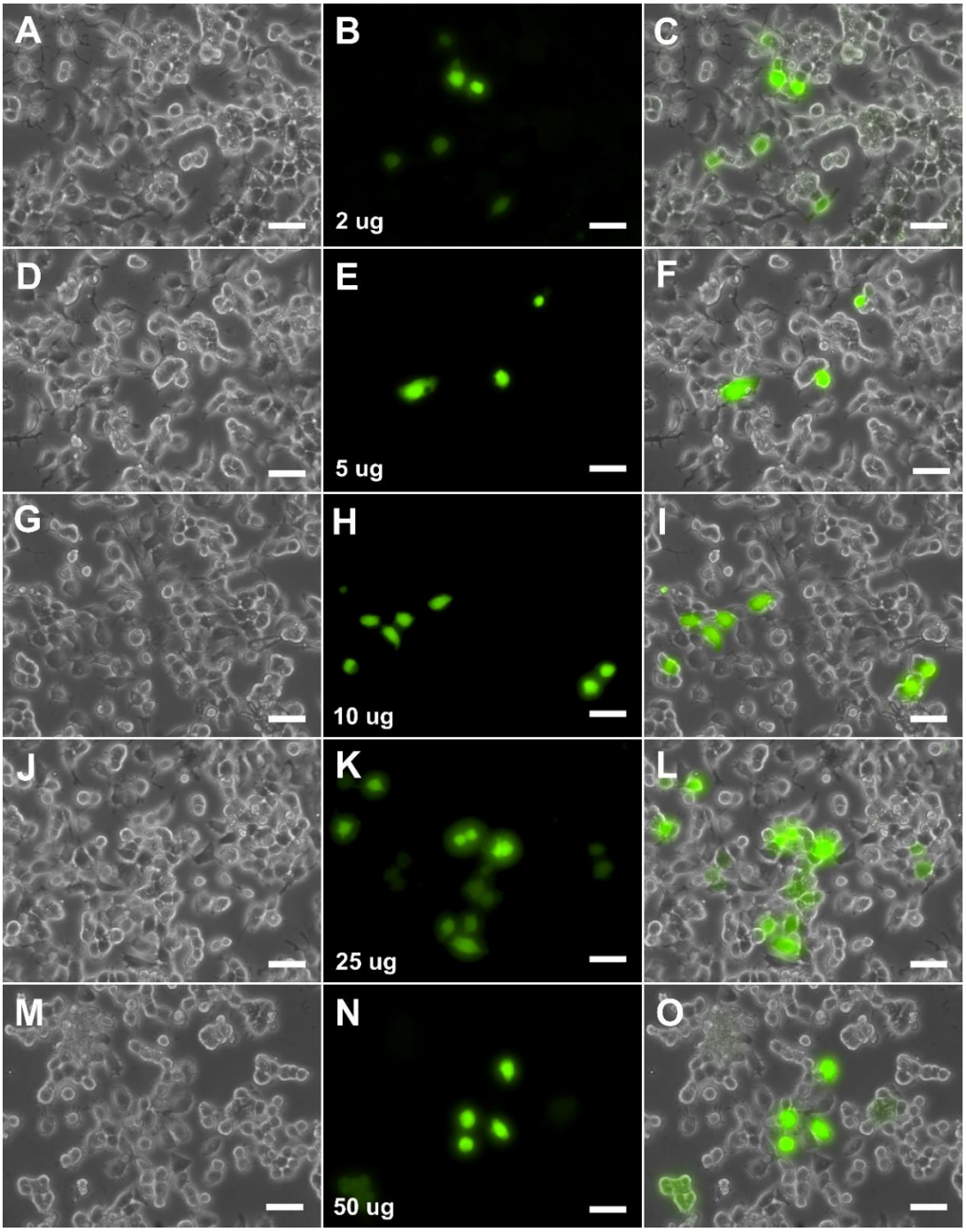

Figure 4.2.14. Clover dose (µg) response in LNB transfected ND7/23 cells. Phase (A, D, G, J), fluorescence (B, E, H, K) and overlay (C, F, I, L) images acquired with 20X objective showing clover expression in transfected ND7/23 cells with supercoiled clover 0-50 µg/mg LNB (0.5 mg/ml) after 48 hrs. All scale bars measure 50 µm.

We next determined the transfection efficiency in both HEK and ND7/23 cells with varying loads (0-50µg/mg) of clover DNA (linear and supercoiled) with a constant LNB

concentration (0.5 mg/ml). Clover expression was quantified employing Western blotting assays 48 hrs post-transfection with LNB (Fig. 4.2.15-16). The results show that for both supercoiled and linearized constructs, clover is expressed in both cell lines at all cDNA loading values, including the lowest i.e. 2 µg/mg. In all constructs and cell lines, we also observe the same trend i.e. as µg/mg loading is increased, initally clover/vinculin ratio increases up to 5 µg/mg in supercoiled construct transfected cells (Fig. 4.2.15) and 10 µg/mg in linearized construct transfected cells (Fig. 4.2.16) and then, the expression of clover (indicated by clover/vinculin) saturates at a value even though µg/mg loading is increased up to 50. This indicates that for both cell lines, the LNB system has a maximum transfection efficiency beyond which adding more DNA will not help improve efficiency. This is a reasonable result as we had observed earlier that supercoiled DNA loading on NBs reaches saturation loading at 10 µg/mg. Interestingly, although the NB loading curves (Fig. 4.2.2 B) showed that linearized DNA loading did not saturate, our transfection results show that there is saturation of clover expression beyond ~10 µg/mg linearized DNA loading. The results also indicate that clover expression, determined by the clover/vinculin ratio, was higher in ND7/23 cells for all cDNA loads tested (Fig. 4.2.15). On the other hand, HEK cells exhibited greater clover expression when transfected with LNBs loaded with linear cDNA (Fig. 4.2.16). Although clover transfection can be obtained with LNBs loaded with either supercoiled or linearized cDNA, the relative expression levels when transfected with the LNB system are cell type dependent.

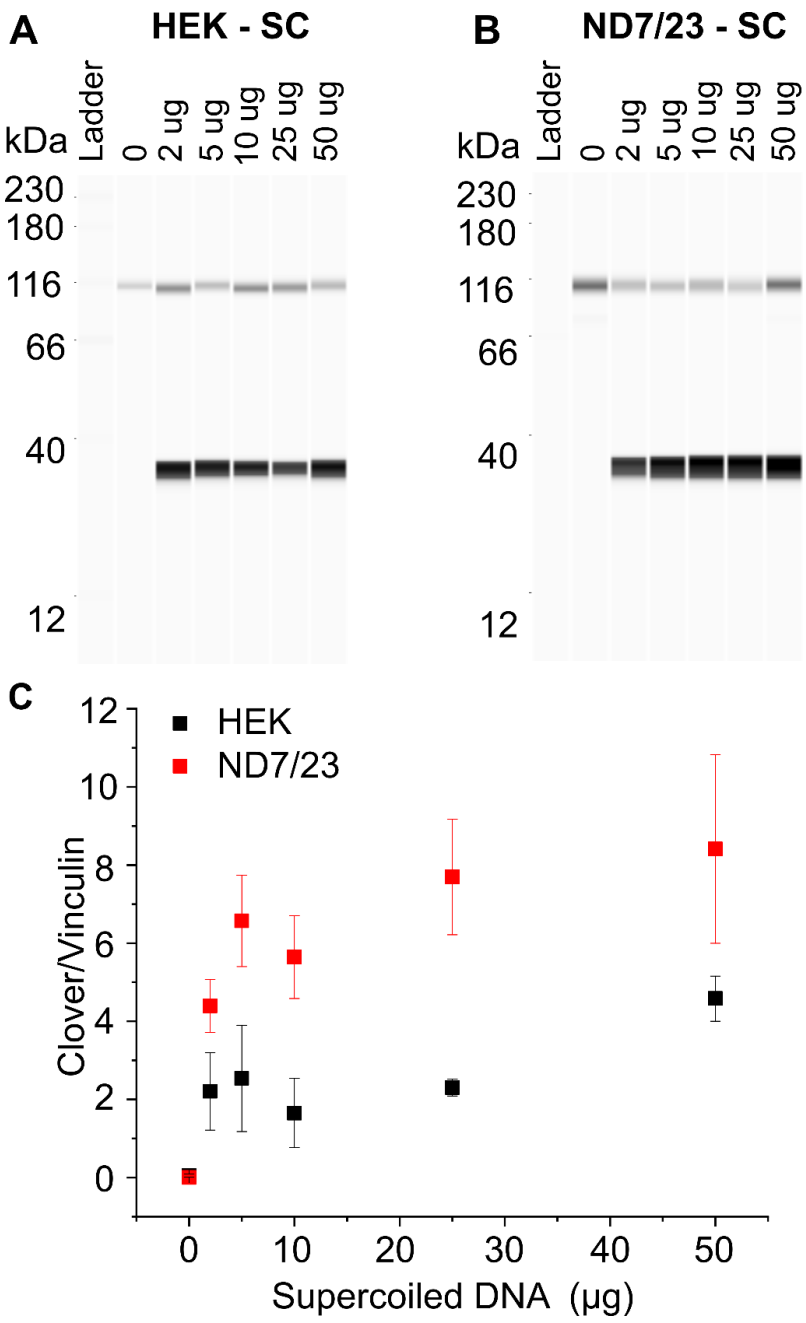

Figure 4.2.15. Dose response of supercoiled clover expression in HEK and ND7/23 cells. A, B. Western blot experiments illustrating clover expression in HEK cells and ND7/23 cells 48 hrs post-transfection with LNBs (0.5 mg/ml) loaded with varying (0- 50 µg/mg) supercoiled (SC) cDNA loading. The 36 kDa band represents clover expressed in each sample and the 116 kDa represents vinculin as the loading control. C. Graph shows the densitometric analysis of the Western blots for relative clover and vinculin expression. The values represent the mean with standard deviation of 2 independent experiments.

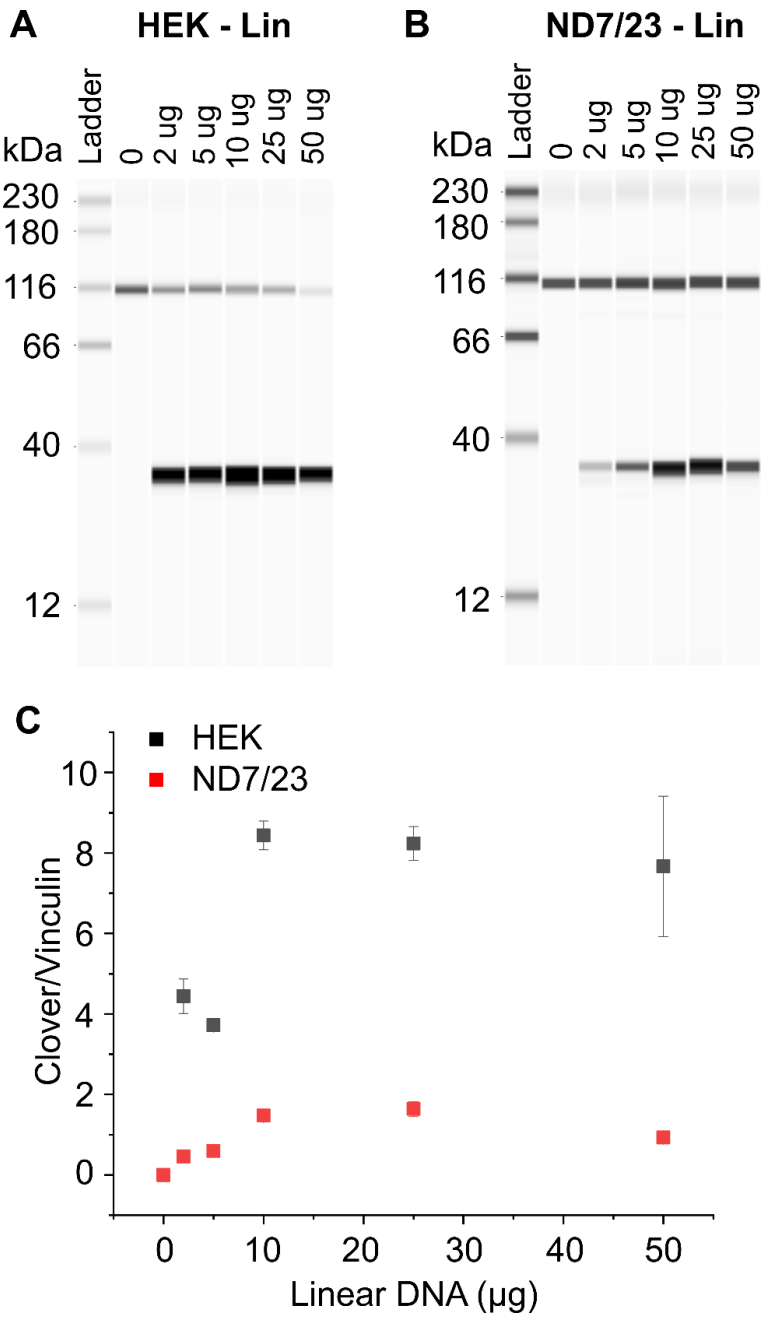

Figure 4.2.16. Dose response of linearized clover expression in HEK and ND7/23 cells. A, B. Western blot experiments illustrating clover expression in HEK cells and ND7/23 cells 48 hrs post-transfection with LNBs (0.5 mg/ml) loaded with varying (0- 50 µg/mg) linearized (Lin) cDNA loading. The 36 kDa band represents clover expressed in each sample and the 116 kDa represents vinculin as the loading control. C. Graph shows the densitometric analysis of the Western blots for relative clover and vinculin expression. The values represent the mean with standard deviation of 2 independent measurements of a representative experiment.

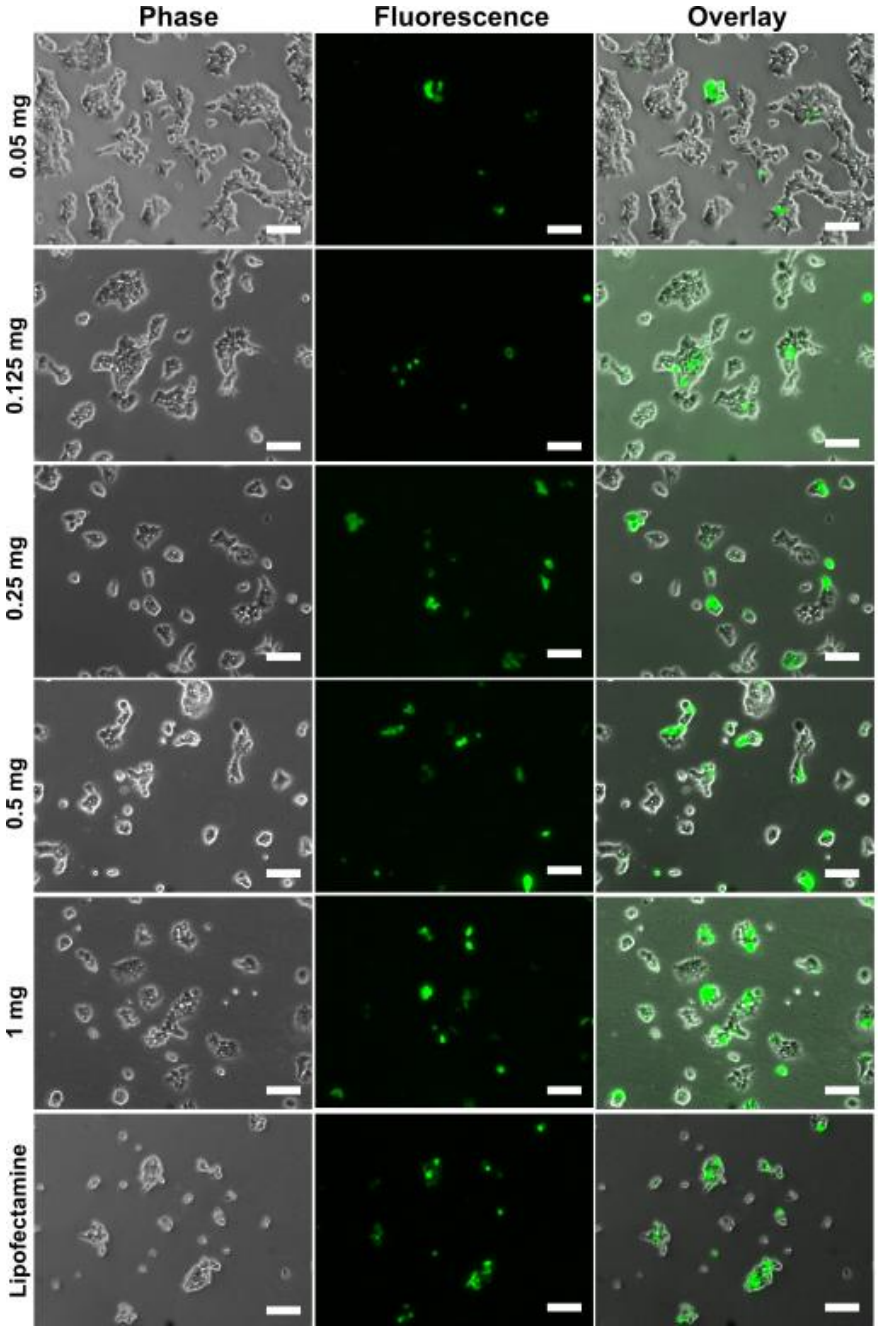

Figure 4.2.17. LNB dose-dependent transfection of HEK cells with linearized clover cDNA. Phase (left), fluorescence (middle) and overlay (right) images acquired with a 10x objective of HEK cells 48 hrs post-transfection with varying concentrations of LNB (0.05-1 mg/ml) loaded with 10 µg/mg linearized clover cDNA. The samples were analyzed in flow cytometry for viability and toxicity trends (Figure 4.2.19). Bottom row represents positive control used in flow cytometry with Lipofectamine 2000 (4 µg) 24 hrs post-transfection. All scale bars measure 100 µm.

We also determined the effect of varying LNB concentration (0-1 mg/ml) on the transfection efficiency of HEK cells. For this, we loaded a fixed dose of linearized cDNA

(10 µg/mg) and transfected HEK cells at 0.05, 0.125, 0.250, 0.50 and 1.0 mg/ml concentrations for 48 hrs. Our results (Fig. 4.2.17) shows that increasing LNB concentration increases transfection efficiency up to 0.5 mg/ml. Beyond that, no further improvement of transfection efficiency is observed, and it seems like the system has reached its saturation efficiency. As before, fluorescence microscopy results being qualitative, we confirmed this dose response trend quantitatively using flow cytometry (Fig. 4.2.19 B). We observe in Figure 4.2.19B that the number of clover expressing cells as a % of healthy cell population increases from 2-10% with increasing LNB concentration. The transfection efficiency for single cells is also represented in Fig. 4.2.19A scatter plot (% of cells counted from quadrants I and II). The representative plot (in black) indicates that a plateau was reached at concentrations greater than 0.5 mg/ml. This suggests that higher LNB concentrations approach saturation of possible expression in HEK cells. Under our conditions, saturation in expression was reached at 10% for clover, calculated with a Hill fit of the data, slope of 0.12 and non-linear regression of 0.99. Thus, we see from these data (Fig. 4.2.17 and 4.3.19) that 0.5 or 1 mg/ml LNB concentrations give the maximum possible expression in HEK cell line and are therefore the best concentrations to use for future applications. We also compared our transfection efficiencies with Lipofectamine 2000 (4 µg supercoiled clover loaded) and found that with microscopy, Lipofectamine has a similar transfection efficiency as 1 mg/ml LNB (Fig. 4.2.19 bottom row). Quantitatively, our flow cytometry results (Fig. 4.2.19) determined the transfection efficiency of Lipofectamine to be 15%. However, Lipofectamine transfection was not optimized separately for this study and was simply used as positive control for our flow cytometry runs.

III. Characterization of the toxicity of the LNB system

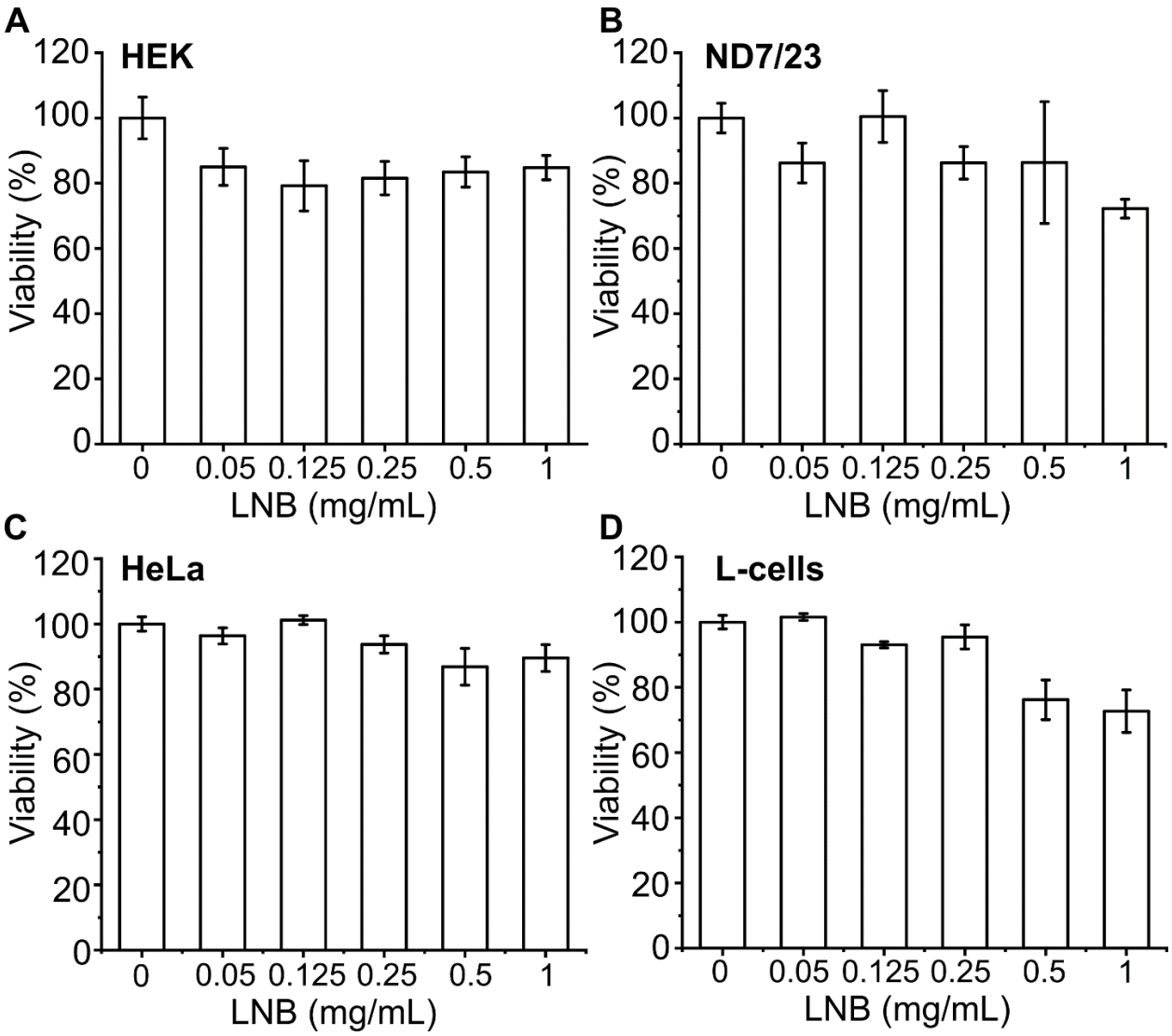

Figure 4.2.18. Determination of LNB toxicity. A-D. Viability (% live cells) measurement with the MTT assay of cells incubated in LNBs (0-1 mg/ml). The summary plots depict mean ± SEM, performed in triplicate. 0 mg/ml data point refers to cells treated only with 1:1 Opti-MEM and DPBS, and not exposed to LNBs.

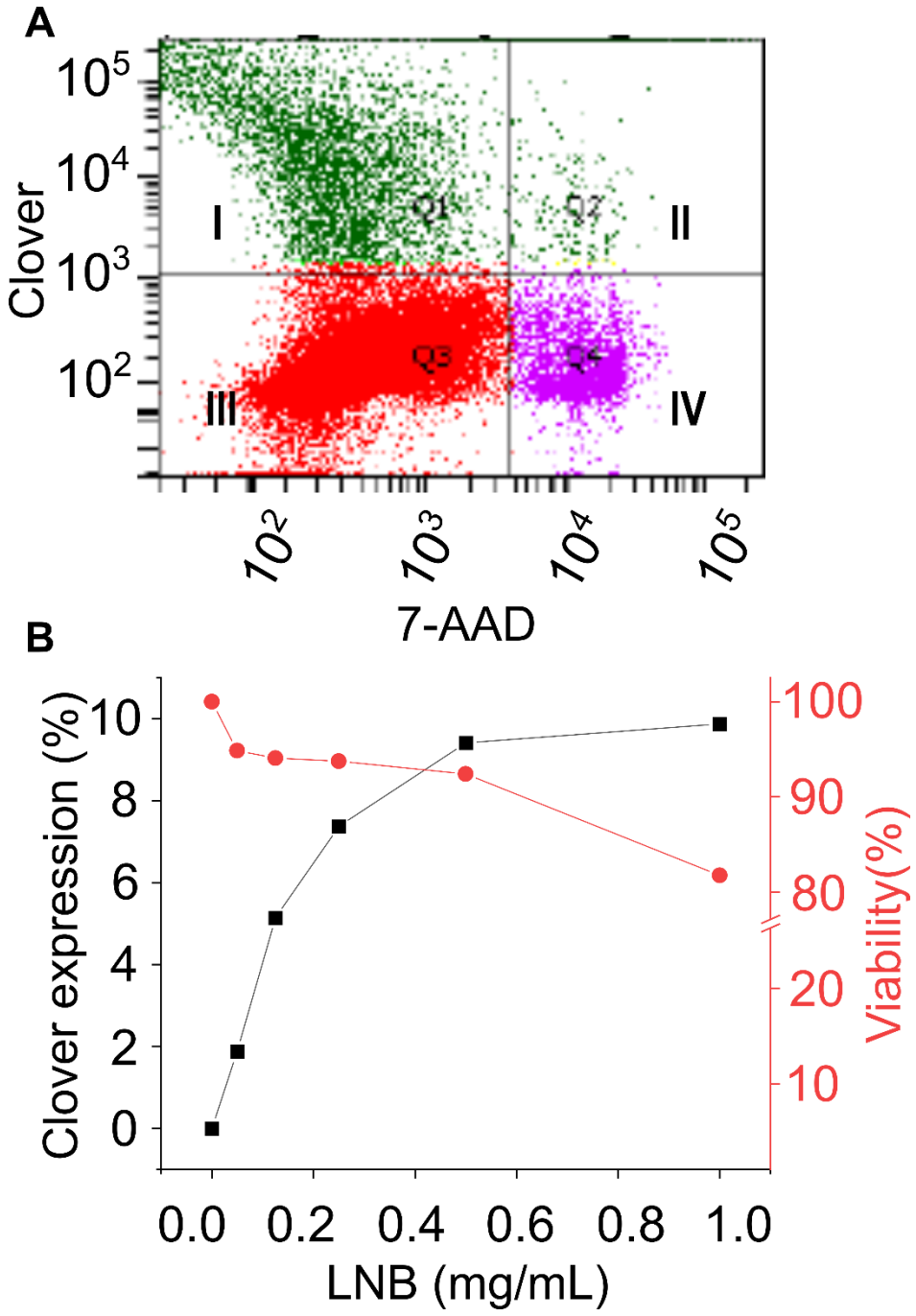

Figure 4.2.19. Transfection vs. toxicity of the LNB transfection system. A. Flow cytometry scatter plots showing single HEK cell populations with respect to clover emission (y-axis) and live/dead dye 7-AAD emission (x-axis). Quadrant Q1(I) shows live cells expressing clover (9.1%), Q2 (II) shows dead cells expressing clover (1%), Q3 (III) shows live cells with no/negligible clover expression (82.8%) and Q4 (IV) shows dead cells with no/negligible clover expression (7.1%). This scatter plot was collected from HEK cells treated with 0.5 mg/ml NBs loaded with 10µg/mg linearized clover cDNA for 48 hrs. B. Plot of HEK cell viability (red) and clover expression (black) 48 hrs post-transfection with varying LNB concentrations (0.05-1.0 mg/ml) loaded with 10 µg/mg linearized clover cDNA.

Table 4.2.3. LNB concentration dependent flow cytometry parameters. Cluster population % are reported above for all LNB concentrations tested with transfected HEK cells in flow cytometry assay. These events were gated out and were excluded from % GFP positive population analysis. Among the clover-expressing cells, further live/dead gating in the 7AAD channel (Quadrant II in Figure 4.2.19 A) was applied to determine percentage of dead clover-expressing cells at various LNB transfection concentrations shown above.

LNB conc. (mg/ml)	% Events from clusters	% Clover Positive, dead cells
0.000	23	N/A
0.050	37	0.1
0.125	33	0.6
0.250	33	0.6
0.500	28	0.9
1.000	29	1.4

Determination of the optimized LNB concentration for future applications not only depends on the highest achievable transfection efficiency but also the least toxicity to the cell populations. To determine LNB toxicity, we first characterized using MTT assay, the overall apoptosis induced by only LNBs with no DNA payload at various concentrations 0-1 mg/ml (Fig. 4.2.18). These results show cell viability compared to vehicle treatment in all 4 cell lines i.e., HEK, ND7/23, HeLa, and L-cells, 4 hrs post LNB treatment. The plots shown in Figure 4.2.18 A-D indicate that at the highest LNB concentration tested (1 mg/ml), toxicity was highest (~28%) for both ND7/23 and L-cells when compared to both HEK and HeLa cells. However, HEK cells showed a consistent toxicity (~16%) for all concentrations tested (Fig. 4.2.18 A). These results suggest that for these cell lines, a 4 hr transfection period with LNBs will result in toxicity ranging from 10 to 28% at the highest concentration (1 mg/ml) tested and lower toxic effects with LNBs at 0.125 mg/ml.

Next, we determined with flow cytometry (Fig. 4.2.19) how the cell viability changed for HEK cell populations with the same range of LNB concentrations (0.05-1 mg/ml) 48 hrs post transfection with 10 µg/mg linearized clover loading. Linearized clover was chosen for this study as our previous Wes blots showed that in HEK cells linearized clover has higher clover expression. Cell viability in the flow cytometry experiments was tested using a viability dye 7-aminoactinomycin D (7-AAD) which is a DNA intercalator dye that can only permeate through dead cell membrane and is not taken up by live cells. Additionally, it is a dye that can be excited with the same 488 nm laser line as GFP but has an emission that is far removed from the GFP emission (647 nm) which allowed us to simultaneously measure GFP expressing and live/dead populations in the transfected cells with two flow cytometry channels. We observed that the cell viability, measured by cell populations with negligible 7AAD emission, (% of cells counted from quadrant I and III, Fig. 4.2.19 A) increased from 82% at 0.05 mg/ml to 95% at 1 mg/ml (red trace, Fig. 4.2.19 B). These results suggest there is a trade-off when LNBs are employed as transfection agents. That is, when high LNB concentrations are used, protein expression levels are higher with a concomitant cell death. To determine the optimal LNB concentration necessary for the highest transfection efficiency, we determined that at 0.5 mg/ml the cell viability is 92% and clover expression levels reach approximately 10%. This value is close to the saturation level of expression while still maintaining >90% cell viability. At this concentration, we also observed approximately 1% dead clover-expressing cells (Table 4.2.3). Thus, 0.5 mg/ml is the optimum LNB concentration necessary to ensure maximum possible expression with greater than 90% cell viability. It should be noted that analysis of the flow cytometry data was performed for single cell

populations, while cell clusters containing both clover- and non-clover-expressing populations were excluded from the analysis (Table 4.2.3).

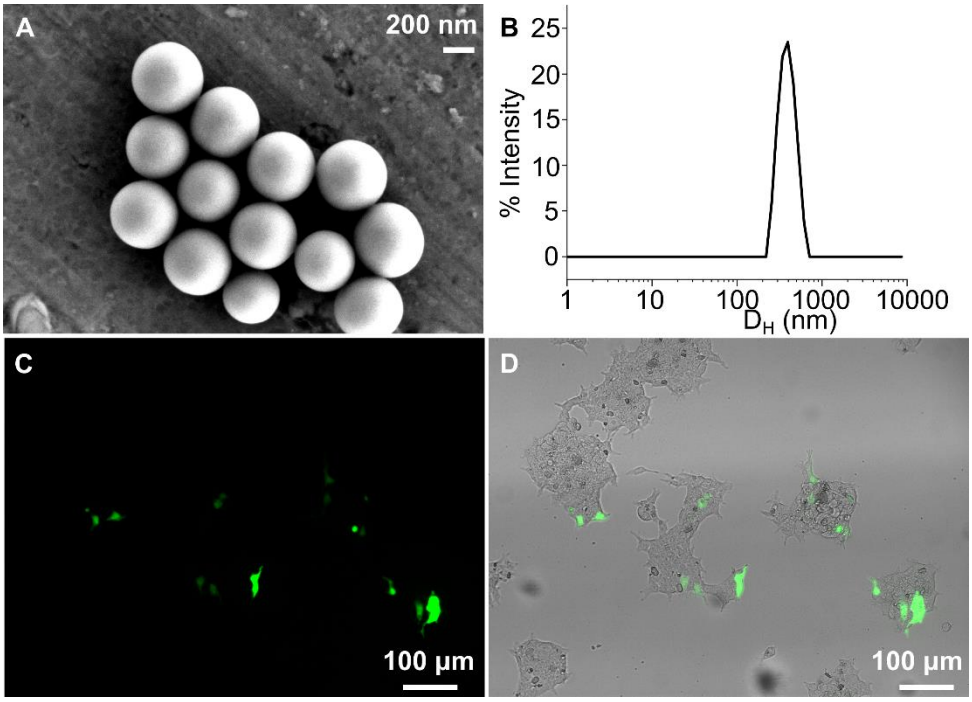

Figure 4.2.20. Transfection of HEK cells with DOPE/DOTAP encapsulated Stöber silica nanoparticles. A. Scanning electron microscopy (SEM) and B. Dynamic Light Scattering (DLS) characterization of Stöber silica nanoparticles after synthesis and purification. DLS data was acquired from ~50µg/ml silica nanoparticles dispersed in water. D_H =415.3 ± 21.9 nm and PDI 0.207 ± 0.043 were measured. C-D Fluorescence microscopy images of 0.5 mg/ml clover cDNA loaded Stöber silica nanoparticles (~9µg clover supercoiled plasmid per mg silica nanoparticles) 48 hrs post transfection in HEK 298 cells captured with a 10x objective. C. Fluorescence channel after pseudo coloring. D. Overlay of the fluorescence and the phase channels for the same field of view.

4.3. DISCUSSION

Vesicle entrapment has been reported as one of the major barriers to delivery of DNA or drugs inside the cytoplasm for a number of non-viral transfection agents including multifunctional silica nanoparticles[2], [3],[4]. Among the strategies to overcome endosomal entrapment, the use of 'helper' lipids to coat NBs was performed in this study. The lipid DOPE was chosen due to its ability to form inverted hexagonal structures that

can easily fuse with cellular lipid bilayers and vesicular compartments and facilitate the release of loaded DNA from the NBs[5]-[6]. DOTAP was chosen as a cationic lipid to stabilize the lipid bilayer on the DNA loaded NB surface and provide colloidal stability in the media. Previously, it was shown that mesoporous silica NBs[7] overcame endosomal entrapment by loading with the endosomolytic compound, chloroquine. However, the drawback was a 'leaky' DNA delivery system. An advantage of lipid coating NB is that the DNA cargo is protected against nuclease degradation during transport. Moreover, the lipids allow for an increase in complexity of the NB system development with the possibility of further functionalization of the outer surface with polymers or peptides to control endocytosis, specific cell/tissue targeting and opsonization properties *in vivo.* Although in the present study we did not employ confocal microscopy imaging to ascertain endosome entrapment, we speculate that the lipid-encapsulated NBs loaded with clover cDNA were released by endosomes due to clover expression, which we observed with fluorescence imaging (Fig. 4.3.11-14, 17) and Western blotting assays (Fig. 4.3.15-16).

Our results showed that NBs are able to load linearized as well as supercoiled DNA with varying efficiencies. The supercoiled cDNA adsorption reached saturation, while linearized cDNA did not exhibit this property. Such differences in surface adsorption behavior of supercoiled and linearized chromosomal DNA have been previously reported on silica based clay mineral surfaces[8],[9]. It is possible that once monolayer adsorption is completed for linearized cDNA a different binding mechanism causes the increase in adsorption, such as additional cooperative binding between the free cDNA and the NB-bound cDNA. Another possible reason could be the morphological differences between the compact, supercoiled DNA and that of the dimensionally larger, more rigid linearized

cDNA which differ in the density and availability of phosphate groups[8]. For example, Poly et al. have suggested that linear DNA has a much higher number of available acidic groups along its length than compact supercoiled DNA for multi-loci interactions with clay surfaces[8]. These differences could alter the affinity, the nature of cDNA interactions[10] (electrostatic, bridging, coordination and/or H-bonding) and protection from nuclease activity[11] in a morphology-dependent manner for silica NB surface adsorption. The presence of the engineered cavity in the silica nanobowls could also affect how DNA (linearized and supercoiled) condenses on the silica nano surface. This may explain the reason for the observed differences in DNA adsorption of nanobowls and Stöber nanoparticles and, ultimately, affect their transfection efficiency. For example, the results shown in Figure. 4.3.20 indicate Stöber nanoparticles exhibited approximately 18% less supercoiled clover cDNA loading and a lower transfection efficiency when compared to equal concentrations of NBs in HEK cells. In the present study, we focused on developing a versatile transfection system employing lipid-coated NBs. Optimization of Stöber nanoparticles as transfection agents is beyond the scope of this study. Future studies are necessary to examine whether these nanoparticles can be optimized in a similar fashion.

The Western blotting assay (Fig. 4.3.15-16) and microscopy imaging results (Fig. 4.3.11-14,17) showed that the LNB transfection system we developed could be used to transfect all cell lines tested with either supercoiled or linearized cDNA. It should be mentioned that the clover expression ratios determined from the Western blot assays reflect protein pooled from cells that express proteins either strongly, weakly, or not at all. The clover amounts detected therefore do not discriminate between protein pooled from weakly or strongly expressing cells. Overall, our results suggest that LNBs loaded with

either linearized or supercoiled cDNA can be employed as transfection agents with the cell lines tested. Thus, the LNB system exhibited versatility in delivering either type of DNA construct with comparable transfection efficiencies.

Previous studies have shown that transfection with appropriately linearized cDNA construct is more likely to become incorporated into the cell's genome resulting in higher success rates of obtaining stably transfected cells when compared to supercoiled cDNA plasmids[12], [13] Further, linearized plasmid bacterial resistance genes have also been considered as the method of choice for vaccinations[14]. The disadvantages of employing linearized cDNA for transfection includes the susceptibility to exonuclease digestion as well as inefficient encapsulation by the lipids used for transfection[13]. Our LNB system showed similar or higher transient transfection efficiencies, including higher DNA condensation capabilities for linearized cDNA constructs as compared to supercoiled plasmids. Linearized DNA transfections are not very common with chemical transfection systems like lipids or Lipofectamine or polymers. This is because of two reasons (a) linearized constructs are prone to exonuclease digestion (b) linearized constructs cannot be efficiently complexed with polymeric or liposome-based delivery systems. However, here we have shown that linearized constructs can not only be successfully loaded onto NBs, but also can lead to successful transfections in cell lines. This opens the possibility of using LNBs as transfection systems of choice for creating stable cell lines for research use or for clinical applications like CAR-T cell therapy. Another advantage of our method of producing linearized cell lines is that our linearization approach is based on primer design with a specific vector sequence and therefore could be easily applied to multiple

genes that share a common vector without the need to reengineer and optimize the PCR module.

The MTT and flow cytometry assays, which measured LNB toxicity with or without DNA loading, showed that cell viability was greater than 80% at the concentration (0.5 mg/ml) employed. When compared to the commercially available Lipofectamine 2000, the viability measured via flow cytometry was approximately 70%. It should be noted that transfection with Lipofectamine 2000 was not optimized under our transfection conditions (i.e., beyond the focus of the present study) and employed as a positive control for flow cytometry assay (Fig. 4.3.19 A-B). Nevertheless, the toxicity measured for LNBs (92.4%) was lower than for Lipofectamine 2000 (70%) with comparable transfection efficiencies as evaluated with fluorescence microscopy (Fig. 4.3.17). However, it is also possible that the incubation time post-transfection we employed may not have been sufficient to allow for further clover expression. For example, the TEM images showed that 24 hrs post-transfection there were lipid-coated NBs that remained within the vesicles (Fig. 4.3.6). The endosomolytic properties of the LNBs within cells is another parameter that can be further tuned. For instance, the use of endosomolytic peptides like H5WYG[2] or incorporation of pH buffering polymers in the outer lipid encapsulation layer of the NBs that can lyse endosomes by the proton sponge effect[15] may serve as an alternative to increase the release of the LNBs that result in greater expression levels.

Chapter 4, in part, has been published in ACS Bioconjugate Chemistry (2020) with coauthors Dr. Ratneshwar Lal and Dr. Victor Ruiz-Velasco. The dissertation author was the primary investigator and author of this material.

4.4 Bibliography

[1] N. C. Shaner, P. A. Steinbach, and R. Y. Tsien, “A guide to choosing fluorescent proteins,” *Nat. Methods*, vol. 2, no. 12, pp. 905–909, Dec. 2005.

[2] C. Argyo, V. Weiss, C. Bräuchle, and T. Bein, “Multifunctional mesoporous silica nanoparticles as a universal platform for drug delivery,” *Chemistry of Materials*, vol. 26, no. 1. American Chemical Society, pp. 435–451, 14-Jan-2014.

[3] Z. J. Chen, S. C. Yang, X. L. Liu, Y. Gao, X. Dong, X. Lai, M.H. Zhu, H.Y. Feng, X.D. Zhu, Q. Lu, M. Zhao and H.Z. Chen, “Nanobowl-Supported Liposomes Improve Drug Loading and Delivery,” *Nano Lett.*, vol. 20, no. 6, pp. 4177–4187, Jun. 2020.

[4] S. A. Smith, L. I. Selby, A. P. R. Johnston, and G. K. Such, “The Endosomal Escape of Nanoparticles: Toward More Efficient Cellular Delivery,” *Bioconjugate Chemistry*, vol. 30, no. 2. American Chemical Society, pp. 263–272, 20-Feb-2019.

[5] B. K. Kim, G. B. Hwang, Y. B. Seu, J. S. Choi, K. S. Jin, and K. O. Doh, “DOTAP/DOPE ratio and cell type determine transfection efficiency with DOTAP-liposomes,” *Biochim. Biophys. Acta - Biomembr.*, vol. 1848, no. 10, pp. 1996–2001, Jul. 2015.

[6] Z. Du, M. M. Munye, A. D. Tagalakis, M. D. I. Manunta, and S. L. Hart, “The Role of the helper lipid on the DNA transfection efficiency of lipopolyplex formulations,” *Sci. Rep.*, vol. 4, no. 1, pp. 1–6, Nov. 2014.

[7] L. Xiong and S. Z. Qiao, “A mesoporous organosilica nano-bowl with high DNA loading capacity-a potential gene delivery carrier,” *Nanoscale*, vol. 8, no. 40, pp. 17446–17450, Oct. 2016.

[8] F. Poly, C. Chenu, P. Simonet, J. Rouiller, and L. J. Monrozier, “Differences between linear chromosomal and supercoiled plasmid DNA in their mechanisms and extent of adsorption on clay minerals,” *Langmuir*, vol. 16, no. 3, pp. 1233–1238, Feb. 2000.

[9] W. H. Yu, N. Li, D. S. Tong, C. H. Zhou, C. X. Lin, and C. Y. Xu, “Adsorption of proteins and nucleic acids on clay minerals and their interactions: A review,” *Applied Clay Science*, vol. 80–81. Elsevier, pp. 443–452, 01-Aug-2013.

[10] X. Nie, Z. Zhang, C. H. Wang, Y. S. Fan, Q. Y. Meng, and Y. Z. You, “Interactions in DNA Condensation: An Important Factor for Improving the Efficacy of Gene Transfection,” *Bioconjug. Chem.*, 2018.

[11] E. Paget, L. J. Monrozier, and P. Simonet, “Adsorption of DNA on clay minerals: protection against DNaseI and influence on gene transfer,” 1992.

[12] G. Stuchbury and G. Münch, “Optimizing the generation of stable neuronal cell lines via pre-transfection restriction enzyme digestion of plasmid DNA,” *Cytotechnology*, vol. 62, no. 3, pp. 189–194, Jun. 2010.

[13] S. McLenachan, J. P. Sarsero, and P. A. Ioannou, “Flow-cytometric analysis of mouse embryonic stem cell lipofection using small and large DNA constructs,” *Genomics*, vol. 89, no. 6, pp. 708–720, Jun. 2007.

[14] P. Johansson, T. Lindgren, M. Lundström, A. Holmström, F. Elgh, and G. Bucht, “PCR-generated linear DNA fragments utilized as a hantavirus DNA vaccine,” *Vaccine*, vol. 20, no. 27–28, pp. 3379–3388, Sep. 2002.

[15] S. A. Smith, L. I. Selby, A. P. R. Johnston, and G. K. Such, “The Endosomal Escape of Nanoparticles: Toward More Efficient Cellular Delivery,” 2018.

Chapter 5

Applications of DNA delivery with NBs

5.1. Controlled Release of DNA from NBs

5.1.1. Introduction

In real clinical applications, a DNA delivery vehicle must spend some time in transport (systemic administration) or in diffusion near the tissue of interest (local injection). In either case, the delivery system will spend some time in the biological milieu where there could be loss of the nucleic acid payload by diffusion or fluid shear forces and subsequent degradation by enzymes like nucleases in the transport/diffusion media. Thus, especially in *in vivo* applications, there is a need to design and develop nucleic acid delivery systems that are able to release the payload at the target site in a controlled manner. Also, as opposed to microinjection or ultrasound based gene delivery techniques[1], where the nucleic acids are available inside the cell cytoplasm right away after transfection, once internalized, a controlled release system can maintain a sustained delivery of nucleic acids in the cell cytoplasm over an extended period of time that maybe therapeutically relevant. Such controlled release of genetic material inside the cell is also difficult to achieve in a viral delivery system. Another application of controlled release in a clinical setting are local injections, drug delivery depots and patches that deliver a therapeutic payload in a target tissue locally over an extended period of time[2]. This is more popularly applied to molecular drugs, but we can envision such similar applications in localized *in vivo* gene delivery as well. For example, silencing shRNA delivery targeting ion channel proteins in neurons of the DRG in the spinal cord can act to transiently reduce pain transmission to the brain. Because of the transient nature of post-transcriptional

protein silencing, a sustained therapeutic dose should be applied locally, say, between L4 and L5 of the spinal cord via regular local injections/locally installed stent. In such a scenario, it is important that the shRNA is not released while in storage or inside the installed stent but is only released upon cellular internalization inside the DRG. Thus, there is a unique space and need in the clinic to develop a gene delivery system that can release nucleic acids in a stimulus-controlled manner in the target.

From a materials design perspective, controlled release nano delivery systems have been reported widely[3], [4], [13], [5]–[12]. Various strategies have been developed to load nucleic acids onto mesoporous silica, metallic nanoparticles, and polymeric nanoparticle systems. For mesoporous silica nanoparticles, duplex DNA structures have often been used as a ‘gate-keeper’ on the pores of the matrix to keep some dye/drug/molecule entrapped until triggered[5]. DNA loading strategies onto the silica surface have taken many approaches For example, (a) 9-acridinamine derivative covalently attached to the silica surface containing the acridine amine intercalator site that binds to duplex DNA and a cleavable disulfide group (b) silica surface conjugated to a DNA hairpin structure whose conformation can be changed with temperature rise/fall to open/close the pores on the mesoporous silica (c) conjugating alkyl terminated duplex DNA with azide functionalized silica surface and using thermal degradation to denature/release one strand from the duplex (d) conjugating maleimide functionalized silica surface with thiol modified oligonucleotide (e) physisorption of single stranded DNA on amine functionalized silica. Such systems have reported using a number of triggers for controlled release i.e., heat, light, pH changes, biomolecular stimuli like glutathione (GSH), exonucleases, DNases, ATP, etc. For gold nanoparticle (plasmonic nanorods and

shells) surfaces, usually the oligonucleotide is thiolated to form an Au-S bond[7]–[9]. Such systems are usually triggered by near IR wavelength radiation which excites these plasmonic nanostructures at their resonant frequency generating local hyperthermia that can either break the Au-S bond (pulsed wave femtosecond laser irradiation) or denature the DNA and lead to subsequent strand displacement (continuous wave laser irradiation)[9]. Polymeric systems usually encapsulate/complex with the genetic payload and release occurs usually by slow polymer degradation and related diffusion of the payload over extended exposure to the biological milieu[12], [13]. Although there are many examples of nucleic acid loading-release mechanisms in the current literature, most of them do not bear any therapeutic value towards gene therapy. This is because, they use single stranded or double stranded oligonucleotides (10-20 bases long) that are much shorter than DNA/mRNA sizes relevant for successful protein expression. A lot of the release strategies that are used in the current literature require DNA denaturation/strand displacement/enzymatic degradation that will not preserve the structural integrity of the DNA to retain its functionality for downstream transcription pathways[5], [8], [9]. There are some reports[14]–[16] of chemical conjugation and subsequent controlled release via cleavable bonds like disulfide reported for silencing RNA non-viral delivery however there are no similar reports for DNA. Thus, although the current literature provides a good foundation to understand mechanisms of controlled release and vector material design strategies, there has not been application of these strategies towards controlled delivery of therapeutically relevant DNA delivery.

In this chapter section 5.1, we address this unmet need by applying the nanobowl system to bind appropriately modified linearized DNA by two different conjugation

chemistries and their release controlled by cleavage of a reducible dithiol bond built into the linearized construct. The rationale for this design is that glutathione can reduce disulfide bonds, and its intracellular concentration is usually ten-fold higher than the extracellular space. This will ensure that the release of DNA is triggered by the cellular internalization of the nanobowl delivery system and the concomitant increase in environmental reducing agents.

5.1.2. Methods

DNA linearization and functionalization.

For cDNA loading and transfections, we chose clover (vector: pcDNA 3.1) and tdTomato, (vector: pEGFP-N1) which code for two high quantum efficiency fluorescent proteins of the GFP family[17]. Polymerase chain reaction (PCR) was performed to introduce either amine or azide functional groups into linear DNA. Forward primers with appropriate functional groups were designed to hybridize at the start of the CMV promoter region of the pcDNA3.1 plasmid containing the clover DNA insert. The modifications at the 5' end of the forward primer was either a carboxyl or an azide group followed by a disulfide bond. The reverse primer was not modified and was designed to hybridize at the end of the polyadenylation sequence of the plasmid. All primers (Integrated DNA Technologies, IDT) were custom designed. The sequences of the primers were the following:

Forward primer (FWD): 5'- GTTGACATTGATTATTGACTAGTTATTAATAGTAAT-3'

Reverse primer (REV): 5'-CCATAGAGCCCACCGCAT-3'

Functionalized forward primers:

FWD-Azide:

5' N_3-C_n-**S-S**-C_n- GTTGACATTGATTATTGACTAGTTATTAATAGTAAT **3'**

(IDT modification code: /5AzideN//iThioMC6-D/)

FWD-Carboxyl:

5' HOOC-C_n-**S-S**-C_n- GTTGACATTGATTATTGACTAGTTATTAATAGTAAT **3'**

(IDT modification code: /5Carboxy1//iThioMC6-D/)

tdTomato primers:

Forward primer (FWD): TAGTTATTAATAGTAATCAATTACGGGGTC

Reverse primer (REV): GCAGTGAAAAAAATGCTTTATTTGTG

PCR was performed using the OneTaq HotStart 2X master mix (New England Biolabs). The PCR products were purified using commercially available standard DNA clean and concentrator kits (Zymo Research, 25 µg columns or Qiagen, 10 µg columns) and reconstituted in DNAse, RNase free molecular biology grade water. The purified products were quantified using the Qubit dsDNA BR assay kit (Thermo-Fisher Scientific) as per manufacturer's protocol. Lin-A & Lin-C refer to linearized cDNA products purified from PCR on supercoiled clover cDNA template with REV and FWD-Azide & FWD-Carboxyl, respectively. All linearized PCR products were visualized on agarose gel electrophoresis to confirm product size (clover ~ 1.7 kbp & tdT ~ 2.4 kbp, data not shown).

NB-DNA loading assay.

The dried, amine-coated NBs were resuspended in Dulbecco's Phosphate Buffered Saline DPBS (with Ca^{2+} and Mg^{2+}; Thermo-Fisher Scientific) with light sonication for 5 mins at a final 1 mg/ml concentration. In addition, 2—50 µg of supercoiled or linearized cDNA was added to 1 ml (1 mg/ml) of NB-DPBS solution and allowed to bind overnight at 4^{o}C with gentle shaking. The linkers, N-hydroxysuccinimide (NHS) and 1-ethyl-3-(3-dimethylaminopropyl)-carbodiimide (EDC; both from Thermo-Fisher Scientific), were employed for chemisorption of Lin-C on NBs in 2-(N-Morpholino) ethanesulfonic acid (MES)-buffered saline (Thermo-Fisher Scientific). Initially, Lin-C (10 µg) was pretreated with 2 mM EDC and 5 mM NHS in 0.1 M MES buffer for 30 mins at room temperature before addition to the 1 mg/ml NB-DPBS solution and overnight incubation. For azido-DBCO click chemistry, the amine-functionalized NBs were first conjugated overnight with click chemistry linker dibenzo cyclooctyne i.e. DBCO-NHS (Click Chemistry Tools) in dimethyl sulfoxide (DMSO, Sigma Aldrich), washed 4 times in ethanol and dried before DPBS re-constitution at 1 mg/ml. Afterwards, Lin A (10µg) was added to DBCO-coated NBs resuspended in DPBS and allowed to mix overnight. Once the DNA was loaded, the NBs were centrifuged at 3221g for 30 mins and the supernatants were collected for DNA quantification with Qubit assay kit (Thermo-Fisher Scientific). All loading efficiencies (%) were calculated as µg cDNA bound*100/µg cDNA added per mg NB.

NB-DNA release assay.

Amine- and DBCO-functionalized NBs were loaded with Lin-C and Lin-A at 10 µg/mg NB as described above. Following an incubation period (24 hrs), NBs were

centrifuged at 3200g for 30 mins and the supernatant was then decanted. The linearized cDNA-loaded NBs were then gently reconstituted in 500 mM β-mercaptoethanol (Sigma Aldrich) containing DPBS (with Ca^{2+} and Mg^{2+}) at 2 mg/ml concentration in a 500 µl final volume. Control NBs were loaded with Lin-C or Lin-A reconstituted in DPBS at a final concentration of 2 mg/ml. Both control and β-mercaptoethanol samples were placed in a heat block (37^{o}C) for 4, 24 and 48 hrs. After each incubation period, the NBs were centrifuged at 3200g for 30 mins and the supernatant was decanted and used to measure cDNA concentration in triplicate with the Qubit dsDNA assay kit. DPBS with 500mM β-mercaptoethanol only was confirmed to have no background in the Qubit dsDNA assay.

5.1.3. Results

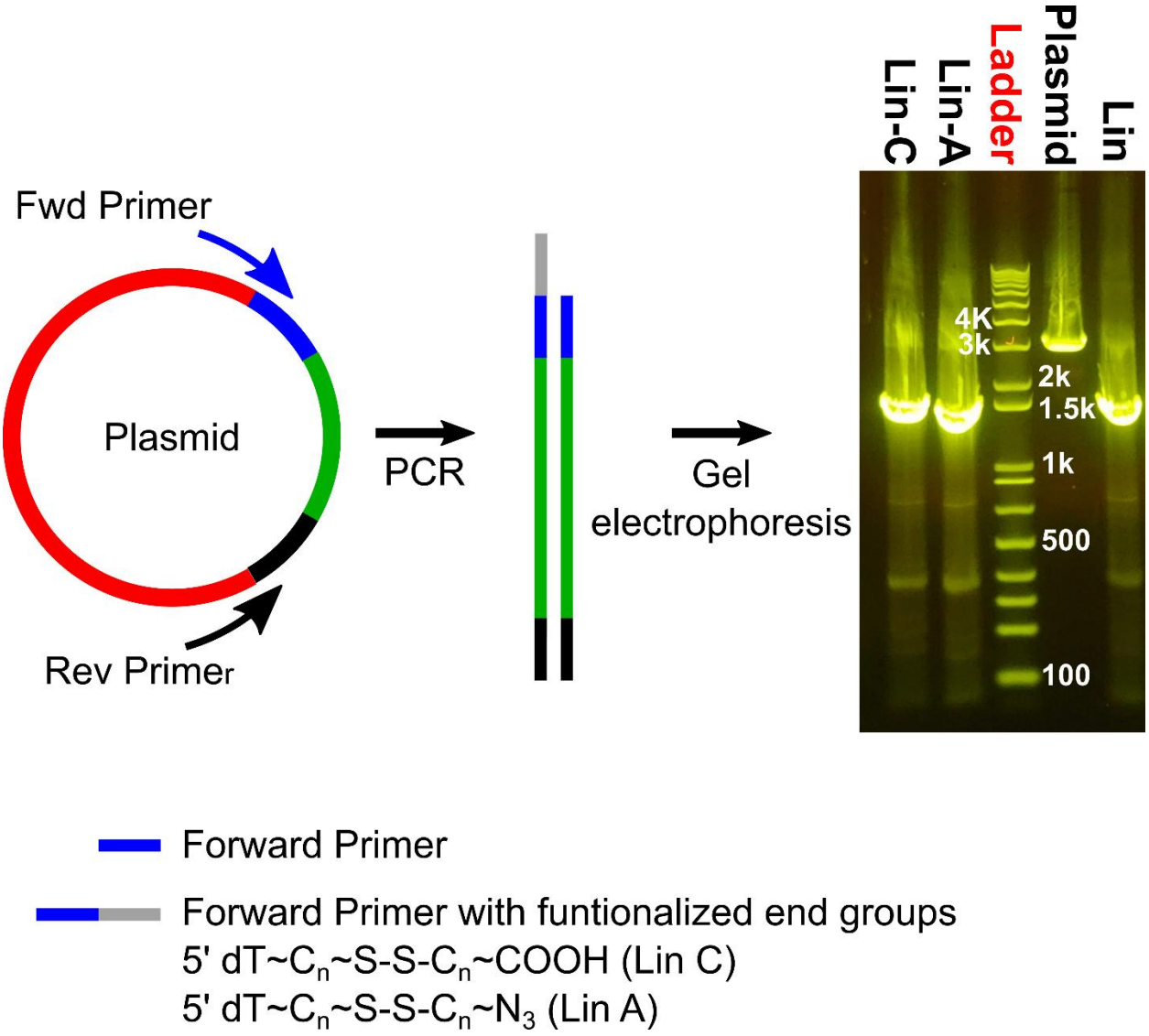

Figure 5.1.1. Synthesis of functionalized linear constructs from a supercoiled plasmid template. Using polymerase chain reaction (PCR) and appropriately functionalized forward primers, carboxyl (Lin-C) or azide (Lin-A) terminated linearized DNA was synthesized. Each type of functionalization also contained an intermediate disulfide group between the first 5' nucleotide of the forward primer sequence and the terminal carboxyl or azide groups. Gel electrophoresis performed on column purified functionalized constructs show bands between 1.5 and 2 kbp. All markings on ladder are in base pairs (bp). Each sample had a loading of ~0.76 µg/lane and ladder ~ 0.5 µg/lane.

In this set of experiments, we characterized the controlled release of linearized clover DNA, containing cleavable disulfide groups, chemisorbed on the NBs. We employed PCR forward primers (Fig.5.1.1) that would allow for the incorporation of a disulfide bond linked to a terminating carboxyl (Lin-C) or azide (Lin-A) group. Our gel

electrophoresis results (Fig. 5.1.1.) show that the Lin-A and Lin-C linearized constructs derived out of clover plasmid had similar size as the linearized product with no functional groups (~1.7 kbp). The chemisorption to NBs (Fig. 5.1.2) was accomplished employing either EDC linker-based conjugation chemistry (Lin-C) or azido-DBCO click chemistry (Lin-A). Complete adsorption of DNA (10 µg/mg) was observed by 24 hrs. However, the release properties for both chemistries was different. That is, in the presence of a reducing agent, the total release of Lin-C-NB (red symbols) and Lin-A-NB (black symbols) were 41% and 17%, respectively (Fig. 5.1.3). However, we also detected non-specific release in the absence of a reducing agent for both chemistry types. They were 34% and 9% for Lin-C-NB and Lin-A-NB, respectively (Fig. 5.1.3). These observations suggest that the final adsorption on the NBs is caused by both specific chemisorption and non-specific physisorption. Although Lin-C-NB exhibited a higher overall DNA release within 48 hrs, 16% of the DNA released was a result of disulfide bond cleavage. On the other hand, 45% of the DNA released from Lin-A-NB resulted from cleavage of the disulfide bond. An overall release of less than 50% of the total NB-bound cDNA was observed in the *in vitro* release assay with either chemistry (Fig. 5.1.3).

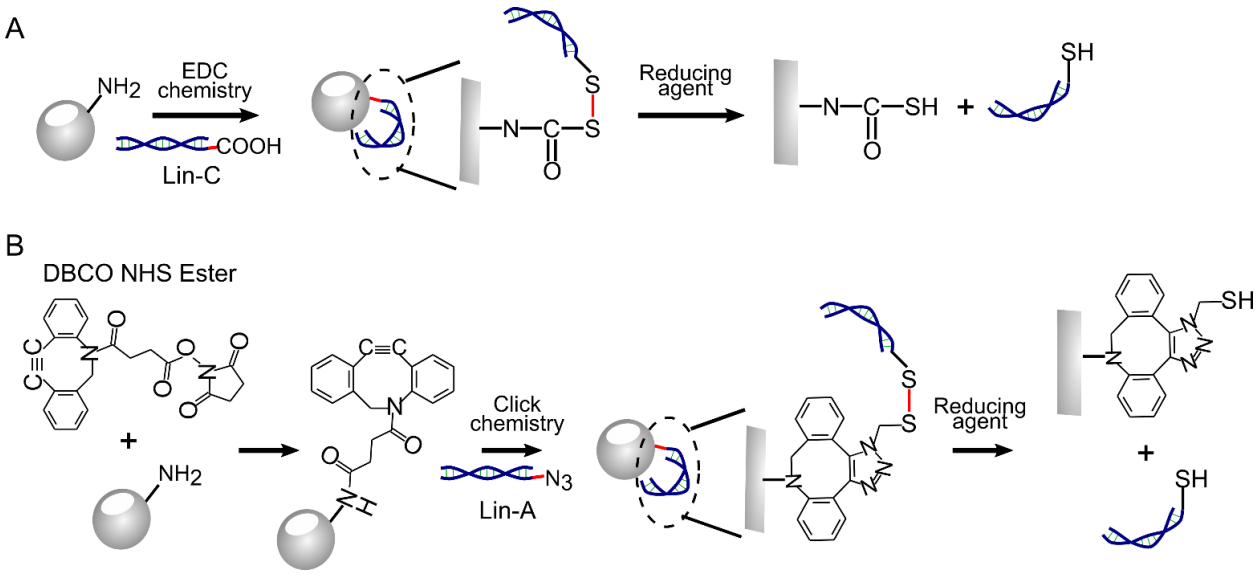

Figure 5.1.2. Types of linear DNA chemisorption schemes used with NBs. A. Amine group on NB was covalently linked to carboxyl terminated linearized DNA with an EDC linker (EDC conjugation chemistry) B. Amine coated NBs were first conjugated with DBCO NHS ester to confer DBCO functionality on NBs followed by attachment of azido terminated linearized cDNA on DBCO functionalized NBs by click chemistry.

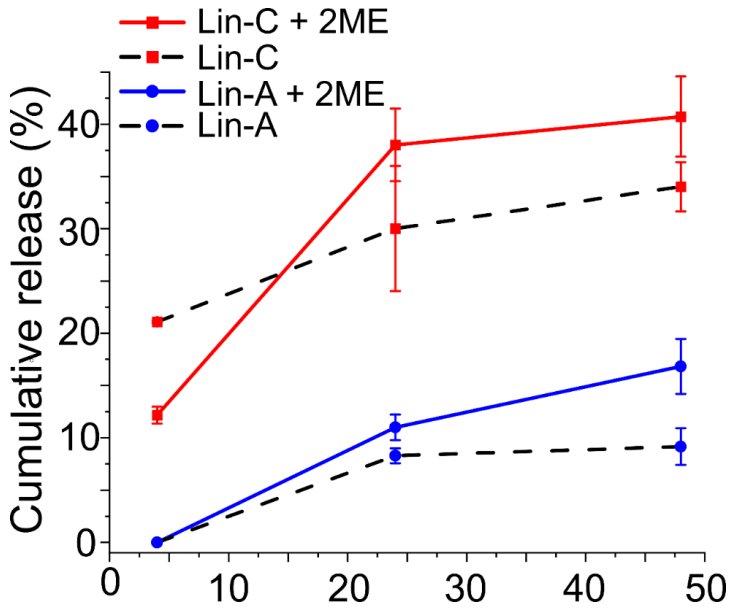

Figure 5.1.3. Types of linear DNA chemisorption schemes used with NBs. 48 hr release profile of carboxylated (Lin-C) and azido-functionalized (Lin-A) linearized cDNA from NB surfaces in DPBS with or without β-mercaptoethanol at 37°C. All release data were normalized to total loaded amount i.e., 10 µg/mg. Error bars indicate standard deviation from triplicate experiments.

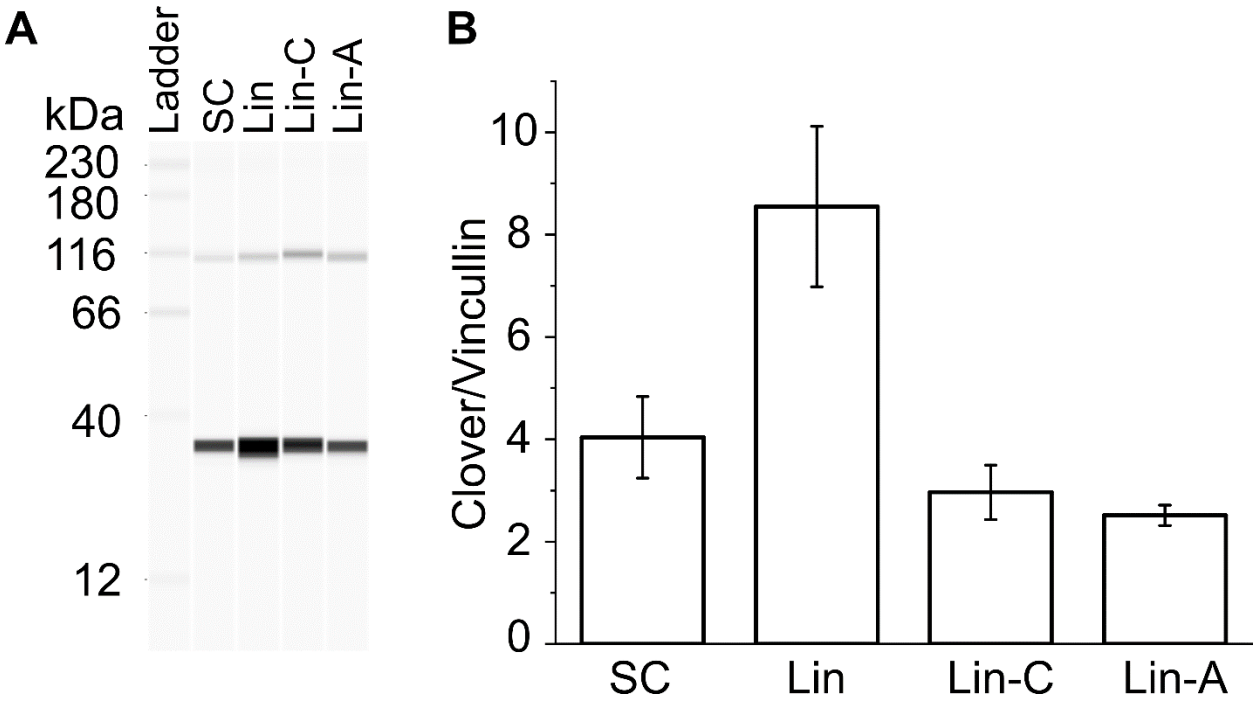

Figure 5.1.4. Clover expression from 4 constructs delivered by LNB. A. Western blotting plot illustrating clover expression (36 kDa) in HEK cells 48 hrs post-transfection with 0.5 mg/ml LNB loaded with Lin-A, Lin-C, Linear (Lin) and supercoiled (SC) cDNA at 10 µg/ mg LNB. Vinculin was used as the loading control (116 kDa). B. Mean (± std dev) relative expression levels of clover/vinculin in HEK cells when transfected with supercoiled (SC), linear (Lin), carboxylated linear (Lin-C) and azido-linear (Lin-A) when loaded with 10 µg/mg LNB (0.5 mg/ml). Numbers in B obtained from densitometric analysis of Wes data.

HEK, ND7/23, HeLa and L- cells were then transfected with either Lin-C-LNB or Lin-A-LNB clover cDNA and clover expression was examined 48 hrs post-transfection by Western blots (Fig. 5.1.4) and microscopy (Fig. 5.1.5-6). Comparison of clover expression in HEK cells (Fig. 5.1.4) confirmed that Lin-C and Lin-A loaded LNBs resulted in successful transfection. Furthermore, the clover/vinculin ratios determined from Western blotting (Fig. 5.1.4. B) show Lin-C having greater clover expression than Lin-A in HEK cells (Lin C: 2.96 ± 0.53; Lin A: 2.51 ± 0.20). Figure 5.1.4.B also shows that linear clover loaded LNBs leads to at least double or more clover expression in HEK cells than either Lin-C or Lin-A loaded LNBs. Figure 5.1.5-6 shows microscopy images of all 4 cell lines transfected with LNBs loaded with Lin-C (Fig. 5.1.5) or Lin-A (Fig. 5.1.6.). These images

confirm that clover is expressed successfully in all 4 cell lines with both Lin-C and Lin-A loaded LNBs.

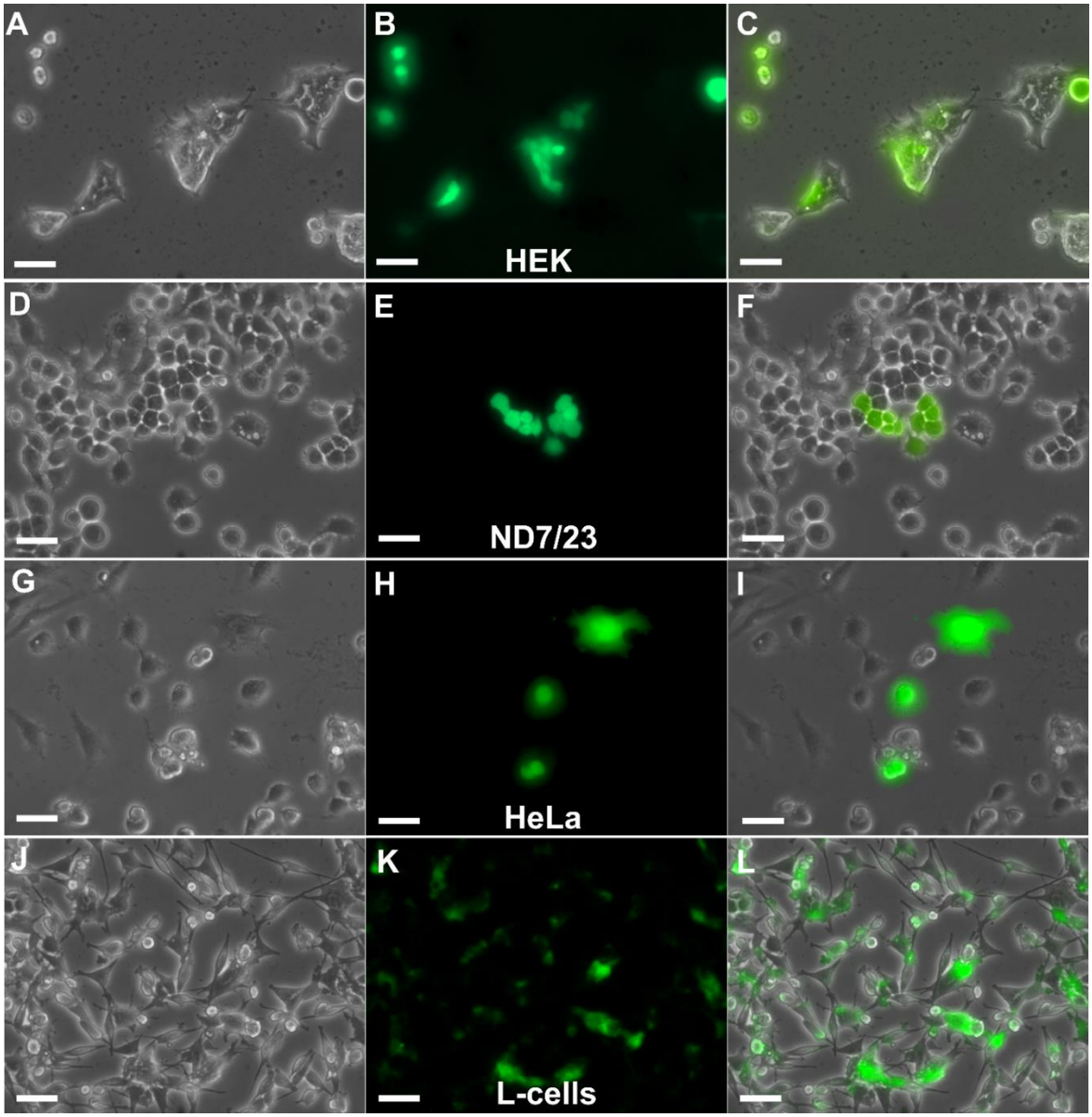

Figure 5.1.5. Transfection of 4 cell lines with carboxyl functionalized linearized Clover (Lin-C). Phase (left), fluorescence (center) and overlay (right) images acquired with a 20X objective showing clover expression in HEK, ND7/23, HeLa and L- cells following transfection with LNB-loaded (0.5 mg/ml) with Lin-C cDNA (10 µg/mg). Scale bars indicate 50 µm.

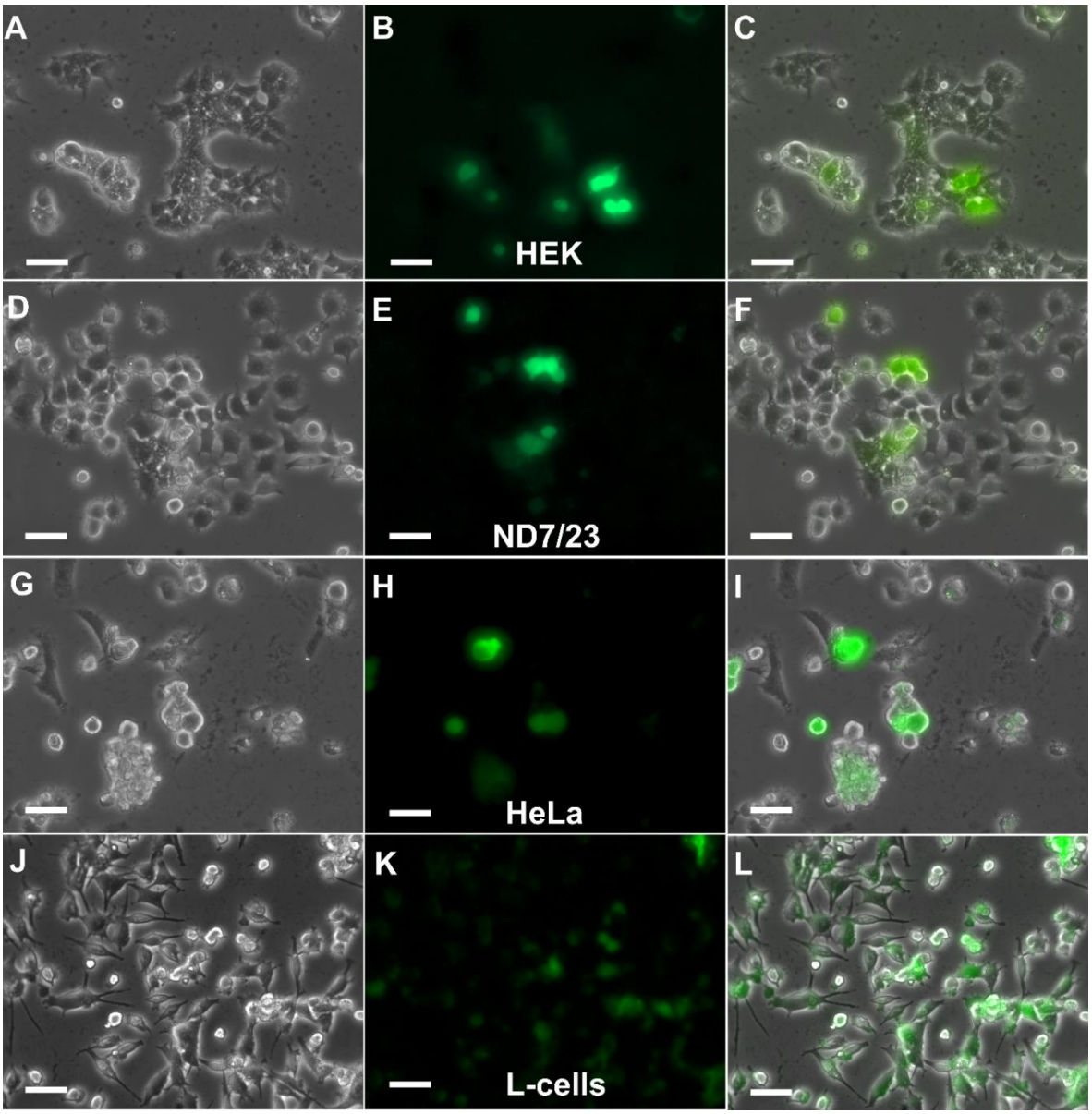

Figure 5.1.6. Transfection of 4 cell lines with azide functionalized linearized Clover (Lin-A). Phase (left), fluorescence (center) and overlay (right) images acquired with a 20X objective showing clover expression in HEK, ND7/23, HeLa and L- cells following transfection with LNB-loaded (0.5 mg/ml) with Lin-A cDNA (10 µg/mg). Scale bars indicate 50 µm.

5.1.5. Discussion

We demonstrated that the PCR-based linearization technique allows for incorporation of specific functional groups on the linearized cDNA enabling chemisorption and controlled release of cDNA from surfaces. Our release studies from NBs loaded with

linearized cDNA show that the choice of conjugation chemistry is advantageous in order to control the release rate of cDNA. That is, the reducing agent-specific release is more than double for click chemistry than EDC-based conjugation chemistry. This is partly due to the pH of the solution employed. Under our conditions (i.e., pH = 7.4) electrostatics driven physisorption on the amine functionalized NB surface is even more likely for Lin-C. As a result, both chemisorption and physisorption take place simultaneously during loading of Lin-C and during release it is much more likely to re-physisorb back to the amine-coated NB surface. Steric hindrance applied at the NB-buffer interface in the form of biocompatible polymers like PEG can also help in favoring chemisorption and minimizing post-release physisorption. Furthermore, in the present study, the disulfide/azide or disulfide/carboxyl groups were added to only the forward primers for PCR. This leaves room to further tune the NB-DNA release properties by incorporating these chemical groups to the forward as well as the reverse PCR primers during the linearization step.

One major advantage of loading NBs with linearized cDNA is that the DNA can be easily functionalized with a variety of terminal chemistries for efficient conjugation to surfaces and release using cleavable bonds built into the primer design. This also underscores the advantage of using the PCR amplification method (over enzymatic digestion of restriction sites on the plasmid template) to synthesize linearized constructs from plasmid templates as it allows for an easy way to incorporate functional moieties into the linearized construct.

In a biological system, the disulfide group is assumed to be broken by reducing agents such as glutathione (GSH) which is found in the cytoplasm and facilitated the

release of DNA from the NBs. GSH concentrations are tenfold higher inside the cellular environment[18] than the extracellular space thereby making the release controllable post cellular internalization and endosomal release of the LNBs. This becomes a crucial feature in *in vivo* applications where LNBs are likely to spend a greater time circulating in the plasma/CSF before becoming internalized. The ability to chemisorb and release DNA in a controlled manner also puts LNB system at a more advantageous position than simple liposome-based systems where DNA complexation and release cannot be easily controlled with chemical conjugations.

5.2. DNA delivery in DRG neurons

5.2.1. Introduction

Despite their high transfection efficiency in dividing cells under *in vitro* conditions, inorganic nanomaterials have had limited success in transfection of non-dividing cells, such as neurons. Neuron transfection approaches typically employ viruses, physical non-viral techniques (i.e. nuclear or cytoplasmic injections, electroporation and magnetofection) and chemical techniques (i.e. lipofection or PEI)[19]. The physical techniques have high efficiencies, though not scalable to *in vivo* applications, while chemical techniques can be toxic for non-dividing cells. This presents a unique opportunity to design nanomaterials as transfection agents for both dividing and non-dividing cells with a high transfection efficiency and minimal cytotoxicity compared to current transfection technologies. Employment of nanomaterials, including the inorganic type, has had limited use for transfection of neurons. Nevertheless, there are reports of *in vivo* gene delivery to the brain[20], [21]. Here we demonstrate the applicability of LNBs in neuronal transfection *in vitro* and *ex vivo* in the DRG derived from a rat model.

5.2.2. Methods

NB uptake and cDNA transfection of acutely isolated rat sensory neurons.

The animal studies were approved by the Penn State College of Medicine Institutional Animal Care and Use Committee (IACUC) approved the animal studies. Sprague-Dawley rats were initially anaesthetized with CO_2 and rapidly decapitated with a laboratory guillotine. The DRG neurons (L_4 and L_5) and SCG neurons were isolated as described previously[22], [23]. Both DRG and SCG tissue were then cleared of connective tissue in ice-cold Hanks' balanced salt solution. Thereafter, the tissue was enzymatically dissociated in Earle's balanced salt solution containing 0.6 mg/ml collagenase D (Roche Applied Science), 0.4 mg/ml trypsin (Worthington Biochemical), and 0.1 mg/ml DNase (Sigma-Aldrich) in a shaking water bath at 35°C for 60 mins. Thereafter, the neurons were dispersed by vigorous shaking, centrifuged twice for 6 mins at 44xg, and resuspended in Minimum Essential Media (MEM, Thermo-Fisher Scientific) supplemented with 10% fetal bovine serum, 1% penicillin-streptomycin, and 1% glutamine (Thermo-Fisher Scientific). Finally, the neurons were plated onto 35 mm poly-L-lysine-coated dishes and stored in a humidified incubator supplied with 5% CO_2/95% air at 37°C. For internalization experiments, the neurons were exposed to NBs (30 µg/ml), mixed in DPBS:Opti-MEM for 4 hrs, rinsed in warm DMEM and fixed as per TEM fixation protocols. For LNB internalization experiments, LNBs (0.5 mg/ml) were added as above and applied to the neurons for 4 and 24 hrs prior to fixation as per TEM protocols. For transfection of DRG neurons, the dissociated cells were incubated for 4 hrs with 0.5 mg/ml LNB that were loaded with 10 µg/mg supercoiled clover cDNA. The neurons were fixed in 4% paraformaldehyde (PFA) 48 hrs post-transfection. Afterwards, phase contrast and

fluorescence images were acquired as described above. In another set of experiments, the non-dissociated DRG tissue (L_4 and L_5) were placed in a 96-well plate and incubated initially in DMEM with 3% DMSO in order to dissociate the meningeal layer at 37^{o}C for 30 mins. Thereafter, the tissue was incubated in 300 µl LNB (1 mg/ml) loaded with 32 µg/mg linearized tdT at 37^{o}C for 6 hrs. For internalization study, amine-NBs were conjugated to Cy3-NHS (Lumiprobe Inc.) in DMSO, washed, dried, coated with DOPE/DOTAP as described before, and finally re-dispersed in 1:1 OMEM:DPBS at 1 mg/ml and 0.5 mg/ml concentrations, respectively. The tissue was gently rinsed 3 times in warm DMEM and then incubated for 72 hrs at 37^{o}C in DMEM supplemented with growth factor (15 ng/ml ciliary derived growth factor, 15 ng/ml nerve growth factor and 6 ng/ml glial derived neurotrophic factor). After the incubation period, the tissue was dissociated employing the protocol described above and plated on poly-L-lysine-coated 35 mm tissue culture dish for fluorescence imaging.

Fluorescence Microscopy.

Phase contrast and fluorescence images were obtained with a Nikon TE2000 microscope, an Orca-ER CCD camera (Hamamatsu Photonics), iVision software for acquisition (Biovision Tech.) and Photo Fluor II (89 North) for illumination. The images were processed, and pseudo-colored with iVision in accordance with the appropriate filters used for the fluorescence channel.

Transmission electron microscopy (TEM).

Tissue samples were fixed with 2.5% glutaraldehyde and 2% paraformaldehyde (Electron Microscopy Sciences) in 0.1 M phosphate buffer (pH 7.4) and further fixed in

1% osmium tetroxide (Electron Microscopy Sciences) in 0.1 M phosphate buffer (pH 7.4) for 60 mins. Samples were dehydrated in a graduated ethanol series, acetone and embedded in LX-112 (Ladd Research). The sections (60 nm) were stained with uranyl acetate and lead citrate (Electron Microscopy Sciences) and viewed in a JEOL JEM 1400 Transmission Electron Microscope (JEOL USA Inc.). All images were taken at 60 kV. All measurements were performed in the Microscopy Imaging Core, Penn State College of Medicine, PA.

5.2.3. Results

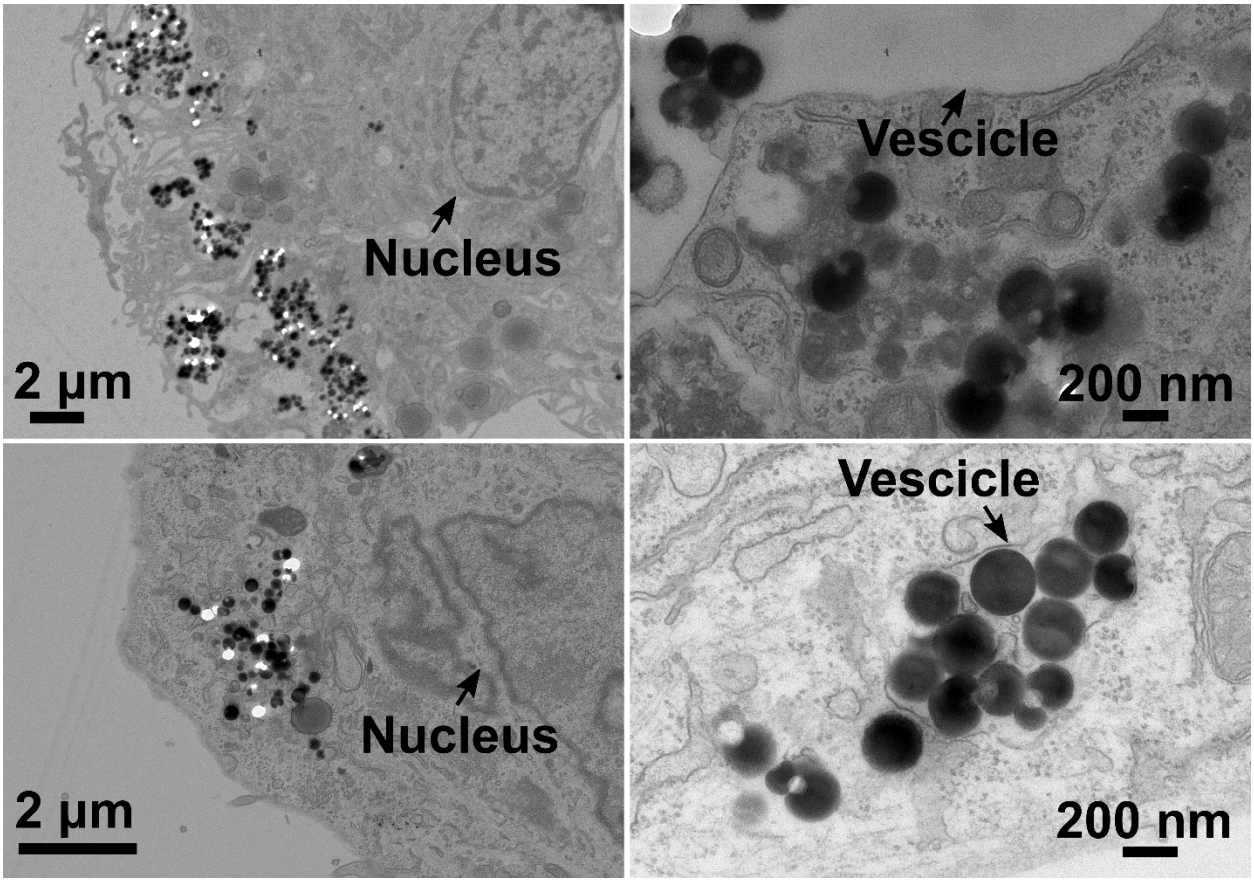

Figure 5.2.1. Transfection of DRG neurons with LNBs. TEM images of acutely dissociated DRG neurons acquired 4 (top) and 24 (bottom) hour post-treatment with DOPE/DOTAP coated NBs i.e. LNBs (0.5 mg/ml). The images were taken from negatively stained 60 nm tissue sections.

We examined whether clover cDNA loaded LNBs (0.5 mg/ml) could be employed to transfect acutely dissociated rat DRG neurons. The LNBs were loaded with supercoiled

clover cDNA (10 µg/mg). The TEM micrographs acquired at 4 (Fig. 5.2.1, top) and 24 hrs (Fig. 5.2.1, bottom) post-transfection show that LNBs remain internalized within the cytoplasm. The micrographs also depict several LNB clusters that are free of vesicular encapsulation post-endocytosis. Figure 5.2.2 A-D are phase and fluorescence images of acutely dissociated DRG tissue. The images show that both neurons (Fig. 5.2.2 A-B) and glial cells (Fig. 5.2.2 C-D) expressed clover within 48 hrs of *in vitro* transfection post-dissociation.

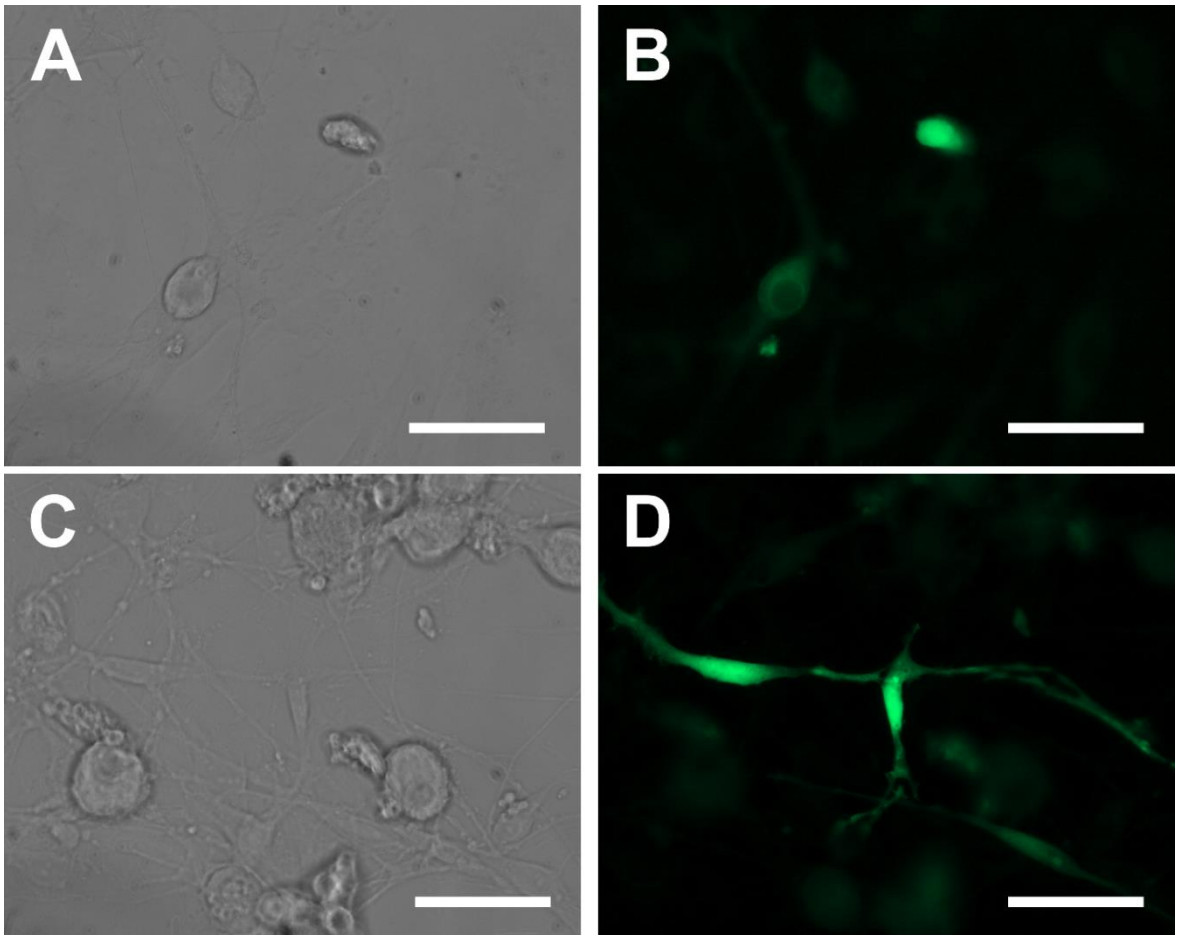

Figure 5.2.2. *In vitro* transfection of acutely dissociated neurons and glia with LNBs. Microscopy images depicting clover expression in pre-dissociated Dorsal Root Ganglion (DRG) neurons (A,B) and glial cells (C,D) 48 hrs post-transfection (*in vitro*) with clover cDNA-loaded (10 µg/mg) LNBs (0.5 mg/ml). Phase (A,C) and fluorescence images (B,D) were taken with a 40X objective. Scale bars depict 50 µm. All fluorescence images (B,D) were pseudo colored.

Whether DRG tissue, prior to enzymatic dissociation, could be transfected with LNBs was also tested. First, we tested if NBs could get internalized *ex vivo* in DRG. Cy3-tagged LNBs showed successful internalization in whole DRG tissue (Fig. 5.2.3 A-B) after a DMSO treatment for the dissolution of the meningeal layer to aid transfection.

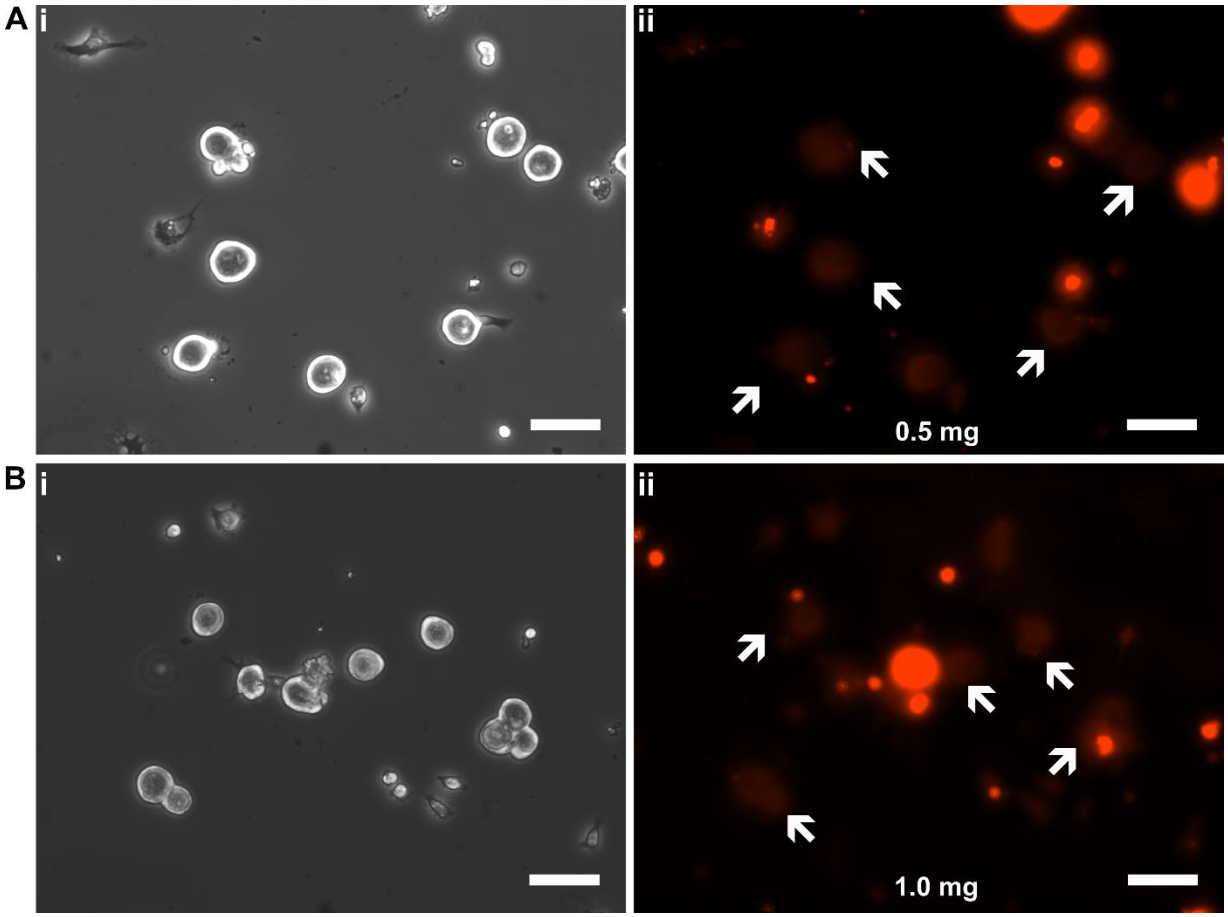

Figure 5.2.3. Internalization of Cy3-tagged LNBs in DRG tissue. A. and B. Internalization of Cy3-tagged LNBs in rat DRG tissue incubated 6 hrs in 0.5 or 1 mg/ml Cy3-LNBs. The DRG tissue was enzymatically dissociated 6 hrs post-transfection period. Phase (i) and fluorescence images (ii) were acquired with a 20X objective. White arrows indicate dissociated neurons. Scale bars indicate 50 µm.

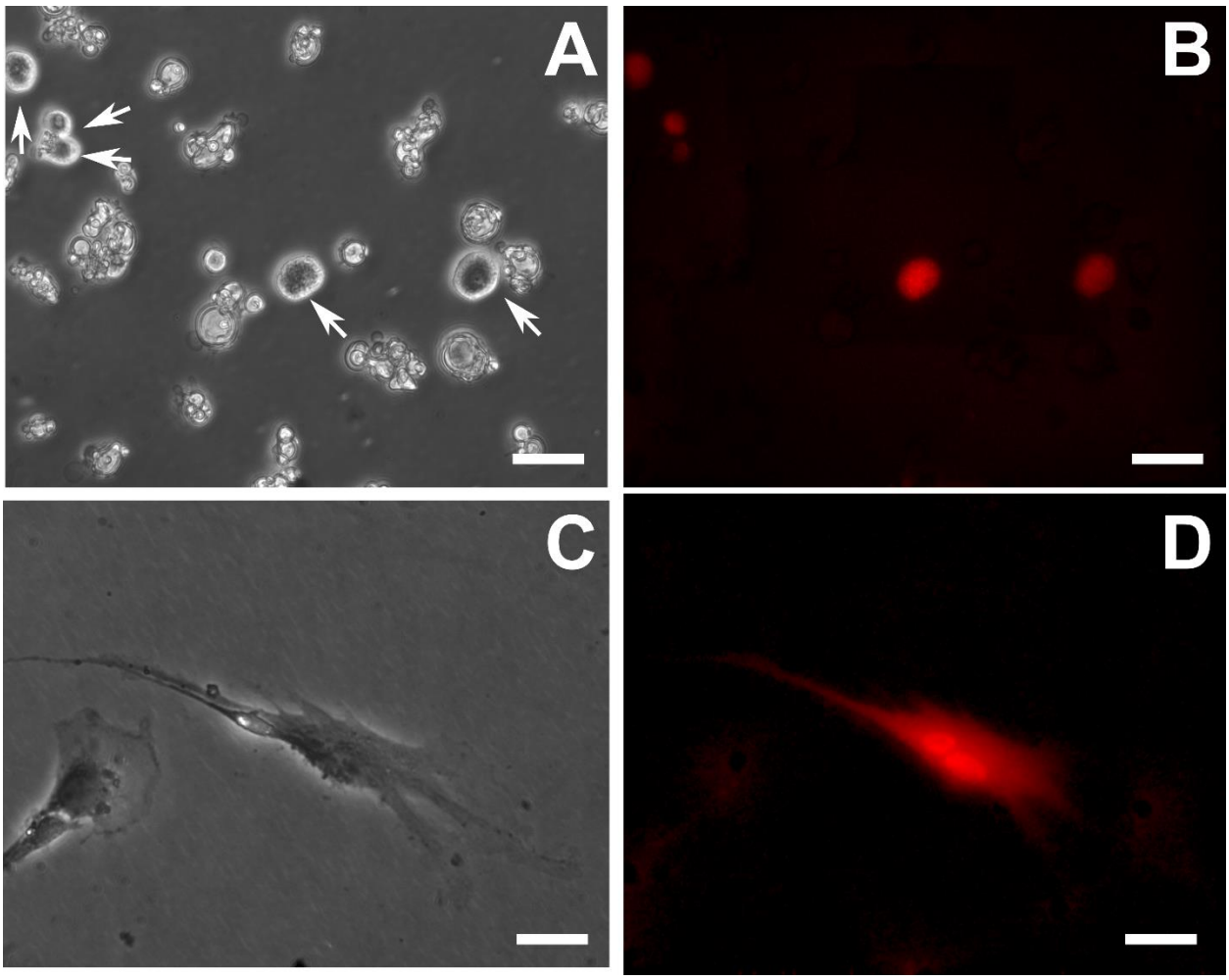

Figure 5.2.4. *Ex vivo* transfection of acutely dissociated neurons and glia with LNBs. Phase (A, C) and fluorescence (B,D) images of acutely dissociated DRG neurons (A-B) and glia (C-D) taken 72 hrs post-transfection (*ex vivo*) of DRG tissue with LNBs (1 mg/ml) loaded with tdTomato (50 µg/mg). The images were acquired with a 20X objective. Scale bars depict 50 µm.

In this set of experiments, cDNA coding for the fluorescent protein tdTomato was employed. The DRG tissue was incubated for 6 hrs with LNBs (1 mg/ml) loaded with linearized cDNA (50 µg/mg). The DRG tissue was dissociated 72 hrs post-transfection and the neurons were then plated in 35 mm dishes. The fluorescence images shown in Figure 5.2.4 indicate that DRG neurons (Fig. 5.2.4 A-B) as well as glia (fig. 5.2.4 C-D) were successfully transfected with tdTomato cDNA-containing LNBs.

5.2.4. Discussion

We have demonstrated here that we can successfully transfect DRG tissues *in vitro* and *ex vivo* with linearized and supercoiled cDNA construct. Our results show transfections in both neurons and glial cells. Our *in vitro* DRG transfection experiments reveal that LNBs transfect more glial cells than neurons. The NBs used in this study have been previously demonstrated to be multifunctional by IONP functionalization and Au coating that gives it the ability to be magnetically guided, localized and used for IR or MRI based diagnostics[24]. Therefore, this study shows promise of *in vivo* therapeutic and diagnostic applications of LNBs within a neuronal context.

Our studies showed that these NBs are non-specific and are taken up in cell lines of different origins (Chapter 2 and 3), neurons, and glia. For more targeted applications, this LNB design needs further development to add target specificity and IONP attachment for magnetic localization. Other ways to specifically target LNBs to neurons over glia or connective tissue is to functionalize the outer lipid layer with neuron targeting proteins. One such protein characterized in literature is herpes simplex virus (HSV) gD-1 protein, which is an anchoring protein of the HSV virus known to specifically infect sensory neurons via Nectin-1 receptors[25]. In addition, incorporating polymers like polyethylene glycol (PEG) in the form of functionalization or physical introduction in the lipid bilayer are needed to improve the stability of the LNBs in protein rich media (beyond the time scales of *in vitro* transfection) and to further facilitate *in vivo* transport. LNBs at their current design were unable to cross the meningeal layer in intact DRG tissue enough to cause successful transfection, and we therefore facilitated their tissue uptake by partial dissolution of the meningeal layer with DMSO. Fundamental transport studies of LNBs in

connective tissues like the meninges needs further exploration with or without magnetic guidance to be a viable non-viral *in vivo* transfection agent.

5.3. Co-transfection of GPCR and GIRK in HEK cells

5.3.1. Introduction

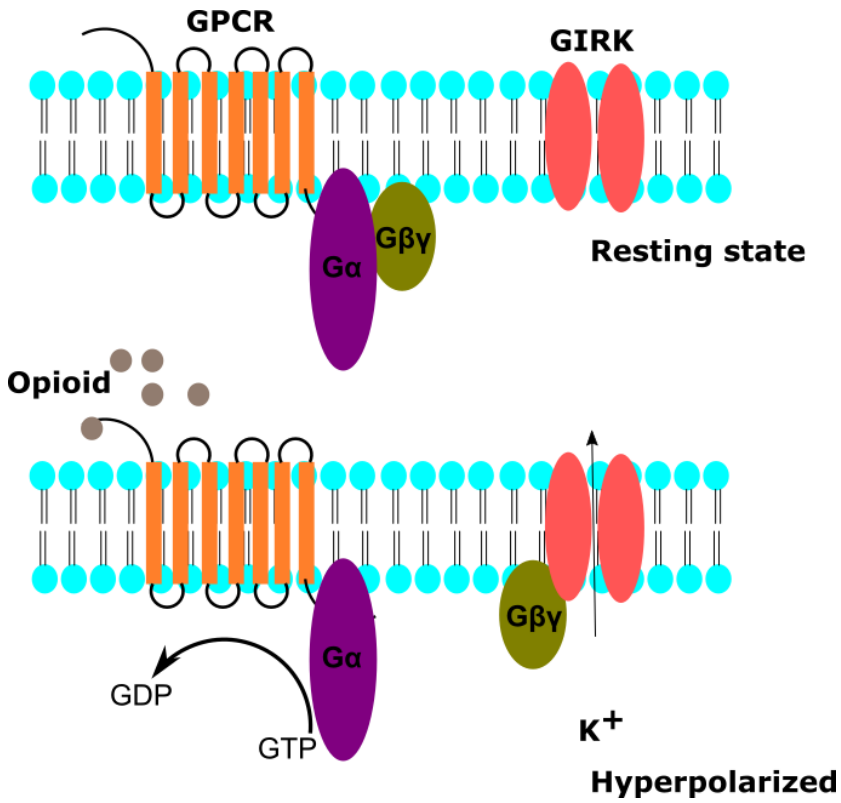

Figure 5.3.1. GPCR-GIRK signaling in neurons. The schematic shows a G-protein coupled receptor (GPCR) in the cell membrane with its transmembrane, intracellular (Gα, Gβγ) and extracellular domain. The latter binds to an opioid agonist. Post-binding, following an intracellular GTP to GDP conversion, the Gβγ subunit separates from the GPCR and binds to the inversely rectifying potassium channel (GIRK) to cause K^+ ion efflux and membrane hyperpolarization.

G-protein coupled inwardly rectifying potassium channels (GIRKs) are specialized K^+ ion channels which reduce neuron excitability and are key players in the inhibitory response of neurons in the central nervous system (CNS) [26],[27],[28].These channels can be controlled by various receptors like the G-protein coupled opioid receptor family, which in turn are known to be stimulated by opioid agonists in a dose-dependent manner. Specifically, the molecular mechanism of this coupling is depicted in Figure 5.3.1. In the

cell's resting state, the intracellular K^+ concentration is held slightly higher than that of the extracellular medium. Thus, the resting membrane potential is held slightly above the equilibrium potential of K^+. When an agonist binds to the extracellular N-terminus of the GPCR, it starts a signaling cascade, part of which is the separation of Gβγ subunit from the GPCR complex and its subsequent binding to the GIRK tetramer. This triggers the opening of the GIRK channel and the resulting outward K^+ current. This hyperpolarizes the membrane and decreases cell excitabilities, thus regulating the heart rate and both the excitatory and inhibitory neurotransmissions. From a pharmacological viewpoint, GIRK is a potential therapeutic target for epilepsy and bipolar disorder. In neurons of the CNS, functional GIRK channels are known to be heterodimers of subunits within the GIRK 1-5 family[26],[28]. One example of clinical application of an *in vitro* transfection system is therefore to develop stably transfected cell lines that can act as therapeutic model systems for *in vitro* testing and optimizations of drug candidates. Such *in vitro* models are not only cheaper and easier to use than primary neurons but also can act as a no-background system without interference from endogenous receptor pathways that are present in the neuronal targets.

Thus, in the following work, we have used the LNBs to co-transfect HEK cells with GIRK 1 and GIRK 4 as well as opioid GPCRs i.e., μ opioid receptor (MOR) or κ opioid receptor (KOR). HEK cells were chosen as an *in vitro* model because, unlike neurons of the CNS, they do not endogenously express GIRKs and can be easily transfected. Thus, HEK cells provide a clean background to study GPCR-GIRK coupling. By characterizing the HEK membrane potential changes in response to varying doses of opioids, we were

able to confirm the presence of all 3 transfected proteins simultaneously, thereby demonstrating the ability of LNBs to deliver multiple constructs successfully.

5.3.2. Methods

Co-transfection of HEK cells with opioid receptors and GIRK1 and GIRK4 channels.

In this set of experiments, HEK cells were plated on glass-bottom 96-well plates at 35,000 cells/well 24 hrs prior to the experiment. In one set of experiments, the cells were transfected with 200 µl of 0.5 mg/ml LNBs loaded with yellow fluorescent protein (YFP)-tagged µ-opioid receptor (YFP-MOR), GIRK1 and GIRK4 cDNA constructs at a 2:1:1 construct ratio of a total 15 µg. In the second set, the cells were transfected with kappa opioid receptor (KOR), GIRK1 and GIRK4 cDNA constructs at a ratio of 1:1:1 with a total of 15 µg cDNA/well. Microscopy images were taken from one set of HEK cells 48 hrs after transfection and subsequent fixation with 4% PFA. Phase contrast and fluorescence images were obtained with a Nikon TE2000 microscope, an Orca-ER CCD camera (Hamamatsu Photonics), iVision software for acquisition (Biovision Tech.) and Photo Fluor II (89 North) for illumination. The images were processed, and pseudo-colored with iVision in accordance with the appropriate filters used for the fluorescence channel. 48 hrs post-transfection, the cells were loaded with the voltage sensitive blue dye (FLIPR membrane potential assay kit blue, Molecular Devices) at 37^{o}C for 30 mins. Afterwards, fluorescence measurements (540 nm emission) were acquired at 2 sec intervals with the FlexStation 3 microplate reader (Molecular Devices). After a stable baseline of 30 secs was obtained, the specific opioid receptor agonists were applied to each well at different concentrations. Opioids used in this study i.e., fentanyl, oxycodone (µ opioid agonists), U-50488 and U-69593 (κ opioid agonists) were ordered from Sigma Aldrich. Control wells

received FLIPR buffer only. The maximum % reduction in fluorescence signal from baseline (signal before t<=30 sec) within the 180 sec reading time interval (proportional to cell hyperpolarization) was plotted against logarithmic agonist (opioid) concentration range (log M) and fit with Hill equation to obtain the concentration-response plots.

5.3.3. Results

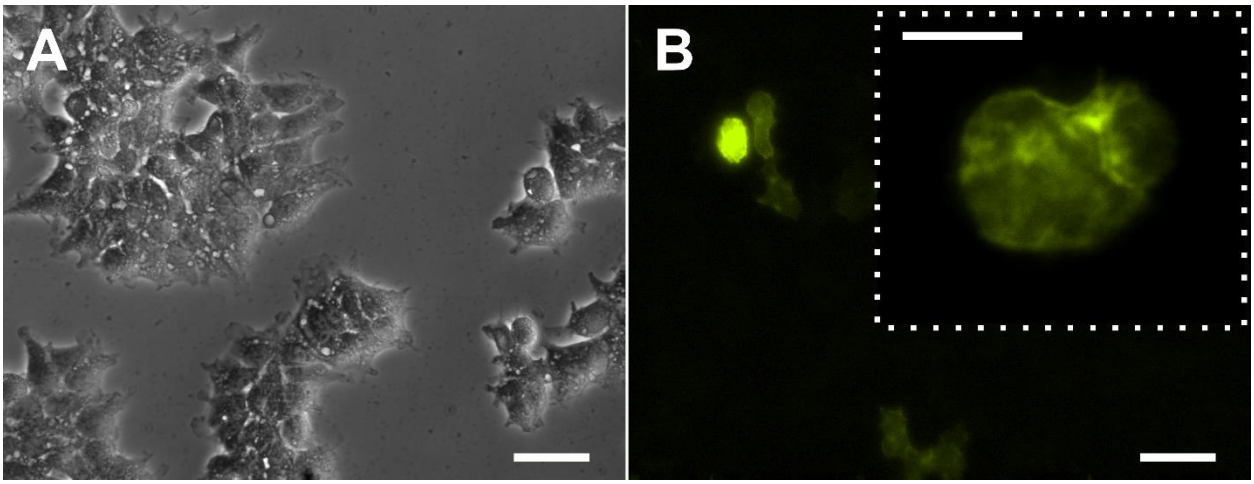

Figure 5.3.2. YFP-tagged MOR expression in HEK cells with LNB transfection. A. Phase contrast and B. fluorescence images of HEK cells transfected with LNBs (0.5 mg/ml) loaded with YFP-MOR, GIRK1 and GIRK4 cDNA plasmids. Images were acquired with a 20X objective (scale bar 50 μm). Inset in (B) depicts a fluorescence image acquired with a 40X objective (scale bar 50 μm).

We examined whether LNBs coated with multiple cDNA constructs could be employed to obtain simultaneous protein expression. HEK cells were transfected with LNBs loaded with three cDNA constructs coding for the yellow fluorescent protein-tagged μ opioid receptor (YFP-MOR), G-protein-coupled inwardly rectifying K^+ channels 1 (GIRK1) and GIRK 4. HEK cells do not naturally express these proteins and, thus, provide a suitable null background. Stimulation of MOR leads to G protein-mediated opening of GIRK1/4 channel dimers and results in cellular hyperpolarization. In order to demonstrate successful opioid-dependent membrane potential changes, we first tested if the expressed MORs were trafficked into the cell membrane post-transfection with a Yellow

Fluorescent Protein (YFP) tagged MOR construct. Figure 5.3.2 shows phase and fluorescent images of HEK cells transfected with the YFP-MOR cDNA constructs 48 hrs post-transfection. The fluorescent images of YFP emission (40x inset of Figure 5.3.2) confirms that the YFP is not distributed in the cytoplasm and is rather localized in the cell membrane as is expected of a trans-membrane protein like MOR.

We optimized a fast, high throughput assay employing a microplate reader with a robotic system which added agents to the 96-well plate seeded with the transfected HEK cells. We employed the FLIPR membrane potential assay kit to measure the opioid-mediated stimulation of MOR and activation of GIRK1 and GIRK4 channels, leading to cellular hyperpolarization. This assay comprises of a proprietary lipophilic, anionic dye (excited at 488 nm) that partitions across the plasma membrane of live cells in a membrane potential dependent manner. When the cell depolarizes, more dye enters the cells, binds to the intracellular organelles and proteins, which causes a concomitant increase in the dye's fluorescence. Similarly, when the cell hyperpolarizes, the more dye leaves the cells, thereby decreasing the concentration of intracellular membrane/protein-bound dye concentration.

Figure 5.3.3A shows the fluorescence signals of 3 individual wells with HEK cells expressing YFP-MOR, GIRK1 and GIRK4 before and following addition of vehicle (black trace), 50 (green trace) and 100 μM (blue trace) oxycodone, a high affinity MOR agonist. Following a 30 sec stable baseline, vehicle or agonist application was performed. It can be observed that the vehicle did not exert an overt effect on the fluorescence signal, while oxycodone at either concentration caused a decrease in fluorescence, indicative of cell hyperpolarization (i.e., stimulation of GIRK channels). Figure 5.3.4 shows the

concentration-response relationship of the oxycodone-mediated decrease in fluorescence. A fit of the data with the Hill equation resulted in an EC_{50} value of 32.6 µM for oxycodone. We also tested the effect of fentanyl, another high affinity MOR agonist, on the membrane potential of transfected HEK cells (Fig. 5.3.3B). It can be observed that the decrease in fluorescence was dose-dependent for 5 (green trace) and 30 (blue trace) µM fentanyl. The former caused a 17.1% decrease, while application of the latter led to a 21.2% decrease (Fig. 5.3.3B).

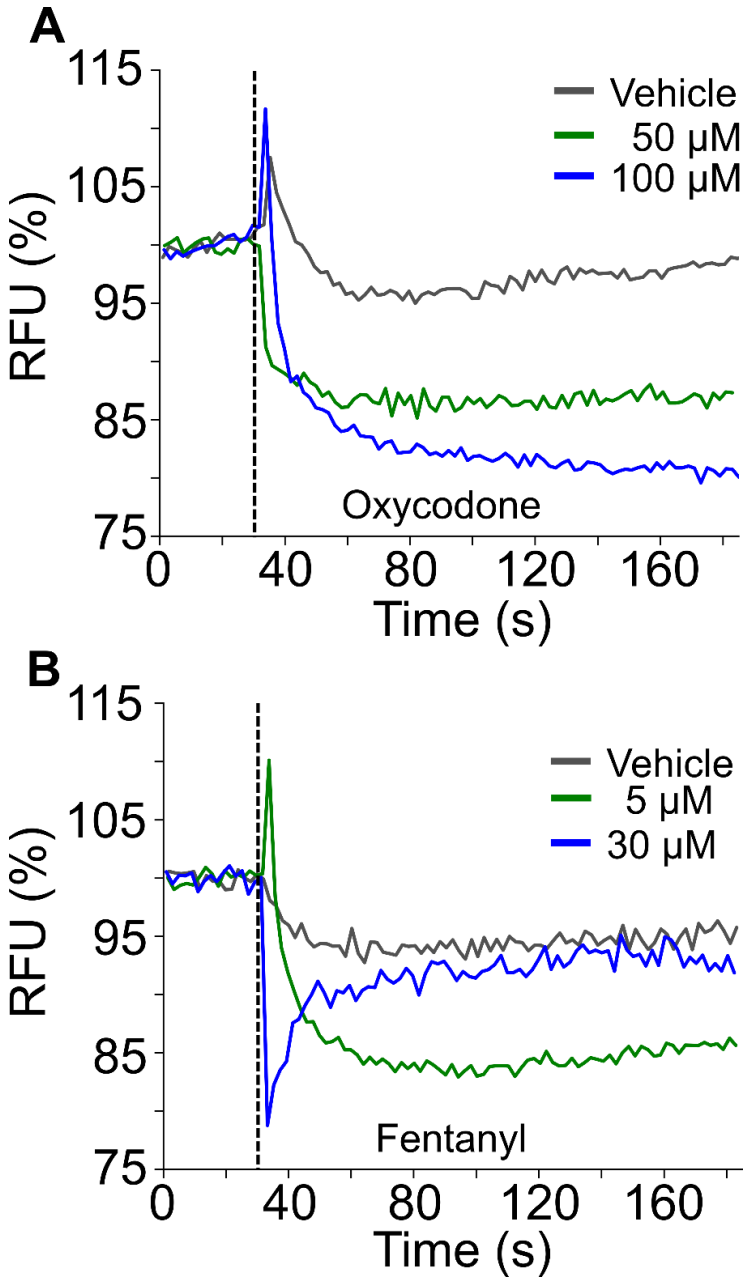

Figure 5.3.3. MOR targeting opioid dose-response of LNB transfected HEK cells. Raw traces of fluorescence signals before and during MOR agonist A. Oxycodone B. Fentanyl application (dotted line at t=30 sec) in HEK cells transfected with GIRK1, GIRK4 and YFP-MOR Y-axis depicts the % change in relative fluorescence units (RFU).

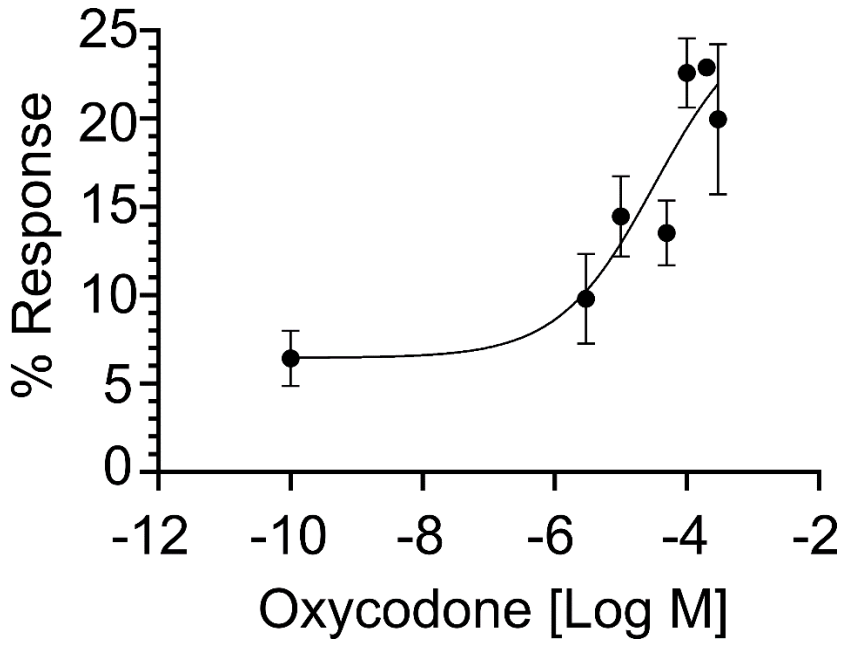

Figure 5.3.4. Oxycodone concentration-response of LNB transfected HEK cells. The graph shows the concentration-response relationship of oxycodone applied to MOR transfected HEK cells. Each point in represents the mean % change of the RFU. The smooth curves were obtained by fitting the points to the Hill equation. Error bars indicate SEM of triplicate measurements. The HEK cells in this study were incubated for 48 hrs post- transfection with 0.5 mg/ml LNB loaded with cDNA constructs for GIRK1, GIRK4 and YFP-MOR.

We next tested whether another opioid receptor subtype, kappa opioid receptor (KOR), could be co-transfected similarly with GIRK1 and GIRK4 in HEK cells. The fluorescence signals shown in Figure 5.3.5 A depicts the changes in membrane potential of HEK cells co-expressing the three cDNA constructs following exposure to the high affinity KOR agonist, U-50488. Similar to the changes observed with MOR stimulation, application of 5 (green) and 30 µM (blue) U-50488 resulted in a dose-dependent cellular hyperpolarization. The representative U-50488 concentration-response relationship is depicted in Figure 5.3.6. After the data was fit to the Hill equation, the calculated EC_{50} for U-50488 was 7.95 µM. Thereafter, we examined the effect of a second KOR agonist, U-69593 (Fig. 5.3.5.B). Application of either 5 or 50 µM U-69593 lead to a 21% in fluorescence (Fig. 5.3.5).

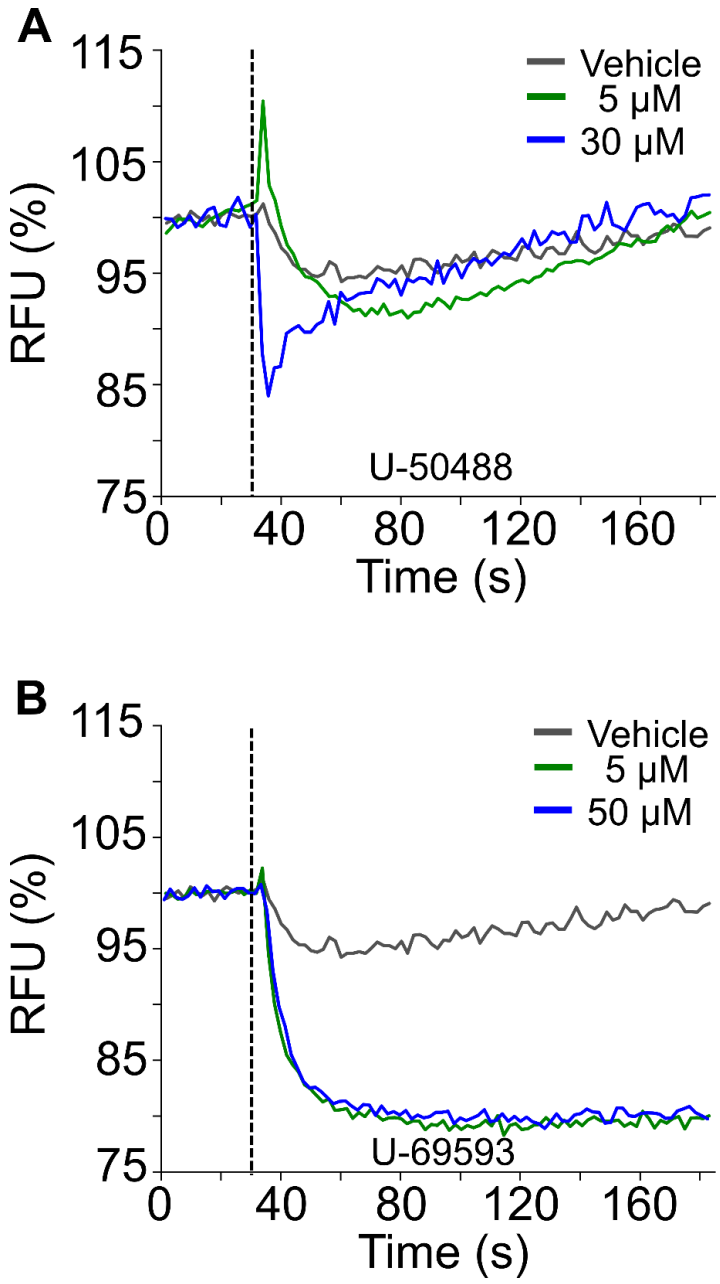

Figure 5.3.5. KOR targeting opioid dose-response of LNB transfected HEK cells. Raw traces of fluorescence signals before and during KOR agonist A. U-50488 B. U-69593 application (dotted line at t=30 sec) in HEK cells transfected with GIRK1, GIRK4 and κ opioid receptors (KORs). Y-axis depicts the % change in relative fluorescence units (RFU).

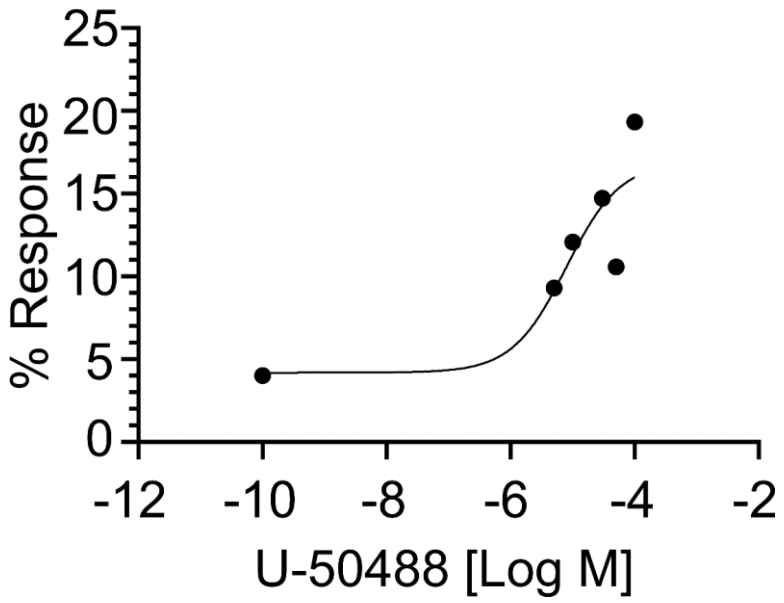

Figure 5.3.6. U-50488 concentration-response of LNB transfected HEK cells. The graph shows the concentration-response relationship of U-50488 applied to KOR transfected HEK cells. Each point in represents the mean % change of the RFU. The smooth curves were obtained by fitting the points to the Hill equation. The HEK cells in this study were incubated for 48 hrs post transfection with 0.5 mg/ml LNB loaded with cDNA constructs for GIRK1, GIRK4 and KOR.

5.3.3. Discussion

Our results demonstrate that LNBs can be employed to transfect multiple constructs simultaneously, in a relatively fast, inexpensive, and reliable manner in order to determine the pharmacological profile of G-protein coupled receptors, such as opioid receptors. The GPCR subfamily of opioid receptors μ, κ and δ are clinical targets for a massive number of pharmacological studies especially in the area of newer drug design[29] and understanding mechanisms of desensitization, tolerance, and addiction of highly potent opioids such as fentanyl[30]. The use of high throughput signaling assays like FLIPR© therefore hold unprecedented clinical value in the face of the current opioid crisis. Finally, the FlexStation 3 results (Fig. 5.3.2-6) suggest that pharmacological studies can still be performed with the transfection efficiency we obtained. That is, expression

levels for both opioid receptors and GIRK channels were sufficient to obtain functional coupling of G protein coupled receptors with ion channels. The pharmacological parameters determined were comparable to published reports[31]–[34].

Through these 3 applications i.e. (a) controlled DNA release (b) *in vitro* and *ex vivo* DRG neuron transfections (c) co-transfection of GIRK and GPCR in HEK cells have demonstrated that the LNB non-viral gene delivery system is versatile and applicable in many clinically relevant systems.

Chapter 5, in part, has been published in ACS Bioconjugate Chemistry (2020) with coauthors Dr. Ratneshwar Lal and Dr. Victor Ruiz-Velasco. The dissertation author was the primary investigator and author of this material.

5.4 Bibliography

[1] S. Mehier-Humbert and R. H. Guy, “Physical methods for gene transfer: Improving the kinetics of gene delivery into cells,” *Advanced Drug Delivery Reviews*, vol. 57, no. 5. Elsevier, pp. 733–753, Apr. 05, 2005, doi: 10.1016/j.addr.2004.12.007.

[2] C. S. Filgueira, S. R. Igo, D. K. Wang, M. Hirsch, D. G. Schulz, B. A. Bruckner, and A. Grattoni, “Technologies for intrapericardial delivery of therapeutics and cells,” *Advanced Drug Delivery Reviews*, vol. 151–152. Elsevier B.V., pp. 222–232, Nov. 01, 2019, doi: 10.1016/j.addr.2019.02.006.

[3] A. K. Pannier and L. D. Shea, “Controlled release systems for DNA delivery,” *Mol. Ther.*, vol. 10, no. 1, pp. 19–26, 2004, doi: 10.1016/j.ymthe.2004.03.020.

[4] Z. Li, W. Ho, X. Bai, F. Li, Y. jui Chen, X. Q. Zhang, and X. Xu, “Nanoparticle depots for controlled and sustained gene delivery,” *J. Control. Release*, vol. 322, no. March, pp. 622–631, 2020, doi: 10.1016/j.jconrel.2020.03.021.

[5] S. B. Hartono, N. T. Phuoc, M. Yu, Z. Jia, M. J. Monteiro, S. Qiao, and C. Yu, “Functionalized large pore mesoporous silica nanoparticles for gene delivery featuring controlled release and co-delivery,” *J. Mater. Chem. B*, vol. 2, no. 6, pp. 718–726, 2014, doi: 10.1039/c3tb21015d.

[6] C. H. Lu and I. Willner, “Stimuli-Responsive DNA-Functionalized Nano-/Microcontainers for Switchable and Controlled Release,” *Angew. Chemie - Int. Ed.*, vol. 54, no. 42, pp. 12212–12235, 2015, doi: 10.1002/anie.201503054.

[7] J. Zheng, Y. Nie, S. Yang, Y. Xiao, J. Li, Y. Li, and R. Yang, “Remote-controlled release of DNA in living cells via simultaneous light and host-guest mediations,” *Anal. Chem.*, vol. 86, no. 20, pp. 10208–10214, 2014, doi: 10.1021/ac502280z.

[8] R. Huschka, J. Zuloaga, M. W. Knight, L. V. Brown, P. Nordlander, and N. J. Halas, “Light-induced release of DNA from gold nanoparticles: Nanoshells and nanorods,” *J. Am. Chem. Soc.*, vol. 133, no. 31, pp. 12247–12255, 2011, doi: 10.1021/ja204578e.

[9] A. M. Goodman, N. J. Hogan, S. Gottheim, C. Li, S. E. Clare, and N. J. Halas, “Understanding Resonant Light-Triggered DNA Release from Plasmonic Nanoparticles,” *ACS Nano*, vol. 11, no. 1, pp. 171–179, 2017, doi: 10.1021/acsnano.6b06510.

[10] D. Trentin, J. Hubbell, and H. Hall, “Non-viral gene delivery for local and controlled DNA release,” *J. Control. Release*, vol. 102, no. 1, pp. 263–275, 2005, doi: 10.1016/j.jconrel.2004.09.029.

[11] L. Chen, J. Di, C. Cao, Y. Zhao, Y. Ma, J. Luo, Y. Wen, W. Song, Y. Song, and L. Jiang, “A pH-driven DNA nanoswitch for responsive controlled release,” *Chem. Commun.*, vol. 47, no. 10, pp. 2850–2852, 2011, doi: 10.1039/c0cc04765a.

[12] C. Nowald, B. T. Käsdorf, and O. Lieleg, “Controlled nanoparticle release from a hydrogel by DNA-mediated particle disaggregation,” *J. Control. Release*, vol. 246, pp. 71–78, 2017, doi: 10.1016/j.jconrel.2016.12.015.

[13] H. Cohen, R. J. Levy, J. Gao, I. Fishbein, V. Kousaev, S. Sosnowski, S. Slomkowski, and G. Golomb, “Sustained delivery and expression of DNA encapsulated in polymeric nanoparticles,” *Gene Ther.*, vol. 7, no. 22, pp. 1896–1905, 2000, doi: 10.1038/sj.gt.3301318.

[14] S. H. Kim, J. H. Jeong, S. H. Lee, S. W. Kim, and T. G. Park, “PEG conjugated VEGF siRNA for anti-angiogenic gene therapy,” *J. Control. Release*, vol. 116, no. 2 SPEC. ISS., pp. 123–129, Nov. 2006, doi: 10.1016/j.jconrel.2006.05.023.

[15] X. F. Ma, J. Sun, C. Qiu, Y. F. Wu, Y. Zheng, M. Z. Yu, X. W. Pei, L. Wei, Y. J. Niu, W. H. Pang, Z. J. Yang, J. C. Wang, and Q. Zhang, “The role of disulfide-bridge on the activities of H-shape gemini-like cationic lipid based siRNA delivery,” *J. Control. Release*, vol. 235, pp. 99–111, Aug. 2016, doi: 10.1016/j.jconrel.2016.05.051.

[16] N. W. S. Kam, Z. Liu, and H. Dai, “Functionalization of carbon nanotubes via cleavable disulfide bonds for efficient intracellular delivery of siRNA and potent gene silencing,” *J. Am. Chem. Soc.*, vol. 127, no. 36, pp. 12492–12493, Sep. 2005, doi: 10.1021/ja053962k.

[17] N. C. Shaner, P. A. Steinbach, and R. Y. Tsien, “A guide to choosing fluorescent proteins,” *Nat. Methods*, vol. 2, no. 12, pp. 905–909, Dec. 2005, doi: 10.1038/nmeth819.

[18] H. J. Forman, H. Zhang, and A. Rinna, “Glutathione: Overview of its protective roles, measurement, and biosynthesis,” *Molecular Aspects of Medicine*, vol. 30, no.

1–2. Pergamon, pp. 1–12, Feb. 01, 2009, doi: 10.1016/j.mam.2008.08.006.

[19] D. L. Puhl, A. R. D'Amato, and R. J. Gilbert, "Challenges of gene delivery to the central nervous system and the growing use of biomaterial vectors," *Brain Research Bulletin*, vol. 150. Elsevier Inc., pp. 216–230, Aug. 01, 2019, doi: 10.1016/j.brainresbull.2019.05.024.

[20] I. Roy, M. K. Stachowiak, and E. J. Bergey, "Nonviral gene transfection nanoparticles: function and applications in the brain," *Nanomedicine: Nanotechnology, Biology, and Medicine*, vol. 4, no. 2. NIH Public Access, pp. 89–97, Jun. 2008, doi: 10.1016/j.nano.2008.01.002.

[21] D. J. Bharali, I. Klejbor, E. K. Stachowiak, P. Dutta, I. Roy, N. Kaur, E. J. Bergey, P. N. Prasad, and M. K. Stachowiak, "Organically modified silica nanoparticles: A nonviral vector for in vivo gene delivery and expression in the brain," *Proc. Natl. Acad. Sci. U. S. A.*, vol. 102, no. 32, pp. 11539–11544, Aug. 2005, doi: 10.1073/pnas.0504926102.

[22] M. Farrag, J. K. Drobish, H. L. Puhl, J. S. Kim, P. B. Herold, M. P. Kaufman, and V. Ruiz-Velasco, "Endomorphins potentiate acid-sensing ion channel currents and enhance the lactic acid-mediated increase in arterial blood pressure: effects amplified in hindlimb ischaemia," *J. Physiol.*, vol. 595, no. 23, pp. 7167–7183, Dec. 2017, doi: 10.1113/JP275058.

[23] W. Margas, K. Sedeek, and V. Ruiz-Velasco, "Coupling Specificity of NOP Opioid Receptors to Pertussis-Toxin-Sensitive Gα Proteins in Adult Rat Stellate Ganglion Neurons Using Small Interference RNA," *J. Neurophysiol.*, vol. 100, no. 3, pp. 1420–1432, Sep. 2008, doi: 10.1152/jn.90405.2008.

[24] A. H. Mo, P. B. Landon, K. S. Gomez, H. Kang, J. Lee, C. Zhang, W. Janetanakit, V. Sant, T. Lu, D. A. Colburn, S. Akkiraju, S. Dossou, Y. Cao, K. F. Lee, S. Varghese, G. Glinsky, and R. Lal, "Magnetically-responsive silica-gold nanobowls for targeted delivery and SERS-based sensing," *Nanoscale*, vol. 8, no. 23, pp. 11840–11850, Jun. 2016, doi: 10.1039/c6nr02445a.

[25] S. M. Richart, S. A. Simpson, C. Krummenacher, J. C. Whitbeck, L. I. Pizer, G. H. Cohen, R. J. Eisenberg, and C. L. Wilcox, "Entry of Herpes Simplex Virus Type 1 into Primary Sensory Neurons *In Vitro* Is Mediated by Nectin-1/HveC," *J. Virol.*, vol. 77, no. 5, pp. 3307–3311, 2003, doi: 10.1128/JVI.77.5.3307-3311.2003.

[26] V. Ruis-Velasco and S. R. Ikeda, "Heterologous expression and coupling of G protein-gated inwardly rectifying K+ channels in adult rat sympathetic neurons," *J. Physiol.*, vol. 513, no. 3, pp. 761–773, 1998, doi: 10.1111/j.1469-7793.1998.761ba.x.

[27] J. M. Lewohl, W. R. Wilson, R. D. Mayfield, S. J. Brozowski, R. A. Morrisett, and R. A. Harris, "G-protein-coupled inwardly rectifying potassium channels are targets of alcohol action," *Nat. Neurosci.*, vol. 2, no. 12, pp. 1084–1090, 1999, doi: 10.1038/16012.

[28] J. Zhang, S. S. G. Ferguson, L. S. Barak, S. R. Bodduluri, S. A. Laporte, P. Y. Law, and M. G. Caron, “Role for G protein-coupled receptor kinase in agonist-specific regulation of μ-opioid receptor responsiveness,” *Proc. Natl. Acad. Sci. U. S. A.*, vol. 95, no. 12, pp. 7157–7162, 1998, doi: 10.1073/pnas.95.12.7157.

[29] H. C. S. Chan, D. McCarthy, J. Li, K. Palczewski, and S. Yuan, “Designing Safer Analgesics via μ-Opioid Receptor Pathways,” *Trends Pharmacol. Sci.*, vol. 38, no. 11, pp. 1016–1037, 2017, doi: 10.1016/j.tips.2017.08.004.

[30] V. C. Dang and M. J. Christie, “Mechanisms of rapid opioid receptor desensitization, resensitization and tolerance in brain neurons,” *Br. J. Pharmacol.*, vol. 165, no. 6, pp. 1704–1716, 2012, doi: 10.1111/j.1476-5381.2011.01482.x.

[31] D. A. Volpe, G. A. M. M. Tobin, R. D. Mellon, A. G. Katki, R. J. Parker, T. Colatsky, T. J. Kropp, and S. L. Verbois, “Uniform assessment and ranking of opioid Mu receptor binding constants for selected opioid drugs,” *Regul. Toxicol. Pharmacol.*, vol. 59, no. 3, pp. 385–390, Apr. 2011, doi: 10.1016/j.yrtph.2010.12.007.

[32] A. Knapman, M. Santiago, Y. P. Du, P. R. Bennallack, M. J. Christie, and M. Connor, “A continuous, fluorescence-based assay of μ-opioid receptor activation in AtT-20 cells,” *J. Biomol. Screen.*, vol. 18, no. 3, pp. 269–276, Mar. 2013, doi: 10.1177/1087057112461376.

[33] B. J. Vliet, A. H. Mulder, and A. N. M. Schoffelmeer, ?“-Opioid Receptors Mediate the Inhibitory Effect of Opioids on Dopamine-Sensitive Adenylate Cyclase in Primary Cultures of Rat Neostriatal Neurons,” *J. Neurochem.*, vol. 55, no. 4, pp. 1274–1280, Oct. 1990, doi: 10.1111/j.1471-4159.1990.tb03135.x.

[34] M. K. Pugsley, E. J. Yu, and A. L. Goldin, “U-50,488H, a Kappa Opioid Receptor Agonist, is a More Potent Blocker of Cardiac Sodium Channels than Lidocaine,” 2000.

Chapter 6

Silencing RNA and anti-inflammatory drug co-delivery with magnetic NBs

6.1 Introduction

An outbreak of infection caused by a novel coronavirus (SARS-Cov-2) from the severe acute respiratory syndrome (SARS) family that started in Wuhan, China in December 2019, rapidly spread across the world infecting millions, and was declared a pandemic by the World Health Organization (WHO) by the name Covid19 in March 2020[1]–[4]. By August 2020, more than 17 million cases and over 675,000 deaths due to Covid-19 were reported across the globe. Although public safety protocols were rapidly put into action to limit the spread of infection, like government mandated shutdowns, social distancing, widespread asymptomatic testing and sanitization, it became clear that without Covid19 vaccines and better therapeutics, the death toll from this pandemic cannot be controlled. This led to the widespread efforts in the research and biotech industry domains towards the development of (a) vaccines (b) therapeutics to battle Covid19. Through “Operation Warp Speed”, the US government approved $9.5 billion towards the development and manufacturing of vaccines that can proceed at parallel with research. Since January 2020, there have been hundreds of clinical trials[5], [6] towards vaccine development. As of today, several vaccine candidates (Pfizer-BioNTech, Oxford-AstraZeneca, Moderna) have shown 70-90% efficiencies in their Phase 2 clinical trials[5]–[9]. In many of these vaccine candidates in clinical trials, the ability to engineer nanomaterials to deliver nucleic acids/viral spike proteins is being investigated. Parallel to vaccine development, the scientific community has mobilized towards better understanding of the Covid19 pathophysiology, the role of therapeutics like anti-

inflammatory drugs and silencing RNA therapeutics, and the applicability of nanotechnology[10]–[14] for targeted, controlled delivery of molecular[12], [15] and nucleic acid based therapeutics[16], [17]/vaccine candidates[5],[18]. Thus, this pandemic has ushered in a new era of applying nano delivery systems for therapeutic interventions in infectious diseases like Covid19.

Dexamethasone (Dex) is a potent anti-inflammatory and immune-suppressive glucocorticoid, which in its native state is hydrophobic and sparingly soluble in water. In a randomized clinical trial, the RECOVERY collaborative group supported by the National Health Service (NHS) in the UK, it was found that among patients receiving oxygen support with or without intubation, the 28 day mortality reduced with dexamethasone treatment[15], [19] of 6 mg oral or IV every day for up to 10 days (29.3% vs 41.4% in the invasive oxygen support group; 23.3% vs 26.2% with non-invasive oxygen support). Silencing RNA is a short (20-30 bp), double stranded oligonucleotide which can lead to post-transcriptional knockdown in protein expression via the RISC pathway in the cell cytoplasm[20], [21]. In this pathway, the guide strand of the silencing RNA forms a complex with Argonaute-2, identifies its complementary sequence on the mRNA strand and cleaves it, thereby preventing downstream translation of mRNA into protein[20], [21]. There are widespread efforts towards identifying a library of sequences targeting therapeutically relevant regions in the SARS-Cov-2 genome for Covid19 targeted silencing RNA based therapeutics development. Several targets in the 29 kbp SARS-Cov-2 genome have been identified[2], [3], [17], [22], [23] like 14 open reading frames (ORFs) that code for 27 structural and non-structural proteins and sections in its genome responsible for expression of 4 proteins (S, E, M and N proteins). One drawback of

silencing RNA based therapeutics is their inherent instability in blood, inherent immunogenicity, and inability to easily cross the cell membrane[21]. Therefore, silencing RNA has been conjugated to or encapsulated in various delivery systems[21], [24]–[30] to overcome these delivery challenges like polymers, lipids, peptides, antibodies, aptamers and nanoparticles like solid lipid nanoparticles[24], [25], [28]–[31], gold nanoparticles[29], [32], [33], silica nanoparticles[28], [34], [35] and metal organic frameworks[36], [37]. Biotech companies like Vir Biotechnology (San Francisco, USA), Alnylam Pharmaceuticals (Boston, USA), Sirnaomics (Gaithersberg, USA) and OliX Pharmaceuticals (Suwan, South Korea) are working on such SARS-Cov-2 genome targeted siRNA therapeutics.

With Covid19, there is an urgent need to develop multi-functional silencing RNA/drug delivery system that can release their payload in a controlled manner. In the previous chapters, we have shown that the silica NB gene delivery system is a biocompatible, versatile, and efficient DNA delivery system. In this chapter, we will develop the NB system to co-deliver Covid19-relevant molecular (Dexamethasone) and nucleic acid-based (siRNA) therapeutics in a stimulus-controlled manner. Furthermore, for applications of localized delivery and hyperthermia control, we have also demonstrated a magnetic NB system.

6.2. Methods

Synthesis of magnetic NBs.

Amine coated NBs were prepared as described in previous chapters. Using EDC conjugation chemistry, carboxyl functionalized SPIONS (10-15 nm, Ocean Nanotech)

were attached to amine coated NBs. To achieve this 2 mM EDC (Sigma Aldrich) and 5 mM NHS (Sigma Aldrich) in pH 5.7 MES buffer (Sigma Aldrich) was added to amine NBs at 1 mg/ml in pH 7.4 DPBS. To this was added 10 ul of 5 mg/ml SPION and the mixture was allowed to stir at high speed overnight. The next day, the NBs were purified by washing in DPBS 2 times, followed by water, followed by ethanol. The purified magnetic NBs were allowed to dry under vacuum and then re-dispersed in appropriate buffers for downstream use.

siRNA loading on NBs.

Silencing RNA was purchased from Sigma Aldrich with a custom terminal amine functionality, di-sulfide group, and a fluorophore (Atto 590). AmC6 is -NH_2 group. ThiC6 is -S-S- group. Sense strand: 5' [Atto 590] UUGAAUACACCAAAAGAUCACAUU 3'. Anti-sense strand: 5' [AmC6][ThiC6] AAUGUGAUCUUUUGGUGUAUUCAA 3'. Silencing RNA was either physisorbed or chemisorbed on NBs or magnetic NBs. For physisorption, silencing RNA in molecular biology grade water was mixed with 1 mg/ml NB or magnetic NB in DPBS with Ca and Mg. They were allowed to mix gently on a rotator for 30 mins at 4^{o}C. Centrifugation was used to wash out unbound siRNA. For chemisorption, EDC-NHS conjugation chemistry was used similar to Chapter 5.1.

Dexamethasone loading on NBs.

FITC labelled dexamethasone (Dex) was purchased from Sigma Aldrich. Appropriate amounts of Dex solution in methanol was mixed with DPPC and DOTAP (chloroform solutions, Avanti Polar Lipids) in a glass vial. The ratio between Dex and lipid mass was varied between 1:10, 1:5, 1:2, 1:1 and 2:1 (see results for more details). The

mixture was vacuum dried to create a uniform lipid film. The lipid film was hydrated with DPBS into a 1mg/ml solution. Following hydration, the lipid solution was sonicated under ice for 15 mins and allowed to mix with 1 mg/ml NB in DPBS. Following lipid coating, excess lipids/Dex was washed out by repeated centrifugal washing in DPBS. To characterize loading, the Dex loaded NBs were mixed with methanol, sonicated, spun down, and supernatant was collected for spectral analysis of emission at 520 nm to determine concentration. Following a calibration curve of emission vs. concentration, the concentration of the released Dex was determined.

siRNA release assay.

siRNA loaded NBs were washed in DPBS once to remove unbound siRNA. Then, the NBs were redispersed in fresh DPBS and kept on a heat block set to 37^{o}C for 4 , 24 and 48 hrs. At each time point, the NBs were spun down, and the supernatant was quantified for siRNA concentration using a Thermo Fisher Nanodrop One.

Dexamethasone release assay.

NBs loaded with dexamethasone were dispersed in DPBS and kept at 37^{o}C for 4, 24 and 48 hrs. The particles were spun down by centrifugation and the supernatant was mixed 1:1 with methanol. Concentration of dexamethasone was measured from this solution using the plate reader as described above.

Toxicity assays.

Toxicity assays were performed using MTT as previously described in Chapter 4. NBs were either magnetic or non-magnetic, coated with DPPC/DOTAP and used in 0.5-0.05 mg/ml concentrations in DPBS/Opti-MEM.

Internalization of siRNA/Dex loaded NBs.

NBs were loaded with siRNA and then coated with DPPC/DOTAP. After centrifugal purification, the siRNA loaded NBs were redispersed at 0.5 mg/ml and allowed to incubate for 4 hrs. After 4 hrs, live cells were imaged with fluorescence microscopy as per previously established protocols in Chapters 3-5.

SQUID magnetization measurements

Magnetization measurements at different temperatures were obtained from SPION conjugated NBs in the form of a dry powder (1.0 mg, 10nm & 1.2 mg, 15 nm) with a Superconducting Quantum Interference Device (SQUID) Magnetometer (Quantum Design) courtesy of Dr. Rinehart at the department of Chemistry, UCSD.

ICP-MS (Inductively coupled plasma mass spectrometry)

1 mg of each of the 15 nm and 10 nm conjugated NBs (dried) were treated with HF, followed by HNO_3, internal standards were added, and analyzed with an ICP-MS (Thermo Fisher Scientific) at the Isotope Geochemistry Laboratory (Scripps Institute of Oceanography, La Jolla).

6.3. Results

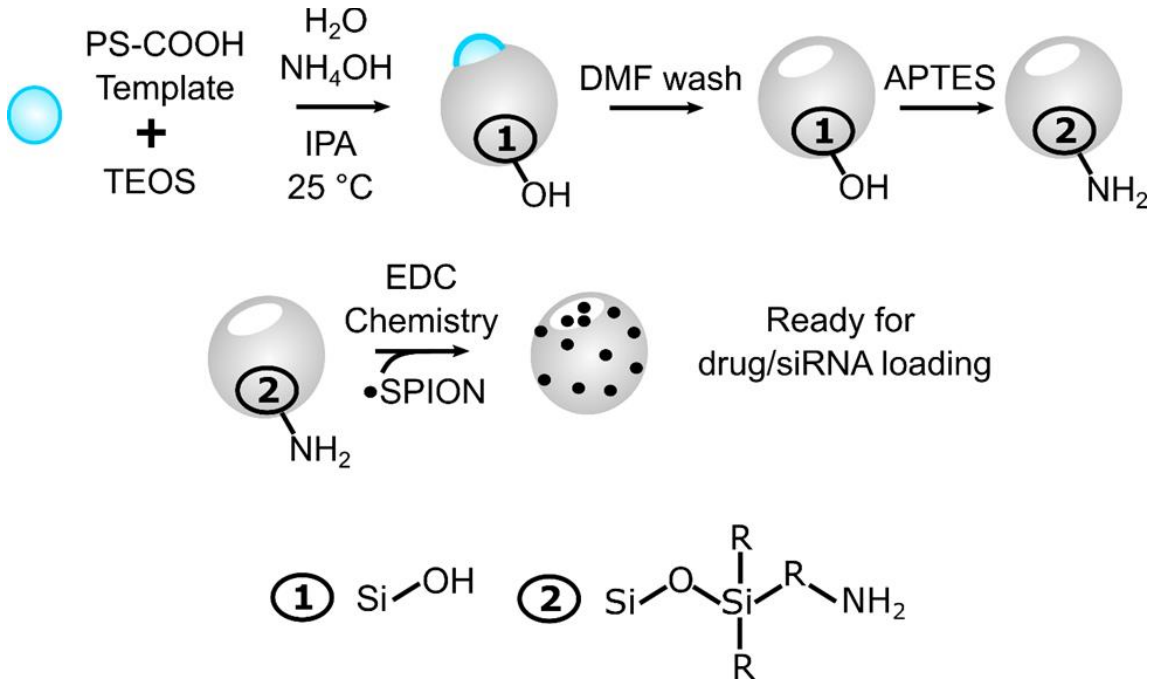

Figure 6.1. Schematic showing synthesis of magnetic NBs. Schematic shows that NBs are first synthesized with poly condensation of tetraethyl orthosilicate (TEOS) around a 100 nm polystyrene (PS) template at room temperature. Post synthesis, the NBs are purified and incubated with dimethyl formamide (DMF) at 60°C for 3 hrs, followed by silanization with 3-aminopropyl triethoxysilane (APTES). Amine functionalized NBs are conjugated with 15 nm superparamagnetic iron oxide nanoparticles (SPION) using EDC crosslinker chemistry. For more details refer to methods.

Figure 6.1 shows the schematic of NB synthesis and subsequent preparation steps to attach superparamagnetic iron oxide particles (SPION) via EDC-NHS conjugation chemistry. This chemistry relies on first modifying the NB surface after DMF wash with APTES to give it an amine functionality as described in previous chapters. ICP-MS studies show that we get a loading of 2.3 ± 0.09 µg/mg NB and 3.19 ± 0.11 µg/mg NB mass loading of SPIONS for 10 nm and 15 nm diameters, respectively. Figure 6.2 shows the morphology of NBs before (Fig. 6.2 A-B) and after attachment of SPIONS (Fig. C-F) with SEM and TEM imaging. DLS results (Fig. 6.2 G and Table 6.1) indicate that upon attachment of SPIONS of 10 nm size, NBs undergo a 12 nm increase in hydrodynamic

diameter in water and a concomitant change in surface zeta potential from positively charged (amine functionalized, 37 mV) to positively charged (SPION conjugated, -38 mV) in water. This is likely caused due to the fact that SPIONs used in this study are negatively charged themselves, with a coating of carboxyl terminated moieties.

Functional SQUID measurements show that due to SPION conjugation, NBs have superparamagnetic properties as shown in Figure 6.3. As applied magnetic field is increased from zero to 70000 Oe, we see that the NB-SPION conjugate shows increasing magnetic moment until it reaches saturation around 5000 Oe, at 1.8 emu/g for 10 nm (Fig. 6.3 A) and 1.5 emu/g for 15 nm (Fig. 6.3 B) SPION conjugated NBs. Changing temperatures i.e., 25, 37 and 42^{O}C do not have any significant changes on the magnetic moment of these materials. Furthermore, the slope of the Figure 6 A-B graphs indicate the magnetic susceptibilities of 2.3e-9 and 1.9e-9 for 10 nm and 15 nm conjugated SPIONS, respectively. These results indicate the possibility that NBs can be used for various downstream magnetic applications like magnetic localization, generation of local hyperthermia, etc.

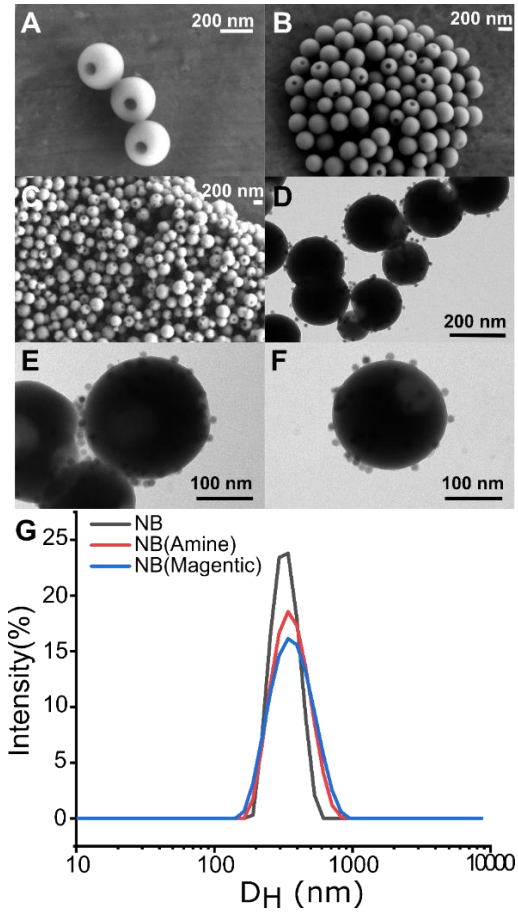

Figure 6.2. Characterization of NBs with and without SPIONS. Scanning electron microscopy of NBs after DMF wash and removal of PS core (A-B) and NBs after conjugation with SPIONS and subsequent purification. D-F. Transmission electron microscopy (TEM) images of SPION conjugated NBs after purification and removal of unbound SPIONS. G. Raw dynamic light scattering (DLS) spectra of scattering intensity to hydrodynamic diameter (D_H) of NBs after PS core removal (NB), NBs after APTES functionalization (NB-Amine) and NBs after SPION conjugation and purification (NB magnetic). These data show representative D_H values from 3 experiments.

Table 6.1. Size and surface charge properties of NBs and magnetic NBs in water.

NB chemistry	D_H (nm)	PDI	Zeta Potential (mV)
NB	318.1 ± 7.8	0.024 ± 0.017	-34.5 ± 0.574
NB+Amine	343.4 ± 5.3	0.114 ± 0.037	+36.8 ± 0.834
Magnetic NB	355.2 ± 4.3	0.181 ± 0.017	-37.6 ± 1.370

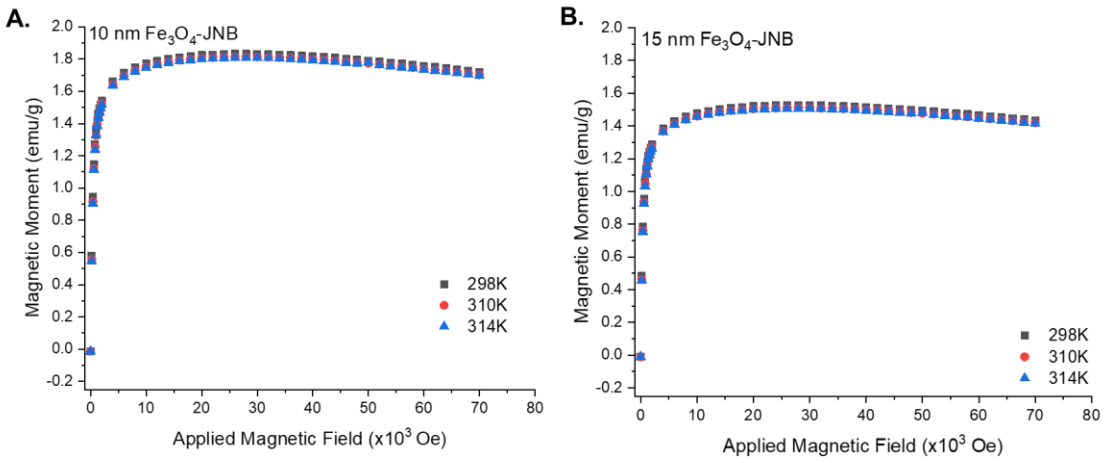

Figure 6.3 Magnetic characterization of IONP conjugated NBs. Magnetization curves obtained with SQUID for 10 nm (A) and 15 nm (B) iron oxide nanoparticles conjugated to NBs by EDC conjugation due to application of 0-70,000 Oe magnetic field at 298K i.e., 25^{O}C (black square), 310K i.e.,37^{O}C (red circle) and 314K i.e., 42^{O}C (blue triangle). Magnetic moments normalized to the total mass (NB+IONP) are plotted on the y-axis (emu/g). 1.77313 ± 0.03644 emu/g; χ = 2.32x10^{-3}; χ = 2.39x10^{-3}, 1.47761 ± 0.02857 emu/g; χ = 1.93x10^{-3} were calculated for the 10 and 15 nm SPION attached NBs, respectively. Mass normalizations were done with respect to the whole mass of the composite ~ 1 mg (10 nm) and 1.2 mg (15 nm). Fe content in the composites as per ICP-MS measurements were 2.3 ± 0.09 µg/mg (10 nm) and 3.19 ± 0.11 µg/mg (15 nm).

Table 6.2. siRNA loading values of NBs and magnetic NBs.

Chemistry of NBs	ug/mg
Amine (physisorption)	3.87
COOH (chemisorption)	5.03
NB-magnetic (physisorption)	2.87
NB-magnetic (chemisorption)	2.03

In the next set of experiments, we loaded silencing RNA on NBs with or without SPIONS (Table 6.2 and Fig. 6.4). We tested both physisorption, i.e., mixing in silencing RNA with amine terminated NBs, as well as chemisorption. For chemisorption, the silencing RNA was designed with a disulfide group and amine functionality on the 5' end of the anti-sense strand (Fig. 6B). For characterization, the siRNA also had a fluorophore (ATTO 590) conjugated to the 5' end of the sense strand (Fig. 6B). To achieve chemisorption on non-magnetic NBs, the amine functionalized NBs were further treated with succinic anhydride to confer carboxyl functionality. Magnetic NBs had carboxyl

functionality on the SPIONS attached to the NB surface. This was followed by EDC conjugation chemistry with the amine functionalized siRNA and the carboxylated NBs as described in Figure 6.4 B. Loading measurements (Table 6.2) with Nanodrop showed that the highest loading was achieved in carboxyl terminated NBs (chemisorption) and the least was achieved in magnetic NBs (chemisorption). We have not quantified the carboxyl densities in NB vs magnetic NB, but our results indicate that carboxylation over the NBs gives better siRNA loading. In addition, we have also confirmed siRNA loading on NBs with fluorescence spectrometry (Fig. 6.4B). The bound siRNA (green trace, Fig. 6.4B) shows emission at the same peak (632 nm) as free siRNA (red trace, Fig. 6.4B) but with attenuation in signal intensity possibly due to fluorophore quenching near NB surface.

Next, we determined the drug loading capacity of the LNB system. For this study we chose a combination of DPPC and DOTAP as this combination is known to have a transition temperature around $40^{O}C$ that would be applicable for heat triggered release of drugs. To demonstrate drug loading, we chose a hydrophobic drug Dexamethasone (FITC fluorophore conjugated) which was mixed in with the DPPC/DOTAP mixture prior to lipid bilayer formation and subsequent hydration in buffered media. The liposomes were formed by sonication and subsequently coated onto the NBs. For our loading experiments (Fig. 6.5), we gradually increased the lipid:Dex ratio from 10:1, 5:1, 2:1, 1:1 to 1:2. In each case, after loading, the NBs were treated with methanol to dissolve the lipid layer and the quantity of Dex loaded was determined spectrophotometrically by comparing fluorescence emission at 520 nm against a pre-determined standard fluorescence emission vs. concentration calibration curve. Our results (Fig. 6.5 B) show that as the lipid:Dex ratio is increased, the drug loading % increases up to 1:1 and then

reduces back to 10%. The maximum loading is achieved at 1:1 lipid:Dex feeding ratio (Fig. 6.5 B).

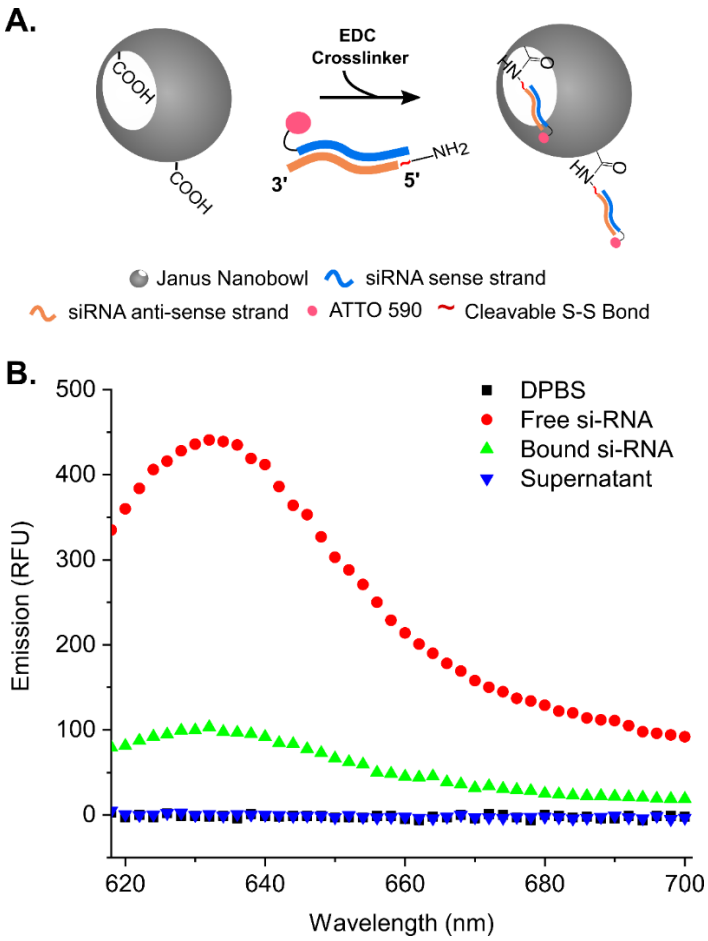

Figure 6.4. Silencing RNA loading on NBs. A. Schematic of silencing RNA loading (chemisorption) on NBs. The 5' end of the anti-sense strand has a cleavable disulfide group and amine terminated functional modification. The 5' end of the sense strand is conjugated to a fluorescent dye (Atto 590). The amine functionality is used to conjugate the silencing RNA to the nanobowl via a carboxyl functionality on the nanobowl using EDC crosslinker chemistry. Without EDC crosslinkers, the same loading protocol would give us physisorbed siRNA. B. Emission spectra in DPBS of free and nanobowl bound siRNA with Atto 590 dye. Nanobowl concentration used here for bound siRNA emission measurements is 1 mg/ml with a 2µg siRNA added, incubated, and washed by centrifugation to remove unbound siRNA. All emission spectra were obtained with a 590 nm excitation and collection of emission at 2 nm resolution. Graph depicts average spectra of triplicate experiments.

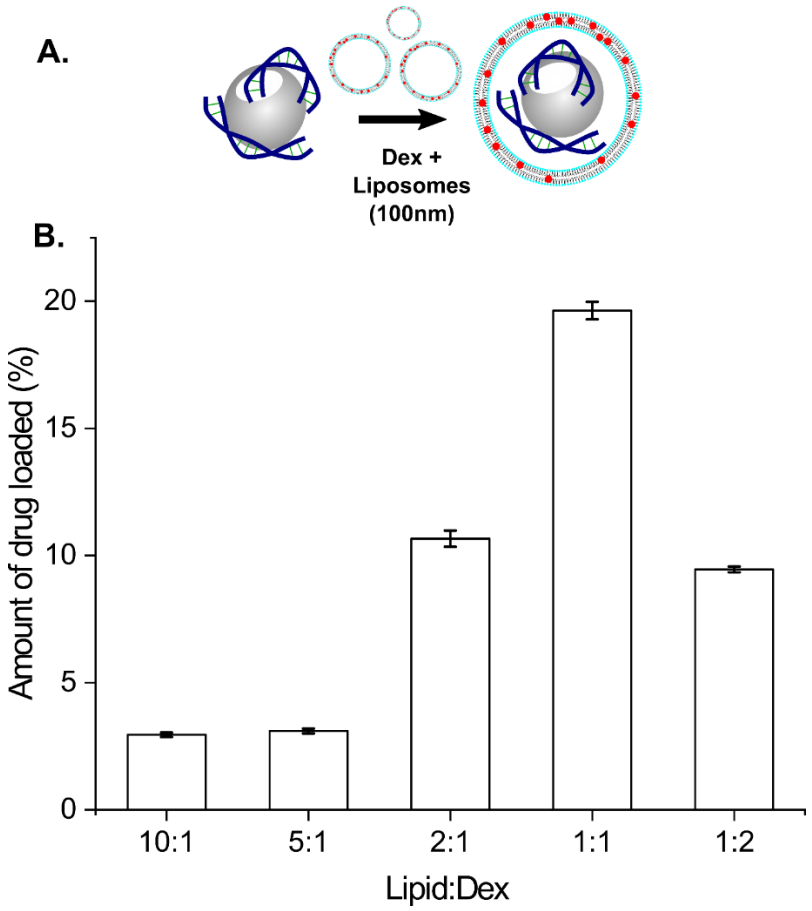

Figure 6.5. Loading of Dexamethasone on DPPC and DOTAP coated NBs. A. Schematic of Dexamethasone (Dex) loading on NBs. Dexamethasone is loaded first on the liposomes and then the Dex loaded liposomes were allowed to mix with NBs for encapsulation. Excess liposomes/free Dex was removed by repeated centrifugal washing in DPBS. B. % of Dex loading (µg of Dex loaded/ µg of Dex loaded + NB mass) is plotted with respect to lipid:Dex ratio.

In the next set of experiments, we determined the release properties of silencing RNA and Dex from the NB system. To determine release of silencing RNA from NBs, we suspended siRNA loaded NBs without lipids in 400 mM DTT containing DTT held at 37^{O}C. The release profile (Fig. 6.6 A) shows that the cumulative amount of siRNA released increases with time and reaches a saturation plateau at around 10% for siRNA physisorbed on NB (black trace), chemisorbed on NBs (red trace) and chemisorbed on magnetic NBs (green trace). However, the release of physisorbed siRNA from magnetic

NBs (blue trace) continues increasing until 48 hrs and has the maximum overall cumulative release (80%) of all types tested.

We also studied the release of Dex from NBs and magnetic NBs (Fig. 6.6 B) at 37^{O}C in buffered aqueous media (DPBS). Our results show that the amount of Dex released at 37^{O}C increased with time for types of NBs and reached saturation release at 4 hrs (magnetic NBs, red trace) and at 18-24 hrs (non-magnetic NBs, black trace). The overall cumulative release of Dex was higher for magnetic NBs (48%) than non-magnetic NBs (27%). Room temperature measurements of 48 hr cumulative release (dashed lines in Fig. 6.6B) show less Dex release than their 37^{O}C counterparts i.e., 25% (magnetic NBs) and 15% (NBs), respectively.

In the next set of experiments, we characterized internalization of siRNA loaded NBs (ATTO 590 tagged) in HEK cell line (Fig. 6.7). Our microscopy images show that there is co-localization of fluorescence from siRNA loaded NB clusters (white arrows, Fig. 6.7) and cell growth clusters 4 hrs post treatment and subsequent washing. This indicates that the internalization of siRNA loaded NBs is very likely. However, as shown in previous chapters, further TEM imaging studies are required for conclusive evidence of internalization.

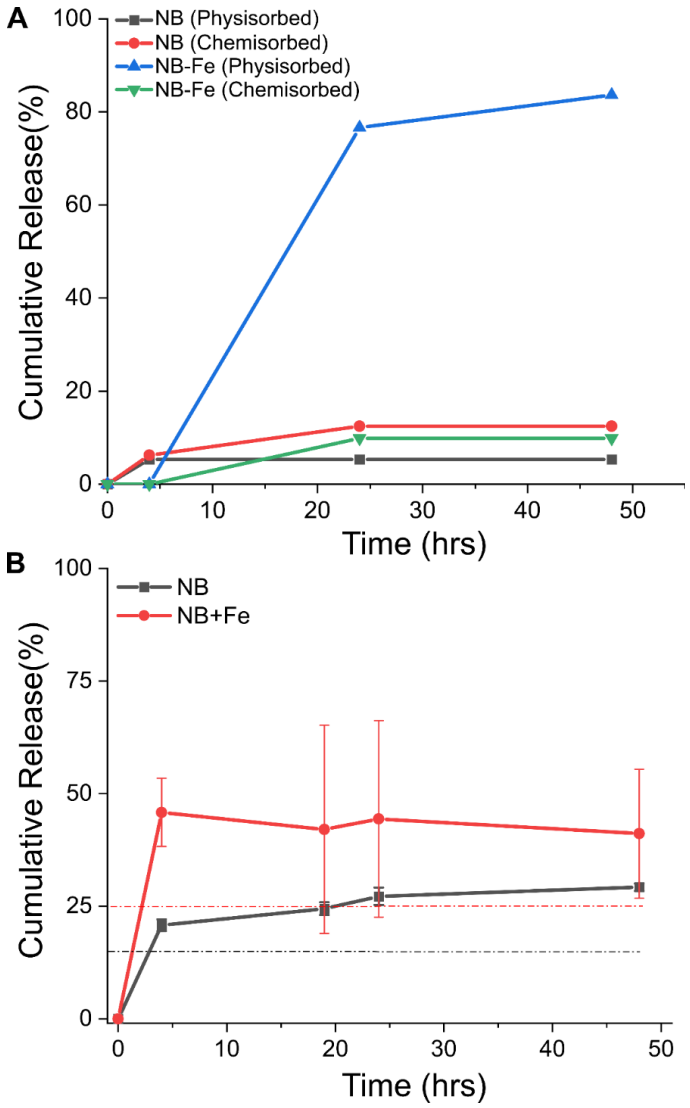

Figure 6.6. 48 hr silencing RNA and Dexamethasone release from NBs. A. Cumulative release over 48 hrs of siRNA bound in different ways to NBs or magnetic NBs with respect to time in DPBS with DTT (400 mM) as the reducing agent at 37°C. B. Cumulative release of FITC labeled Dexamethasone from lipid coated NBs (black line) or magnetic NBs (red line) over a period of 48 hrs in DPBS at 37°C. Error bars indicate standard deviation from 3 experiments. Dotted lines indicates the total release in 48 hrs for NBs (black) and magnetic NBs (red) at room temperature.

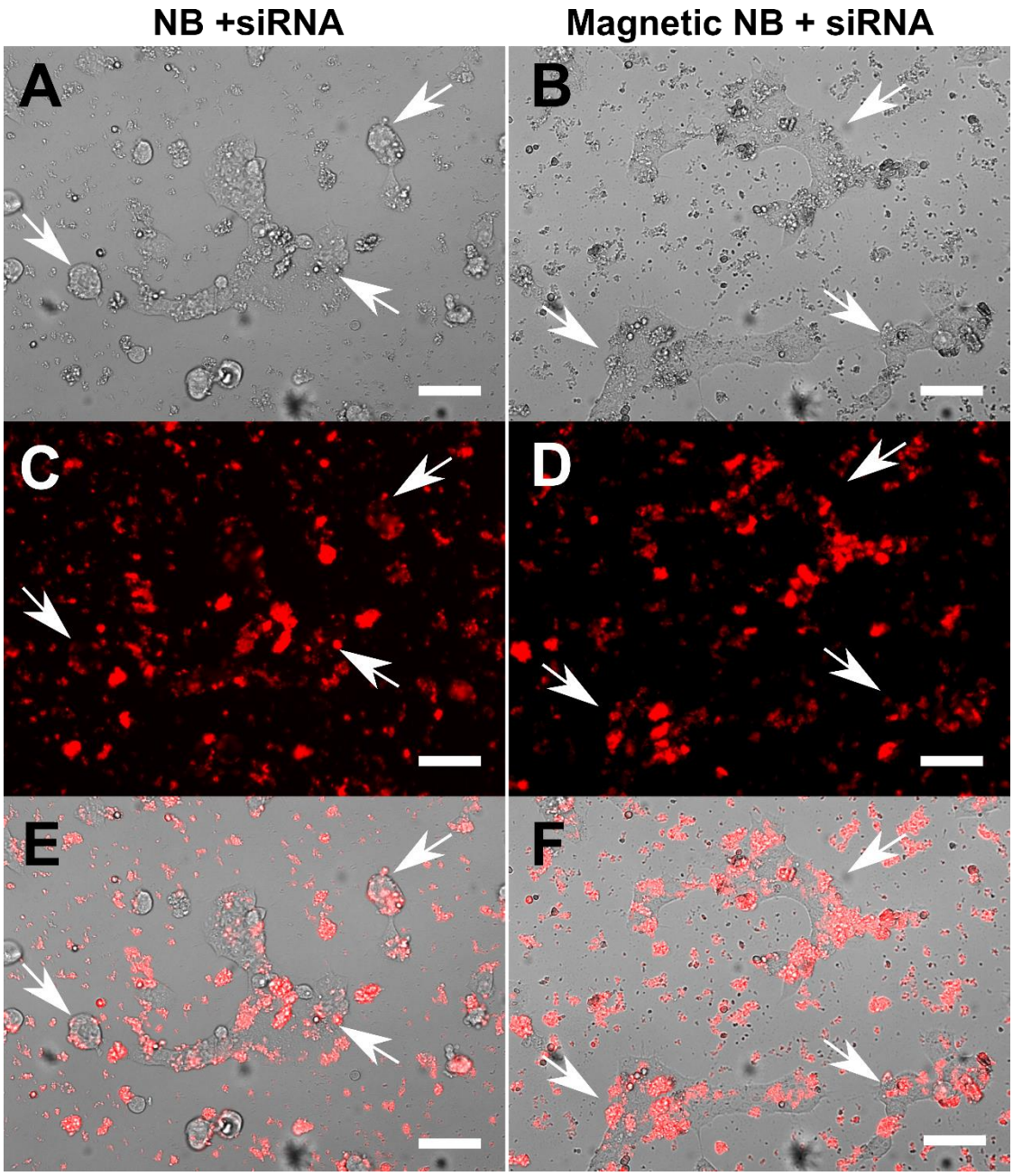

Figure 6.7. Silencing RNA loaded NB delivery in HEK 298 cells. Phase (A,B), fluorescence (C,D) and overlay (E,F) microscopy images of NBs loaded with Atto 590 dye tagged silencing RNA after incubation at 0.25 mg/ml NB for 4 hrs and subsequent washing (three times) with warm supplemented DMEM media. Images were taken with a 10x objective with 590/620 nm filter set up and subsequently pseudo colored. A single field of view representative of 3 repeat experiments is shown here for NB with siRNA (A,C,E) and magnetic NB with siRNA (B,D,F). Arrows indicate clusters of silencing RNA loaded NBs that co-localize with HEK cell clusters on a 35 mm petri dish. Scale bar indicates 100 µm.

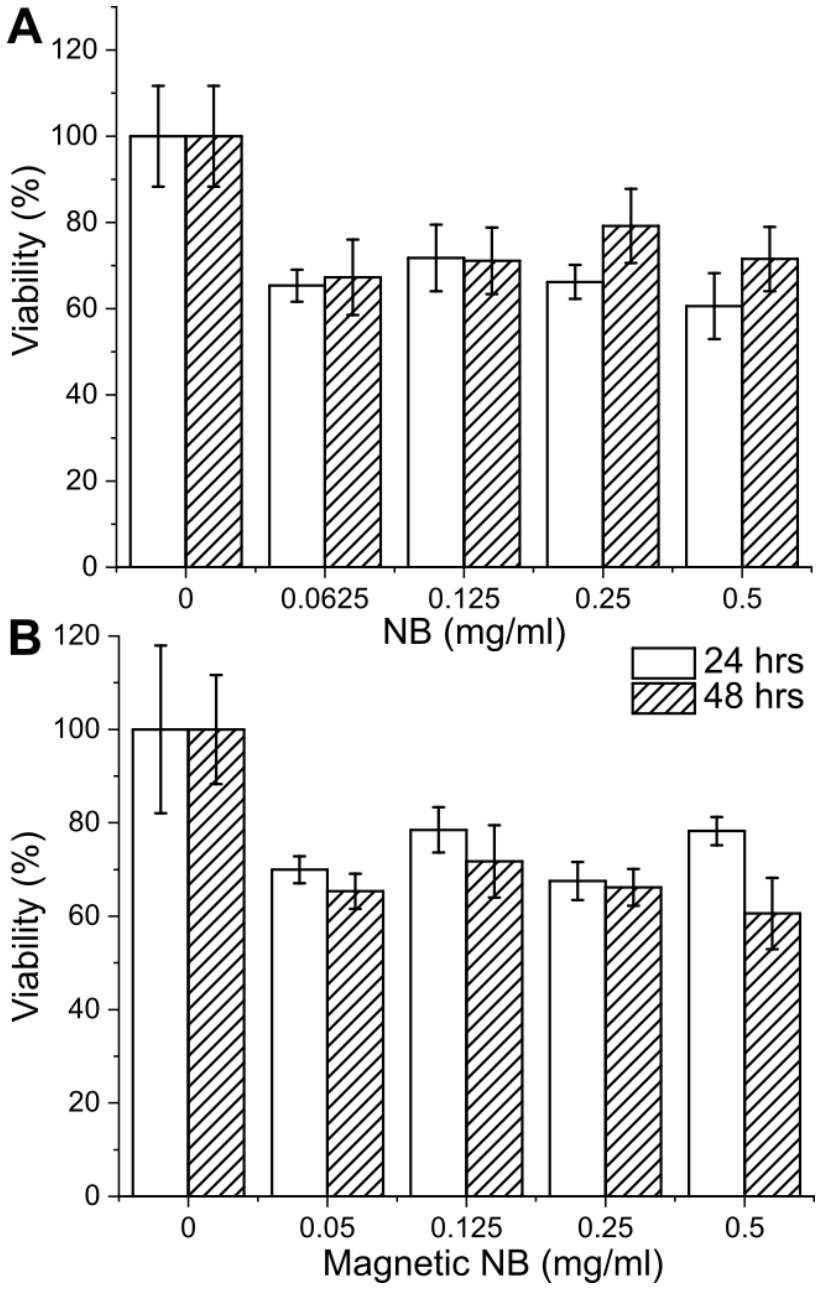

Figure 6.8. Dose dependent 48 hr toxicity of NBs or magnetic NBs with therapeutics. MTT viability (%) with respect to NB doses varying from 0-0.5 mg/ml. All data were normalized to live cell viability which received only buffer (DPBS:Opti-MEM) as treatment. Error bars indicate standard deviation of n=4 experiments. Data shown from siRNA and Dexamethasone loaded (A) NBs and (B) magnetic NBs with lipid coating. NB with only siRNA showed 89% (0.5 mg/ml) to 94% (0.05 mg/ml) viability. Magnetic NBs showed 78% (0.5 mg/ml) to 82% (0.05 mg/ml) viability by themselves and with siRNA showed 83% (0.5 mg/ml) to 90% (0.05 mg/ml), respectively.

Finally, we performed MTT viability assay *in vitro* on HEK cell cultures and determined the toxic exposure to cells at 24 and 48 hrs post treatment with Dex and

siRNA co-loaded LNBs (Fig. 6.8 A) and magnetic LNBs (Fig. 6.8 B). For NBs, we observe that at lower concentrations (0.06 or 0.125 mg/ml) the viability is unchanged 67% and 71%, respectively, between 24 and 48 hrs. At higher concentrations (0.25 and 0.5 mg/ml) ,the 48 hr viability increases to 79% and 71% from 66% and 61%, respectively. For magnetic NBs, the 48 hr viabilities are consistently lower than their 24 hr values (Fig. 6.8 B). Overall, our results show no significant difference between toxicities of siRNA/Dex loaded magnetic and non-magnetic NBs within a 24-48 hrs window.

6.4 Discussion

Our work here lays the foundation of a magnetically triggered siRNA and drug nano-delivery system relevant in Covid19 or other therapeutics. Although we didn't demonstrate actual silencing effect of siRNA-NB conjugate, the siRNA chosen in this study was a 22 base pair sequence designed to target the N-region of the SARS-Cov-2 genomic RNA [16], [22], [38] and tested with BLAST search to prevent overlaps with essential protein coding RNAs.

Our silencing RNA release experiments done over a 48 hr period at 37^{O}C buffered media did not contain RNase inhibitor. This means that the release properties we observed could be underestimated due to varying levels of siRNA degradation during the 48 hr assay. Future work should address this by addition of RNase inhibitor to the buffer in which release properties were tested. SiRNA degradation also prevented us from testing internalization with fluorescence microscopy as incubations >4 hrs seemed to degrade the dye with concomitant loss of fluorescence from the samples. Endosomal entrapment inside an acidic vesicle post internalization may additionally degrade the dye or the siRNA or both. Also, such internalization studies were done with physisorbed

siRNA on amine NBs, encapsulated with lipids. This might also lead to additional diffusion of siRNA away from the NB surface post internalization.

At 4 hrs, our fluorescence microscopy results with 0.5 mg/ml siRNA loaded NBs show the cell morphology was affected by the NB treatment. Our toxicity data show that there is 29-35% HEK cell toxicity of LNB or magnetic LNBs when co-loaded with siRNA and Dex. In Chapter 4, we determined HEK cell toxicity to be ~16% in response to treatment of LNBs in the same concentration range. This indicates that adding siRNA/Dex to the NBs doubles their toxicity to HEK cells. Part of this observation can be explained by the fact that Dexamethasone is a well-known cancer drug which is known to induce apoptosis *in vitro*[39]–[42]. Thus, more characterizations are required (i.e., Dex only, siRNA only loaded LNBs) to further confirm the cause of this higher toxicity. Our results showed that magnetic NB treated HEK cells are 78% (0.5 mg/ml) to 82% (0.05 mg/ml) viable and with siRNA (~ 4µg/mg) show 83% (0.5 mg/ml) to 90% (0.05 mg/ml), respectively.

In our Dex release studies, we have shown that by increasing the temperature from 25^{O}C to 37^{O}C, we could almost double the amount of drug released *in vitro*. The release of the drug occurs likely due to the phase change of the lipid encapsulation layer from ordered gel phase to the disordered liquid crystalline phase. In this case, the DPPC/DOTAP layer had a phase transition temperature around 37^{O}C. However, for *in vivo* applications, 48% release at 37^{O}C i.e., body temperature, will lead to a non-specific loss in the payload. For *in vivo* applications, this design should be modified to include lipids like DSPE with higher transition temperatures (18:0 Phosphatidylethanolamine, T_m

= 74^{O}C). Additionally, application of alternating magnetic field will achieve the local hyperthermia needed for such drug release from NBs.

In conclusion, in Chapter 6, we have shown that the LNB transfection system developed in the earlier chapters can be modified and optimized into a magnetically functionalized siRNA/drug delivery system. Future work will focus on the characterization of this system to optimize post-transcriptional protein silencing effect via the RISC pathway. Clinically, co-delivery of silencing RNA/Dexamethasone is not only relevant in Covid19 but also various types of cancers[40], [41].

Chapter 6, in part, is being prepared for patent application with Dr. Ratneshwar Lal as co-author. The dissertation author was the primary author of this chapter.

6.5 Bibliography

[1] P. Zhou, X. Lou Yang, X. G. Wang, B. Hu, L. Zhang, W. Zhang, H. R. Si, Y. Zhu, B. Li, C. L. Huang, H. D. Chen, J. Chen, Y. Luo, H. Guo, R. Di Jiang, M. Q. Liu, Y. Chen, X. R. Shen, X. Wang, X. S. Zheng, K. Zhao, Q. J. Chen, F. Deng, L. Liu, B. Yan, F. Zhan, Y. Wang, G. Xiao and Z. Shi, “A pneumonia outbreak associated with a new coronavirus of probable bat origin,” *Nature*, vol. 579, no. 7798, pp. 270–273, 2020, doi: 10.1038/s41586-020-2012-7.

[2] S. Khan, R. Siddique, M. A. Shereen, A. Ali, J. Liu, Q. Bai, N. Bashir, and M. Xue, “Emergence of a Novel Coronavirus, Severe Acute Respiratory Syndrome Coronavirus 2: Biology and Therapeutic Options,” 2020, doi: 10.1128/JCM.

[3] B. S. Chhikara, B. Rathi, and J. Singh, “Chemical Biology LETTERS Corona virus SARS-CoV-2 disease COVID-19: Infection, prevention and clinical advances of the prospective chemical drug therapeutics.” Accessed: Nov. 24, 2020. [Online]. Available: http://thesciencein.org/cbl.

[4] R. J. Mason, “Pathogenesis of COVID-19 from a cell biology perspective,” *Eur. Respir. J.*, vol. 55, no. 4, pp. 9–11, 2020, doi: 10.1183/13993003.00607-2020.

[5] “Covid vaccine update: Tracking progress against coronavirus - Washington Post.” https://www.washingtonpost.com/graphics/2020/health/covid-vaccine-update-coronavirus/ (accessed Nov. 24, 2020).

[6] J. Hodgson, “The pandemic pipeline,” *Nat. Biotechnol.*, vol. 38, no. 5, pp. 523–532, May 2020, doi: 10.1038/d41587-020-00005-z.

[7] C. Keech, G. Albert, I. Cho, A. Robertson, P. Reed, S. Neal, J. S. Plested, M. Zhu, S. Cloney-Clark, H. Zhou, G. Smith, N. Patel, M. B. Frieman, R. E. Haupt, J. Logue, M. McGrath, S. Weston, P. A. Piedra, C. Desai, K. Callahan, M. Lewis, P. Price-Abbott, N. Formica, V. Shinde, L. Fries, J.D. Lickliter, P. Griffin, B. Wilkinson, and G.M. Glenn, “Phase 1–2 Trial of a SARS-CoV-2 Recombinant Spike Protein Nanoparticle Vaccine,” *N. Engl. J. Med.*, pp. 1–13, Sep. 2020, doi: 10.1056/nejmoa2026920.

[8] “Covid-19: Oxford University vaccine is highly effective - BBC News.” https://www.bbc.com/news/health-55040635 (accessed Nov. 24, 2020).

[9] M. Wadman, “Will a small, long-shot U.S. company end up producing the best coronavirus vaccine?,” *Science (80-.).*, Nov. 2020, doi: 10.1126/science.abf5474.

[10] R. Medhi, P. Srinoi, N. Ngo, H. V. Tran, and T. R. Lee, “Nanoparticle-Based Strategies to Combat COVID-19,” *ACS Appl. Nano Mater.*, vol. 3, no. 9, pp. 8557–8580, 2020, doi: 10.1021/acsanm.0c01978.

[11] “Nanotechnology versus coronavirus,” *Nat. Nanotechnol.*, vol. 15, no. 8, p. 617, 2020, doi: 10.1038/s41565-020-0757-7.

[12] G. Li and E. De Clercq, “Therapeutic options for the 2019 novel coronavirus (2019-nCoV),” *Nat. Rev. Drug Discov.*, vol. 19, no. 3, pp. 149–150, 2020, doi: 10.1038/d41573-020-00016-0.

[13] S. Talebian, G. G. Wallace, A. Schroeder, F. Stellacci, and J. Conde, “Nanotechnology-based disinfectants and sensors for SARS-CoV-2,” *Nat. Nanotechnol.*, vol. 15, no. 8, pp. 618–621, 2020, doi: 10.1038/s41565-020-0751-0.

[14] E. V. R. Campos, A. E. S. Pereira, J. L. De Oliveira, L. B. Carvalho, M. Guilger-Casagrande, R. De Lima, and L. F. Fraceto, “How can nanotechnology help to combat COVID-19? Opportunities and urgent need,” *J. Nanobiotechnology*, vol. 18, no. 1, pp. 1–23, 2020, doi: 10.1186/s12951-020-00685-4.

[15] M. Lester, A. Sahin, and A. Pasyar, “The use of dexamethasone in the treatment of COVID-19,” *Ann. Med. Surg.*, vol. 56, no. July, pp. 218–219, 2020, doi: 10.1016/j.amsu.2020.07.004.

[16] S. Ghosh, S. M. Firdous, and A. Nath, “Sirna could be a potential therapy for covid-19,” *EXCLI Journal*, vol. 19. Leibniz Research Centre for Working Environment and Human Factors, pp. 528–531, 2020, doi: 10.17179/excli2020-1328.

[17] “Prospects for RNAi Therapy of COVID-19 _ Enhanced Reader.pdf.”

[18] M. D. Shin, S. Shukla, Y. H. Chung, V. Beiss, S. K. Chan, O. A. Ortega-Rivera, D. M. Wirth, A. Chen, M. Sack, J. K. Pokorski, and N. F. Steinmetz, “COVID-19 vaccine development and a potential nanomaterial path forward,” *Nat. Nanotechnol.*, vol. 15, no. 8, pp. 646–655, 2020, doi: 10.1038/s41565-020-0737-y.

[19] “Dexamethasone in Hospitalized Patients with Covid-19 — Preliminary Report,” *N. Engl. J. Med.*, pp. 1–11, 2020, doi: 10.1056/nejmoa2021436.

[20] P. Gonzalez-Alegre, “RNA Interference,” *Encycl. Mov. Disord.*, vol. 418, no. July, pp. 47–49, 2010, doi: 10.1016/B978-0-12-374105-9.00192-1.

[21] R. Kanasty, J. R. Dorkin, A. Vegas, and D. Anderson, “Delivery materials for siRNA therapeutics,” *Nat. Mater.*, vol. 12, no. 11, pp. 967–977, Nov. 2013, doi: 10.1038/nmat3765.

[22] M. R. Islam, M. N. Hoque, M. S. Rahman, A. S. M. R. U. Alam, M. Akther, J. A. Puspo, S. Akter, M. Sultana, K. A. Crandall, and M. A. Hossain, “Genome-wide analysis of SARS-CoV-2 virus strains circulating worldwide implicates heterogeneity,” *Sci. Rep.*, vol. 10, no. 1, pp. 1–9, 2020, doi: 10.1038/s41598-020-70812-6.

[23] J. P. Broughton, X. Deng, G. Yu, C. L. Fasching, V. Servellita, J. Singh, X. Miao, J. A. Streithorst, A. Granados, A. Sotomayor-Gonzalez, K. Zorn, A. Gopez, E. Hsu, W. Gu, S. Miller, C. Y. Pan, H. Guevara, D. A. Wadford, J. S. Chen and C.Y. Chiu, “CRISPR–Cas12-based detection of SARS-CoV-2,” *Nat. Biotechnol.*, vol. 38, no. 7, pp. 870–874, 2020, doi: 10.1038/s41587-020-0513-4.

[24] J. H. Jeong, H. Mok, Y. K. Oh, and T. G. Park, “SiRNA conjugate delivery systems,” *Bioconjug. Chem.*, vol. 20, no. 1, pp. 5–14, 2009, doi: 10.1021/bc800278e.

[25] S. Yonezawa, H. Koide, and T. Asai, “Since January 2020 Elsevier has created a COVID-19 resource centre with free information in English and Mandarin on the novel coronavirus COVID- 19 . The COVID-19 resource centre is hosted on Elsevier Connect , the company ’ s public news and information ,” no. January, 2020.

[26] J. Wang, Z. Lu, M. G. Wientjes, and J. L.-S. Au, “Delivery of siRNA Therapeutics: Barriers and Carriers,” *AAPS J.*, vol. 12, no. 4, pp. 492–503, Dec. 2010, doi: 10.1208/s12248-010-9210-4.

[27] Y. Dong, D. J. Siegwart, and D. G. Anderson, “Strategies, design, and chemistry in siRNA delivery systems,” *Adv. Drug Deliv. Rev.*, vol. 144, pp. 133–147, 2019, doi: 10.1016/j.addr.2019.05.004.

[28] M. S. Draz, B. A. Fang, P. Zhang, Z. Hu, S. Gu, K. C. Weng, J. W. Gray, and F. F. Chen, “Nanoparticle-mediated systemic delivery of siRNA for treatment of cancers and viral infections,” *Theranostics*, vol. 4, no. 9, pp. 872–892, 2014, doi: 10.7150/thno.9404.

[29] S. J. Tan, P. Kiatwuthinon, Y. H. Roh, J. S. Kahn, and D. Luo, “Engineering nanocarriers for siRNA delivery,” *Small*, vol. 7, no. 7, pp. 841–856, 2011, doi: 10.1002/smll.201001389.

[30] B. Kim, J. H. Park, and M. J. Sailor, “Rekindling RNAi Therapy: Materials Design Requirements for In Vivo siRNA Delivery,” *Adv. Mater.*, vol. 31, no. 49, pp. 1–23, 2019, doi: 10.1002/adma.201903637.

[31] G. Sahay, W. Querbes, C. Alabi, A. Eltoukhy, S. Sarkar, C. Zurenko, E. Karagiannis, K. Love, D. Chen, R. Zoncu, Y. Buganim, A. Schroeder, R. Langer, and D. G. Anderson, “Efficiency of siRNA delivery by lipid nanoparticles is limited by endocytic recycling,” *Nat. Biotechnol.*, vol. 31, no. 7, pp. 653–658, 2013, doi: 10.1038/nbt.2614.

[32] B. Esteban-Fernández De Ávila, C. Angell, F. Soto, M. A. Lopez-Ramirez, D. F. Báez, S. Xie, J. Wang, and Y. Chen, “Acoustically Propelled Nanomotors for Intracellular siRNA Delivery,” *ACS Nano*, vol. 10, no. 5, pp. 4997–5005, 2016, doi: 10.1021/acsnano.6b01415.

[33] Á. Artiga, I. Serrano-Sevilla, L. De Matteis, S. G. Mitchell, and J. M. De La Fuente, “Current status and future perspectives of gold nanoparticle vectors for siRNA delivery,” *J. Mater. Chem. B*, vol. 7, no. 6, pp. 876–896, 2019, doi: 10.1039/c8tb02484g.

[34] H. K. Na, M. H. Kim, K. Park, S. R. Ryoo, K. E. Lee, H. Jeon, R. Ryoo, C. Hyeon, and D. H. Min, “Efficient functional delivery of siRNA using mesoporous silica nanoparticles with ultralarge pores,” *Small*, vol. 8, no. 11, pp. 1752–1761, 2012, doi: 10.1002/smll.201200028.

[35] M. Wang, X. Li, Y. Ma, and H. Gu, “Endosomal escape kinetics of mesoporous silica-based system for efficient siRNA delivery,” *Int. J. Pharm.*, vol. 448, no. 1, pp. 51–57, 2013, doi: 10.1016/j.ijpharm.2013.03.022.

[36] C. He, K. Lu, D. Liu, and W. Lin, “Nanoscale metal-organic frameworks for the co-delivery of cisplatin and pooled siRNAs to enhance therapeutic efficacy in drug-resistant ovarian cancer cells,” *J. Am. Chem. Soc.*, vol. 136, no. 14, pp. 5181–5184, 2014, doi: 10.1021/ja4098862.

[37] J. Zhuang, H. Gong, J. Zhou, Q. Zhang, W. Gao, R. H. Fang, and L. Zhang, “Targeted gene silencing in vivo by platelet membrane-coated metal-organic framework nanoparticles,” *Sci. Adv.*, vol. 6, no. 13, 2020, doi: 10.1126/sciadv.aaz6108.

[38] M. A. Marra, S. J. M. Jones, C. R. Astell, R. A. Holt, A. Brooks-wilson, Y. S. N. Butterfield, J. Khattra, J. K. Asano, S. A. Barber, S. Y. Chan, A. Cloutier, S. M. Coughlin, D. Freeman, N. Girn, O. L. Griffith, S. R. Leach, M. Mayo, H. Mcdonald, S. B. Montgomery, P. K. Pandoh, A. S. Petrescu, A. G. Robertson, J. E. Schein, A. Siddiqui, D. E. Smailus, J. M. Stott, G. S. Yang, F. Plummer, A. Andonov, H. Artsob, N. Bastien, K. Bernard, T. F. Booth, D. Bowness, M. Czub, M. Drebot, L. Fernando, R. Flick, M. Garbutt, M. Gray, A. Grolla, S. Jones, H. Feldmann, A. Meyers, A. Kabani, Y. Li, S. Normand, U. Stroher, G. A. Tipples, S. Tyler, R. Vogrig, D. Ward, B. Watson, R. C. Brunham, M. Krajden, M Petric, D. M. Skowronski, C. Upton, and R. L. Roper, “The Genome Sequence of the SARS-Associated Coronavirus,” vol. 300, no. May, pp. 1399–1405, 2003.

[39] K. S. McColl, H. He, H. Zhong, C. M. Whitacre, N. A. Berger, and C. W. Distelhorst, “Apoptosis induction by the glucocorticoid hormone dexamethasone and the calcium-ATPase inhibitor thapsigargin involves Bcl-2 regulated caspase activation,”

Mol. Cell. Endocrinol., vol. 139, no. 1–2, pp. 229–238, 1998, doi: 10.1016/S0303-7207(98)00051-3.

[40] D. Chauhan, P. Pandey, A. Ogata, G. Teoh, S. Treon, M. Urashima, S. Kharbanda, and K. C. Anderson, “Dexamethasone induces apoptosis of multiple myeloma cells in a JNK/SAP kinase independent mechanism,” *Oncogene*, vol. 15, no. 7, pp. 837–843, 1997, doi: 10.1038/sj.onc.1201253.

[41] F. Xu, A. Gardner, Y. Tu, P. Michl, D. Prager, and A. Lichtenstein, “Multiple myeloma cells are protected against dexamethasone-induced apoptosis by insulin-like growth factors,” *Br. J. Haematol.*, vol. 97, no. 2, pp. 429–440, 1997, doi: 10.1046/j.1365-2141.1997.592708.

[42] C. M. Jacobs, M. D. Trinh, T. Rootwelt, J. Lømo, and R. E. Paulsen, “Dexamethasone induces cell death which may be blocked by NMDA receptor antagonists but is insensitive to Mg2+ in cerebellar granule neurons,” *Brain Res.*, vol. 1070, no. 1, pp. 116–123, 2006, doi: 10.1016/j.brainres.2005.10.093.

Chapter 7

Conclusions and future work

7.1 Conclusions

In this work, we have outlined the development and characterization of a novel non-viral delivery gene delivery system with a lipid-silica hybrid nanomaterial called lipid encapsulated silica nanobowls (LNB). In this chapter, I will recapitulate its various properties, advantages, disadvantages, and future work that can be done with this system.

Cellular & tissue internalization

In summary, we have shown that the LNB system can successfully get internalized in a dose dependent, non-specific manner (0.05-1 mg/ml) *in vitro* in 4 different cell lines and acutely dissociated DRG neurons. Higher LNB concentrations show higher uptake *in vitro* and maximum uptake is observed for all cell lines at 1 mg/ml. The overall uptake efficiency eventually dictates the transfection efficiency and therefore improvement in the efficiency of uptake is one of the ways to improve the system. Other studies have shown that silica nanoparticles get endocytosed at different rates at different sizes, the uptake being less efficient as the hydrodynamic diameter increases [1]. Assuming this trend holds for LNBs as well, one way to improve uptake efficiency is to reduce the core size of the NB in the LNB system. Previous work has shown that NB core size is tunable by using different polystyrene core sizes [2]. In this work, we used a 100 nm PS core, however, 50

nm core-based NB synthesis is possible, and those NBs will have a lower hydrodynamic diameters and likely a better cellular uptake efficiency.

Ex vivo experiments also show successful LNB internalization in neurons of whole DRG tissues, although the LNBs were unable to successfully penetrate the meningeal layer outside of the whole DRG tissue and their transport inside the tissue was aided by dissolution of the connective tissue by pre-treatment with DMSO. Local *in vivo* injections showed that the NBs could successfully get internalized in DRG neurons post injection near the L4 and L5 of the rat spinal cord. Further tissue dissociations showed uptake by individual neurons. Rat salivary gland also showed successful uptake of Cy3-tagged NBs that were injected locally. These results show that NB uptake is fast (happens within 4 hrs of treatment and can retain up to at least 24 hrs) and ubiquitous cells of various origins.

Biocompatibility

The MTT and flow cytometry assays, which measured LNB toxicity with or without DNA loading, showed that cell viability was greater than 80% at the concentration (0.5 mg/ml) employed. When compared to the commercially available Lipofectamine 2000, the viability measured via flow cytometry was approximately 70%. Nevertheless, the toxicity measured for LNBs (92.4%) was lower than for Lipofectamine 2000 (70%) with comparable transfection efficiencies as evaluated with fluorescence microscopy

Transfection efficiency

We have characterized the transfection efficiency of the NB system in 4 different ways (a) Fluorescence microscopy (b) Western blotting (c) Flow Cytometry (d) Recapitulation of functional coupling between GIRK-opioid receptors in HEK cells. Our fluorescence microscopy and flow cytometry results showed about 10% transfection efficiency at the optimized LNB concentration (mg/ml). These experiments determined the expression by presence or absence of fluorescence from the reporter gene clover. In the case of fluorescence microscopy, the images only gave us a qualitative idea about transfection efficiency. On the other hand, while flow cytometry was quantitative, about 30% of healthy cell population was discarded from analysis of clover expression because of them being larger cell clusters (only single cells could be counted). However, from flow cytometry, we find that at the most optimized NB dosage (0.5 mg/ml), we get 10% transfection efficiency with 90% viability calculated from single cell population only, whereas, with Lipofectamine we get 15% transfection with 70% viability. This result highlights that although we get 33% less transfection than Lipofectamine, LNBs are less toxic by 29%. However, we did not optimize the Lipofectamine dosage conditions for our cell culture conditions and simply used it as a positive control for flow cytometry. The Western blotting technique did allow us to determine clover expression levels (Chapter 4) and the results demonstrated a very good signal. Finally, the FlexStation 3 results (Chapter 5) suggest that pharmacological studies can still be performed with the transfection efficiency we obtained. That is, expression levels for both opioid receptors and GIRK channels were sufficient to obtain functional coupling of G protein coupled receptors with ion channels. The pharmacological parameters determined were

comparable to published reports[3]–[6]. However, the transfection efficiency of the LNB system can be improved with future work.

Payload agnostic

We have shown that the NB system is versatile and payload agnostic. It can be used for condensation and loading of (a) supercoiled DNA (b) linearized DNA (c) mRNA (d) silencing RNA (e) hydrophobic drugs. The ability to successfully load, release and cause *in vitro* protein expression with linearized constructs is particularly useful as linearized constructs can be relevant for the generation of stable cell lines for clinical research[7], pharmacology[8], [9], CAR-T immunotherapy[10], etc. as well as for vaccine development[11].

Controlled release of DNA and drugs

In this work, we showed that linearized DNA and silencing RNA can be conjugated to the NB surface with cleavable chemistries like disulfide bonds which can be broken by intracellular molecules like Glutathione (GSH). Our *in vitro* results show that controlled release of DNA and siRNA was possible from the NB surface with reducing agents like DTT. We also showed that the type of conjugation chemistry on linearized DNA determines the relative amounts of physisorption and chemisorption as well as the overall amount of DNA released. However, all types of conjugation chemistries led to successful transfection in HEK cells with varying efficiencies, lesser than their unfunctionalized linearized DNA counterparts by a factor of 2 (Wes clover/vinculin ratios, Chapter 5). In Chapter 6, we have also shown that in addition to silencing RNA, hydrophobic drugs like

Dexamethasone (Dex) can also be incorporated in the lipid coating of the LNBs. This led to the ability to release Dex by disruption of the lipid bilayer with heat. In our results, we have shown that increasing the ambient temperature from 25^{o}C to 37^{o}C led to almost twice as much Dex release in both magnetic and non-magnetic NBs. This suggests that if we were to use, say, an alternating magnetic field near the magnetic NBs and caused local hyperthermia, we would increase drug release even more. Also, incorporation of pH sensitive polymers[12] like pNIPAM can also lead to pH-controlled release as the NBs get endocytosed into acidic vesicles.

Ability to carry multiple genetic constructs

Our results showed that NBs can be used to load supercoiled as well as linearized DNA constructs at high loading efficiencies i.e., 11 µg/mg supercoiled clover, 25 µg/mg linearized clover and 2-5 µg/mg silencing RNA. The loading saturates for supercoiled DNA but does not for linearized constructs. Our calculations suggest that supercoiled DNA has the least amount of copy number per mg NB, 4 times as much for linearized DNA and 80 times as much for double stranded silencing RNA. These results suggest that different constructs have different interactions on the NB surface and likely to adopt different adsorption conformations at the interface. Furthermore, post adsorption, the NB surface becomes more negatively charged as we showed that post-clover plasmid adsorption at 10 µg/mg, the zeta potential changes from +37 mV to -49 mV. We also showed that NBs can carry 3 different supercoiled constructs (Chapter 5) when loaded simultaneously and also lead to successful co-expression of all the proteins coded by

them which, in turn, can also show their expected functional coupling in HEK cells in response to opioid doses.

Incorporation of magnetic functionality

In Chapter 6, we showed that NBs can be functionalized with superparamagnetic iron oxide nanoparticles to confer on them the ability to be magnetized. Although such functionalization has been shown with these NBs before, this is the first time it was shown that such magnetic NBs can be used for silencing RNA/drug loading and controlled release. This means that the NB system under development in Chapter 6 can be used, in theory, in conjunction with external magnetic fields for localization and guiding *in vivo* as well as for inducing local hyperthermia for drug release. Magnetic properties can also enable such NB system to be used for diagnostics like MRI. The saturation in NB magnetization was obtained ~5000 Oe which translates to 0.5T (in air) magnetic field, which is within the bounds of clinically acceptable values in MRI (0.5-3 T).

7.2 Future work

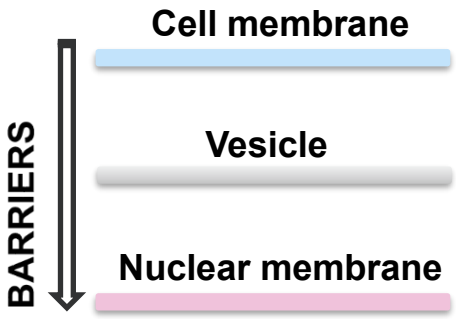

Figure 7.2.1. Improvement strategies of LNB design linked to the barriers to nucleic acid delivery. The first barrier to transfection is the cell membrane, followed by vesicular entrapment/release and then the nuclear membrane (true for DNA delivery only).

Future work will consist of improving the transfection efficiency of this system by adding complexities/modifications to the LNB design to improve efficiency of overcoming the barriers shown in Figure 7.1. To improve passage through the cell membrane i.e., NB uptake efficiency, we could use smaller NB core size, add targeting proteins to access the receptor mediated endocytosis pathway as well and add stabilizing polymers on the outer layer of the LNB to improve colloidal stability so a greater number of cells could come in contact with the LNBs in a given concentration. To improve escape from vesicular entrapment, we can tune the compositional ratio of DOPE to DOTAP and/or add pH buffering polymers or endosomolytic peptides like H5WYG. Further, to help the nuclear membrane delivery of DNA, we can tune the NB surface charge density for optimal release kinetics post endosomal release. To demonstrate the effect of lipid composition tuning and addition of polymeric component into the lipid encapsulation layer of the LNBs, we transfected HEK cells with LNBs coated with 1:1 DOPE:DOTAP or 1:1:0.1 DOPE:DOTAP:DOPE-PEG. Our results (Fig. 7.2) show that there is some improvement in the transfection efficiency of clover expression *in vitro* as determined qualitatively using fluorescence microscopy. To quantitatively measure and compare protein expression with the two different types of lipid compositions on LNBs, we need assays like flow cytometry and/or Western Blotting as demonstrated in previous chapters. Nevertheless, this shows a possible starting point for future improvements in the LNB design. The DOPE-PEG used here had an NHS terminal group which will further allow us to conjugate proteins/peptides for targeting or endosomolytic properties using their primary amines.

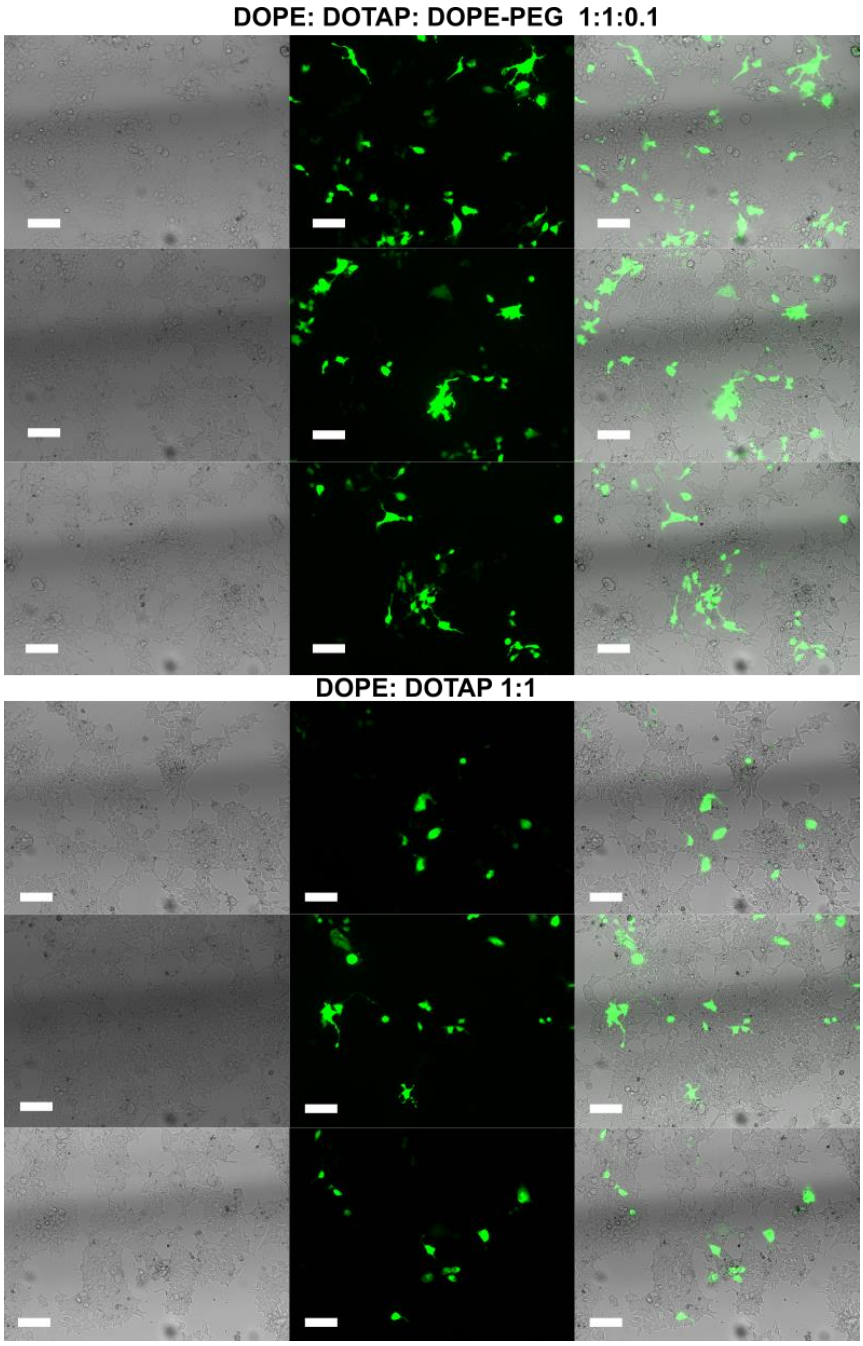

Figure 7.2.2. Effect of tuning lipid encapsulation layer composition on the transfection efficiency of LNBs. Phase (left), fluorescence (center) and overlay (right) microscopy images HEK cells 48 hrs post transfection with 0.25 mg/ml LNB acquired with a 10x objective. Top set of images show LNBs coated with 1:1:0.1 DOPE:DOTAP:DOPE-PEG while the bottom set represents the usual LNB formulation from Chapters 4-5 with 1:1 DOPE:DOTAP. 3 different fields of view are shown representative of 2 independent measurements. Scale bar indicates 50 µm. Check Chapter 4 (methods section) for more details.

Future work will also focus on leveraging the engineered cavity for loading SPIONS, small molecule drugs, etc. which are small enough to fit, while leaving the outer surface for DNA/RNA/siRNA loading. We have shown here that NBs can be delivered *in vivo* in neurons and salivary glands as well as optimized the LNB system for successful *in vitro/ex vivo* transfections. The silencing RNA delivery work (Chapter 6) will have a possible future direction in demonstrating, quantifying, and optimizing the silencing properties of NBs targeted towards a specific protein of interest. Future work will also explore *in vivo* transfections with LNBs in these target organs, and characterization of biodistribution and clearance of the LNB system *in vivo*.

7.3 Bibliography

[1] Q. Gan, D. Dai, Y. Yuan, J. Qian, S. Sha, J. Shi, and C. Liu, “Effect of size on the cellular endocytosis and controlled release of mesoporous silica nanoparticles for intracellular delivery,” *Biomed. Microdevices*, vol. 14, no. 2, pp. 259–270, 2012, doi: 10.1007/s10544-011-9604-9.

[2] A. H. Mo, P. B. Landon, C. D. Emerson, C. Zhang, P. Anzenberg, S. Akkiraju, and R. Lal, “Synthesis of nano-bowls with a Janus template,” *Nanoscale*, vol. 7, no. 2, pp. 771–775, Jan. 2015, doi: 10.1039/c4nr05153j.

[3] D. A. Volpe, G. A. M. M. Tobin, R. D. Mellon, A. G. Katki, R. J. Parker, T. Colatsky, T. J. Kropp, and S. L. Verbois, “Uniform assessment and ranking of opioid Mu receptor binding constants for selected opioid drugs,” *Regul. Toxicol. Pharmacol.*, vol. 59, no. 3, pp. 385–390, Apr. 2011, doi: 10.1016/j.yrtph.2010.12.007.

[4] A. Knapman, M. Santiago, Y. P. Du, P. R. Bennallack, M. J. Christie, and M. Connor, “A continuous, fluorescence-based assay of μ-opioid receptor activation in AtT-20 cells,” *J. Biomol. Screen.*, vol. 18, no. 3, pp. 269–276, Mar. 2013, doi: 10.1177/1087057112461376.

[5] B. J. Vliet, A. H. Mulder, and A. N. M. Schoffelmeer, ?“-Opioid Receptors Mediate the Inhibitory Effect of Opioids on Dopamine-Sensitive Adenylate Cyclase in Primary Cultures of Rat Neostriatal Neurons,” *J. Neurochem.*, vol. 55, no. 4, pp. 1274–1280, Oct. 1990, doi: 10.1111/j.1471-4159.1990.tb03135.x.

[6] M. K. Pugsley, E. J. Yu, and A. L. Goldin, “U-50,488H, a Kappa Opioid Receptor Agonist, is a More Potent Blocker of Cardiac Sodium Channels than Lidocaine,” 2000.

[7] K. Büssow, “Stable mammalian producer cell lines for structural biology,” *Curr. Opin. Struct. Biol.*, vol. 32, no. Table 1, pp. 81–90, 2015, doi: 10.1016/j.sbi.2015.03.002.

[8] B. A. Jordan, S. Cvejic, and L. A. Devi, “Opioids and their complicated receptor complexes,” *Neuropsychopharmacology*, vol. 23, no. 4, pp. S5–S18, 2000, doi: 10.1016/S0893-133X(00)00143-3.

[9] E. Malatynska, Y. Wang, R. J. Knapp, S. Waite, S. Calderon, K. Rice, V. J. Hruby, H. I. Yamamura, and W. R. Roeske, “Human delta opioid receptor: Functional studies on stably transfected Chinese hamster ovary cells after acute and chronic treatment with the selective nonpeptidic agonist SNC-80,” *J. Pharmacol. Exp. Ther.*, vol. 278, no. 3, pp. 1083–1089, 1996.

[10] X. Wang and I. Rivière, “Clinical manufacturing of CAR T cells: Foundation of a promising therapy,” *Molecular Therapy - Oncolytics*, vol. 3. p. 16015, 2016, doi: 10.1038/mto.2016.15.

[11] F. Kendirgi, N. E. Yun, N. S. Linde, M. A. Zacks, J. N. Smith, J. K. Smith, H. McMicken, Y. Chen, and S. Paessler, “Novel linear DNA vaccines induce protective immune responses against lethal infection with influenza virus type A/H5N1,” *Hum. Vaccin.*, vol. 4, no. 6, pp. 410–419, 2008, doi: 10.4161/hv.4.6.6177.

[12] G. Kocak, C. Tuncer, and V. Bütün, “PH-Responsive polymers,” *Polym. Chem.*, vol. 8, no. 1, pp. 144–176, 2017, doi: 10.1039/c6py01872f.